

*Electrochemical and Shell-isolated
Nanoparticle Enhanced Raman Spectroscopy
(SHINERS) Approaches to Probing Novel
Catalytic Nanomaterials*



Oliver Donovan-Sheppard M.Sc.

Department of Chemistry

Cardiff University

A thesis submitted for the degree of

Doctor of Philosophy

December 2018

Acknowledgements

Firstly, I would like to thank my supervisors, Professor Gary Attard, Dr Andy Wain and Professor Damien Murphy for the support and guidance throughout my PhD.

I would also like to thank the many members of the electrochemical surface science group at Cardiff University, who helped create a productive and enjoyable working environment. Specifically, I would like to thank Dr Peter Jenkins, Dr Ashley Brew and Dr Katherine Hunter for helping me learn the foundations of electrochemistry and how to apply this in a practical sense. I would also like to thank Dr Shaoliang Guan for teaching me the SHINERS method and for his input on collaborative projects.

Finally, I would like to thank my family for the great support and patience they gave to me throughout my PhD study.

Abstract

The surface sensitivity of asymmetric catalytic hydrogenation was investigated by utilising platinum single crystal surfaces and a novel in-situ analytical combination of cyclic voltammetry and shell-isolated nanoparticle enhanced Raman spectroscopy (SHINERS). The adsorption behaviour of aqueous Ethyl Pyruvate (EP) on a range of well-defined platinum surfaces, both with and without the presence of electrolytically evolved hydrogen and the chiral modifier Cinchonidine (CD), was monitored by both cyclic voltammetry and Raman spectroscopy. Two key surface intermediates of Ethyl Pyruvate (EP) were identified, the first being the half-hydrogenated state (HHS), reported previously by Attard *et al.* This intermediate is formed by the addition of a hydrogen atom to the keto-carbonyl group. The presence of second intermediate was also detected, this new species was not present in previous surface enhanced Raman spectroscopy (SERS) spectra and is attributed to chemisorbed EP bound in the μ_2 (C, O) configuration. The degree of surface occupation of each intermediate was shown to be sensitive to the structure of the catalyst surface. The new μ_2 (C, O) adsorbate was solely present in large quantities on pristine Pt{111} and Pt{100} surfaces. The HHS was only detected in the spectra on these surfaces after the introduction of low coordination defect sites through electrochemical roughening. Similar spectra were produced for intrinsically defected surfaces Pt{110}, Pt{321} and Pt{721}. This was an indicator that for the HHS to form, low coordination sites on the catalyst surface are required. The differing populations of both the intermediate states was further investigated by density functional theory (DFT) calculations, which supports the findings. The μ_2 (C, O) state was found to have an appreciably higher stability on the Pt{111} in comparison to the Pt{221} surface. A mechanism was proposed that the μ_2 (C, O) EP adsorbate was a precursor to the HHS, with the rates of hydrogen addition on the different surfaces impacting on the population of each adsorption state. With a slow rate of addition of the first hydrogen leading to a low steady-state population of the HHS on terrace sites. The impact of these findings was discussed with regards to enantioselective catalysis and catalyst design.

The in-situ combination of cyclic voltammetry and SHINERS was applied to shape-controlled platinum nanoparticles, a more realistic catalytic system and a new asymmetric hydrogenation of α,β -unsaturated aldehydes with limited success. The potential and issues with this analytical approach are also discussed in depth.

Abbreviations

AES	Auger electron spectroscopy
AFM	Atomic force microscopy
APTMS	(3-Aminopropyl) trimethoxysilane
ATR-IRS	Attenuated total reflectance – infrared spectroscopy
BCC	Body centred cubic
BET	Brunauer–Emmett–Teller
CALD	Cinnamaldehyde
CD	Cinchonidine
COL	Cinnamyl alcohol
CV	Cyclic voltammetry
CVD	Chemical vapour deposition
DFT	Density functional theory
ee	Enantiomeric excess
EL	Ethyl lactate
EP	Ethyl pyruvate
FCC	Face centred cubic
HCALD	Hydrocinnamaldehyde
HCP	Hexagonal close pack
HER	Hydrogen evolution reaction
HHS	Half hydrogenated state
HOMO	Highest occupied molecular orbital
HREELS	High-resolution electron energy loss spectroscopy
H _{UPD}	Hydrogen under potential deposition
I.D.	Inner diameter
IHP	Inner Helmholtz plane
IR	Infrared
IRRAS	Infrared reflection absorption spectroscopy
LEED	Low-energy electron diffraction
LSPR	Localized surface plasmon resonance
LUMO	Lowest unoccupied molecular orbital
MP	Methyl pyruvate
NEXAFS	Near edge x-ray absorption fine structure
NIR	Near infrared
O.D.	Outside diameter
OHP	Outer Helmholtz plane

ORR	Oxygen reduction reaction
OTE	Optically transparent electrode
PAA	Polyacrylic acid (sodium salt)
PBE	Perdew-Burke-Ernzerhof
PEM	Proton exchange membrane
PEMFC	Proton exchange membrane fuel cell
PTFE	Polytetrafluoroethylene
RAIRS	Reflection-absorption infrared spectroscopy
RDE	Rotating disk electrode
SC	Simple cubic
SEC	Spectroelectrochemistry
SEM	Scanning electron microscopy
SERS	Surface enhanced Raman spectroscopy
SFG	Sum frequency generation
SHINERS	Shell isolated nanoparticle enhanced Raman spectroscopy
STM	Scanning tunnelling microscopy
TEM	Transmission electron microscopy
TOF	Turnover frequency
UHV	Ultra-high vacuum
UV	Ultraviolet
VASP	Vienna ab initio simulation package
VIS	Visible
XANES	X-ray absorption near edge structure
XPS	X-ray photoelectron spectroscopy
XRD	X-ray diffraction

Table of Contents

Abbreviations.....	4
Chapter 1 – Introduction.....	9
1.1 Perspective of Early Catalysis.....	9
1.2 Fundamentals of heterogeneous catalysis	10
1.3 Hydrogenation Catalysis	11
1.4 Selectivity in Catalysis – Asymmetric Catalysis	13
1.5 Catalyst Structure.....	17
1.6 Catalyst Support.....	19
1.7 Surface Science	24
1.8 Surface Orientated Analytical Techniques.....	26
1.9 Raman Spectroscopy.....	27
1.10 Electrocatalysis.....	29
1.11 Electrochemistry	33
1.12 Spectroelectrochemistry.....	35
1.13 Shape Controlled-Nanoparticles	38
1.14 References	42
Chapter 2 – Theoretical Background	51
2.1 Surface Structure	51
2.1.1 Structure of well-defined surfaces.....	51
2.1.2 Single crystal surfaces	53
2.1.3 Miller index notation	54
2.2 Shape controlled nanoparticles	56
2.2.1 The Role of Capping Agents	58
2.3 Adsorption	59
2.4 Cyclic Voltammetry	61
2.4.1 Electrochemical Processes.....	62
2.4.2 Electrochemical Double Layer.....	64
2.4.3 CV of Polycrystalline Platinum	66
2.4.4 CV of Platinum Single Crystal Electrodes and Shaped Nanoparticles.....	69
2.5 Raman Spectroscopy.....	71
2.5.1 Raman Spectroscopy - Light Scattering.....	71
2.5.2 Surface Enhanced Raman Spectroscopy (SERS).....	76
2.5.3 Surface selection rules	78

2.5.4 Fluorescence	79
2.6 References	81
Chapter 3 – Experimental	84
3.1 introduction	84
3.2 Cyclic Voltammetry	84
3.3 The Spectroelectrochemical Flowcell	85
3.4 Au@Pt Core-shell Nanoparticle Synthesis	87
3.5 Au@SiO ₂ Core-shell Nanoparticle Synthesis.....	87
3.6 SERS and SHINERS Preparation Procedure	89
3.7 Shaped Pt Nanoparticle Synthesis methods.....	92
3.8 Collaborative data.....	95
3.9 References	96
Chapter 4 - Enantioselective Hydrogenation of Ethyl Pyruvate	97
4.1 - Literature review.....	97
4.1.1 Proposed Adsorption States of EP on Platinum Surfaces	97
4.1.2 Proposed Interactions Between EP and the Alkaloid Modifier.....	101
4.1.3 Electrochemical Investigation of EP Hydrogenation on Pt Basal Planes.....	108
4.2 - Results.....	109
4.2.1 Raman and SERS Investigation of EP Hydrogenation on Polycrystalline Pt.....	109
4.2.2 SHINERS Investigation of EP Hydrogenation on Pt Basal Planes	112
4.2.3 SHINERS Investigation of EP Hydrogenation on High Index Pt Surfaces.....	115
4.2.4 DFT Modelling and Calculations of EP Adsorption on Terrace and Step Sites.....	120
4.3 Discussion.....	125
4.4 Conclusion.....	127
4.5 References	127
Chapter 5 - Ethyl Pyruvate Hydrogenation on Shape Controlled Pt Nanoparticles.....	132
5.1 Literature Review	132
5.1.1 Shaped Platinum Nanoparticles.....	132
5.2 Results.....	134
5.2.1 Characterisation of shaped Pt nanoparticles.....	134
5.2.2 Spectroscopic analysis of EP adsorption on Pt shaped nanoparticles	140
5.3 Discussion.....	144
5.4 Conclusion.....	146
5.5 References	147
Chapter 6 - Selective Hydrogenation of α,β Unsaturated Aldehydes.....	150
6.1 Literature review.....	150

6.1.1 Reaction Pathway for the hydrogenation of α,β -unsaturated Aldehydes.....	150
6.1.2 Adsorption of α,β -unsaturated Aldehydes on Pt surfaces.....	151
6.1.3 Selective Hydrogenation of Cinnamaldehyde.....	154
6.1.4 Influence of the Catalyst and Support on Selectivity.....	156
6.1.5 Influence of Substituent Groups on Selectivity.....	157
6.2 Results and Discussion	159
6.2.1 Cyclic Voltammetry Investigation into Cinnamaldehyde adsorption	159
6.2.2 Cyclic Voltammetry Investigation into Cinnamyl Alcohol and Hydrocinnamaldehyde Adsorption.	162
6.2.2 SERS Investigation of Cinnamaldehyde Hydrogenation on Platinum	165
6.3 Conclusion and further work	168
6.4 - References	169
Chapter 7 - Conclusion.....	172
7.1 Introduction	172
7.2 Hydrogenation of Ethyl Pyruvate.....	172
7.3 Further Work.....	174
7.4 References	176

Chapter 1 – Introduction

1.1 Perspective of Early Catalysis

The earliest instances of metallic catalyst research can be traced back to pre-1800, with both Joseph Priestley and Martinus van Marum independently observing the dehydrogenation of alcohol on metal catalysts(1). The role of the metal in this reaction was reduced to being a heat source; in 1813, Louis Jacques Thénard discovered that ammonia is decomposed into nitrogen and hydrogen when passed over various red-hot metals(2). 10 years later with assistance from Pierre Dulong, Thénard discovered differing reaction rates when using several different metals(3). This appears to be the earliest reported activity in catalysis and can be classed as the first real recognition of heterogeneous catalysis. However, the term “catalysis” was not introduced until Berzelius(4). He proposed the presence of a catalytic force, which facilitated catalysis through the decomposition of various bodies.

Through collaboration on an international scale catalysis developed expeditiously over the coming decades. With strong socioeconomic influences, industrial scale catalysis was an essential aim. A particular issue was the production of ammonia for fertiliser, which relied on an inadequate coal extraction process for ever increasing populations(5). Attempts at fixation of atmospheric nitrogen through various routes were disfavoured due to the large energy requirements(6, 7). Interest in a direct synthesis route was enhanced by work from Heri-Louis Le Chatelier on reaction equilibrium and thermodynamics of ammonia synthesis(8). Unfortunately, an explosion ended his research on this topic, but a prominent German chemist Fritz Haber took up the mantle. After significant research and motivated by a fierce rivalry with Walther Nernst, Haber presented a high pressure ammonia synthesis method utilising an Osmium catalyst to BASF researchers in 1910(9, 10). Whilst this represented a ground-breaking discovery, considerable further developments were needed to make the synthesis viable on an industrial scale. Bosch and Mittasch undertook this project for BASF, and not only were high pressure developments required, a more suitable catalyst also needed to be identified. The new catalyst developed was an iron catalyst with a

small amount of aluminium; the revised industrial synthesis of ammonia was introduced by Bosch in 1913(11). Both Haber and Bosch received Nobel prizes for their contributions. This prompted the wide-scale production of ammonia with modern ammonia production plants still utilising this principal world-wide (as of 2010, 131 million tonnes of ammonia were produced) (12).

1.2 Fundamentals of heterogeneous catalysis

Looking into catalysis from a fundamental perspective, a catalyst provides an alternative path for a chemical reaction which is more complex and has a lower activation energy in comparison to an uncatalyzed reaction. The overall change in free energy of the catalysed reaction is equal to that of the uncatalyzed reaction, demonstrating that a catalyst won't change the thermodynamics of a reaction, only the kinetics. Figure 1 demonstrates the differences between catalysed and uncatalyzed reactions and breaks down the catalysed reaction to three important phases: the bonding of the reactants to the catalyst, the reaction on the catalyst surface to form the product and the separation of the product from the catalyst surface.

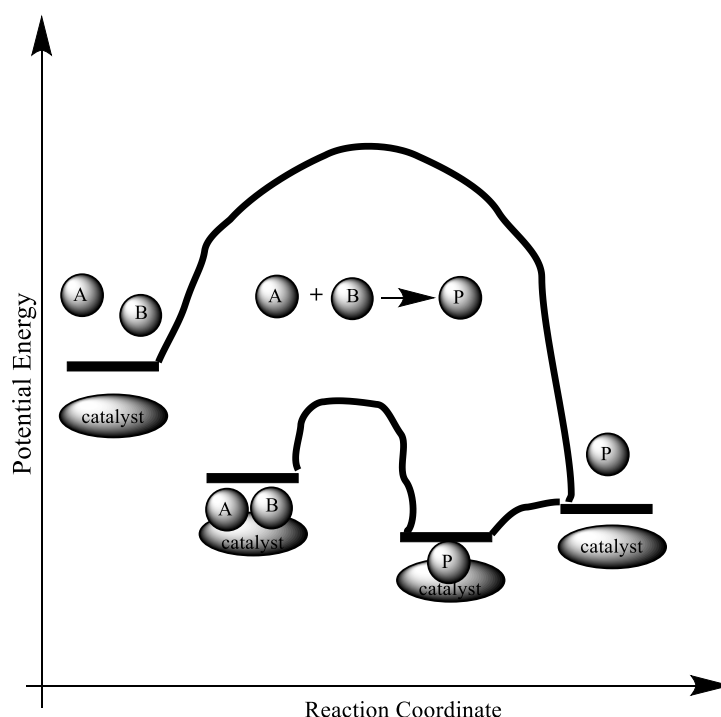


Figure 1.1: Potential energy diagram comparing a heterogeneous catalyzed reaction with an uncatalyzed reaction. Reprinted from (13).

The three phases of the catalytic reaction defined in figure 1.1 need to be given extensive consideration when designing and implementing a catalyst in a reaction. Examples of neglecting to consider the interactions of the reactants with the catalyst, can impact on the performance of the catalyst throughout the process. If one of the reactants has a much stronger affinity for the catalyst surface than the other, then that reactant will dominate the surface of the catalyst and lead to a very low rate of conversion. A similar case can be seen if both the reactants or the product form a strong bond to the catalyst surface, acting as a poison to the catalyst. In reality, the catalytic mechanism is much more complex than this.

1.3 Hydrogenation Catalysis

Heterogeneous catalytic hydrogenations are significant reactions, that find widespread industrial applications in fine chemicals, pharmaceuticals, agrochemicals, flavours and fragrances (14, 15). The basic mechanism of hydrogenation reactions on metal surfaces was first explored notably by Horiuti and Polanyi (16). The key role of the catalyst is to facilitate the adsorption of dissociated hydrogen atoms and the unsaturated bond that needs to be hydrogenated. Then the hydrogen is incorporated step-wise forming a half-hydrogenated state through the process. While this framework helps to visualise the process, it neglects to mention many complications within the mechanism. The adsorption mode of the reactant is paramount in the hydrogenation reaction and can influence the reaction greatly. The majority of literature approaches this through the adsorption of olefins, identifying two distinct adsorption modes. The first, being a strongly adsorbed di- σ arrangement. In this arrangement the C=C bond rehybridizes to form two metal-carbon covalent bonds. The second is a weaker π -bonded mode, which barely perturbs the molecule with a small shift electron density (17, 18). The previously mentioned Horiuti-Polanyi mechanism is likely to require the di- σ adsorbate as a prerequisite for the first hydrogenation step. It is also conceivable that the adsorbate can transition between the two defined states and would need to adopt the di- σ state before hydrogen addition, however there is no literature evidence for this pathway to date. Recently a second hydrogenation pathway has been identified, a more direct hydrogenation with the addition of two hydrogen atoms simultaneously(19, 20). This demonstrates the dynamic and complex nature of the initial step in the hydrogenation reaction and is only exacerbated by more complex molecules with multiple unsaturated bonds, which will be discussed in more detail in later chapters.

Another source of complexity is the state of the metal surface, most fundamental research is carried out on pristine metal surfaces. This would not be representative of a catalyst surface in reaction conditions. The metal surface has been known to promote the partial dehydrogenation of olefins to produce new surface species, which have been shown to be in the alkylidyne ($\text{Pt}\equiv\text{C-R}$) form (21, 22). The carbonaceous species have been proven not to be an intermediate in the hydrogenation pathway of olefins, as their hydrogenation and removal from the surface have rates several orders slower than that of the olefin (23, 24).

The effect that the carbonaceous adsorbate has on the hydrogenation reaction is an area of debate, it is occupying metal sites so can be classed as a poison to the catalyst and has been shown to block the approach of organic molecules in studies on Pt{111} surfaces (25, 26).

The dissociative adsorption of hydrogen is a key factor in this mechanism and along with recombinative desorption has been extensively studied on late transition metals with surface sensitive techniques and has determined the kinetics to be fast, even in mild conditions (27, 28). These investigations were carried out under conditions that were far from the catalytic conditions and little data can be provided for hydrogen uptake at these more applicable conditions. Recently, a more pertinent study has emerged tracking hydrogen adsorption kinetics on Pt surfaces with a mixture of ethene, hydrogen and deuterium (29). Two intriguing observations raised in this study were that at low adsorption coverages of ethene the rate of ethane and HD formation are comparable, leading to the suggestion that hydrogen adsorption could be rate limiting under reaction conditions. The second observation is that once a threshold is reached at roughly 80% conversion of the olefin, the rate of hydrogen isotope scrambling sharply increases. This significant rate increase was not accompanied by an increase in the rate of ethene hydrogenation, but RAIRS data from the investigation showed a decrease in the coverage of carbonaceous adsorbates, leading to free Pt sites (30). These observations demonstrate the complex and dynamic interactions between the adsorbates. It is proposed that key to controlling the rate of hydrogenation is by controlling the concentration of ethene in the reaction mixture. For reaction mixtures higher than 1% ethene the dominant adsorbate is the carbonaceous species to the point of saturation, severely limiting ethene hydrogenation by site-blocking. At 1% ethene concentration the dominant surface adsorbate is adsorbed ethene, with the

rate of formation of ethane increasing significantly with lowering the olefin concentration, until a steady-state is reached at mixtures with lower than 10 ppm of ethene.

1.4 Selectivity in Catalysis – Asymmetric Catalysis

At present, catalysts are used in over 80 % of all chemical industrial processes, contributing to approximately 35 % of the world's GDP(31, 32). The emphasis of catalysis has shifted from reaction rate to selectivity, as a highly selective catalyst can alleviate the environmental impact of a catalytic reaction. Negating the expense of separation and disposal of unwanted by-products is also an area of importance to industrial catalytic processes. In terms of catalyst design, the parameters that control selectivity are typically more sensitive, difficult to adjust and can differ from those that dictate the rate of the reaction(32). Generally, heterogeneous catalysts are favoured over their homogeneous counterparts. This can be attributed to the well-known advantages, such as ease of separation, efficient recycling, minimization of metal traces in the product, facile handling and production of the catalyst and control of the process(33). The vast differences between catalyst types is also evident in asymmetric catalysis, particularly in stages of development. With homogeneous catalysis being representative of an established field, in comparison to the less mature heterogeneous asymmetric catalytic fields.

The field of heterogeneous asymmetric catalysis is vast and can be divided into the following significant subdivisions:

1. Immobilised homogeneous catalysts
2. Chiral catalysts or catalysts modified with chiral modifiers
3. Diastereoselective reactions of chiral substrates on achiral catalysts

Many attribute the early success of asymmetric catalysis to pioneering work by Noyori with BINAP ligands in the 1980's. This demonstrated the effectiveness and selectiveness of ligands in catalysis, eventually leading to a Nobel prize for collaborative efforts with Knowles and Sharpless in the development of asymmetric catalysis(34-37). A group of chiral ligands

emerged from the pack due to their versatility and modular structure: BINAP(38), Salens(39), bisoxazolines(40), tartrate(37) and Cinchona ligands(41). With a secondary group emerging more recently based on organophosphorus compounds(42, 43).

The efficiency of homogeneous catalysts can be improved through immobilisation, as catalyst recycling is improved and contamination by trace metals can be further minimised. While deriving a heterogeneous catalyst from a homogeneous counterpart has some mutually beneficial design features, with the established mechanistic understanding of homogeneous catalysis and the aforementioned efficiency traits of heterogeneous catalysts. Issues arise through the introduction of the support to the homogeneous system, with the support playing a pivotal, yet poorly understood role in the immobilised catalyst system. By anchoring the catalyst to a support through a ligand linkage further complication can impinge on the performance of the catalyst. This can be attributed to unwanted interactions between the support and the metal-ligand complex, the geometry of the catalyst can be disturbed by the support and access to the active site can be limited.

With the aforementioned issues associated with the immobilisation technique; attention shifted back to a more traditional heterogeneous approach. Chirally modified catalysts are a promising field due facile and inexpensive synthesis, but a significant detraction from the technique is the complexity and ambiguity of the chiral mechanism. This was a major stumbling block to the progress of chiral modified catalyst systems, since the early success of the technique in the 1970's. Few systems have experienced success, but continued research into these systems is slowly yielding understanding of the mechanisms occurring within each system. Early research into chiral modified catalysts was dominated by nickel-tartaric acid and platinum-cinchona alkaloid systems (44, 45). These systems rose in popularity due to the high enantiomeric excesses (95%) that could be achieved for a narrow range of substrates. The nickel-based catalyst is suitable for the hydrogenation of C=O moieties present in 1,3- β -diketones, 2-alkanones(46), β -ketosulfones and β -ketoesters(47-50). The hydrogenation of a simple β -ketoester: methyl acetoacetate (MAA) to methyl 3-hydroxybutyrate (MHB) (Figure 1.2) yields important precursors for many pharmaceutical applications.

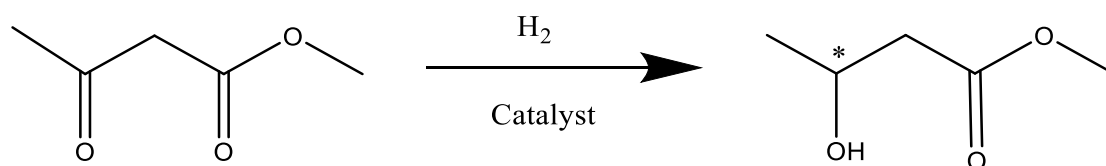


Figure 1.2: Enantioselective Hydrogenation of MAA to MHB

The extensive research in to the asymmetric hydrogenation of MAA on nickel-based catalysts has revealed that the enantiodifferentiation of the catalyst is sensitive to parameters such as pH, solvent, temperature and use of co-modifiers. Interestingly, the enantioselectivity of the reaction can be reversed by replacing the L – tartaric acid modifier with the R enantiomer (50). While the effects of each parameter on enantiodifferentiation is well documented, the origin of the enantiodifferentiation is a more complex and vague mechanism. In order to analyse the mechanism, complex “real world” catalysts need to be substituted for well-defined single crystal surfaces. The spectroscopic probing of tartaric acid adsorption geometry and subsequent self-assembled arrays on Cu {110} surfaces have been delineated as a source of enantiodifferentiation. As demonstrated in figure 1.3 the macroscopic assembly of adsorbate chains are not symmetrical to the underlying surface, creating chiral nanochannels. These nanochannels are also in a non-symmetrical direction to the surface, therefore, creating chiral spaces on the Cu surface. The restricted surface environment provided by the nanochannels forces hydrogenation of one enantioface of MAA, once the molecule docks in the preferential orientation.

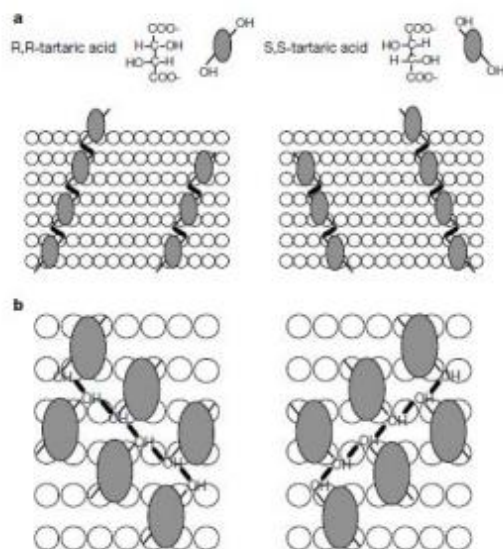


Figure 1.3: Alignment and intermolecular hydrogen-bonding interactions of the α -hydroxy groups of the enantiomers of TA, left (R,R) and right (S,S). The thick lines demonstrate extended hydrogen-bonding. In (a) the interactions dictate the direction of chain grow; in (b) they “weave together” the three molecular chains. Reprinted from (51).

A slightly different case is presented for the adsorption of tartaric acid on nickel single crystal surfaces. The bitartrate adsorbate species are organised in one-dimensional chains on Ni surfaces as opposed to the two-dimensional arrays on copper surfaces. Even more profound, is the effect the adsorption has on catalyst surface. Studies have indicated that adsorption leads to a highly strained bitartrate-Ni₄ complex, resulting in the reorganisation of the surface Ni atoms into chiral arrangements(52, 53).

Above are examples of two prominent methods for creating a chiral environment on the catalyst surface, the former being an imprinting method with a modifier and the latter through rearrangement of the surface atoms. Asymmetric leaching is also a proposed method of introducing chirality, however, much like the imprinting method suffers from a lack of active chiral sites(54, 55). In fact, these strategies have failed thus far to produce an enantioselective catalyst with reasonable technical potential. Chiral solids have been investigated but are limited in abundance and surface rearrangements at reaction conditions continues to blight meaningful progress.

In attempts to understand enantioselective catalysis, chiral metal surfaces have been produced, using the Clavilier method(56). A high miller index surface can be thought of as chiral if the kink site has uneven step lengths either side. The enantiomeric surfaces can be

assigned as either R or S using the Cahn-Ingold-Prelog rules, however differences in reaction kinetics between the two enantiomeric surfaces have been difficult to establish. Examples of enantiospecific reactions are limited, but a few instances have been observed. The desorption energy of R-3-Methyl-Cyclohexanone differs by 0.22 kcal/mol on the Cu(643)^R and Cu(643)^S surfaces, another case of enantiodifferentiation was exhibited on the Ag(643)^R surface. In which, the orientations of R and S 2-Butanoxy groups differ on the surface(57). Attard et al revealed the surface sensitivity of the electro-oxidation of glucose on chiral platinum single crystal electrodes, with the degree of enantioselectivity being dependent on the surface density of kink sites(58). While the use of chiral single crystal surfaces may be useful in gaining understanding of surface interactions during chiral catalysis, but due to the freedom of the reactant on the surface and limited number of chiral sites, employment of chiral single crystal surfaces in catalysis may not be viable.

1.5 Catalyst Structure

Another key influence on the hydrogenation reaction is the structure and possible reconstruction of the catalyst surface. Until recent studies, catalytic hydrogenation reactions have been considered to be structure insensitive (59, 60). Nevertheless, advances in nanoparticle synthesis and in-situ characterisation techniques have aided in producing data supporting the structure sensitivity of the hydrogenation reaction. Examples include: {100} facets of Pt nanocubes are particularly active for C=C bond hydrogenation for 2-butene (61), Somorjai *et al* presented evidence of the rate of cyclohexene dehydrogenation proceeding more rapidly on Pt{100} sites in comparison to Pt{111} structures (62), Baiker *et al* demonstrated that both ee and rate increased with increasing the ratio of Pt{111}/Pt{100} surface sites after the addition of a chiral modifier (63). Despite the promising recent research and advances in nanotechnology, the application of shape specific nanoparticles in catalysis still has many issues to overcome before it becomes a viable option. A pertinent area of concern is the dynamic nature of surface sites, particularly on the nanoscale and in the catalytic environment (64). There are numerous ways a supported metal catalyst can

alter in structure outlined by figure 4. Studies of shaped nanoparticles at elevated temperatures ($> 200\text{ }^{\circ}\text{C}$) in the presence of O_2 , H_2 or N_2 displayed degradation (65), shapes with sharp edges that have lower coordination numbers were particularly susceptible to degradation and to further compound the effect of leaching the liberated platinum atoms can act as catalysts (66, 67).

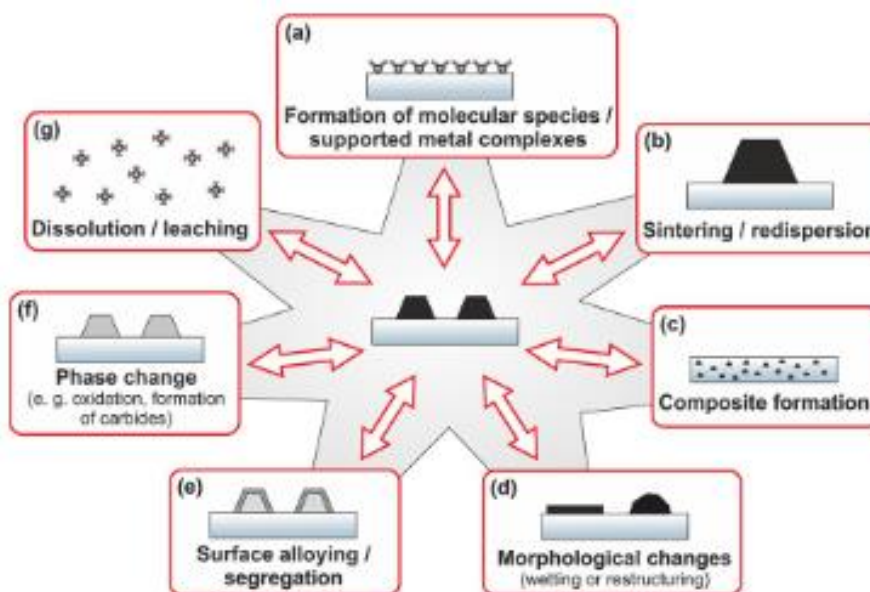


Figure 1.4: Examples of structural changes of supported metal nanoparticles due to changes in the environmental conditions reprinted from (68).

As well as considering morphology changes for shape-controlled nanoparticles it is also important that after synthesis the nanoparticles are put through an extensive cleaning process. Cleaning is necessary to remove residual surfactant utilised to direct the growth of the nanoparticle as it blocks the surface sites of the nanoparticle. Suitable cleaning procedures are few and far between as most cause restructuring of the nanoparticle surface (64, 69), these details will be further discussed in chapter 3.

1.6 Catalyst Support

A final consideration in catalyst design that can influence catalytic reactions is the role of the support. The incorporation of an appropriate support to a catalytic system is of vital importance for the practical application of catalysts. The support provides a large surface area, in which to disperse a small amount of catalyst, which is pertinent when the catalyst comprises of expensive metals such as platinum, ruthenium, etc. As well as reducing the amount of catalyst required, the support is also beneficial in adding mechanical resistance to the catalyst and dictating the physical form of the catalyst. While producing a supported catalyst is desirable for the aforementioned benefits, care must be taken to preserve the intrinsic activity of the bulk catalyst as a bare minimum. Many factors must be considered when adapting from bulk to supported catalyst, with each decision having a bearing on the characteristics of the final supported catalyst. The processing method, parameters and post-processing treatments all add to the intricacy of the process. Popular supported catalyst preparation methods include: Impregnation, ion exchange, grafting and chemical vapour deposition (CVD)(70-73). To demonstrate the impact of varying the parameters of the method on the produced supported catalyst, the impregnation method can be taken as an example.

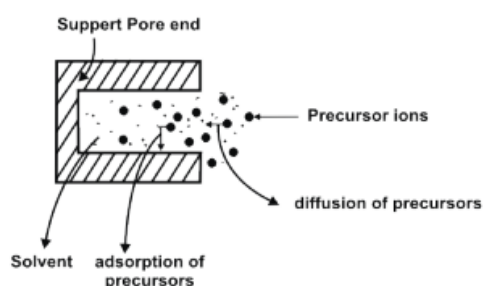
The impregnation method can be further classified into either a wet or dry impregnation, as shown in figure 1.5. Dry impregnation consisting of the addition of a precursor solution to a previously dried support, the volume of the precursor solution is equal to the pore volume of the support. As soon as the support is placed in contact with the precursor solution, the solution is drawn into the pores by capillary suction. As long as sufficient wetting of the pores occurs there should be no excess solution remaining outside of the pore space. A drawback of using capillary suction is that air pockets can become imprisoned in the pores and compressed under capillary forces. Considerable forces can be exerted on the pore walls by the air pockets and in cases where the walls are weak, they can break down degrading the mechanical properties of the supported catalyst.

Wet impregnation has subtle differences to the dry method, the first being that the support pore space is filled with solvent. The solvent used is the same as the one in the precursor solution. The next step is to introduce the wetted support to the precursor solution, capillary suction is not applied in this method, so the only driving force for impregnation is

the concentration gradient from bulk precursor solution to the solution in the pores of the support. The advantage of this technique is that the pores are not subjected to high pressure, due to the absence of capillary suction. However, this technique is much slower in comparison to the dry impregnation method and is unsuitable if the interaction between the precursor and support is too weak to guarantee deposition.

The distribution of the precursor within the support differs for each iteration of the impregnation method, with dry impregnation being more complex than wet impregnation. For wet impregnation the distribution of the precursor is governed by the diffusion of the solutes within the pores (described by Fick's law) and the adsorption of the solute onto the support. The wet impregnation method is also impacted by diffusion and adsorption, with an additional factor to consider, brought about by pressure driven capillary flow. This phenomenon can be represented by Darcy's law, which introduces viscosity as a parameter. For aqueous solutions in the common concentration range for impregnation, viscosity increases proportionally with concentration. Viscosity and concentration have opposing effects on the precursor diffusion, with high concentration promoting diffusion and high viscosity hindering diffusion.

(a) Wet impregnation



(b) Dry impregnation

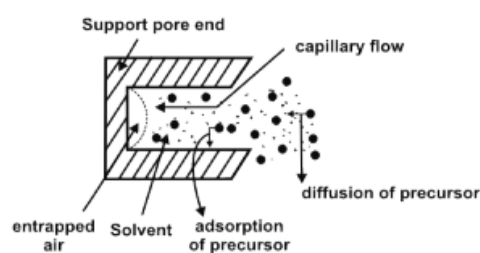


Figure 1.5: Schematic representation of basic processes involved during impregnation of precursors on porous support reprinted from (74).

The impregnation process has now been completed, but further steps are required to produce a supported catalyst. The solvent used in the impregnation step needs to be eliminated through a suitable drying procedure. This is typically achieved through heating at

a temperature slightly above the boiling point of the solvent, in an oven with a flow of suitable gas (air, oxygen, nitrogen, etc.). As well as the temperature used for drying, the heating rate affects the drying process. When modelling the drying process, an outward convective flow of the solution towards the mouth of the pellet needs to be considered. This outward flow can be described by Darcy's law and is favoured by the low viscosity of the solution, due to the evaporation of the solvent at the pore mouth. The convective flow causes an increase in precursor concentration at the mouth of the pellet, as a result of this and in accordance with Fick's law, an inward back diffusion of the precursor occurs. Figure 1.6 shows two drying processes that take place during the impregnation method. For the first process, constant rate period of drying, the precursor distribution is dependent on the relative contributions of adsorption, convection and back diffusion (with high rate of solvent flow). The falling rate period occurs as the solvent recedes into the pores and evaporation takes place within the pore. The drying process is determined to be slow if the constant rate period of drying predominates and fast if the falling rate period is the governing process.

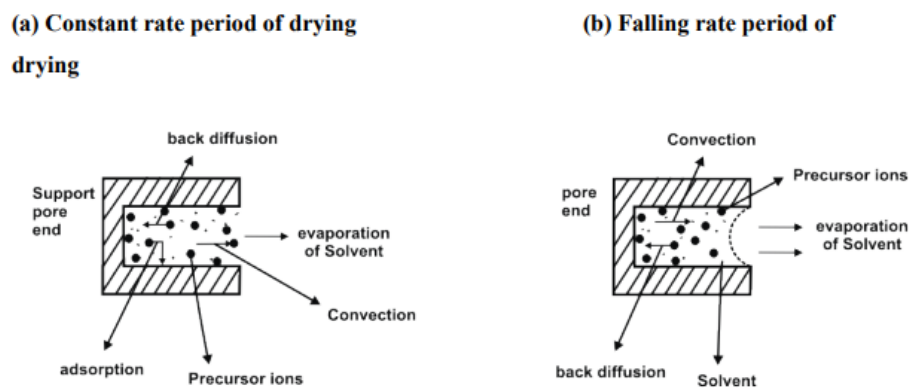


Figure 1.6: Schematic representation of the drying process during the impregnation method reprinted from (74).

The different conditions of impregnation and drying can produce vastly different types of precursor distribution, figure 1.7 details three types of the possible distributions. The first distribution presented is the egg shell type, in which, the precursor is accumulated predominately at the pore wall. This distribution is facilitated through situations where the precursor is strongly adsorbed to the support, the viscosity of the precursor solution is high, or the drying conditions are slow. Interestingly, if slow drying conditions are in place egg

shell distribution can be achieved even with low viscosity solutions and weak adsorption conditions. The conditions for the egg yolk distribution, like the shape suggests, is directly opposing to the egg shell distribution. The egg yolk type supported catalyst is produced if during impregnation a competing ion has a stronger adsorption interaction with the pore wall, or if the fast-drying regime is predominantly used the back diffusion produces the egg yolk distribution. Uniform distribution is the third and final distribution type, which is produced when weakly adsorbed solutes are allowed enough impregnation time. Uniform distribution can also be achieved if competitive precursors have equal affinity to the support or the precursor solution is concentrated and viscous. A gentle drying process and room temperature of the course of several hours also helps promote a uniform catalyst distribution.



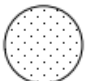
Precursor distribution	Conditions of Impregnation and drying
Egg shell distribution 	<ol style="list-style-type: none"> 1. Strong adsorption of precursors during impregnation 2. High viscosity of impregnating solution 3. Slow drying regime for low concentration, low viscosity and weak adsorption conditions
Egg yolk distribution 	<ol style="list-style-type: none"> 1. In presence of competitor ions that have stronger interaction with the supports 2. Fast drying regime with predominant back diffusion
Uniform distribution 	<ol style="list-style-type: none"> 1. Precursors and competitors interact equally with the surface. 2. Impregnating solution is concentrated and viscous 3. Room temperature drying with weakly adsorbing precursors

Figure 1.7: Distribution of precursor and the corresponding impregnation and drying conditions, reprinted from (74).

Other parameters to consider when trying to produce a supported catalyst with a particular distribution is pH of the solution/solid. pH influences the most abundant species in solution to be deposited on the support, for solids pH controls surface charge and numbers of charged sites. The pH of the impregnation system can be adjusted, commonly nitric acid, carboxylic acids and ammonia are utilised for this as they can be removed through decomposition during thermal treatment. Regarding thermal treatment, after the removal of the solvent, further heat treatment is necessary to convert the impregnation product into

a catalytically useful form. The further heat treatment is known as calcination, in which, the impregnation precipitate is heated in the presence of air or oxygen. The heating process is often utilised to burn any residual organics or oxidise the sample, during calcination numerous changes can occur to the catalyst. These changes include: Chemically bound water is removed at high temperatures, changes in phase distribution due to material crystallisation at higher temperatures, heat treatment similar to the environment encountered in a reactor ensures structural stability during reactions, changes in pore size distribution and decrease in surface area due to sintering and active phase generation due to hydroxide conversion to oxide. The extent of change in the physical characteristics of the catalyst are dependent on temperature, heating rate, heating time and gaseous environment.

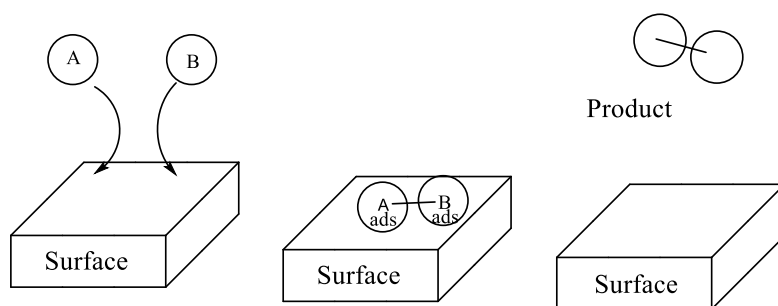
Mainly, solid catalysts are used in industrial processes as there are many benefits. For instance, improving thermal and mechanical resistance and ensuring effective heat conductivity in the reactor. The common forms of a solid catalyst are Pellets, extrudates, granules and spheres. With the respective production methods giving the operator fine control over the shape and shape distribution of the catalyst. The overall goal of catalyst design and production is to produce a highly efficient catalyst and the above procedures and parameter choices intrinsically impact the catalyst with regards to selectivity and conversion. The supported catalyst has many aforementioned advantages over unsupported catalysts, however, there are some negative impacts of introducing a support to a catalytic system. Mass transport issues and unwanted side reactions are two of the more facile issues, a more intricate and often overlooked phenomena is the catalyst-support interactions. The strong metal-support interaction is well-known and describes the reduced chemisorption following high temperature reduction, due to the formation of an atomic layer of the support material on the surface of the nanoparticle (75). A broader view of metal-support interactions was proposed by Campbell (76), encompassing beneficial electronic interactions (Charge transfer (77), ligand effects (78, 79), etc) and geometric interactions (strain, dispersion, etc (80, 81)) between the support and nanoparticle. It was hoped that greater understanding of the metal-support interactions could allow the tuning of the chemical and electronic properties on the metal sites, to achieve better catalytic effects. This potential was demonstrated by Rodriguez and co-workers with small platinum clusters experiencing large electronic perturbations when in contact with ceria (82). Another

great example to highlight the benefits of metal-support interactions is the Fischer-Tropsch synthesis of ethanol, in which, the selectivity of ethanol is increased when using the Rh/TiO₂ vs the Rh/SiO₂ catalyst-support system (83). Further research on the Pt/CeO₂ catalytic system show increased activity with the introduction of a secondary supporting material TiO₂ (82). This research has given rise to an exciting new type of two-phase supported material. Basic research has commenced on these catalytic systems and may represent a promising route in utilising metal-support interactions in catalyst design.

1.7 Surface Science

The breath of information presented in previous sections for the nature and performance of various catalytic systems, highlights the advancement of the field of catalysis. This rapid development of catalysis can be attributed to improvements in associated technologies, better understanding of the catalytic processes, and also progress in analytical techniques. The role of surface science in catalysis has been crucial and one of the first vital contributions to the field was from Irving Langmuir(84). Langmuir derived a simple relationship between adsorption on a solid surface to the pressure of the gas at equilibrium; this allowed the rate expressions to partial pressures to be developed in the case of unknown surface coverage(85). Applying adsorption theory to surface catalysed reactions, assuming adsorption and desorption steps would be fast relative to the surface reaction step, allowed for the interpretation of kinetic data for various catalytic reactions in the late 1920's(86). This mechanism became known as the Langmuir-Hinshelwood mechanism. A second differing mechanism was proposed in 1938 by D. Eley and E. Rideal, in which only one of the reactants was assumed to adsorb on the surface while the other reacted from the gas phase, with the product desorbing from the surface(87).

Langmuir-Hinshelwood Mechanism



Eley-Rideal Mechanism

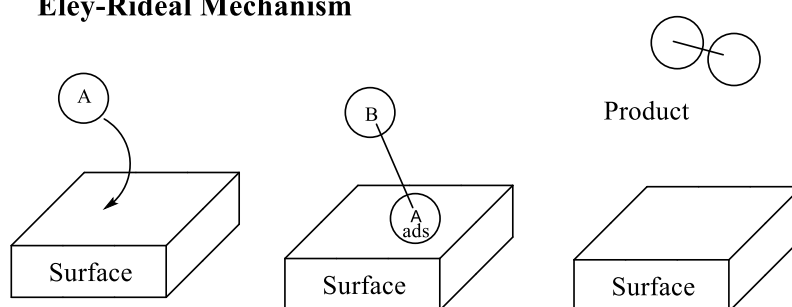


Figure 1.8: Schematic representing the Langmuir-Hinshelwood and Eley-Rideal mechanisms.

Based on the adsorption theory developed to this point, a new method utilised this knowledge to probe the surface area of catalysts. This is known as BET theory, which was developed by S. Brunauer, P. Emmett and E. Teller(88). The gaseous adsorbate utilised in this method does not react with the material surface and will also adsorb inside any pores on the surface. Being able to normalise catalytic results with regards to surface area is vital when comparing catalysts of different morphologies and types. These basic characterising methods for catalysis gave greater understanding of the catalytic process, enabling surface scientists for the first time to change their approach to developing new catalysts from a trial and error method towards a more fundamental approach. In order to achieve this goal an array of characterisation methods were developed to better understand the intricate details associated with a catalyst structure and function. The numerous surface sensitive characterisation techniques that were developed included Auger electron spectroscopy (AES)(89, 90) and X-ray photoelectron spectroscopy (XPS)(91, 92), for studying the chemical composition of the catalyst surface. Techniques such as scanning and transmission electron

microscopy (SEM,TEM)(93, 94), X-ray diffraction (XRD)(95), low energy electron diffraction (LEED)(96), atomic force microscopy (AFM)(97) and scanning tunnelling microscopy (STM)(93) are all viable surface characterisation methods. These techniques would be used as topological probes, and combinative studies of a catalyst using a variety of the previously mentioned techniques can yield extensive information. However, the sheer complexity of catalytic processes still makes mechanistic understanding a challenging area.

1.8 Surface Orientated Analytical Techniques

The morphology of the catalyst can play a very important role in catalysis, with many reactions having some aspect of surface sensitivity. The size of the catalyst can have a significant impact on the catalyst. Decreasing the size of the catalyst to nanometer ranges, increases the fraction of surface atoms and the surface to volume ratio of the catalyst. This can have a significant impact on catalytic activity and shifted the focus of catalyst development to a bottom-up approach(98). A prominent example of this type of surface sensitive catalytic reaction was highlighted with alkene reactions over platinum catalysts. Reactions such as alkene hydrogenolysis (99) and isomerisation (100) were found to be strongly dependent on nanoparticle size, while reactions like cyclopropane ring opening (101) and olefin hydrogenation (102) were independent of nanoparticle size. This led to the classification of reactions into three categories: Structure-insensitive, structure sensitive dependent on reaction conditions and structure sensitive. The relationship between size and structure of the nanoparticle are closely interlinked and well-studied, since it is well known that the relative quantities of terraces, steps and kinks alter with differing nanoparticle sizes (103). Contrary to this, the interactions of reactants with these surface features are less well defined and understood. Vibrational spectroscopy can give insight into the surface specific interactions, with the use of single crystals and model catalytic surfaces. The common spectroscopic methods used to study the complex reactions occurring in heterogeneous catalysis are based on infra-red techniques, namely infrared external reflectance absorption spectroscopy (IRRAS) (104), attenuated total reflection spectroscopy (ATR-IRS) (105) and sum frequency generation (SFG) vibrational spectroscopy (62, 106). Vibrational techniques can give detailed information about adsorption geometry, surface coverages and surface intermediates to name a few, but one of the biggest advantages of vibrational spectroscopy over previously mentioned characterisation techniques, is that it

does not rely on an ultra-high vacuum (UHV) conditions. The versatility of the technique therefore allows for in-situ analysis, often under catalytic conditions, which will give invaluable industrially relevant insights into the catalytic reaction.

1.9 Raman Spectroscopy

As a supplementary or alternative method to IR based vibrational techniques, Raman spectroscopy has experienced a resurgence in popularity in recent years after extensive development of the technique(107-109). The basis of Raman spectroscopy is the scattering of light through interactions with molecules, the scattering can be elastic (Rayleigh) or inelastic (Raman). The Raman scattering can be associated to the vibrational energy levels of the molecule with the incident photon losing energy (stokes) or gaining energy (anti-stokes). The gross selection rule for Raman spectroscopy is that the vibration must lead to a change in polarizability, this is less restrictive than an oscillating dipole for IR, allowing symmetrical molecules to be Raman active. The theoretical aspects of Raman spectroscopy are discussed further in chapter 2.5. Despite many positives, the low sensitivity of the technique due to the weak Raman scattering meant it was overlooked as a viable spectroscopic technique for the analysis of catalytic surfaces (110). This remained the status quo for many years, until the pioneering work of Fleischmann with roughened silver electrode surfaces (111). This study is regarded as the first report of Surface Enhanced Raman Spectroscopy (SERS), although a complete explanation for the enhancement was not proposed until 3 years later. Two groups worked independently on a rate enhancement theory and agreed that surface area or adsorbate concentration could not adequately explain the rate enhancement. Each group proposed two differing signal enhancement mechanisms, specifically, Jeanmaire and Van Duyne proposed the electromagnetic enhancement theory (112), whereas Albrecht and Creighton proposed the charge-transfer theory (113). (chapter 2.5.2) Although the origin of the signal enhancement is still an area of debate, it has not interfered with the progress in developing the SERS technique.

The coinage metals (Au, Ag and Cu) are classic SERS substrates, due to the strength of the enhancement and the fact that the localised surface plasmon resonances (LSPR) of each material cover the visible and near-infrared regions, which can be attributed to the electronic properties of the materials (114). While a lot of catalysts are based upon the aforementioned metals, expanding the variety of substrates amenable to SERS analysis was

crucial for wide-spread use of the technique. Additional metals have since been shown to be a viable SERS surfaces such as: Li (115), Na (116), K (117), Cs (117), Rb (117), Al (116), Ga (116), In (115, 116), Pt (118) and Rh (107). While these are viable SERS surfaces, the intensity and reproducibility of the enhancement is optimum for the coinage metals. With the considerable advancements in nanoscience, synthesis of nanoparticles has progressed to be able to produce core-shell nanoparticles (119, 120). This allows less viable SERS surfaces of catalytic interest to “borrow” enhancement from a coinage metal core. The core-shell SERS studies has revealed many interesting findings of relevance to catalysis by availing of Au@Pt (122), Au@Pd (123), Au@Rh (109), Au@Ru (109), Au@Co (108) and Au@Ni (108) core-shell systems to expand the SERS to transition metal surfaces. The popularity of SERS soared after the substrate expansion to incorporate many commonly used catalytic surfaces, although a significant hurdle still impeded the wide-spread adoption of the technique. The primary issue was that SERS activity is achieved by either roughening surfaces or utilising core-shell nanoparticles, and this limits SERS analysis to high index surfaces only. This was addressed by the work of Tian *et al.*, with the establishment of shell isolated nanoparticle enhanced Raman spectroscopy (SHINERS) (123). This technique also utilises a core-shell nanoparticle and borrows SERS activity from the gold or silver core, but the shell is composed of silicon dioxide. The SiO₂ shell renders the nanoparticle chemically and electronically inert, acting as antennas on the surface enhancing and relaying the Raman scattering. The SHINERS technique has further expanded the number of substrates viable for analysis, enabling access to a variety of fields including biochemistry, biosensing, catalysis, electrochemistry and materials science. SERS is highly sensitive and selective technique for biosensing and has been employed as a powerful tool in the detection of various diseases such as cancer, Alzheimer’s and Parkinson’s disease (124, 125). Work is ongoing on the development of SERS-based *in vivo* glucose sensors for quality of life improvements for diabetic patients (126). SERS is a powerful tool in biomedical science and is set to play a key role in the future developments of the field. SERS has also been utilised in some real-world applications in the characterisation of artwork by tracing the origins of dyes to authenticate the history of the pieces(127). SERS nanotags are a promising application of the technique for the authentication and labelling of certain objects. This is particularly pertinent to brand security and encoding luxury goods or currency. With the constant

improvement of equipment SERS is becoming ever more accessible with hand held instruments.

1.10 Electrocatalysis

Electrocatalysis is a special field in electrochemistry which is significant for future catalytic challenges and has enjoyed substantial growth since the eighties. Electrocatalysis in the coming years is expected to be a key route for reliable, affordable and environmentally friendly energy and chemicals production. The development of electrocatalysis and electrochemical based technologies requires an interdisciplinary approach from chemistry, materials science, physics and engineering. As more is uncovered on the topic, the applications of electrocatalysis has shifted from fundamental academic purposes to technical industrial use. Common and popular applications include: fuel cells, sensors and battery technology (128-130). A key objective for science is to develop an abundant, clean and renewable future energy source. Molecular hydrogen represents a promising candidate, with a high energy density in comparison to most commonly used fuels and non-polluting products. The realisation of hydrogen powered fuel cells faces several technological challenges, with the relatively high operating temperature (60-90 °C) and an appropriate system for large scale hydrogen production, storage and distribution. Additionally, the required material for the electrodes are usually precious platinum group metals. The electrode surface undergoes structure and element specific interactions with electrolytic substrates and thus should be regarded as specific catalytic surfaces, not just interfaces for the exchange of electrons. Vast amounts of research has been conducted on the material and structure of the electrodes employed in fuel cells, specifically, for the oxygen reduction reaction (ORR) which is a critical reaction for proton exchange membrane fuel cells (PEMFC) and a lot of information has been garnered (131, 132). Researchers have highlighted four essential characteristics for an effective PEMFC catalyst, which are high activity, selectivity, stability and resistance to poisoning. When evaluating the activity of a catalyst, the Sabatier principle of the ideal interaction between a substrate and catalyst should be considered (133). Which requires the catalyst to adsorb species with strength to allow a reaction to occur, but weakly enough to release the product from the surface. This

principle can be eloquently demonstrated in figure 1.9, with the Baladin plot demonstrating the superiority of platinum group metals for the ORR.

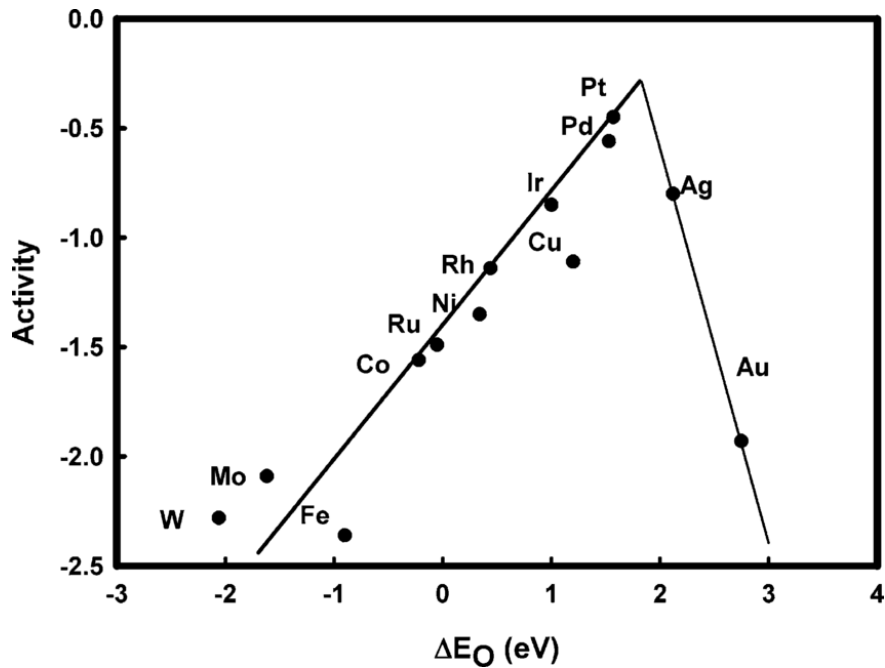


Figure 1.9: Baladin plot of oxygen reduction activity as a function of oxygen binding energy, reprinted from (134)

The ORR can have two branching reaction pathways in acidic media, with both pathways represented in figure 1.10. The first and preferred pathway is the dissociative pathway and follows a concerted four electron transfer process leading to the direct formation of water.

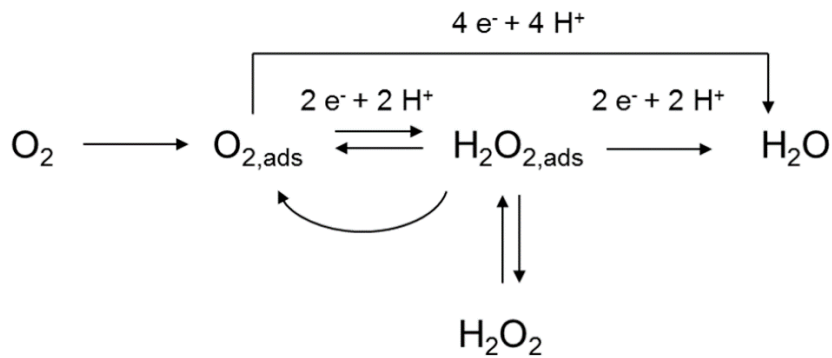
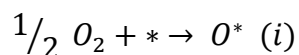


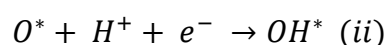
Figure 1.10: Schematic demonstrating possible pathways of associative and dissociative mechanisms, reprinted from (135).

The dissociative pathway can be broken down into the following five reactions:

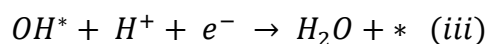
- First oxygen adsorbs onto the metal surface and the oxygen-oxygen breaks to give adsorbed oxygen atoms.



- The single oxygen atoms are protonated by the incoming flow of H^+ across the PEM and reduced by an incoming flow of electrons from the anodic process to produce a surface bound hydroxyl group.

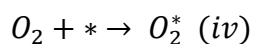


- The surface bound hydroxyl group is further reduced and protonated to give water, which then leaves the metal surface.

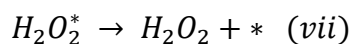
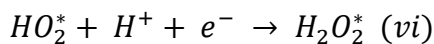
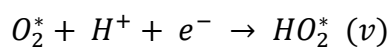


The associative pathway is an alternative two electron transfer route, which produces hydrogen peroxide. This is an undesirable pathway as the hydrogen peroxide that is produced diffuses into the PEM, resulting in degradation of the membrane (136). The details of the mechanism of the associative pathway is ambiguous, but may proceed as follows:

- Firstly, the oxygen bond is not broken upon adsorption to the metal surface.



- The adsorbed oxygen is protonated and reduced twice to produce hydrogen peroxide in a two-electron route and finally desorb from the surface.



The second requirement of selectivity can be evaluated specifically by which pathway the ORR commences through, with the dissociative pathway being the preferential route. An investigation using scanning electrochemical microscopy to determine the amount of H_2O_2 produced on various metal catalysts, has demonstrated platinum and $Pd_{80}Co_{20}$ surfaces to be highly selective (near 100%) (137). With gold being relatively poor, this can be associated to the binding energies of oxygen on the various metal surfaces in figure 1.9.

A suitable metal catalyst must be able to withstand the harsh environment within the fuel cell. The low pH levels, high temperature, rapid fluctuations in potential, reactive radicals and strong oxidants cause dissolution of many transition metals. Furthermore, those that can resist dissolution tend to form oxide films, while preventing dissolution also inhibits the ORR. The thermodynamic stability of various metals has been tested under fuel cell conditions, from the investigation noble metals such as gold, iridium and platinum emerge as highly stable. Whereas, metals such as nickel, cobalt and iron are significantly corroded when subjected to the reaction conditions (138). From the handful of stable metals, platinum is the only viable pure metal for use in PEMFC's due to its superior activity and selectivity.

In a similar vein to catalyst stability, a resistance to poisoning by impurities is essential for a fuel cell catalyst. Impurities in both the air streams and the hydrogen may have a negative impact on the PEMFC and with the multitude poisons and poisoning mechanisms it can be difficult account for them all when evaluating a suitable catalyst. For Pt in PEMFC applications sulphur species and carbon monoxide are two of the most debilitating (139). Feasibly there are two ways of protecting the catalyst: by keeping the poisons out of the fuel cell system or by alloying platinum with a metal with a lower susceptibility to poisoning. The impurities in the hydrogen stream can be effectively minimised by having a strict quality specification for the source of the hydrogen for the fuel cell. While eliminating the introduction of impurities is important, a more robust catalyst is also desirable. Research has demonstrated increased CO tolerance from platinum-ruthenium alloy anodes and similar improvements can be seen for Pd-Ru electrodes (140).

From an economical perspective the high loading of platinum for catalysts employed in PEMFC's leads to a high cost. For PEMFC's to become economically viable the Pt loading needs to be reduced, this can be achieved through the application of supported shape specific Pt nanoparticles. Fundamental studies have determined for Pt based electrocatalysts, Pt {111} facets to be most active (141), with a small nanoparticle size preferred to maximise the electrochemically active surface area and minimise the amount of platinum required. Stability of the nanoparticles is an area of improvement and further research would be beneficial in this regard. Pt based alloys could also help alleviate the economic issue, with the fabrication and evaluation of potential alloys being a particularly

active area of research. An ever-expanding library of alloys have been evaluated, with Pt-lanthanide and Pt₃Ni(111) showing promising potential (142). Developing analytical, synthetic and computational techniques will all contribute significantly to bright future of fuel cell technology.

1.11 Electrochemistry

Cyclic Voltammetry (CV) is an example of a powerful technique in electrochemistry and can be employed to probe surface coverage, site-specific adsorption, stability of reactants as well as reaction kinetics. The technique is commonly employed to investigate the reduction and oxidation processes of molecular species (143, 144). Alternatively, the technique can be used to characterise electrocatalytic surfaces (145, 146). The characteristic shape of platinum single crystal and polycrystalline platinum surface CV's are well established and have been intensely studied (147, 148). In order to produce a cyclic voltammogram a three-electrode set up is required, which includes a counter, working and reference electrode. The working electrode potential is ramped linearly versus time in cyclic phases, with the current response of the working electrode plotted versus the applied potential. The potential is measured between the working electrode and the reference electrode, while the current is measured between the working electrode and the counter electrode. The working electrode carries out the electrochemical event of interest, it is imperative the electrode surface is extremely clean and has a well-defined surface area. The working electrode can be varied depending on the application from single crystals to polycrystalline surfaces to nanoparticles coated on a glassy carbon electrode. The reference electrode like its name suggests is used as a reference point against which the potential of other electrodes can be measured in an electrochemical cell, thus typically the potential is reported vs a specific reference. A few popular reference electrodes include the saturated calomel electrode (SCE), standard hydrogen electrode (SHE), Ag/AgCl electrode and Pd/H electrode. These electrodes have well-defined potential windows and converting potentials between electrodes can easily be done if the electrolyte solution is consistent. In this study the Pd/H electrode is utilised for electrochemical analysis. The Pd/H electrode takes advantage of the fact that Pd can store 900 times its volume of hydrogen, through the formation of α and β Pd hydride phases. The electrode can store electrolytically generated hydrogen to maintain potential, which is

advantageous in this study (149). The counter electrode is required to complete the circuit with current flowing between the working and counter electrode. To ensure that the kinetics of the reaction occurring at the counter electrode does not inhibit those occurring at the working electrode, the surface area of the counter needs to be greater than that of the working electrode and usually takes the form of platinum wire or mesh. The electrolytes used in these systems are acidic with perchloric acid and sulphuric acid preferred, due to the breath of literature characterising platinum surfaces in these electrolytes. In each case H^+ is the cation and the anions are ClO_4^- and SO_4^- respectively. Subtle differences in the anions lead to differences in the adsorptions of the electrolytes, with the sulphate having a specific adsorption in comparison to the perchlorate, this should be considered when analysing adsorbate species (150). When setting up the electrochemical system it is important to degas the electrolyte solution with an inert gas such as nitrogen, to ensure removal of redox active molecular oxygen. The cell used to carry out the electrochemical analysis can also greatly impact the types of analysis available. A key aspect in electrochemical analysis is mass transport which usually govern electrolytic reactions, especially when dealing with dilute solutions. In a static cell mass transport to the electrode surface is controlled through diffusion, using a rotating disk electrode (RDE) convection is the major driving force for mass transport. An RDE setup can be used to analyse reaction kinetics and determine diffusion coefficients, very important parameters for electrocatalytic reactions (151). To perform electrochemical synthesis on industrial scales a flow cell system is the most viable. The planning of these systems is more complex than a static cell, but give enhanced reproducibility and performance (152). The flow cell can be operated in two ways, a single pass with high conversion or by recycling the reactant solution between the cell and reservoir, dependent on the reaction and the requirements. Flow electrolysis is an exciting electrochemical field and is contributing much to overcoming the barriers that have limited the popularity and viability of electrosynthesis.

1.12 Spectroelectrochemistry

Spectroelectrochemistry (SEC) can be viewed as the combination of reaction-orientated electrochemistry and species-focused spectroscopy, essentially trying to determine the “how” and “what” of a reaction. Conventional electrochemistry is a powerful and influential analytical technique that has been employed to determine concentrations, energy data (redox potentials) and reaction mechanisms via kinetic analysis. There are numerous interfacial electrochemical techniques, each with subtle differences, Figure 1.11 gives an appreciation for this.

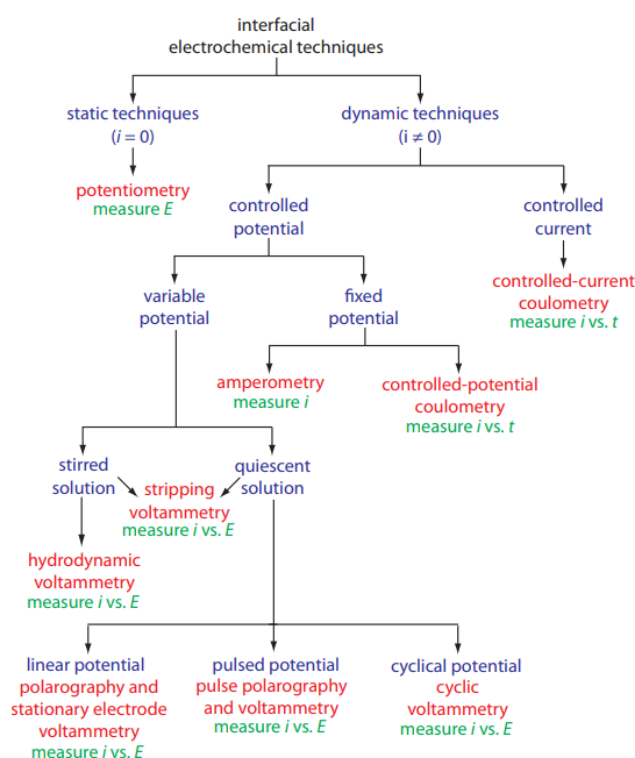


Figure 1.11: Schematic of the numerous interfacial electrochemical techniques, reprinted from (153).

However, this approach does not give a complete picture of what is occurring during the reaction as species that are formed as either intermediates or products cannot be identified. In order to characterise these species, spectroscopic methods need to be applied in conjunction with the electrochemical technique. Typical spectroscopic methods utilised in SEC include absorption spectroscopy in the ultraviolet (UV), visible (VIS), near-infrared (NIR), infrared (IR) regions, Raman spectroscopy and magnetic resonance techniques such as electron paramagnetic resonance (EPR) (154). These spectroscopic methods probe electronic and

vibrational transitions, which allow an abundance of information to be garnered on the species involved in the reaction. Creating the optimal conditions for spectroelectrochemical measurements can be challenging and present numerous practical considerations. When designing the cell, the transparency of the cell material, electrode and electrolyte must be sufficient. Optically transparent electrodes (OTEs) are often required and the search for new OTE materials is ever expanding and developing along with the SEC technique. The first OTE was presented by Kuwana in 1964, based on Sb-doped SnO₂ glass, which was utilised in measuring the absorption features of electrochemical species, thus being one of the first iterations of SEC (155). Electrode materials have developed over the years, with SEC systems utilise either indium-tin oxide electrodes, partially transparent grids from noble metals, or use of fibre optics which allow the transmission of the changes occurring at the electrode surface layer (156). The response time of the system being probed is another consideration, with intermediates often being short-lived and undergo rapid further reactions. The response time of the cells used in SEC are typically much longer than sweep rates for cyclic voltammetry, this can obfuscate reversibility characterisation of electrochemical reactions for SEC. The impact of this response incompatibility can be limited by decreasing the electrolyte thickness around the working electrode, by implementing an optically transparent thin-layer electrode (OTTLE) cell, see figure 1.12.

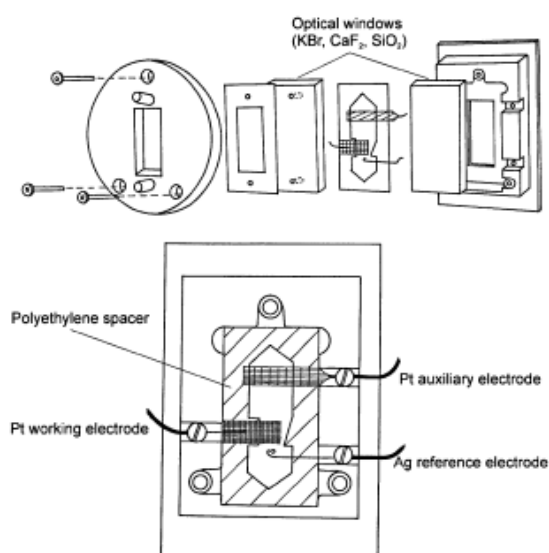


Figure 1.12: Design schematic of optically transparent thin-layer electrode (OTTLE) cell, reprinted from (156)

Another significant concern for SEC investigations is the analyte concentration, with some SEC measurements requiring higher concentrations for band intensity. The increased concentration can lead to inconsistencies in the electrochemical analysis, especially if a chemical reaction occurs. UV and IR spectroscopies can be limited by the absorption of the cell window, in these cases special CaF₂ windows must be employed and appropriate solvents for the desired technique. Often the practical application of SEC is a compromise between all the considerations mentioned above.

The combination of SERS has emerged as a powerful analytical tool for the study of electrochemical interfaces. Tian and co-workers have made significant contributions to expanding the breadth and depth of understanding of the SERS SEC (157). The group has successfully employed SERS SEC to characterise adsorption configurations and elucidate electrochemical reaction mechanisms, while developing the methodology and available substrates for electrochemical SERS. An eloquent demonstration of SERS SEC's analytical prowess is shown by pyridine on different metal surfaces. The frequencies and the intensities of SERS of pyridine are correlated to the adsorption orientation and the chemical interaction between pyridine and the metal surface. Further developments have been achieved with the SERS SEC technique, with greater SERS enhancements allowing time-resolved SERS to be carried out. This allows the comparison of bulk and potential controlled surface spectra to probe the flux of surface species. More recently, the SHINERS technique has been introduced and has substantially increased the substrates available to SERS techniques. Logically, the SHINERS technique has been implemented into SEC investigations with great success, probing the formation and process of interfacial species in Li-ion batteries (158). The aforementioned SEC investigations heavily focus physical interfacial interactions with an emphasis on catalytic reactions, but spectroelectrochemistry has multidisciplinary applications. Biological research areas are utilising SEC, specifically EC-SERS to probe biometric interactions linked with Alzheimer's, Parkinson's and Huntington's disease (159). Despite the achievements of SEC, significant challenges still hold the field back from widespread application. Firstly, spectroelectrochemistry is highly dependent on OTEs. Therefore, developing OTEs with high transparency and smaller size. Secondly, equipment needs to be improved to facilitate high accurate and sensitive characterisation, with ultrafast detection. Thirdly, in order to study more convoluted and diverse processes,

complex multi-SEC methods need to be developed. Lastly, for widespread adoption of SEC in the life sciences, some critical issues need to be addressed. The issues can be related to the need for precise control of temperature, wide redox potential window and strong solution interference, all of which are crucial in cells and living organisms. The SEC technique has a promising future in the analytical field, with continual development of the technology and understanding of the complex theory.

1.13 Shape Controlled-Nanoparticles

With the help of sophisticated analytical techniques, a lot of information on catalytic reactions has been established, so that when designing a catalyst, these vital parameters relating to the reaction mechanism should be considered. With nanoscience allowing ever more increasing control of all aspects of a catalyst structure, a suitable synthesis method can in principle be tailored to produce an almost optimal catalyst. In terms of surface sensitivity, shape-controlled nanoparticle synthesis therefore becoming less obscure since complex shapes can now be achieved (160, 161). By selecting suitable capping agents (162, 163), reducing agents (164-166), metal precursors and reaction conditions, the synthesis of almost any shape imaginable is possible (167). As more and more information is brought to light about the intricacies of surface interactions in catalysis, shape-controlled nanoparticles can be employed as catalysts. Catalytic reactions that have been proven to have site specific selectivity or increased activity, will benefit from the utilisation of shape-controlled nanoparticles (168). Shape-controlled nanoparticles have been utilised in many heterogeneous catalytic reactions, with examples including work by El-Sayed on propylene hydrogenation on shaped nanoparticles which showed {100} orientated cubic nanoparticles were less active than truncated octahedral nanoparticles due to the presence of the {111} surface (169). Zaera *et al.*, studied the isomerisation of 2-butenes on tetrahedral, cubic and spherical platinum nanoparticles and concluded the {100} facets of the cubes were particularly active for C=C hydrogenation (61). Shaped nanoparticles are also heavily involved in electrocatalysis, especially for the oxygen reduction reaction (170) and alcohol oxidation (171, 172).

The encompassing theme of the literature presented above is that catalysis plays a huge socio-economic role in the world and it would be beneficial to all to develop improved surface sensitive techniques to facilitate and enable the improved designed of future catalysts. The analysis and understanding of fundamental surface science is therefore vital in fulfilling that need for progress and will hopefully propel catalyst design from a trial and error approach to a more fundamental bottom up design process. The present work on developing a better understanding of the reaction mechanisms and improving the analytical methods to study them, will be a worthwhile investment for the future of catalysis. This thesis encompasses the importance of catalytic research, with a focus on the detailed characterisation of metal nanoparticles by advanced surface sensitive techniques, in order to improve our understanding of heterogeneous catalysis and assist the future development of catalysts.

The ideal techniques for the synthesis of metallic nanoparticles should be reproducible with the ability to precisely control the shape, size and monodispersity of the nanoparticles. A bottom-up route is preferred in most cases to a top-down approach, with the methods being categorised into electrochemical, radiochemical and chemical reduction methods (160, 173-175). A liquid phase system is commonly used in nanoparticle synthesis, with nucleation and growth being critical in dictating the shape of the nanoparticle. Newly formed atoms in the solution aggregate to form nuclei, the nuclei grow to form a seed. The crystallinity of the seed is determined by minimising the surface free energy and plays an important role in determining the final shape of the nanoparticle as shown in figure 1.13. The surface free energies corresponding to face-centered cubic noble metal nanoparticles increases in the order of $\alpha_{(111)} < \alpha_{(100)} < \alpha_{(110)}$ (176).

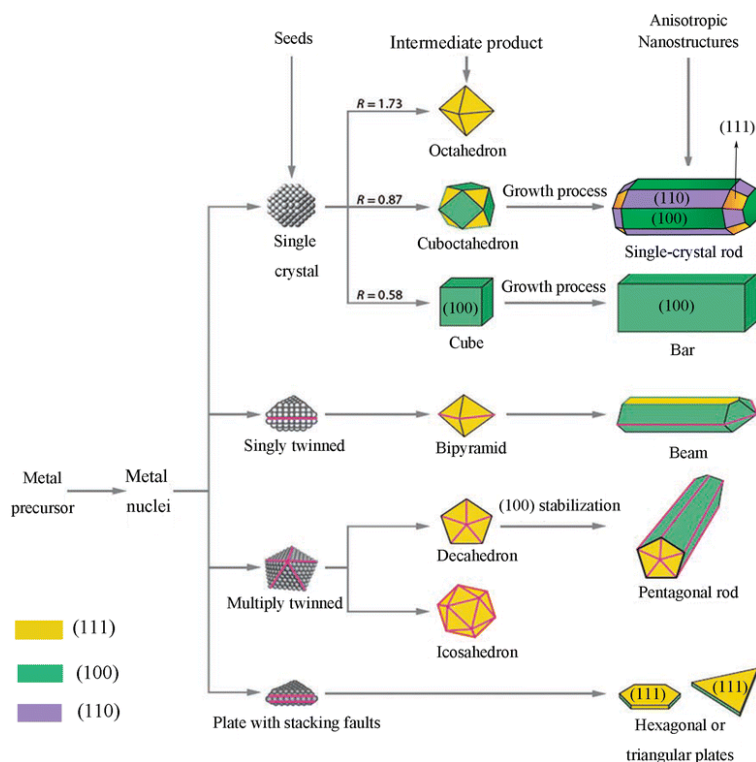


Figure 1.13: A schematic illustrating various stages of the reaction that leads to the formation of noble-metal nanoparticles with different shapes. After the formation of nuclei (small clusters), they become seeds with a single-crystal, singly twinned, or multiply twinned structure. Stacking faults in the seeds results in plate-like structures. Green, orange, and purple represent the (100), (111), and (110) facets, respectively (177).

Being able to control the growth of the nanoparticle is key to dictating the shape, in colloidal systems metallic nanoparticles are attracted to each other through van der Waals forces. The addition of a capping agent can counteract these attractive forces by electrostatic or steric stabilisation. The critical role of the capping agent is the selective adsorption on a particular crystallographic plane, inducing anisotropic growth of the nanocrystal. The capping agent interacts with the surface atoms through functional groups participating in dynamic adsorption and desorption. The binding affinity of the capping agent is dependent on the geometry of the different facets, growth is limited on strongly bond facets and as a result is preserved and exposed in the final nanoparticle. Xia and co-workers eloquently demonstrated the contrasting effects capping agents can have on the nanoparticle shape. By keeping reaction conditions the same and altering the capping agent from sodium citrate to PVP the shape of the silver nanoparticles altered from octahedrons to cubes (178). A number of capping agents have been identified and utilised in shaped nanoparticle synthesis, and when selecting from the vast collection the type of metal, targeted morphology and application of the nanoparticles needs to be considered. In this

investigation platinum nanoparticles of various shapes are analysed, and a variety of synthesis methods are employed with differing capping and reducing agents used to produce said nanoparticles. Spherical nanoparticles have a very facile synthesis method that is based on a water-in-oil microemulsion. The surfactant (Brij 30) forms micelles in the system that can be referred to as “nanoreactors”, providing a suitable environment for controlled nucleation and growth. The reduction of the platinum precursor by hydrazine is fast, taking only a few minutes for the precursor to be fully reduced. The synthesis exhibits excellent reproducibility and shows similarities with templated synthesis methods (179). The synthesis of cubic and tetrahedral/octahedral nanoparticles is more complex, with more variables in the synthesis and slower reduction times using hydrogen as a reducing agent. Oxygen needs to be purged from the reaction vessel prior to reduction to eliminate oxidative etching of the platinum nanoparticles. Sodium polyacrylate (PAA) is used as the capping agent in the synthesis and the ratio of capping agent to metal precursor is adjusted to yield either cubic nanoparticles (1:1) or tetrahedral nanoparticles (5:1).

In addition to the use of a capping agents, additives can be utilised to influence anisotropic growth of nanoparticles. Specifically, halides have demonstrated powerful structure influencing effects with examples including the use of bromide to obtain well-defined gold nanorods, while iodide hindering the formation of nanorods and inducing the formation of nanoplates (180). Potassium bromide has been employed in the synthesis of preferentially {100} orientated nanoparticles with an increase in size of the nanoparticle in addition to the shape influence (181). However, selectivity can be an issue and nanoparticle agglomeration make morphology identification difficult.

Recently, a particular synthesis method has garnered a great deal of attention as it facilitates the production of very well-defined platinum nanocubes. A major versatile constituent of the synthesis is oleylamine which can assume the role of capping agent, solvent, reducing agent and is stable at high temperatures. These attractive characteristics mean oleylamine is being employed in a variety of shaped nanoparticle synthesis methods (182). In the synthesis employed in this study oleylamine is used in combination with oleic acid and gaseous carbon monoxide to produce highly ordered platinum nanocubes, with narrow shape and size selectivity. The carbon monoxide is believed to play a dual role as both a reducing and growth directing agent. The interaction of CO with platinum surfaces

has been studied intensely and it has been demonstrated to have preferential adsorption on specific surfaces of various metals. Adsorption of CO on Pt surfaces is much stronger on the {100} surface than the {111} facets, which would account for the strong cubic nature of the platinum nanoparticles (165). This synthesis method has produced cubic nanoparticles of the highest order of all the synthesis methods employed in this study, which can be qualitatively expressed by cyclic voltammograms of the nanoparticles, with specific reference to the {100} terrace section of the CV (chapter 5.2.1).

1.14 References

1. A. Robertson, The early history of catalysis. *Platinum Metals Review* **19**, 64-69 (1975).
2. L. J. THÉNARD, in *Annales de Chimie*. (1813), vol. 85, pp. 61-64.
3. L. J. Thenard, *Traité de chimie élémentaire, théorique et pratique*. (Canongette et compagnie, 1829), vol. 1.
4. J. Berzelius, Quelques Idées sur une nouvelle Force agissant dans les Combinaisons des Corps Organiques. *Ann. Chim* **61**, 146-151 (1836).
5. E. Shoko, B. McLellan, A. Dicks, J. D. Da Costa, Hydrogen from coal: production and utilisation technologies. *International Journal of Coal Geology* **65**, 213-222 (2006).
6. H. Davy, Electro-chemical researches, on the decomposition of the earths; with observations on the metals obtained from the alkaline earths, and on the amalgam procured from ammonia. *Philosophical Transactions of the Royal Society of London* **98**, 333-370 (1808).
7. W. Ostwald. (Google Patents, 1907).
8. H. L. Le Chatelier, Sur un énoncé général des lois des équilibres chimiques. *Comptes Rendus Académie des Sciences* **99**, 786-789 (1884).
9. F. Haber, R. Le Rossignol. (Google Patents, 1910).
10. F. Haber, G. Van Oordt, Über die Bildung von Ammoniak den Elementen. *Zeitschrift für anorganische und allgemeine Chemie* **44**, 341-378 (1905).
11. C. Bosch, A. Mittasch. (Google Patents, 1911).
12. A. F. M. Silver *et al.*, MINERAL COMMODITY SUMMARIES 2011.
13. I. Chorkendorff, J. W. Niemantsverdriet, *Concepts of modern catalysis and kinetics*. (John Wiley & Sons, 2017).
14. N. Arai, T. Ohkuma, Design of molecular catalysts for achievement of high turnover number in homogeneous hydrogenation. *The Chemical Record* **12**, 284-289 (2012).

15. R. Noyori, T. Ohkuma, Asymmetric catalysis by architectural and functional molecular engineering: practical chemo- and stereoselective hydrogenation of ketones. *Angewandte Chemie International Edition* **40**, 40-73 (2001).
16. I. Horiuti, M. Polanyi, Exchange reactions of hydrogen on metallic catalysts. *Transactions of the Faraday Society* **30**, 1164-1172 (1934).
17. F. Zaera, An organometallic guide to the chemistry of hydrocarbon moieties on transition metal surfaces. *Chemical Reviews* **95**, 2651-2693 (1995).
18. E. Stuve, R. Madix, Use of the π - σ parameter for characterization of rehybridization upon adsorption on metal surfaces. *The Journal of Physical Chemistry* **89**, 3183-3185 (1985).
19. Y. Dong, M. Ebrahimi, A. Tillekaratne, F. Zaera, Direct Addition Mechanism during the Catalytic Hydrogenation of Olefins over Platinum Surfaces. *The journal of physical chemistry letters* **7**, 2439-2443 (2016).
20. R. Zhou *et al.*, Parahydrogen enhanced NMR reveals correlations in selective hydrogenation of triple bonds over supported Pt catalyst. *Physical Chemistry Chemical Physics* **17**, 26121-26129 (2015).
21. M. Salmeron, G. Somorjai, Desorption, decomposition, and deuterium exchange reactions of unsaturated hydrocarbons (ethylene, acetylene, propylene, and butenes) on the platinum (111) crystal face. *The Journal of Physical Chemistry* **86**, 341-350 (1982).
22. A. Tillekaratne, J. P. Simonovis, M. F. Lopez Fagundez, M. Ebrahimi, F. Zaera, Operando studies of the catalytic hydrogenation of ethylene on Pt (111) single crystal surfaces. *ACS Catalysis* **2**, 2259-2268 (2012).
23. F. Zaera, G. Somorjai, Hydrogenation of ethylene over platinum (111) single-crystal surfaces. *J. Am. Chem. Soc.;(United States)* **106**, (1984).
24. F. Zaera, Surface chemistry of hydrocarbon fragments on transition metals: towards understanding catalytic processes. *Catalysis letters* **91**, 1-10 (2003).
25. S. Davis, F. Zaera, B. Gordon, G. Somorjai, Radiotracer and thermal desorption studies of dehydrogenation and atmospheric hydrogenation of organic fragments obtained from [¹⁴C] ethylene chemisorbed over Pt (111) surfaces. *Journal of Catalysis* **92**, 240-246 (1985).
26. J. Simonovis, A. Tillekaratne, F. Zaera, The Role of Carbonaceous Deposits in Hydrogenation Catalysis Revisited. *The Journal of Physical Chemistry C* **121**, 2285-2293 (2017).
27. M. Salmeron, R. Gale, G. Somorjai, Molecular beam study of the H₂-D₂ exchange reaction on stepped platinum crystal surfaces: Dependence on reactant angle of incidence. *The Journal of Chemical Physics* **67**, 5324-5334 (1977).
28. R. A. Olsen, L. B. Juurlink, in *Dynamics of Gas-Surface Interactions*. (Springer, 2013), pp. 101-129.
29. Y. Dong, F. Zaera, Kinetics of hydrogen adsorption during catalytic reactions on transition metal surfaces. *Catalysis Science & Technology* **7**, 5354-5364 (2017).
30. J. Simonovis, F. Zaera, Abrupt increase in hydrogen diffusion on transition-metal surfaces during hydrogenation catalysis. *Chemical Science* **7**, 4660-4666 (2016).
31. A. Corma, F. Melo, S. Mendioroz, J. Fierro, *12th international congress on catalysis*. (Elsevier, 2000), vol. 130.
32. F. Zaera, The surface chemistry of heterogeneous catalysis: Mechanisms, selectivity, and active sites. *The Chemical Record* **5**, 133-144 (2005).
33. A. Baiker, Chiral catalysis on solids. *Current Opinion in Solid State and Materials Science* **3**, 86-93 (1998).
34. a. A. Miyashita *et al.*, Synthesis of 2, 2'-bis (diphenylphosphino)-1, 1'-binaphthyl (BINAP), an atropisomeric chiral bis (triaryl) phosphine, and its use in the rhodium (I)-catalyzed asymmetric hydrogenation of α -(acylamino) acrylic acids. *Journal of the American Chemical Society* **102**, 7932-7934 (1980).
35. R. Noyori, Asymmetric hydrogenation. *Acta Chemica Scandinavica* **50**, 380-390 (1996).
36. W. S. Knowles, R. Noyori. (ACS Publications, 2007).

37. T. Katsuki, K. B. Sharpless, The first practical method for asymmetric epoxidation. *Journal of the American Chemical Society* **102**, 5974-5976 (1980).
38. R. Noyori, H. Takaya, BINAP: an efficient chiral element for asymmetric catalysis. *Accounts of Chemical Research* **23**, 345-350 (1990).
39. L. Canali, D. C. Sherrington, Utilisation of homogeneous and supported chiral metal (salen) complexes in asymmetric catalysis. *Chemical Society Reviews* **28**, 85-93 (1999).
40. G. Desimoni, G. Faita, K. A. Jørgensen, C₂-symmetric chiral bis (oxazoline) ligands in asymmetric catalysis. *Chemical reviews* **106**, 3561-3651 (2006).
41. K. Kacprzak, J. Gawroński, Cinchona alkaloids and their derivatives: versatile catalysts and ligands in asymmetric synthesis. *Synthesis* **2001**, 0961-0998 (2001).
42. M. J. Burk, Modular phospholane ligands in asymmetric catalysis. *Accounts of chemical research* **33**, 363-372 (2000).
43. M. J. Burk, C₂-symmetric bis (phospholanes) and their use in highly enantioselective hydrogenation reactions. *Journal of the American Chemical Society* **113**, 8518-8519 (1991).
44. Y. Izumi, M. Imaida, H. Fukawa, S. Akabori, Asymmetric hydrogenation with modified Raney nickel. I. Studies on modified hydrogenation catalyst. II. *Bulletin of the Chemical Society of Japan* **36**, 21-25 (1963).
45. Y. Orito, S. Imai, S. Niwa, ASYMMETRIC HYDROGENATION OF METHYL PYRUVATE USING PT-C CATALYST MODIFIED WITH CINCHONIDINE. *Nippon Kagaku Kaishi*, 1118-1120 (1979).
46. T. Osawa, T. Harada, A. Tai, Enantio-differentiating Hydrogenation of 2-Alkanones over asymmetrically modified nickel catalyst and its application to the preparation of optically pure 2-alkanols. *Journal of Catalysis* **121**, 7-17 (1990).
47. A. A. Choliq, J. Watanabe, T. Misaki, Y. Okamoto, T. Sugimura, Enantioselective hydrogenation of β -aryl- β -ketoester over α -hydroxy acid-modified Raney nickel catalysts: competitive hydrogenation with methyl acetoacetate. *Tetrahedron: Asymmetry* **27**, 657-662 (2016).
48. S. Nakagawa, T. Sugimura, A. Tai, A substrate specific chiral modifier activation on enantio-differentiating hydrogenation over tartaric acid-modified Raney nickel. *Chemistry letters* **27**, 1257-1258 (1998).
49. Y. Izumi, Modified Raney nickel (MRNi) catalyst: Heterogeneous enantio-differentiating (asymmetric) catalyst. *Adv. Catal* **32**, 215-271 (1983).
50. Y. Izumi, Methods of Asymmetric Synthesis—Enantioselective Catalytic Hydrogenation. *Angewandte Chemie International Edition in English* **10**, 871-881 (1971).
51. M. O. Lorenzo, C. Baddeley, C. Muryn, R. Raval, Extended surface chirality from supramolecular assemblies of adsorbed chiral molecules. *Nature* **404**, 376 (2000).
52. W. Hofer, V. Humblot, R. Raval, Conveying chirality onto the electronic structure of achiral metals:(R, R)-tartaric acid on nickel. *Surface science* **554**, 141-149 (2004).
53. V. Humblot, S. Haq, C. Muryn, R. Raval, (R, R)-Tartaric acid on Ni (110): the dynamic nature of chiral adsorption motifs. *Journal of Catalysis* **228**, 130-140 (2004).
54. R. A. Sheldon, H. Van Bekkum, *Fine chemicals through heterogeneous catalysis*. (John Wiley & Sons, 2008).
55. M. A. Keane, The importance of modifier pH in the generation of enantioselective nickel catalysts. *Catalysis letters* **19**, 197-209 (1993).
56. J. Clavilier, R. Faure, G. Guinet, R. Durand, Preparation of monocrystalline Pt microelectrodes and electrochemical study of the plane surfaces cut in the direction of the {111} and {110} planes. *Journal of Electroanalytical Chemistry and Interfacial Electrochemistry* **107**, 205-209 (1980).
57. A. J. Gellman, J. D. Horvath, M. T. Buelow, Chiral single crystal surface chemistry. *Journal of Molecular Catalysis A: Chemical* **167**, 3-11 (2001).
58. A. Ahmadi, G. Attard, J. Feliu, A. Rodes, Surface reactivity at "chiral" platinum surfaces. *Langmuir* **15**, 2420-2424 (1999).

59. R. A. Van Santen, Complementary structure sensitive and insensitive catalytic relationships. *Accounts of chemical research* **42**, 57-66 (2008).
60. M. Boudart, Catalysis by supported metals. *Adv. Catal* **20**, 153-166 (1969).
61. I. Lee, F. Zaera, Catalytic conversion of olefins on supported cubic platinum nanoparticles: Selectivity of (100) versus (111) surfaces. *Journal of Catalysis* **269**, 359-366 (2010).
62. K. R. McCrea, G. A. Somorjai, SFG-surface vibrational spectroscopy studies of structure sensitivity and insensitivity in catalytic reactions: cyclohexene dehydrogenation and ethylene hydrogenation on Pt (1 1 1) and Pt (1 0 0) crystal surfaces. *Journal of Molecular Catalysis A: Chemical* **163**, 43-53 (2000).
63. E. Schmidt, A. Vargas, T. Mallat, A. Baiker, Shape-selective enantioselective hydrogenation on Pt nanoparticles. *Journal of the American Chemical Society* **131**, 12358-12367 (2009).
64. G. Somorjai, The experimental evidence of the role of surface restructuring during catalytic reactions. *Catalysis letters* **12**, 17-34 (1992).
65. C. Kim, M. Min, Y. W. Chang, K.-H. Yoo, H. Lee, Chemical and thermal stability of Pt nanocubes synthesized with various surface-capping agents. *Journal of nanoscience and nanotechnology* **10**, 233-239 (2010).
66. R. Narayanan, M. A. El-Sayed. (ACS Publications, 2005).
67. R. Narayanan, M. A. El-Sayed, Effect of nanocatalysis in colloidal solution on the tetrahedral and cubic nanoparticle shape: electron-transfer reaction catalyzed by platinum nanoparticles. *The Journal of Physical Chemistry B* **108**, 5726-5733 (2004).
68. K. F. Kalz *et al.*, Future challenges in heterogeneous catalysis: understanding catalysts under dynamic reaction conditions. *ChemCatChem* **9**, 17-29 (2017).
69. F. Zaera, The surface chemistry of metal-based hydrogenation catalysis. *ACS Catalysis* **7**, 4947-4967 (2017).
70. J. Schwarz, The adsorption/impregnation of catalytic precursors on pure and composite oxides. *Catalysis today* **15**, 395-405 (1992).
71. P. Barbaro, F. Liguori, Ion exchange resins: catalyst recovery and recycle. *Chemical reviews* **109**, 515-529 (2008).
72. T. Maschmeyer, F. Rey, G. Sankar, J. M. Thomas, Heterogeneous catalysts obtained by grafting metallocene complexes onto mesoporous silica. *Nature* **378**, 159 (1995).
73. J.-E. Um, W. J. Yoon, H.-W. Choi, W.-J. Kim, Effective modification of Pd surfaces with TiO₂ promoters using selective chemical vapor deposition and the effect on catalytic performance improvement. *Journal of Industrial and Engineering Chemistry* **20**, 4183-4187 (2014).
74. K. P. De Jong, *Synthesis of solid catalysts*. (John Wiley & Sons, 2009).
75. S. Tauster, Strong metal-support interactions. *Accounts of Chemical Research* **20**, 389-394 (1987).
76. C. T. Campbell, Catalyst-support interactions: electronic perturbations. *Nature chemistry* **4**, 597 (2012).
77. G. Pacchioni, Electronic interactions and charge transfers of metal atoms and clusters on oxide surfaces. *Physical Chemistry Chemical Physics* **15**, 1737-1757 (2013).
78. J. K. Nørskov, F. Abild-Pedersen, F. Studt, T. Bligaard, Density functional theory in surface chemistry and catalysis. *Proceedings of the National Academy of Sciences*, 201006652 (2011).
79. J. Kitchin, J. K. Nørskov, M. Barteau, J. Chen, Modification of the surface electronic and chemical properties of Pt (111) by subsurface 3d transition metals. *The Journal of chemical physics* **120**, 10240-10246 (2004).
80. E. D. Hermes, G. R. Jenness, J. Schmidt, Decoupling the electronic, geometric and interfacial contributions to support effects in heterogeneous catalysis. *Molecular Simulation* **41**, 123-133 (2015).

81. C.-T. Yang, B. C. Wood, V. R. Bhethanabotla, B. Joseph, The effect of the morphology of supported subnanometer Pt clusters on the first and key step of CO₂ photoreduction. *Physical Chemistry Chemical Physics* **17**, 25379-25392 (2015).
82. A. Bruix *et al.*, A New Type of Strong Metal–Support Interaction and the Production of H₂ through the Transformation of Water on Pt/CeO₂ (111) and Pt/CeO_x/TiO₂ (110) Catalysts. *Journal of the American Chemical Society* **134**, 8968-8974 (2012).
83. G. R. Jenness, J. Schmidt, Unraveling the role of metal–support interactions in heterogeneous catalysis: oxygenate selectivity in Fischer–Tropsch synthesis. *ACS Catalysis* **3**, 2881-2890 (2013).
84. I. Langmuir, The adsorption of gases on plane surfaces of glass, mica and platinum. *Journal of the American Chemical Society* **40**, 1361-1403 (1918).
85. I. Langmuir, The constitution and fundamental properties of solids and liquids. Part I. Solids. *Journal of the American Chemical Society* **38**, 2221-2295 (1916).
86. C. Hinshelwood. (Oxford, 1940).
87. D. Eley, E. Rideal, Parahydrogen conversion on tungsten. *Nature* **146**, 401-402 (1940).
88. S. Brunauer, P. H. Emmett, E. Teller, Adsorption of gases in multimolecular layers. *Journal of the American Chemical Society* **60**, 309-319 (1938).
89. L. Meitner, Über die entstehung der β -strahl-spektralen radioaktiver substanzen. *Zeitschrift für Physik A Hadrons and Nuclei* **9**, 131-144 (1922).
90. P. Auger, The effect of a photoelectric compound. *Journal de Physique et le Radium* **6**, 205-U212 (1925).
91. J. A. Bearden, A. Burr, Reevaluation of X-ray atomic energy levels. *Reviews of Modern Physics* **39**, 125 (1967).
92. J. Jenkin, R. Leckey, J. Liesegang, The development of x-ray photoelectron spectroscopy: 1900–1960. *Journal of electron spectroscopy and related phenomena* **12**, 1-35 (1977).
93. R. Reichelt, in *Science of microscopy*. (Springer, 2007), pp. 133-272.
94. D. B. Williams, C. B. Carter, in *Transmission electron microscopy*. (Springer, 1996), pp. 3-17.
95. B. E. Warren, *X-ray Diffraction*. (Courier Corporation, 1969).
96. J. B. Pendry, *Low energy electron diffraction*. (Academic Press London, 1974).
97. G. Binnig, C. F. Quate, C. Gerber, Atomic force microscope. *Physical review letters* **56**, 930 (1986).
98. G. A. Somorjai, Y. Li, *Introduction to surface chemistry and catalysis*. (John Wiley & Sons, 2010).
99. J. Anderson, Y. Shimoyama, Effect of platinum particle size on hydrocarbon hydrogenolysis' Catalysis. *Proc., 5th Int. Congr. Hightower, J. W, editor* **1**, 695-715 (1973).
100. M. Boudart, A. Aldag, L. D. Ptak, J. Benson, On the selectivity of platinum catalysts. *Journal of Catalysis* **11**, 35-45 (1968).
101. M. Boudart, A. Aldag, J. Benson, N. Dougharty, C. G. Harkins, On the specific activity of platinum catalysts. *Journal of Catalysis* **6**, 92-99 (1966).
102. T. Dorling, R. Moss, The structure and activity of supported metal catalysts: I. Crystallite size and specific activity for benzene hydrogenation of platinum/silica catalysts. *Journal of Catalysis* **5**, 111-115 (1966).
103. B. R. Cuenya, Synthesis and catalytic properties of metal nanoparticles: Size, shape, support, composition, and oxidation state effects. *Thin Solid Films* **518**, 3127-3150 (2010).
104. E. Ozensoy, D. C. Meier, D. W. Goodman, Polarization modulation infrared reflection absorption spectroscopy at elevated pressures: CO adsorption on Pd (111) at atmospheric pressures. *The Journal of Physical Chemistry B* **106**, 9367-9371 (2002).
105. T. Buergi, A. Baiker, Attenuated total reflection infrared spectroscopy of solid catalysts functioning in the presence of liquid-phase reactants. *Advances in Catalysis* **50**, 227-283 (2006).

106. G. Rupprechter, Surface vibrational spectroscopy from ultrahigh vacuum to atmospheric pressure: adsorption and reactions on single crystals and nanoparticle model catalysts monitored by sum frequency generation spectroscopy. *Physical Chemistry Chemical Physics* **3**, 4621-4632 (2001).
107. S. Bilmes, SERS of pyridine adsorbed on rhodium electrodes. *Chemical Physics Letters* **171**, 141-146 (1990).
108. Z.-Q. Tian, B. Ren, J.-F. Li, Z.-L. Yang, Expanding generality of surface-enhanced Raman spectroscopy with borrowing SERS activity strategy. *Chemical Communications*, 3514-3534 (2007).
109. J.-F. Li, A. Rudnev, Y. Fu, N. Bodappa, T. Wandlowski, In Situ SHINERS at Electrochemical Single-Crystal Electrode/Electrolyte Interfaces: Tuning Preparation Strategies and Selected Applications. *ACS nano* **7**, 8940-8952 (2013).
110. A. Campion, P. Kambhampati, Surface-enhanced Raman scattering. *Chemical society reviews* **27**, 241-250 (1998).
111. M. Fleischmann, P. Hendra, A. McQuillan, Raman spectra of pyridine adsorbed at a silver electrode. *Chemical Physics Letters* **26**, 163-166 (1974).
112. R. Van Duyne, RAMAN APPLICATIONS OF RAMAN SPECTROSCOPY IN ELECTROCHEMISTRY. *Le Journal de Physique Colloques* **38**, C5-239-C235-252 (1977).
113. M. G. Albrecht, J. A. Creighton, Anomalous intense Raman spectra of pyridine at a silver electrode. *Journal of the american chemical society* **99**, 5215-5217 (1977).
114. B. Sharma, R. R. Frontiera, A.-I. Henry, E. Ringe, R. P. Van Duyne, SERS: materials, applications, and the future. *Materials today* **15**, 16-25 (2012).
115. M. Moskovits, D. DiLella. (New York: Plenum, 1982).
116. G. Boyd, T. Rasing, J. Leite, Y. Shen, Local-field enhancement on rough surfaces of metals, semimetals, and semiconductors with the use of optical second-harmonic generation. *Physical Review B* **30**, 519 (1984).
117. B. Bozlee *et al.*, Characterization of alkali-metal sols in diethyl ether. Visible extinction and surface-enhanced Raman spectra. *Chemical physics letters* **196**, 437-444 (1992).
118. K. L. Haller *et al.*, Spatially resolved surface enhanced second harmonic generation: Theoretical and experimental evidence for electromagnetic enhancement in the near infrared on a laser microfabricated Pt surface. *The Journal of chemical physics* **90**, 1237-1252 (1989).
119. P. V. Kamat. (ACS Publications, 2002).
120. E. Prodan, C. Radloff, N. J. Halas, P. Nordlander, A hybridization model for the plasmon response of complex nanostructures. *science* **302**, 419-422 (2003).
121. L. Lu *et al.*, Fabrication of core-shell Au-Pt nanoparticle film and its potential application as catalysis and SERS substrate. *Journal of materials chemistry* **14**, 1005-1009 (2004).
122. J.-W. Hu *et al.*, Synthesis of Au@ Pd core-shell nanoparticles with controllable size and their application in surface-enhanced Raman spectroscopy. *Chemical physics letters* **408**, 354-359 (2005).
123. J. F. Li *et al.*, Shell-isolated nanoparticle-enhanced Raman spectroscopy. *Nature* **464**, 392-395 (2010).
124. A. M. Mohs *et al.*, Hand-held spectroscopic device for in vivo and intraoperative tumor detection: contrast enhancement, detection sensitivity, and tissue penetration. *Analytical chemistry* **82**, 9058-9065 (2010).
125. J.-H. An, W. A. El-Said, C.-H. Yea, T.-H. Kim, J.-W. Choi, Surface-enhanced Raman scattering of dopamine on self-assembled gold nanoparticles. *Journal of nanoscience and nanotechnology* **11**, 4424-4429 (2011).
126. K. Ma *et al.*, In vivo, transcutaneous glucose sensing using surface-enhanced spatially offset Raman spectroscopy: multiple rats, improved hypoglycemic accuracy, low incident power,

- and continuous monitoring for greater than 17 days. *Analytical chemistry* **83**, 9146-9152 (2011).
127. C. L. Brosseau, F. Casadio, R. P. Van Duyne, Revealing the invisible: using surface-enhanced Raman spectroscopy to identify minute remnants of color in Winslow Homer's colorless skies. *Journal of Raman Spectroscopy* **42**, 1305-1310 (2011).
 128. M. Winter, R. J. Brodd. (ACS Publications, 2004).
 129. F. Barbir, in *Fuel Cell Technology*. (Springer, 2006), pp. 27-51.
 130. E. Bakker, M. Telting-Diaz, Electrochemical sensors. *Analytical chemistry* **74**, 2781-2800 (2002).
 131. N. Markovic, T. Schmidt, V. Stamenkovic, P. Ross, Oxygen reduction reaction on Pt and Pt bimetallic surfaces: a selective review. *FUEL CELLS-WEINHEIM- 1*, 105-116 (2001).
 132. M. Shao, Q. Chang, J.-P. Dodelet, R. Chenitz, Recent advances in electrocatalysts for oxygen reduction reaction. *Chemical reviews* **116**, 3594-3657 (2016).
 133. H. Knözinger, K. Kochloefl, Heterogeneous catalysis and solid catalysts. *Ullmann's Encyclopedia of Industrial Chemistry*, (2002).
 134. J. K. Nørskov *et al.*, Origin of the overpotential for oxygen reduction at a fuel-cell cathode. *The Journal of Physical Chemistry B* **108**, 17886-17892 (2004).
 135. J. Zhang, *PEM fuel cell electrocatalysts and catalyst layers: fundamentals and applications*. (Springer Science & Business Media, 2008).
 136. R. Borup *et al.*, Scientific aspects of polymer electrolyte fuel cell durability and degradation. *Chemical reviews* **107**, 3904-3951 (2007).
 137. C. M. Sánchez-Sánchez, A. J. Bard, Hydrogen peroxide production in the oxygen reduction reaction at different electrocatalysts as quantified by scanning electrochemical microscopy. *Analytical chemistry* **81**, 8094-8100 (2009).
 138. A. Stassi *et al.*, Electrocatalytic behaviour for oxygen reduction reaction of small nanostructured crystalline bimetallic Pt–M supported catalysts. *Journal of applied electrochemistry* **36**, 1143-1149 (2006).
 139. X. Cheng *et al.*, A review of PEM hydrogen fuel cell contamination: Impacts, mechanisms, and mitigation. *Journal of Power Sources* **165**, 739-756 (2007).
 140. M. Hogarth, T. Ralph, Catalysis for low temperature fuel cells, Part II. The anode challenges. *Platinum Metals Review* **46**, 117-135 (2002).
 141. S. Sui *et al.*, A comprehensive review of Pt electrocatalysts for the oxygen reduction reaction: Nanostructure, activity, mechanism and carbon support in PEM fuel cells. *Journal of Materials Chemistry A* **5**, 1808-1825 (2017).
 142. V. R. Stamenkovic *et al.*, Improved oxygen reduction activity on Pt₃Ni (111) via increased surface site availability. *science* **315**, 493-497 (2007).
 143. N. Elgrishi *et al.*, A Practical Beginner's Guide to Cyclic Voltammetry. *Journal of Chemical Education* **95**, 197-206 (2017).
 144. S. E. Creager, T. T. Wooster, A new way of using ac voltammetry to study redox kinetics in electroactive monolayers. *Analytical chemistry* **70**, 4257-4263 (1998).
 145. J. Solla-Gullón, P. Rodríguez, E. Herrero, A. Aldaz, J. M. Feliu, Surface characterization of platinum electrodes. *Physical Chemistry Chemical Physics* **10**, 1359-1373 (2008).
 146. D. R. Lowde, J. O. Williams, B. D. McNicol, The characterisation of catalyst surfaces by cyclic voltammetry. *Applications of Surface Science* **1**, 215-240 (1978).
 147. N. M. Markovića, S. T. Sarraf, H. A. Gasteiger, P. N. Ross, Hydrogen electrochemistry on platinum low-index single-crystal surfaces in alkaline solution. *Journal of the Chemical Society, Faraday Transactions* **92**, 3719-3725 (1996).
 148. N. Markovic, M. Hanson, G. McDougall, E. Yeager, The effects of anions on hydrogen electrosorption on platinum single-crystal electrodes. *Journal of electroanalytical chemistry and interfacial electrochemistry* **214**, 555-566 (1986).

149. M. W. Shinwari *et al.*, Microfabricated reference electrodes and their biosensing applications. *Sensors* **10**, 1679-1715 (2010).
150. J. Feliu, J. Orts, R. Gomez, A. Aldaz, J. Clavilier, New information on the unusual adsorption states of Pt (111) in sulphuric acid solutions from potentiostatic adsorbate replacement by CO. *Journal of Electroanalytical Chemistry* **372**, 265-268 (1994).
151. F. Opekar, P. Beran, Rotating disk electrodes. *Journal of Electroanalytical Chemistry and Interfacial Electrochemistry* **69**, 1-105 (1976).
152. D. Pletcher, R. A. Green, R. C. Brown, Flow electrolysis cells for the synthetic organic chemistry laboratory. *Chemical reviews* **118**, 4573-4591 (2017).
153. D. Harvey, *Modern analytical chemistry*. (Boston: McGraw-Hill Companies, Inc., 2000).
154. Y. Zhai, Z. Zhu, S. Zhou, C. Zhu, S. Dong, Recent advances in spectroelectrochemistry. *Nanoscale* **10**, 3089-3111 (2018).
155. T. Kuwana, R. Darlington, D. Leedy, Electrochemical Studies Using Conducting Glass Indicator Electrodes. *Analytical Chemistry* **36**, 2023-2025 (1964).
156. W. Kaim, J. Fiedler, Spectroelectrochemistry: the best of two worlds. *Chemical Society Reviews* **38**, 3373-3382 (2009).
157. D.-Y. Wu, J.-F. Li, B. Ren, Z.-Q. Tian, Electrochemical surface-enhanced Raman spectroscopy of nanostructures. *Chemical Society Reviews* **37**, 1025-1041 (2008).
158. S. Hy, Y.-H. Chen, J.-y. Liu, J. Rick, B.-J. Hwang, In situ surface enhanced Raman spectroscopic studies of solid electrolyte interphase formation in lithium ion battery electrodes. *Journal of Power Sources* **256**, 324-328 (2014).
159. R. A. Karaballi, S. Merchant, S. R. Power, C. L. Brosseau, Electrochemical surface-enhanced Raman spectroscopy (EC-SERS) study of the interaction between protein aggregates and biomimetic membranes. *Physical Chemistry Chemical Physics* **20**, 4513-4526 (2018).
160. A. Abedini *et al.*, Recent advances in shape-controlled synthesis of noble metal nanoparticles by radiolysis route. *Nanoscale research letters* **11**, 287 (2016).
161. T. S. Ahmadi, Z. L. Wang, T. C. Green, A. Henglein, M. A. El-Sayed, Shape-controlled synthesis of colloidal platinum nanoparticles. *Science* **272**, 1924 (1996).
162. Y. Sun, B. Mayers, T. Herricks, Y. Xia, Polyol synthesis of uniform silver nanowires: a plausible growth mechanism and the supporting evidence. *Nano letters* **3**, 955-960 (2003).
163. D. Y. Kim *et al.*, Au@ Pd core-shell nanocubes with finely-controlled sizes. *CrystEngComm* **15**, 3385-3391 (2013).
164. K. Matsuzawa, T. Fukushima, M. Inaba, Shape-controlled platinum nanoparticles of different sizes and their electrochemical properties. *Electrocatalysis* **1**, 169-177 (2010).
165. J. Wu, A. Gross, H. Yang, Shape and Composition-Controlled Platinum Alloy Nanocrystals Using Carbon Monoxide as Reducing Agent. *Nano Letters* **11**, 798-802 (2011).
166. Z. S. Pillai, P. V. Kamat, What factors control the size and shape of silver nanoparticles in the citrate ion reduction method? *The Journal of Physical Chemistry B* **108**, 945-951 (2004).
167. Y. Xia, Y. Xiong, B. Lim, S. E. Skrabalak, Shape-controlled synthesis of metal nanocrystals: Simple chemistry meets complex physics? *Angewandte Chemie International Edition* **48**, 60-103 (2009).
168. F. Zaera, Shape-controlled nanostructures in heterogeneous catalysis. *ChemSusChem* **6**, 1797-1820 (2013).
169. J.-W. Yoo, S.-M. Lee, H.-T. Kim, M. El-Sayed, Propylene hydrogenation over cubic Pt nanoparticles deposited on alumina. *Bulletin of the Korean Chemical Society* **25**, 843-846 (2004).
170. M. Inaba *et al.*, Controlled growth and shape formation of platinum nanoparticles and their electrochemical properties. *Electrochimica Acta* **52**, 1632-1638 (2006).
171. C. Susut, G. B. Chapman, G. Samjeské, M. Osawa, Y. Tong, An unexpected enhancement in methanol electro-oxidation on an ensemble of Pt (111) nanofacets: a case of nanoscale

- single crystal ensemble electrocatalysis. *Physical Chemistry Chemical Physics* **10**, 3712-3721 (2008).
172. Z. Peng, H. You, J. Wu, H. Yang, Electrochemical synthesis and catalytic property of sub-10 nm platinum cubic nanoboxes. *Nano letters* **10**, 1492-1496 (2010).
 173. C.-J. Huang, Y.-H. Wang, P.-H. Chiu, M.-C. Shih, T.-H. Meen, Electrochemical synthesis of gold nanocubes. *Materials Letters* **60**, 1896-1900 (2006).
 174. X.-y. Liu, C.-y. Cui, Y.-w. Cheng, H.-y. Ma, D. Liu, Shape control technology during electrochemical synthesis of gold nanoparticles. *International Journal of Minerals, Metallurgy, and Materials* **20**, 486-492 (2013).
 175. P. R. Sajanlal, T. S. Sreeprasad, A. K. Samal, T. Pradeep, Anisotropic nanomaterials: structure, growth, assembly, and functions. *Nano reviews* **2**, 5883 (2011).
 176. G. Wulff, Some Theorems Concerning the Growth and Dissolution Rates of Crystals. *Ger.), Z. Kristallogr* **34**, 449-530 (1901).
 177. Y. Xiong, Y. Xia, Shape-controlled synthesis of metal nanostructures: the case of palladium. *Advanced Materials* **19**, 3385-3391 (2007).
 178. J. Zeng *et al.*, Controlling the shapes of silver nanocrystals with different capping agents. *Journal of the American Chemical Society* **132**, 8552-8553 (2010).
 179. Y. Xie, D. Kocaeefe, C. Chen, Y. Kocaeefe, Review of research on template methods in preparation of nanomaterials. *Journal of Nanomaterials* **2016**, 11 (2016).
 180. N. Garg, C. Scholl, A. Mohanty, R. Jin, The role of bromide ions in seeding growth of Au nanorods. *Langmuir* **26**, 10271-10276 (2010).
 181. R. Antoniassi, L. Otubo, J. Vaz, A. O. Neto, E. Spinacé, Synthesis of Pt nanoparticles with preferential (1 0 0) orientation directly on the carbon support for direct ethanol fuel cell. *Journal of Catalysis* **342**, 67-74 (2016).
 182. S. Mourdikoudis, L. M. Liz-Marzan, Oleylamine in nanoparticle synthesis. *Chemistry of Materials* **25**, 1465-1476 (2013).

Chapter 2 – Theoretical Background

2.1 Surface Structure

2.1.1 Structure of well-defined surfaces

It is evident from discussions in the previous chapter that the chemical and physical properties of a catalytic surface are heavily influenced by the nature of the atoms comprising the surface and their spatial distribution. Surfaces are found to consist of a mixture of flat regions (also known as terraces) and defects (steps, kinks, etc. Figure 2.1).

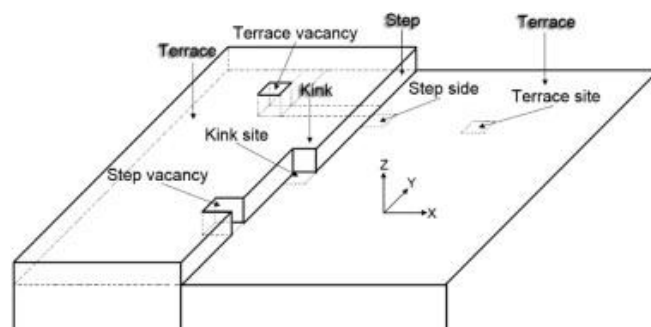


Figure 2.1: Schematic representation of terrace and defect sites on a surface. reprinted from(1)

Since the atomic arrangement around each surface site is different, each site exhibits its own unique surface chemistry and physical response. A key area for catalysis is how the presence of these different sites effects the adsorption and subsequently activity of a catalytic reaction. The influence on activity of a surface can be split into two categories, electronic effects and geometric effects. The geometric effect can be correlated to the coordination number of the surface atoms, with terrace atoms having a high value and defect sites being low. The concentration of defect and terrace sites alter dramatically depending on the crystallite size, with an inverse relationship observed. Depending if a reaction is particularly active on either low or high coordination sites, one could expect a significant variation on catalytic activity (per unit surface atom) with differing particle sizes. However, a purely geometric approach is not accurate. The electronic effect can be explained through d-band theory (figure 2.2), with the chief underlying principle that the

binding energy of an adsorbate to a metal surface is largely dependent on the electronic structure of the surface (2). Briefly, d-band theory can be best explained through visualizing the orbitals of the metal and adsorbate. The metal d-band hybridizes with the σ bonding orbital of the adsorbate to form bonding ($d-\sigma$) and antibonding ($d-\sigma^*$) states. For common transition metal catalysts like platinum the $d-\sigma$ state is full, but the extent of filling of the antibonding state is dependent on the density of the states on the metal surface. An increased filling of the $d-\sigma^*$ state leads to the destabilisation of the metal-adsorbate interaction, thus, the adsorbate is weakly bound to the surface.

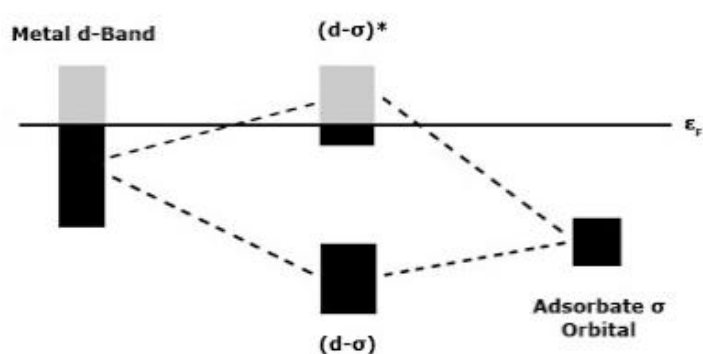


Figure 2.2: Schematic detailing the metal and adsorbate orbital interactions in d-band theory, reprinted from (2).

The fermi level is the highest energy state occupied by electrons in material at absolute zero. From the above model it is apparent that a higher d-band center, with respect to the fermi level, corresponds to an increase in energy and subsequent decrease in filling of the antibonding state. These two theoretical effects can help to model the reactivity of a catalytic surface, but in reality, the surface interactions of catalysts are shrouded in complexity, figure 2.3 demonstrates this in breaking down numerous key parameters to consider on a catalytic surface.

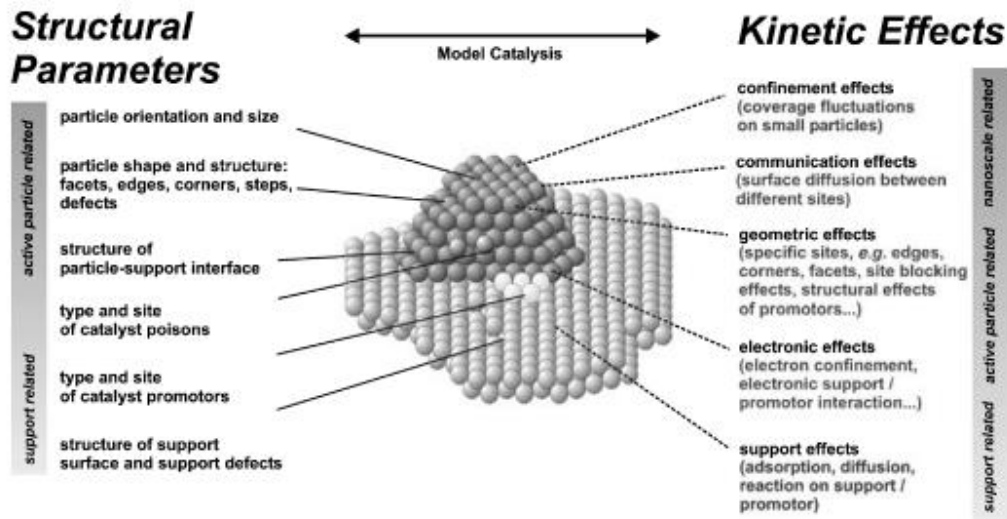


Figure 2.3: Structural parameters and kinetic effects on supported model catalysts, reprinted from (3).

Conducting atomic-level experimental investigations on surfaces of this type is very demanding, as any data collected from this surface will contain contributions from all the surface site types. Isolating the involvement of a specific site would be an arduous, perhaps impossible task. Therefore, it is important for the investigator to implement some form of control to obtain reproducible results. This generally results in the simplification of the surface, by using surfaces with a high ratio of terrace sites to defect sites. Greater complexity can be introduced to the surface, by adding controlled amounts of defect sites. These surfaces can be referred to as *well-defined* and form the basis for fundamental surface science investigations.

2.1.2 Single crystal surfaces

Single crystal surfaces are commonly used as well-defined surfaces for experiments. Single crystal surfaces are formed by cutting through a crystal to expose a specific plane. The specific planes will contain a limited number of well-defined atomic sites. These specific atomic sites can be altered systematically by adjusting the cutting orientation to expose different crystallographic planes. The atomic surfaces produced from this cutting procedure

may be either flat (consisting exclusively of large terraces) or vicinal (consisting of short flat terraces separated by steps)(1). The method for preparing specific single crystal surfaces is outlined by Clavilier *et al*(4), with figure 2.4 detailing the individual steps required for producing a single crystal electrode.

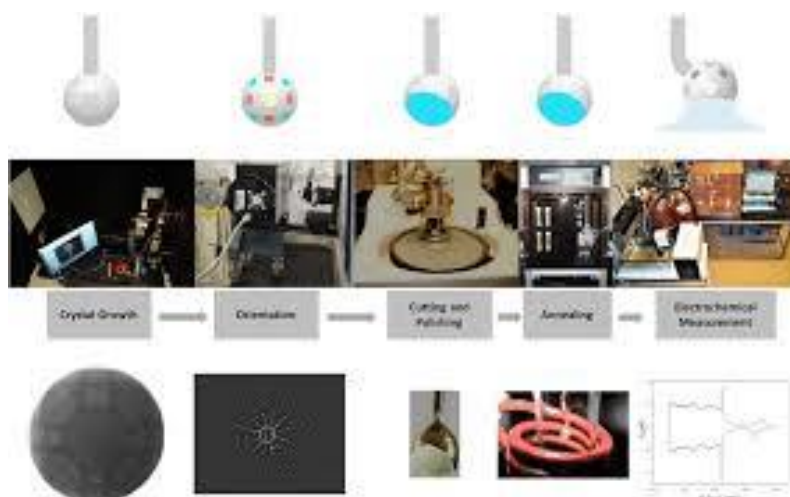


Figure 2.4: Schematic detailing the individual steps of single crystal preparation, reprinted from (5).

2.1.3 Miller index notation

Miller index notation is used to define a given plane and incorporates the bulk and surface structures of the single crystal. The miller index consists of three integers (x, y, z) for bulk cubic structures (simple cubic (sc), face centred cubic (fcc), body centred cubic (bcc)) or four integers (w, x, y, z) for hexagonal close packed (hcp) structures. With platinum single crystal surfaces being the focus of this investigation, the three-integer form of the miller index is of most interest. The miller indices for platinum are defined by three orthogonal lattice vectors, which run along the edges of the crystallographic unit cell. Crystal planes intercept the axes at certain points; which are denoted as $\vec{a}, \vec{b}, \vec{c}$. The distance from the origin to intercept points are denoted a, b, c and in order to denote Miller indices in the h, k, l, form the following equation must be used:

$$\frac{|\vec{a}|}{a} = h, \frac{|\vec{b}|}{b} = k, \frac{|\vec{c}|}{c} = l \text{ (eq 2.1)}$$

An integer value of 0 indicates that the plane is parallel to the respective axis and a negative integer value is denoted with a bar written over the number. If a fraction is present in the h,

k, l notation, all three values are converted to the lowest possible integers while maintaining the original ratios of the values. The three most common Low Miller index surfaces for fcc metals are {111}, {110} and {100} surfaces, also known as the basal planes. Each of the three surfaces are represented schematically in figure 2.5.

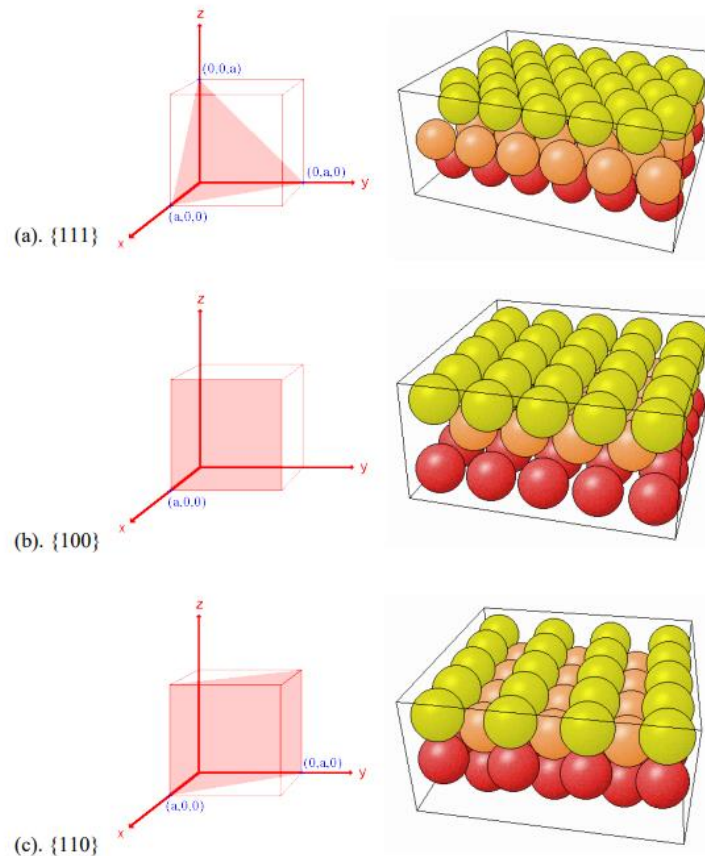


Figure 2.5: Schematic representation of the unit cell and atomic arrangement of the fcc basal planes. Reprinted from (6)

Higher miller indices are denoted by a fractional integer in the h, k, l notation, these surfaces are not flat and usually consist of narrow low index planes separated by steps. It can be more convenient to refer to the plane using microfacet notation(7), which takes the following form:

$$N(x, y, z) \times (u, v, w)$$

Where N is the number of atoms in the terrace, (x, y, z) is the miller index of the terrace and (u, v, w) is the miller index of the step. For example, the (755) surface can be alternatively

expressed as $6(111) \times (100)$, denoting a surface containing 6 atom wide (111) terraces separated by a (100) step. All crystal surfaces can be expressed in terms of combinations of the three low index planes, this is illustrated by the stereographic triangle (figure 2.6). A three-component phase diagram, where each vertex is one of the basal planes. As the surfaces progress from one vertex to the next, the surface terrace sites relating to the original vertex decreases.

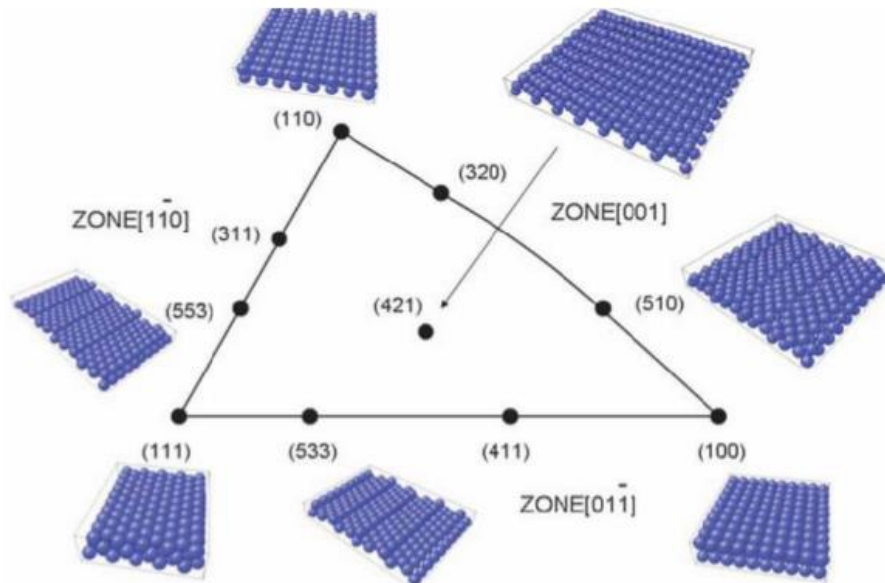


Figure 2.6: Stereographic triangle of fcc single crystal surfaces and their corresponding atomic arrangements. Reprinted from (8)

The stereographic triangle gives an appreciation for the vast amount of single crystal surfaces that can be produced and studied. These surfaces have been utilised to study fundamental heterogeneous surface interactions, giving great insight on surface sensitive reactions(8).

2.2 Shape controlled nanoparticles

A similar stereographic triangle to figure 2.6 can be constructed for shaped nanoparticles (figure 2.7). The faces of the nanoparticles have a surface structure of the indicated miller index and should exhibit similar properties to the corresponding single crystal surfaces.

While control of the surface structure is diminished when compared to single crystal surfaces, with the presence of edges between facets needed to be accounted for.

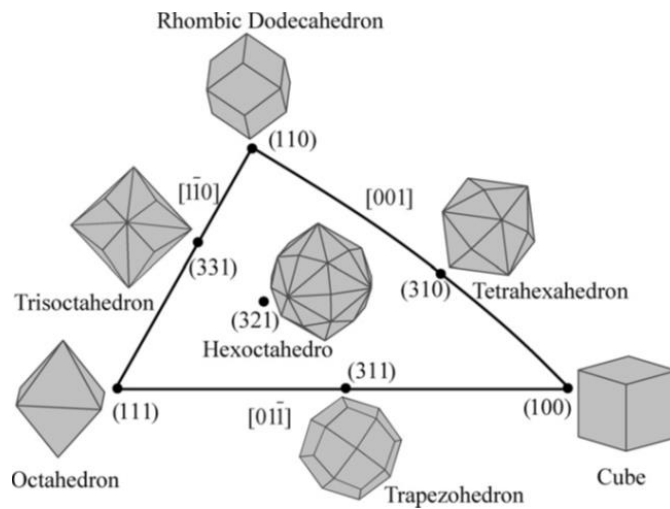


Figure 2.7: Stereographic triangle of polyhedral fcc nanocrystals bound by different crystal planes. Reprinted from(9)

The synthesis of shape-controlled nanoparticles is a much more complicated process in comparison to the preparation of single crystal surfaces. With many of the shaped nanocrystals presented in figure 4 being inherently unstable. The instability of the shaped nanoparticles can be attributed to attempts of the nanoparticle to have the lowest surface energy possible. This phenomenon is referred to by Wulff theorem, which states that a crystal of a given volume will attempt to minimise the total interfacial free energy of the system(10). Interfacial free energy, γ , can be defined as the energy required to create a unit area of “new” surface (eq 2.2)(11). Where G is the Gibbs free energy and A is the surface area.

$$\gamma = (\partial G / \partial A)_{n_i, T, P} \dots (2.2)$$

For a newly formed seed crystal the symmetry of atoms at the surface is altered due to the differing coordination numbers with nearest neighbours in comparison to atoms in the bulk metal. This causes surface atoms to become attracted toward the bulk of the crystal. A restoring force is required to counter this attraction and restore the symmetry of the surface atoms to reflect an ideal surface. This gives rise to a second expression of interfacial

free energy (eq 2.3). Where N_b is the number of broken bonds, ε is the bond strength and ρ_a is the density of surface atoms(12).

$$\gamma = \frac{1}{2} N_b \varepsilon \rho_a \dots (2.3)$$

For an fcc structure with a lattice constant of a , the surface energies of the basal planes can be estimated (eq 2.4). This results in the surface free energies associated with the low-index crystallographic planes being in the order of $\gamma(111) < \gamma(100) < \gamma(110)$. This relation of the surface free energies of basal planes would suggest that the crystal seed should be orientated to incorporate the maximum amount of $\{111\}$ facets possible; which on reflection with the stereographic triangle would suggest an octahedral or tetrahedral shape. However, this is not the case as both octahedrons and tetrahedrons have a larger surface area when compared to a cube of the same volume. The expected shape of the seeds would be truncated octahedrons enclosed by both $\{100\}$ and $\{111\}$ facets, also referred to as a Wulff polyhedron. This shape is almost spherical giving the smallest surface area; allowing surface free energy to be minimised(10).

$$\gamma_{\{100\}} = 4(\varepsilon/a^2), \gamma_{\{110\}} = 4.24(\varepsilon/a^2), \gamma_{\{111\}} = 3.36(\varepsilon/a^2) \dots (2.4)$$

2.2.1 The Role of Capping Agents

In order to overcome the inherent instability associated with shaped nanocrystals, certain synthesis methods utilise stabilising/capping agents. These agents are usually organic or polymeric in nature and possess large carbon chains and usually have an affinity for certain orientations of nano-facets. once bound to that facet, the capping agent acts like “organic armour” blocking the approach of reactants(13). This can direct the growth of the nanoparticle in a specific plane to form shaped nanoparticles. Many capping agents have been employed in nanoparticle synthesis methods to produce an array of nanoparticle shapes(11, 14, 15). A specific example would be the use of polyacrylic acid (PAA) as a capping agent in cubic Pt nanoparticle synthesis. The PAA capping agent was found to have

preferential binding interactions with {100} sites on platinum nanoparticles, this causes a slower growth rate on the {100} sites which means the growth rate of {111} sites are comparatively larger. This dictates the cubic nature of the nanoparticles as the slower growing {100} facets, eventually enclose the surface of the nanocrystal structure(15). The influence of the capping agent on the growth of the nanoparticles is represented schematically in figure 2.8.

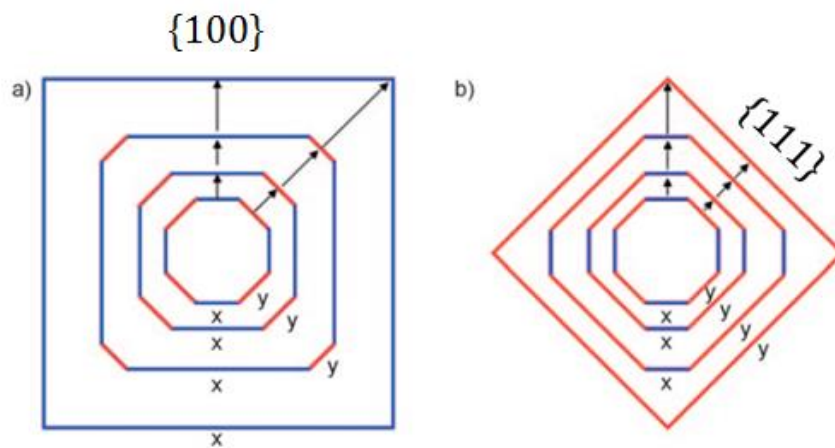


Figure 2.8: Schematic representation of how the growth rate of the {100} and {111} facets can impact the shape of the nanoparticle. Reprinted from (16)

2.3 Adsorption

Adsorption is an important and frequently observed phenomena; with regards to surface electrochemistry. It is important to distinguish the fundamental differences between adsorption and absorption as the two processes entail very different events. Adsorption is the term for a molecule (adsorbate) bonding to the surface (adsorbent); absorption refers to a molecule entering the bulk of the substrate. The amount of adsorption occurring on a surface can be expressed in terms of the fractional coverage of adsorbate (eq 2.5)(1).

$$\theta = \frac{\text{Number of surface sites occupied by adsorbate } (N_s)}{\text{Total number of substrate adsorption sites } (N)} \dots \dots (2.5)$$

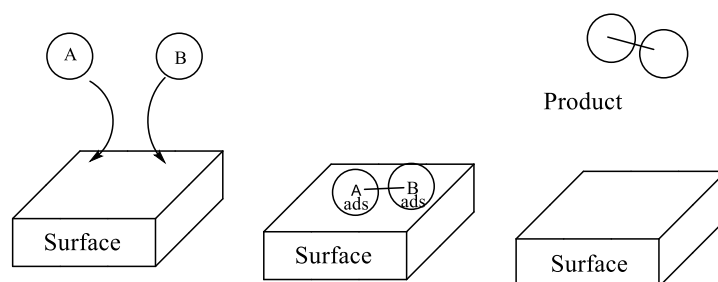
The denotation of the formation of a monolayer is when $\theta=1$, the mechanism of adsorption can be summarised under two main types:

- Associative adsorption is said to occur when a molecule adsorbs on to the surface without fragmentation occurring.
- Dissociative adsorption is said to occur with fragmentation.

Bonding of the adsorbates to the surface can also be split into two classifications, dependent on the scale of the adsorption enthalpy. These two classifications are physisorption and chemisorption. Physisorption is characterised by weak interactions between adsorbate (e.g. gas molecule) and adsorbent (e.g. a solid catalyst surface), whereas chemisorption is characterised by stronger interactions between the two. Chemisorption is also characterised by a chemical reaction between the adsorbent and adsorbate (therefore electron transfer) and the formation of true bonds. Physisorption is a Van der Waals interaction, the adsorbing species barely perturbed. These aspects are reflected in their adsorption enthalpies, generally $<35 \text{ kJ mol}^{-1}$ adsorption enthalpies are observed for physisorption and $>35 \text{ kJ mol}^{-1}$ for chemisorption(1).

The adsorption and desorption phenomena have been extensively applied to heterogeneous catalysis. Two well-known bimolecular mechanisms have been developed to model the different behaviours of adsorbed reactants on surfaces on catalytic substrates. These models are extremely significant to heterogeneous catalysis(17). The first is the Langmuir-Hinshelwood mechanism; which proposes that both reactants adsorb to the surface, migrate/diffuse across the surface and upon collision react and the product desorbs from the surface. The second mechanism is the Eley-Rideal mechanism; which proposes one reactant is adsorbed, reacts with a molecule that is in the secondary phase and the product desorbs from the surface (figure 2.9)

Langmuir-Hinshelwood Mechanism



Eley-Rideal Mechanism

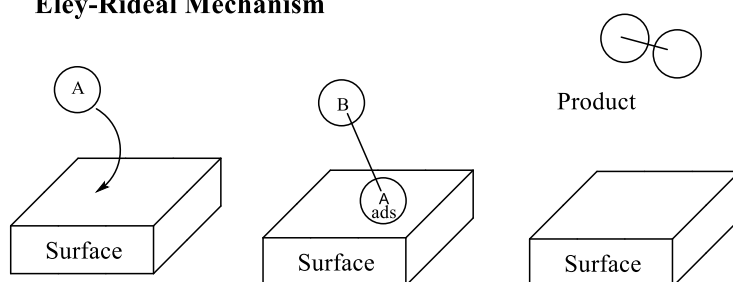


Figure 2.9: Schematic representation of the Langmuir-Hinshelwood and Eley-Rideal mechanisms.

2.4 Cyclic Voltammetry

Cyclic voltammetry (CV) has become a popular tool in the last few decades for studying electrochemical reactions(18). CV uses a three-electrode set-up which involves a working, reference and counter electrode. The electrodes are static and the solution is un-stirred, resulting in characteristic diffusion controlled peaks. To carry out measurements, potential at the working electrode is cycled linearly between low (V_{initial}) and high (V_{final}) values with respect to the reference electrode. When plotting a potential (V) vs. time (t) graph a sawtooth potential waveform is displayed, the gradient of which denotes the scan rate of

the experiment (figure 2.10). Cyclic voltammograms display the current response of the working electrode during the linear potential sweeps. These current responses can be related to oxidation reactions at the electrode interface (positive current) and reduction reactions (negative current).

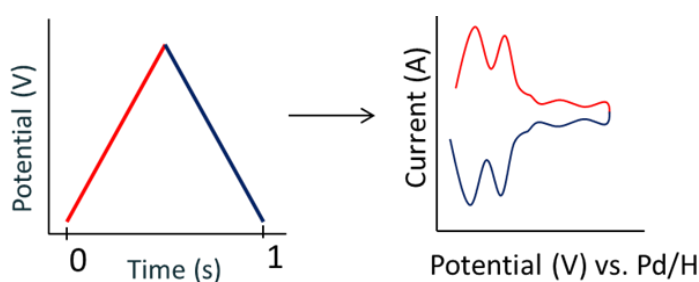


Figure 2.10: Graphical representation of the linear potential sweep and current responses of the CV process. Reprinted from(19)

2.4.1 Electrochemical Processes

An electrochemical process is a chemical reaction that either causes or is caused by the movement of electrical current. These processes are a type of oxidation-reduction reactions in which one atom/molecule transfers electrons to another atom/molecule; this happens over large distances relative to other chemical reactions causing the production of a current. Detecting the produced current will allow an investigation of the adsorption processes occurring. Many biological systems have a basis on electrochemical processes; for instance, the human nervous system(20). The two main processes occurring at the electrode surface are known as Faradaic and Non-faradaic(21, 22). Non-faradaic processes arise because of the presence of the electrochemical double layer, which occurs through the adsorption and desorption of species to and from the electrode surface. No electrons are transferred at the electrode/electrolyte surface and therefore no chemical reactions are taking place. The double layer acts as a capacitor and can become charged due to the adsorption and desorption processes; this will result in the generation of a current. The resulting current of the double can be expressed through an equation (eq 2.6)(23).

$$I_{DL} = A C_{DL} v \dots (2.6)$$

Where I_{DL} is the double layer current (measured in Ampere), A is the surface area of the electrode (measured in cm^2), C_{DL} is the capacitance of the double layer (measured in Farad) and v is the scan rate (measured in V s^{-1}).

Provided that the electron transfer is fast and the peak potential is independent of concentration and sweep rate of the reaction is reversible. The relation between cell potential and the concentration of reduced and oxidised species is given by the Nernst equation (eq 2.7)(24).

$$E = E^0 - \left(\frac{RT}{nF}\right) \ln \left(\frac{[red]}{[ox]}\right) \dots (2.7)$$

Where E is the applied potential, E^0 is the standard potential (at 25°C), R is the universal gas constant, T is the absolute temperature, n is the number of electrons transferred in the reaction, F is the Faraday constant and $[red]$ and $[ox]$ are the concentrations of the reductant and oxidant respectively.

At 25°C the peak current i_p should be identical for forward and reverse reactions and can be calculated by the Randles-Sevcik equation (eq 2.8)(25).

$$i_p = (2.69 \times 10^5) n^{3/2} \cdot A \cdot D_0^{1/2} \cdot v^{1/2} \cdot C_0 \dots (2.8)$$

Where D_0 is the diffusion coefficient in $\text{cm}^2 \text{s}^{-1}$, v is the scan rate and C_0 is the concentration of the electroactive species in the bulk electrolyte solution. It can be seen from the equation that the peak current is proportional to the square root of scan rate; which means if scan rate was increased peak height should increase.

For a reversible reaction in solution, the position of the voltammetric peaks is independent of potential and the separation of the peaks can be expressed with equation 2.9(26).

$$|E_p^{ox} - E_p^{red}| = 2.2 \frac{RT}{nF} = \frac{59}{n} \text{ mV} \dots (2.9)$$

Where E_p^{ox} and E_p^{red} are the peak potentials of the oxidation and reduction processes.

Provided the time for electron transfer to occur allows equilibrium to be reached; at which a small change in applied voltage direction will allow the CV to reverse.

2.4.2 Electrochemical Double Layer

The electrochemical double-layer is an arrangement of charged particles or dipoles occurring at the interface between the electrode and electrolyte. The formation of the layer of charged species reflects the different ionic zones of the electrolyte solution. There are three prevalent models of the electrochemical double layer, the earliest of the three being the Helmholtz model(27). Subsequent models that expanded upon the Helmholtz model were the Gouy-Chapman(28, 29) and Stern-Grahame models(30).

The Helmholtz double-layer model the double-layer is treated as a simple capacitor; in which the model assumes no electron transfer occurs at the electrode and the solution is only comprised of electrolyte. The interactions between ions and the electrode are deemed to be exclusively electrostatic due to the charge density on the electrode as a result or either a deficiency or excess of electrons. In order to conserve the neutrality of the interface ions are attracted and distributed over the electrode surface forming a layer. The distance of approach is limited to the radius of the ion and a single sphere of solvation around each

ion. This results in two layers and the potential drop is confined to an area known as the outer Helmholtz plane (OHP).

The Helmholtz model was adapted by Gouy-Chapman; which changed some of the assumptions. The first assumption to be altered was the belief that ions interacted exclusively through electrostatic interactions; the Gouy-Chapman model considers a continuous distribution of anions and cations in solution, with excess charge distributed over the solution with respect to electrostatic interactions in competition with Brownian motion. This differs to charge be considered exclusively located at the Helmholtz plane. Equilibrium of charged ions with the electrode surface was proposed in which oppositely charged ions to the surface were more concentrated at the interface and decrease with distance from the interface; this region was termed the diffuse layer. The potential exponentially decays from the electrode surface with increased distance; the diffuse layer is temperature and concentration dependent so the fixed distance for the drop in potential is not transferred from the Helmholtz model.

The two models conflict on the compactness of ions and the rigidity of the double layer; Helmholtz model leads to an overestimation and the Gouy-Chapman model leads to an underestimation. This error in estimation is due to the capacitance of two charge arrays having an inverse proportionality with separation distance. In order to reflect this relationship, the Stern-Grahame model combines both the Gouy-Chapman and Helmholtz models leading to two distinct regions of distribution. The first region being the compact or Stern layer in which ions are strongly adsorbed to the electrode surface; consisting of specifically adsorbed ions and non-specifically adsorbed counter ions. The two different adsorbed ions are separated by the inner Helmholtz plane (IHP) and outer Helmholtz plane (OHP). The second layer is the diffuse layer proposed by the Gouy-Chapman model (figure 2.11).

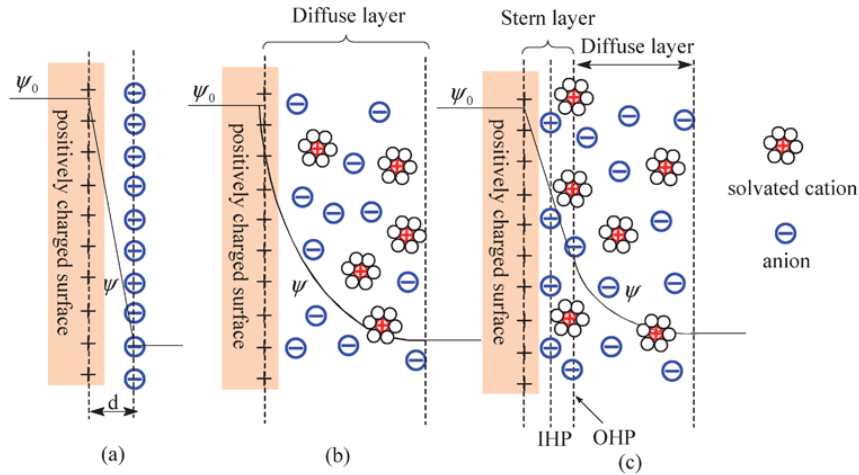


Figure 2.11: Schematic representations of: (a) Helmholtz model, (b) Gouy-Chapman model and (c) Stern-Grahame model. Reprinted from (31)

The capacitance of the electrochemical double-layer can be treated as a combination of the stern and diffuse layer (eq 2.10).

$$\frac{1}{C_{dl}} = \frac{1}{C_H} + \frac{1}{C_{diff}} \dots \dots (2.10)$$

Where C_{dl} is the capacitance of the double layer, C_H is the capacitance of the stern layer and C_{diff} is the capacitance of the diffusive layer.

2.4.3 CV of Polycrystalline Platinum

It is important in all electrochemical studies that a “reproducible electrode surface” is used. What is meant by this is that the electrode must be prepared in such a way that the same surface is obtained every time. Before single crystal experiments were conducted, the polycrystalline platinum surface was characterised first. By continual voltammetric scanning between 0 V (before onset of hydrogen evolution) and 1.6 V (before the onset of oxygen evolution)(32), a reproducible CV of polycrystalline platinum was obtained (figure 2.12).

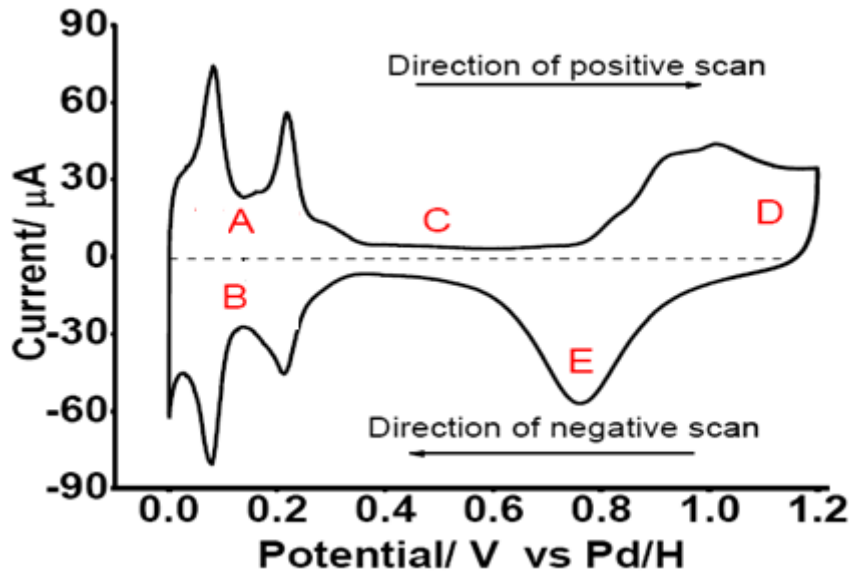
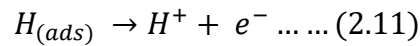


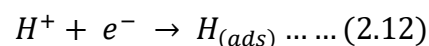
Figure 2.12: CV of polycrystalline Pt in 0.1 M H₂SO₄ reprinted from (199)

Regions A and B correspond to the hydrogen underpotential deposition region H_{UPD}, in which hydrogen is adsorbing and desorbing from the Pt electrode surface. Region A is the region of desorption of hydrogen (eq 2.11)(33)



Showing that desorption causes a transfer of electrons to the bulk electrolyte from the adsorbed hydrogen generating an anodic current.

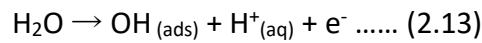
Region B is the adsorption of hydrogen to the electrode surface; there are numerous peaks showing the presence of different surface sites. The reaction follows the reverse of the above reaction (eq 2.12).



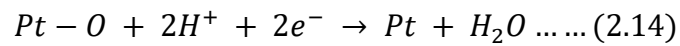
The region marked as C is the double layer region; the only current flowing in this region is due to the capacitance of the electrode with charging occurring in the IHP/OHP. No REDOX

reactions occur in this region; only processes involving the migration of charged species under potentials. The width of the double layer can give important information on the capacitance of the electrode which will depend of material type and surface area.

The region marked D is the oxygen underpotential deposition region where oxygen is adsorbed to the electrode surface at high potentials (eq 2.13).



Region E is known as the oxide stripping region; in which oxides are removed from the surface which happens by this reaction (eq 2.14).



An important feature of this process is that removal of the oxide from the platinum electrode causes the surface to rearrange causing the formation of clusters and roughening of the surface topography(32). For this reason, the potential upper limit will be set 0.85 V in order not to enter the oxide region.

An extensive amount of research has been conducted for electrochemical systems on a variety of substrates in institutions across the world. In order to compare and validate experimental data and theories, results need to be normalised with respect to the real surface area of the electrode. An electrode's geometric surface area does not accurately represent the true surface area of the electrode as it does not account for surface steps, holes, kinks and terraces, which would contribute to increasing the surface area from the geometric one. To measure the real surface area gaseous molecules or atoms can be utilised as a microscopic probe. Through physisorption the gas particles form a monolayer on the electrode surface and by measuring the amount of gas adsorbed and the area occupied by the gas, the real surface area can be calculated using equation 2.15

$$S_r = \frac{n_a N_A}{d_m} \dots\dots (2.15)$$

Where S_r is the real surface area, n_a is the moles of adsorbed gas, N_A is Avogadro's number and d_m is the surface metal atom density. Cyclic voltammetry can be utilised to evaluate the real surface area of the electrode, by applying high cathodic potential causing hydrogen deposition and evolution at the electrode surface (34). The moles of adsorbed gas can be equated to the charge associated with the formation of a monolayer, allowing equation 2.15 to be re-written as equation 2.16.

$$S_r = \frac{Q_m}{ed_m} \dots \dots (2.16)$$

Where Q_m is the charge associated with the formation of a monolayer and e is the charge of an electron. In order to obtain Q_m the current response of the CV would need to be integrated as current can be expressed as change in charge over time. The calculation would also need to consider and subtract the capacitive current demonstrated in the double layer region. The value of d_m can be obtained from unit cell measurements for specific single crystal surfaces and for polycrystalline surfaces the assumption is made that the surface predominately consists of the {100}, {111} and {110} basal planes in equal proportions of 33%. So, for Pt polycrystalline surfaces d_m is $1.3 \times 10^{15} \text{ cm}^{-2}$ and when multiplied by the charge of an electron gives $208 \mu\text{C}/\text{cm}^2$ (35). This highlights the importance of the electrode microtopography in processes that involve the electrode surface.

2.4.4 CV of Platinum Single Crystal Electrodes and Shaped Nanoparticles

CV analysis of the low index planes of platinum single crystals, demonstrated that each of the surfaces gave unique and reproducible responses in the H_{UPD} region of the CV (figure 2.13). The single crystal surfaces have an advantage over the polycrystalline surface as they can utilise the flame annealing process developed by Clavilier *et al* to remove surface impurities before cyclic voltammetry(36).

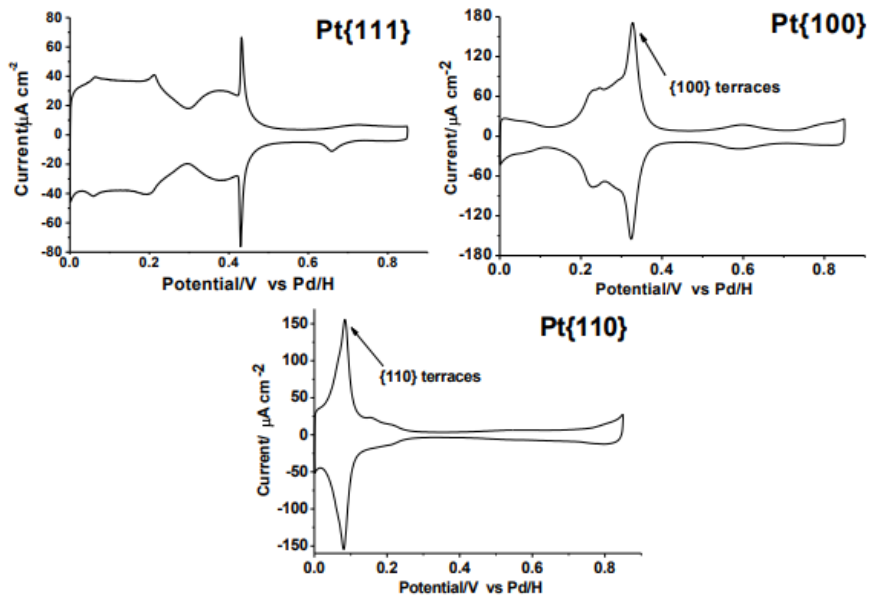


Figure 2.13: CV of Pt basal plane electrodes in 0.1 M H_2SO_4 . Reprinted from (37)

With extensive research of Pt single crystal surfaces of increasing complexity, more understanding was gained of the current response of specific surface sites in the H_{UPD} (38). By applying this knowledge shape-controlled nanoparticles could be characterised in much the same way the lower index single crystals have. Obviously, the shaped nanoparticles will have contributions to the CV from all three of the planes in figure 2.13 to differing extents.

The H_{UPD} region of the shaped nanoparticles CV can yield a lot of information (figure 2.14). With symmetry, good definition and sharpness of the peak are good indications of a clean surface. The region can be broken down into four sections for different surface site contributions(39):

- The peak at 0.125 V can be attributed to {110} type sites.
- The peak at ≈ 0.27 V contains two contributions; the first from {100} steps on {111} terraces and sites close to the steps on {100} terraces.
- The signal between 0.35-0.37 V is attributed to {100} terraces.
- Signals at 0.5 V are attributed to {111} sites.

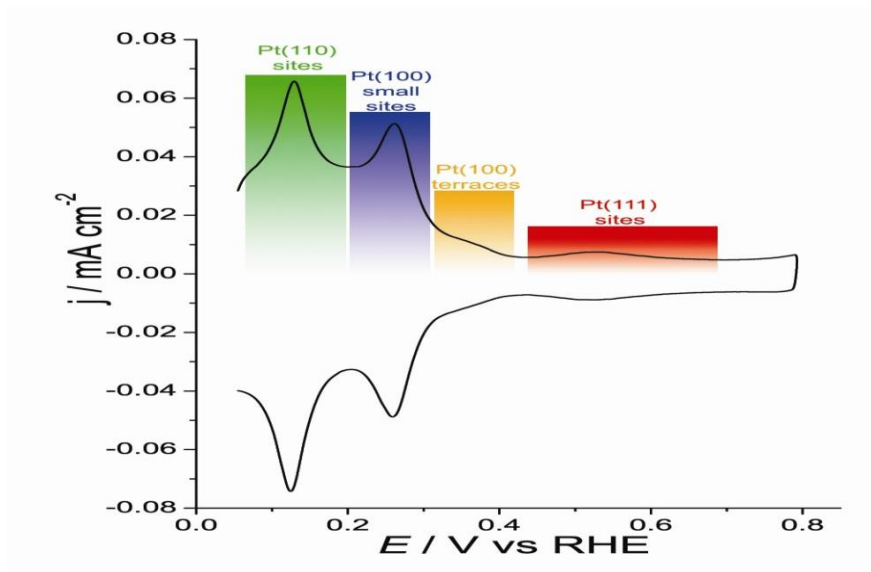


Figure 2.14: CV of shaped Pt nanoparticles in 0.5 M H_2SO_4 .

2.5 Raman Spectroscopy

2.5.1 Raman Spectroscopy - Light Scattering

Quantum Approach- The Raman Effect can be considered as the inelastic scattering of electromagnetic radiation. During this interaction energy is transferred between the photons and the molecular vibrations. Therefore, the scattered photons have a different energy to the incoming photons. The difference in energy between the incident and inelastically scattered photons is called Raman shift and is plotted against intensity in the Raman spectrum. As previously mentioned, the photon can gain or lose energy in the interaction with the molecule. This is dependent on the initial vibrational state of the molecule, with the transition from a higher to a lower vibrational state causing the incident photon to gain energy and produce anti-stokes scattering and vice versa for the stokes scattering, illustrated in figure 2.15. However, if we consider the Boltzmann distribution at room temperature the population of the ground vibrational state will be significantly higher than the elevated states. This causes the anti-stokes scattering to be reduced in intensity, therefore Raman spectroscopy refers exclusively to stokes scattering unless specified otherwise.

Classical Approach- When a molecule is positioned in an electric field \mathbf{E} , an electrical dipole moment \mathbf{P} is induced. The induced dipole moment can be considered as directly proportional to the electrical field:

$$\mathbf{P} = \alpha \mathbf{E} \quad \dots (2.17)$$

The electrical field is caused by electromagnetic radiation (light can be considered as an oscillating electric field). The electric field vector \mathbf{E} on the moment τ is described as:

$$\mathbf{E} = \mathbf{E}_0 \sin (2\pi \nu_0 \tau) \quad \dots (2.18)$$

ν_0 is the vibrational frequency of the electromagnetic radiation. In equation (2.17) the polarizability (α) is a *tensor* (similar to a vector depends on coordinates), which is dependent on the shape and dimensions of the chemical bond. As the chemical bonds change during vibrations, the polarizability is dependent on the vibrations of the molecule. Therefore, it can be stated that the polarizability tensor (α) is dependent on the coordinate of the molecule. A polarizable molecule subjected to an electric field (defined in equation 2.18) will have an oscillating induced dipole, which can be expressed by equation 2.19.

$$\mathbf{P} = \alpha [\mathbf{E}_0 \sin (2\pi \nu_0 \tau)] \quad \dots (2.19)$$

A vibrating molecule will also have an oscillating polarizability, which can be expressed by equation (2.20). Where β is the change in polarizability and ν_{vib} is the characteristic frequency of the molecule.

$$\alpha = \alpha_0 + \beta \sin (2\pi \nu_{vib} \tau) \quad \dots (2.20)$$

Equations 2.19 and 2.20 can be combined to define the induced dipole moment in terms that can encompass both Rayleigh and Raman scattering (2.21).

$$\mathbf{P} = [\alpha_0 \mathbf{E}_0 \sin(2\pi\nu\tau)] + \frac{1}{2} \beta \mathbf{E}_0 [\cos(2\pi(\nu - \nu_{vib})\tau) - \cos(2\pi(\nu + \nu_{vib})\tau)] \quad \dots (2.21)$$

The first term of the equation (7.5) can be attributed to Rayleigh scattering. The second term of the equation represents Raman scattering with anti-stokes ($\nu + \nu_{vib}$) and stokes ($\nu - \nu_{vib}$), which is shifted in frequency from the from the incident radiation. It is also worth noting the term β in the equation which represents a change in polarizability, this has to have a non-zero value for the vibrational mode to be Raman active.

The induced dipole moment can be split into 3 components, each with a different frequency dependence (figure 2.15). The first term corresponds to elastic scattering of the electromagnetic radiation: The induced dipole moment and the incoming electromagnetic radiation are equal in frequency (and energy). This scattering is referred to as Rayleigh scattering. The next two terms in the equation correspond to inelastic scattering and are both forms of Raman scattering. The second term corresponds to the scattered radiation gaining energy and is termed Anti-Stokes scattering. The third term relates to a loss in energy of the scattered radiation and is termed Stokes scattering.

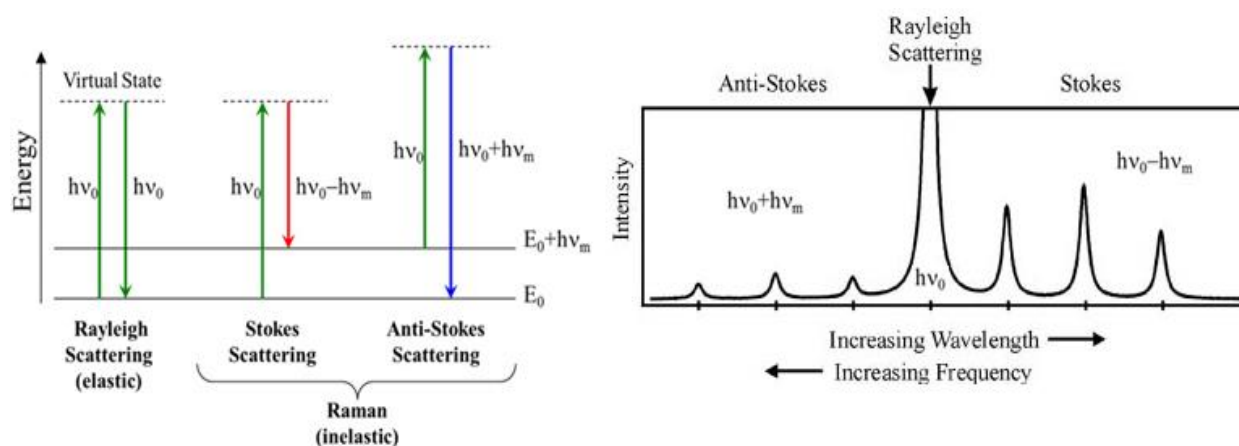


Figure 2.15: Schematic of the energy states in the scattering process

To be Raman active a molecule must have anisotropic polarizability, this is less restrictive than the requirement for a dipole moment, allowing symmetrical molecules to be Raman active. Additionally, the specific selection rule for vibrational Raman spectroscopy is that only $\Delta v = \pm 1$ transitions are allowed, with $\Delta v = +1$ corresponding to Stokes scattering. When trying to visualise the relationship of the electric field with the induced dipole of the molecule the component vector field must be considered. Therefore equation 2.18 can be expanded to account for the x, y and z directions of the electric field and induced dipole (2.20).

$$\begin{aligned}
 P_x &= \alpha_{xx} E_x + \alpha_{xy} E_y + \alpha_{xz} E_z \\
 P_y &= \alpha_{yx} E_x + \alpha_{yy} E_y + \alpha_{yz} E_z \\
 P_z &= \alpha_{zx} E_x + \alpha_{zy} E_y + \alpha_{zz} E_z
 \end{aligned}
 \tag{2.22}$$

In matrix form this is written as.

$$\begin{pmatrix} P_x \\ P_y \\ P_z \end{pmatrix} = \begin{pmatrix} \alpha_{xx} & \alpha_{xy} & \alpha_{xz} \\ \alpha_{yx} & \alpha_{yy} & \alpha_{yz} \\ \alpha_{zx} & \alpha_{zy} & \alpha_{zz} \end{pmatrix} \begin{pmatrix} E_x \\ E_y \\ E_z \end{pmatrix} \quad (2.23)$$

The 3x3 matrix on the right-hand side of equation 2.21 is known as the polarizability tensor and for a vibration to be Raman active one of components of the polarizability tensor needs to change during the vibration.

It is possible to visually demonstrate the polarizability of a molecule by using a three-dimensional polarizability ellipsoid; with the size, shape and orientation of the ellipsoid determined by plotting $1/\sqrt{\alpha_i}$ (in the i direction). For a mode to be Raman active the size, shape and orientation of the ellipsoid needs to be different at the extremes of the vibration (+q, -q). Figure 2.16 illustrates the polarizability ellipsoids for the three vibrational modes of CO₂. The symmetrical stretch (ν_1) demonstrates a size change in the ellipsoid at the extremes of the vibration, therefore, that is a Raman active stretch. Both the asymmetric stretch (ν_3) and bending mode (ν_2) have identical ellipsoids at the extremes of the vibration and are Raman inactive.

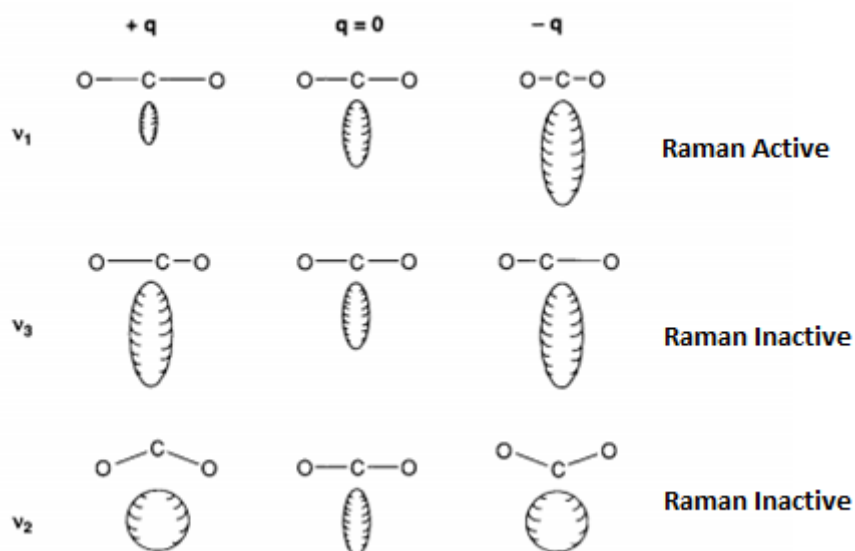


Figure 2.16: Polarizability ellipsoids tracking the change in polarizability during the three vibration modes of CO₂. Reprinted from (40).

It is worth noting for CO₂ that the Raman active ν_1 stretch (that is symmetrical to the centre of symmetry) is inactive in infrared spectroscopy, but the ν_2 and ν_3 vibrations (that is

asymmetrical to the centre of symmetry) are infrared active. This phenomenon is referred to as the mutual exclusion principle and is applicable to any molecules that contain a centre of symmetry.

Another example of the alterations of polarizability in the vibrational modes of the molecule is shown in figure 2.17, with H₂O being the specific molecule. Similarly, to the vibration modes of CO₂ the ν_1 mode of H₂O is Raman active and establishes differences in polarizability during the vibration. The ν_2 vibrational mode displays significant perturbations, with the α_{xx} , α_{yy} and α_{zz} components of the polarizability tensor changing at different rates. The ν_3 vibrational mode shows more subtle alterations with the orientation of the ellipsoid changing during the vibration due to the off-diagonal α_{yz} component.

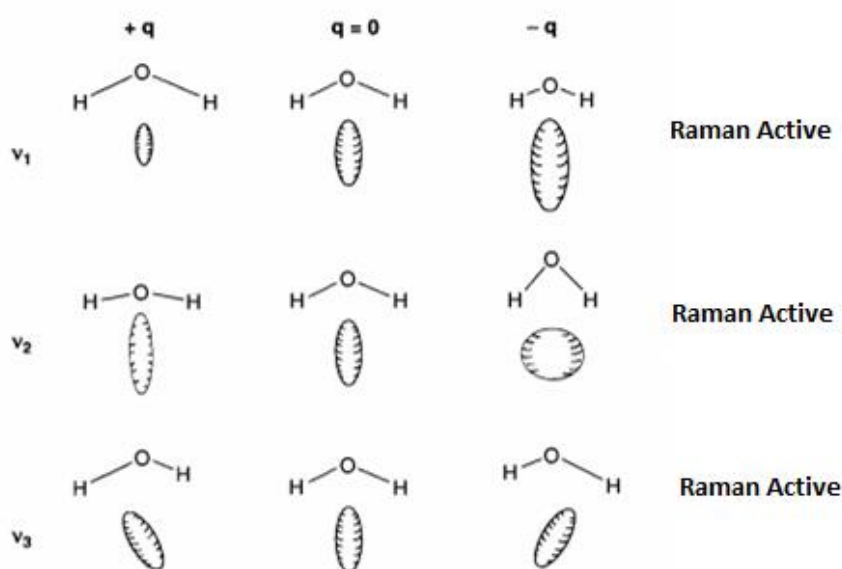


Figure 2.17: Polarizability ellipsoids tracking the change in polarizability during the three vibration modes of H₂O. Reprinted from (40).

The two above examples of CO₂ and H₂O are facile to track using the polarizability ellipsoids, as both are simple triatomic molecules. For the larger more complex molecules group theory provides an eloquent method of determining Raman and IR activities of the normal molecular vibrations. To identify the number of individual vibrational modes in a molecule the formula $3N - 6$ can be applied ($3N - 5$ if linear) where N is the number of atoms in the molecule. It has already been established that a Raman active vibration must cause a change in polarizability. The polarizability tensor has components α_{xx} , α_{xy} , α_{xz} , α_{yy} , α_{yz} , α_{zz} .

Therefore, in group theory the mode must co-appear with one of the terms out of xx, xy, xz, yy, yz, zz.

2.5.2 Surface Enhanced Raman Spectroscopy (SERS)

One of the stumbling blocks for Raman spectroscopy in becoming a widely used spectroscopic technique is the weak intensity of the inelastic scattering. This changed when the first SERS spectrum was recorded in 1974 by Martin Fleischmann *et al*(41). The fledgling technique of SERS was bolstered further in 1977 by Jeanmaire and Van Duyne(42). The origin of the signal enhancement over coinage metal surfaces in particular, is still debated, but two theories have been proposed.

The first theory proposed to explain the enhancement, is the electromagnetic enhancement theory. This theory suggests that the conduction band electrons in a metal are able to move laterally across the surface of the metal. When the surface is subject to an electromagnetic field, these electrons oscillate as a collective, forming what is referred to as a plasmon. The plasmon is confined to the surface and interacts strongly with light. Surface roughness of a metal is required, so that the plasmon can be excited by light and resonates with the incident field, which causes an enhancement of the electric field on the metal surface. The interaction between the electrons in a molecule and the plasmon electrons will then increase the Raman cross-section of the adsorbate(43). For the electric field on a roughened surface, the surface structure is approximated to be a sphere. The small wavelength of the incident light, the plasmon will polarise around the assumed sphere, as described by the Rayleigh approximation(44). The electric field can be described by the following equation(44):

$$E_r = E_0 \cos \theta + g \left(\frac{a^3}{r^3} \right) E_0 \cos \theta \dots \dots (2.24)$$

Where r is the distance from the spheroid surface of radius a, E_0 is the incident field, θ is the angle relative to the direction of the incident field and g is a constant related to the

dielectric constants of the metal and surrounding medium. The dielectric constant can be further described as:

$$g = \frac{[\epsilon_1(\omega_L) - \epsilon_0]}{[\epsilon_1(\omega_L) + 2\epsilon_0]} \dots \dots (2.25)$$

Where ϵ_0 is the dielectric constant of the surrounding medium, ϵ_1 is the dielectric constant of the metal and ω_L is the incident frequency of light. When the dielectric frequency of the metal is equal to $-2\epsilon_0$, an infinite value of g can be obtained. This will significantly increase the local field around the surface adsorbed molecule. With the dependency of the dielectric constant of the metal on the incident frequency of the light, altering the frequency of the light can achieve maximum values of g . This can relate to the superior enhancement on coinage metals as they facilitate a high value for g , within the standard frequency range for Raman spectroscopy(45).

The second theory for the SERS enhancement is the charge transfer theory, which involves interactions between the substrate and adsorbate. When molecules are adsorbed on the metal surface, a chemical bond forms between the adsorbate and the metal substrate enabling charge to resonate between discrete energy states of the molecule and occupied or unoccupied states in the metal depending on the direction of transfer. By participating in this transfer the polarizability of the molecule is altered, increasing Raman emission (46). The charge transfer process can be stimulated by the incident light if it is in resonance with the energy gap of the transition. The charge transfer can either be from the metal to the molecule or vice versa, with each having marginally different processes (figure 2.18).

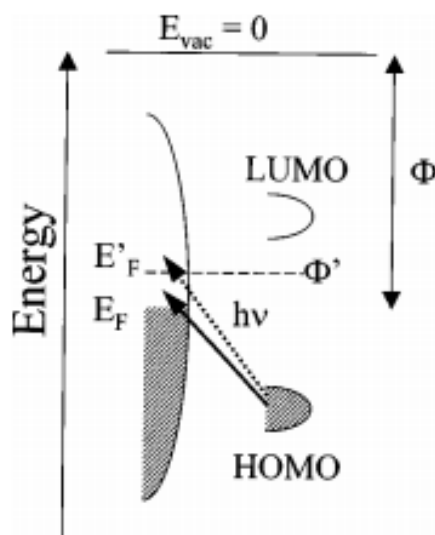


Figure 2.18: Schematic energy level diagram of the charge-transfer process with the metal on the left, the molecular orbitals on the right, E_F representing the Fermi energy level and Φ representing the work function. Reprinted from (47).

The metal to molecule transfer process begins with the absorption of an incident photon and excitation of a conduction band electron of the metal, to an unoccupied state above the Fermi level leaving a hole in the Fermi level. The electron crosses over to an excited state in the molecule, then returns to the hole in metal conduction band and radiates a Raman shifted photon. This causes the molecule to return to the electronic ground state but is left in an excited vibrational state.

The molecule to metal transfer shares a similar process to the previously outlined metal to molecule transfer, with the key differences being that the molecule is electronically excited after adsorption of an incident photon. The electron returns after a transition to the highest unoccupied level of the metal conduction band and the emission of a Raman shifted photon after relaxation of the molecule to the ground state.

2.5.3 Surface selection rules

The role of the surface in SERS must be considered not only for the enhancement of the Raman scattering, but also how it perturbs the molecule after adsorption. The symmetry of

the adsorbed molecule may be lowered by the adjacent surface metal atoms, particularly for chemisorbed species (48). The alterations of the adsorbed molecule to the surface can influence the symmetry of a molecular vibration and whether it is Raman active, causing the appearance of new peaks or the degradation of existing peaks. Comparing bulk Raman spectra to SERS spectra for a given molecule can reveal information on the adsorption geometry of the molecule on that particular surface. In attempts to understand the interaction between the adsorbate and metal surface, surface selection rules have been developed. Moskovits detailed a theoretical approach to surface selection rules, in which, is presented in terms of image charges (49). The interaction of the molecule with the metal surface is represented by an image charge of the molecular dipole in the sub-surface of the metal. The orientation of the adsorbed molecule is important in this theory as if the dipole moment of the adsorbate is parallel to the dipole moment of the image, it will have no net transition dipoles and will dampen the enhancement. However, if the adsorbed molecular dipole moment is perpendicular to the charged image it is reinforced in the composite system leading to an intense Raman shifted signal. The extent of the screening effect of the image charge is dependent on the frequency range of the incident radiation and the type of metal surface, which is more prevalent for infrared spectroscopies in comparison to SERS (49).

2.5.4 Fluorescence

Fluorescence emission is a competing process with Raman spectroscopy and can cause major interference in the measurement of Raman spectra. The intensity of fluorescence is much greater than Raman scattering, therefore even a trace amount of contaminant in the sample that can undergo fluorescence will dominate the spectrum. The process of Raman spectroscopy and fluorescence are very similar with some subtle differences. The key differences between the two phenomena are that upon absorption of the incident photon Raman scattering is excited to a virtual state, but in fluorescence it is a “true” excited state. Fluorescence also participates in non-radiative relaxation in the excited state before returning to the ground state through fluorescence emission, this mechanism is detailed in figure 2.19.

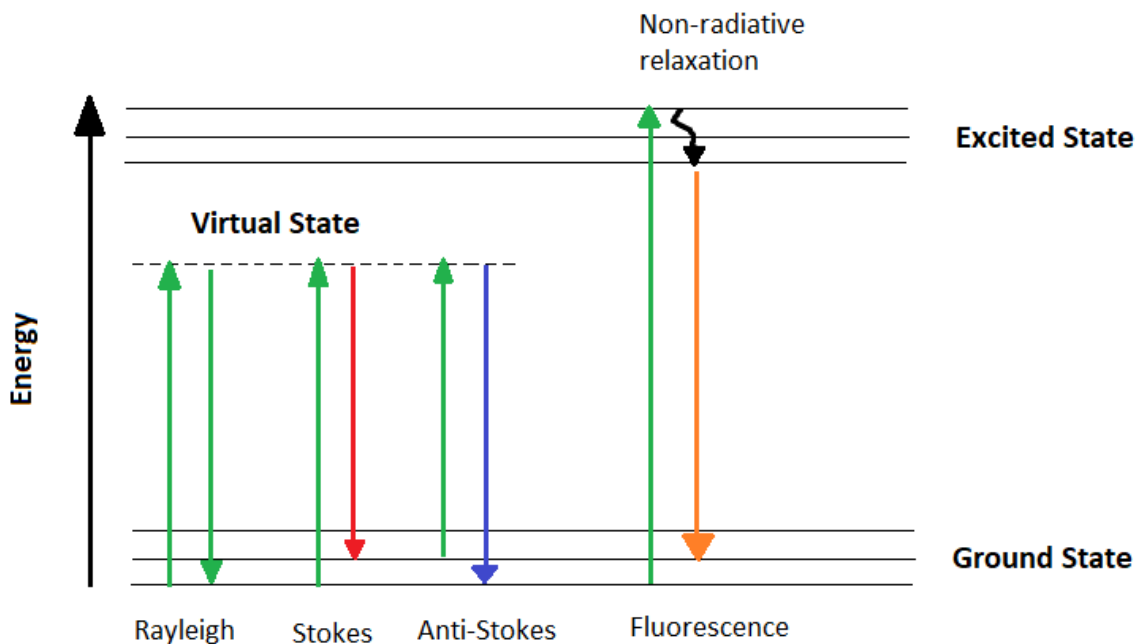


Figure 2.19: Absorption and emission processes for Raman scattering and Fluorescence mechanisms.

As fluorescence is undesirable in Raman and infrared spectroscopy, a great amount of effort has been devoted to developing methods for removing fluorescence. Coherent anti-stokes Raman spectroscopy is a prominent example which requires the use of multiple lasers to pump the target molecule into the excited state, instead of relying on spontaneous Raman emission (50). While this technique is successful and established it is complex and expensive requiring up to three laser beams. Another pertinent method approaches the issue by attempting to resolve the lower intensity Raman scattering from fluorescence dominated spectra, this would be a more compatible approach with regards to existing and established Raman technology (51).

2.6 References

1. G. Attard, C. Barnes, Surfaces. *Oxford Chemistry Primers* **59**, ALL-ALL (1998).
2. J. Rossmeisl, G. S. Karlberg, T. Jaramillo, J. K. Nørskov, Steady state oxygen reduction and cyclic voltammetry. *Faraday discussions* **140**, 337-346 (2009).
3. J. Libuda, S. Schaueremann, M. Laurin, T. Schalow, H.-J. Freund, Model studies in heterogeneous catalysis. From structure to kinetics. *Monatshefte für Chemie/Chemical Monthly* **136**, 59-75 (2005).
4. J. Clavilier, R. Faure, G. Guinet, R. Durand, Preparation of monocrystalline Pt microelectrodes and electrochemical study of the plane surfaces cut in the direction of the {111} and {110} planes. *Journal of Electroanalytical Chemistry and Interfacial Electrochemistry* **107**, 205-209 (1980).
5. N. Arulmozhi, D. Esau, J. van Drunen, G. Jerkiewicz, Design and Development of Instrumentations for the Preparation of Platinum Single Crystals for Electrochemistry and Electrocatalysis Research Part 3: Final Treatment, Electrochemical Measurements, and Recommended Laboratory Practices. *Electrocatalysis* **9**, 113-123 (2018).
6. R. J. Taylor, *Study on the surface adsorbates of an enantioselective, heterogeneously catalysed, hydrogenation reaction*. (Cardiff University (United Kingdom), 2010).
7. M. Van Hove, G. Somorjai, A new microfacet notation for high-Miller-index surfaces of cubic materials with terrace, step and kink structures. *Surface Science* **92**, 489-518 (1980).
8. M. T. Koper, Structure sensitivity and nanoscale effects in electrocatalysis. *Nanoscale* **3**, 2054-2073 (2011).
9. N. Tian, Z.-Y. Zhou, S.-G. Sun, Platinum metal catalysts of high-index surfaces: from single-crystal planes to electrochemically shape-controlled nanoparticles. *The Journal of Physical Chemistry C* **112**, 19801-19817 (2008).
10. G. Wulff, Some Theorems Concerning the Growth and Dissolution Rates of Crystals. *Ger.), Z. Kristallogr* **34**, 449-530 (1901).
11. Y. Xia, Y. Xiong, B. Lim, S. E. Skrabalak, Shape-controlled synthesis of metal nanocrystals: Simple chemistry meets complex physics? *Angewandte Chemie International Edition* **48**, 60-103 (2009).
12. Z. Wang. (ACS Publications, 2000).
13. Z. Niu, Y. Li, Removal and utilization of capping agents in nanocatalysis. *Chemistry of Materials* **26**, 72-83 (2013).
14. D. P. Stankus, S. E. Lohse, J. E. Hutchison, J. A. Nason, Interactions between natural organic matter and gold nanoparticles stabilized with different organic capping agents. *Environmental science & technology* **45**, 3238-3244 (2010).
15. J. M. Petroski, Z. L. Wang, T. C. Green, M. A. El-Sayed, Kinetically controlled growth and shape formation mechanism of platinum nanoparticles. *The Journal of Physical Chemistry B* **102**, 3316-3320 (1998).
16. G. Attard *et al.*, Semi-hydrogenation of alkynes at single crystal, nanoparticle and biogenic nanoparticle surfaces: the role of defects in Lindlar-type catalysts and the origin of their selectivity. *Faraday Discussions*, (2013).
17. R. Baxter, P. Hu, Insight into why the Langmuir–Hinshelwood mechanism is generally preferred. *The Journal of chemical physics* **116**, 4379-4381 (2002).
18. G. A. Mabbott, An introduction to cyclic voltammetry. *J. Chem. Educ* **60**, 697 (1983).
19. M. Ahmed, Cardiff University, (2012).
20. F. C. d. Abreu, P. A. d. L. Ferraz, M. O. Goulart, Some applications of electrochemistry in biomedical chemistry. Emphasis on the correlation of electrochemical and bioactive properties. *Journal of the Brazilian Chemical Society* **13**, 19-35 (2002).
21. C. G. Vayenas, S. Bebelis, I. Yentekakis, H.-G. Lintz, Non-faradaic electrochemical modification of catalytic activity: a status report. *Catalysis Today* **11**, 303-438 (1992).

22. N. Winograd, T. Kuwana, Characteristics of the electrode-solution interface under faradaic and non-faradaic conditions as observed by internal reflection spectroscopy. *Journal of Electroanalytical Chemistry and Interfacial Electrochemistry* **23**, 333-342 (1969).
23. D. Pletcher, *A first course in electrode processes*. (Royal Society of Chemistry, 2009).
24. R. Compton, C. Banks. (World Scientific, New Jersey, 2007).
25. K. B. Oldham, Analytical expressions for the reversible Randles-Sevcik function. *Journal of Electroanalytical Chemistry and Interfacial Electrochemistry* **105**, 373-375 (1979).
26. A. J. Bard, L. R. Faulkner, J. Leddy, C. G. Zoski, *Electrochemical methods: fundamentals and applications*. (wiley New York, 1980), vol. 2.
27. H. v. Helmholtz, Ueber einige Gesetze der Vertheilung elektrischer Ströme in körperlichen Leitern mit Anwendung auf die thierisch-elektrischen Versuche. *Annalen der Physik* **165**, 211-233 (1853).
28. M. Gouy, Sur la constitution de la charge électrique à la surface d'un électrolyte. *J. Phys. Theor. Appl.* **9**, 457-468 (1910).
29. D. L. Chapman, Ll. A contribution to the theory of electrocapillarity. *The London, Edinburgh, and Dublin philosophical magazine and journal of science* **25**, 475-481 (1913).
30. D. C. Grahame, The electrical double layer and the theory of electrocapillarity. *Chemical reviews* **41**, 441-501 (1947).
31. L. L. Zhang, X. Zhao, Carbon-based materials as supercapacitor electrodes. *Chemical Society Reviews* **38**, 2520-2531 (2009).
32. T. Biegler, D. Rand, R. Woods, Limiting oxygen coverage on platinized platinum; relevance to determination of real platinum area by hydrogen adsorption. *Journal of Electroanalytical Chemistry and Interfacial Electrochemistry* **29**, 269-277 (1971).
33. M. Neurock, M. Janik, A. Wieckowski, A first principles comparison of the mechanism and site requirements for the electrocatalytic oxidation of methanol and formic acid over Pt. *Faraday discussions* **140**, 363-378 (2009).
34. J. M. Doña Rodríguez, J. A. Herrera Melián, J. Pérez Peña, Determination of the real surface area of Pt electrodes by hydrogen adsorption using cyclic voltammetry. *Journal of Chemical Education* **77**, 1195 (2000).
35. S. Trasatti, O. Petrii, Real surface area measurements in electrochemistry. *Pure and applied chemistry* **63**, 711-734 (1991).
36. J. Clavilier, Flame-annealing and cleaning technique. *Interfacial Electrochemistry* **2**, (1999).
37. S. Guan, Cardiff University, (2014).
38. J. Clavilier, D. Armand, S. Sun, M. Petit, Electrochemical adsorption behaviour of platinum stepped surfaces in sulphuric acid solutions. *Journal of electroanalytical chemistry and interfacial electrochemistry* **205**, 267-277 (1986).
39. F. J. Vidal-Iglesias, R. M. Arán-Ais, J. Solla-Gullón, E. Herrero, J. M. Feliu, Electrochemical Characterization of Shape-Controlled Pt Nanoparticles in Different Supporting Electrolytes. *ACS Catalysis* **2**, 901-910 (2012).
40. J. R. Ferraro, *Introductory raman spectroscopy*. (Elsevier, 2003).
41. M. Fleischmann, P. J. Hendra, A. J. McQuillan, Raman spectra of pyridine adsorbed at a silver electrode. *Chemical Physics Letters* **26**, 163-166 (1974).
42. R. Van Duyne, RAMAN APPLICATIONS OF RAMAN SPECTROSCOPY IN ELECTROCHEMISTRY. *Le Journal de Physique Colloques* **38**, C5-239-C235-252 (1977).
43. E. Smith, G. Dent, *Modern Raman spectroscopy: a practical approach*. (John Wiley & Sons, 2013).
44. R. J. Gale, *Spectroelectrochemistry: theory and practice*. (Springer Science & Business Media, 2012).
45. A. Campion, P. Kambhampati, Surface-enhanced Raman scattering. *Chem. Soc. Rev.* **27**, 241-250 (1998).

46. A. Otto, The 'chemical'(electronic) contribution to surface-enhanced Raman scattering. *Journal of Raman Spectroscopy* **36**, 497-509 (2005).
47. P. Kambhampati, M. C. Foster, A. Campion, Two-dimensional localization of adsorbate/substrate charge-transfer excited states of molecules adsorbed on metal surfaces. *The Journal of chemical physics* **110**, 551-558 (1999).
48. J. C. Hulteen, M. A. Young, R. P. Van Duyne, Surface-enhanced hyper-Raman scattering (SEHRS) on Ag film over nanosphere (FON) electrodes: surface symmetry of centrosymmetric adsorbates. *Langmuir* **22**, 10354-10364 (2006).
49. M. Moskovits, Surface selection rules. *The Journal of Chemical Physics* **77**, 4408-4416 (1982).
50. W. M. Tolles, J. Nibler, J. McDonald, A. Harvey, A review of the theory and application of coherent anti-Stokes Raman spectroscopy (CARS). *Applied Spectroscopy* **31**, 253-271 (1977).
51. T. Hasegawa, J. Nishijo, J. Umemura, Separation of Raman spectra from fluorescence emission background by principal component analysis. *Chemical Physics Letters* **317**, 642-646 (2000).

Chapter 3 – Experimental

3.1 introduction

Platinum single crystals used in this investigation were prepared in-house, using the technique developed and outlined by Clavilier and Durand(1).

All glassware used in the investigation such as the electrochemical cell are decontaminated before use, using a thorough cleaning process. The first step of the cleaning method is to fill/immerse glassware in permanganic acid overnight (1M sulphuric acid and a few grains (1-3) potassium permanganate), the strong oxidising agent should remove any organic properties. The acid is decanted from the vessel and the glassware is rinsed thoroughly with ultra-pure water ($>18.2\text{M}\Omega\cdot\text{cm}$ resistivity from the Milli-Q water purification system). The glassware is then either boiled or steam cleaned with ultra-pure water for several hours, then the glassware is rinsed one final time with ultra-pure before use. The same procedure is used to clean the spectroelectrochemical flow cell. An extra step prior to this cleaning procedure is required for glassware used in nanoparticle synthesis. Aqua regia treatment is required to remove any residual nanoparticle seeds, as they may influence nanoparticle growth. Due to the sensitive nature of this investigation, it is important impurities are limited and high purity solvents and reagents are required.

3.2 Cyclic Voltammetry

All CV measurements were carried out in a standard two compartment electrochemical cell (figure 3.1). A three-electrode set-up was used in the cell, consisting of a palladium hydride reference electrode, platinum mesh counter electrode and depending on the investigation either a hemispherical polycrystalline gold electrode or a platinum single crystal electrode as the working electrode. Platinum single crystal electrodes were flame annealed and cooled in hydrogen, a hanging meniscus was used to contact the electrolyte in the electrochemical cell(149). Characterisation of shaped platinum nanoparticles on the gold electrode, involves polishing the electrode with grit paper and diamond spray and the electrode surface was rinsed with ultra-pure water. The colloidal nanoparticle solution (3 μl) was drop cast onto the gold electrode and dried under nitrogen. The electrolytes used in these investigations,

were 0.1 M perchloric acid, 0.1 M and 0.5 M sulphuric acid. Electrolytes were degassed by bubbling nitrogen gas through the solution for 30 minutes. All CV data was recorded with a potential sweep rate of 50 mV s^{-1} unless stated otherwise, using a CHI 750 potentiostat.

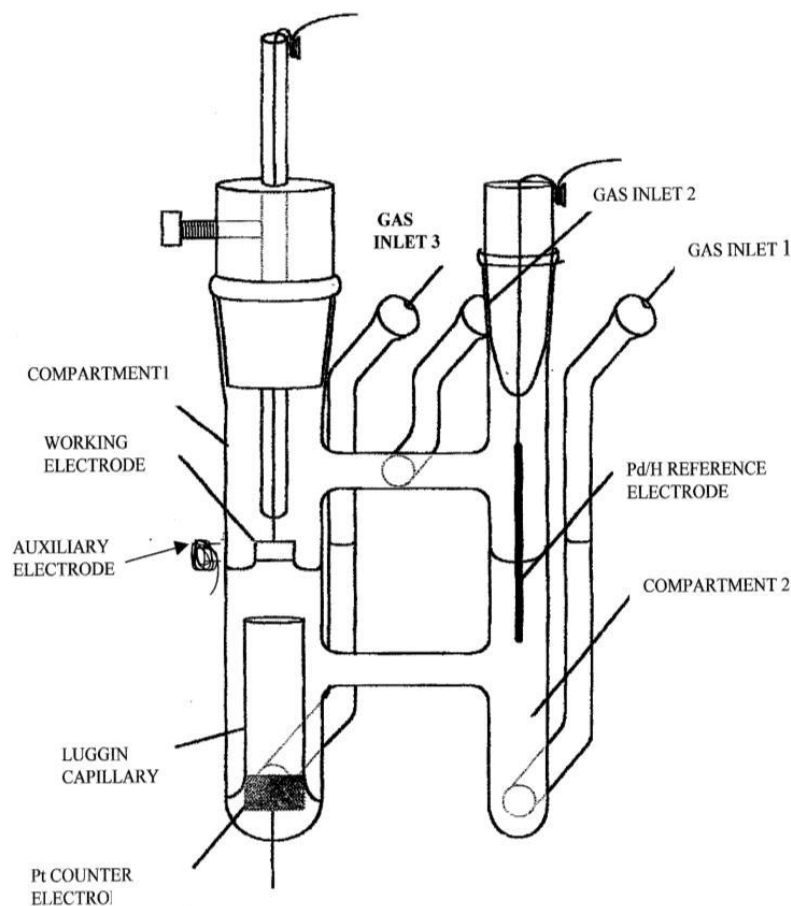


Figure 3.1: The two-compartment electrochemical cell

3.3 The Spectroelectrochemical Flowcell

The spectro-electrochemical flowcell was designed to carry out in situ SERS spectroscopic measurements with electrochemical control of the potential. The main body of the cell was made from PTFE and can shelter three electrodes in a $12 \times 30 \times 1 \text{ mm}$ channel. A $24 \times 50 \text{ mm}$ borosilicate glass spectral window (Sigma-Aldrich, cover glass) was sealed on to the channel using Viton[®] gaskets. In order to avoid contamination, Klingerflon[®] PTFE thread seal tape was used to wrap over the gaskets to prevent contact with electrolytes. Then the glass window was secured in place by hand with an aluminium top-plate and tube clamps. Finally,

PTFE inlet and 105 outlet tubes (1.58 mm O.D. × 0.8 mm I.D) were screwed in to the PTFE block with Supelco® HPLC fittings and then sealed with ferrules (figure 3.2)(3).

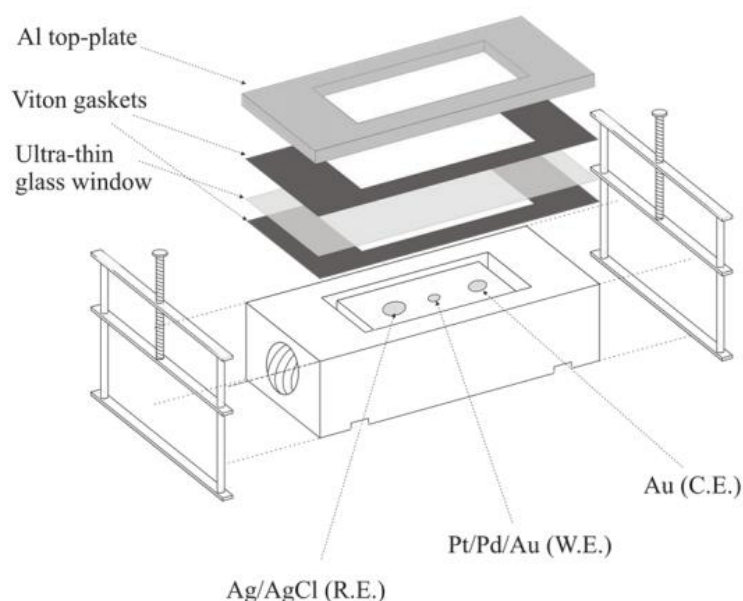


Figure 3.2: Schematic diagram of the flowcell. Reprinted from (3).

Before each experiment the main body of the flow cell is cleaned following the earlier established cleaning process. The viton gaskets are only submerged in permanganic acid for half a minute, rinsed several times with ultra-pure water and submerged in ultra-pure water until needed. The glass window is replaced after every experiment. The counter and reference electrode are flamed and washed with ultra-pure water to remove impurities. Once all the electrodes are in place and the glass window is clamped to the body of the flowcell, wax is used to seal the electrode inlets on the bottom of the flowcell. Solutions were degassed with argon gas and were drawn through the cell and into an appropriate waste container using a single channel peristaltic pump (Cole Parmer, Masterflex C/L) which can deliver a range of volume flow rates from 1.3 to 7.2 mL·min⁻¹.

3.4 Au@Pt Core-shell Nanoparticle Synthesis

The 55 nm gold cores were synthesised using the following method(4):

100ml of 0.01% (by mass) H_{AuCl₄} solution was measured by a measuring cylinder and decanted into a 250ml round bottom flask. The round bottom was placed in a Si oil bath and refluxed at 112^oC for 30 minutes under moderate stirring. Sodium citrate solution (39mM) was prepared by weighing out 0.57g of sodium citrate in a 50ml beaker and was dissolved in ultra-pure water and decanted into a flask, complete transfer of the reductant was ensured by successive rinsing and decanting. 600 μ L of the Sodium citrate solution was pipetted into the round bottom flask containing the H_{AuCl₄}. A colour change from yellow to black to red occurred. Reflux was continued for a further 30 minutes, and then the flask was removed from the Si oil bath and allowed to cool to room temperature.

Preparation of Au@Pt nanoparticles with a 2nm Pt shell(5):

30mL of the Au nanoparticles were measured using a measuring cylinder and decanted into a 100ml round bottomed flask. A 1mM H₂PtCl₆ solution was prepared in 50mL flask and then 1470 μ L was pipetted into the round bottom flask containing the Au nanoparticles. The flask was placed in a water bath and refluxed at 80^oC for 30 minutes. A (5 mM) solution of Ascorbic acid was prepared in a 50mL flask, 1480 μ L of the Ascorbic acid solution was added using a peristaltic pump at its slowest speed for 110 seconds. The solution was refluxed for a further 30 minutes; the solution should appear darker than the original solution of gold nanoparticles.

3.5 Au@SiO₂ Core-shell Nanoparticle Synthesis

The Au@SiO₂ nanoparticles were synthesised using the following method(6):

30mL of the Au nanoparticles previously synthesised were poured into a 100mL round bottom flask. A 1.0mM solution of (3-aminopropyl)-trimethoxysilane (APTMS) was made and 0.4 mL of the APTMS solution was added to the round bottom flask under vigorous stirring for 20 minutes. A Sodium silicate solution (0.54 wt %) was prepared and adjusted to pH 10.28 using 0.1M HCl. 3.2mL of the sodium silicate solution was added to the round bottom flask under vigorous stirring for 20 min. The reaction mixture was heated to 70 ^oC

for 13 min (timed from the start of heating) to yield ultrathin shells (2 nm). Nanoparticles were collected using a centrifuge at 5000rpm for 15 minutes and washed with ultra-pure water using the same settings.

In order to improve the reproducibility and uniformity of the Au@SiO₂ nanoparticles used in the application of Shell Isolated Nanoparticle Enhanced Raman Spectroscopy (SHINERS), testing was carried out on the nanoparticles to ensure thin, pinhole free silica coatings were applied to the gold cores in order to obtain optimal surface enhancement for the SHINERS spectra. Testing was implemented on a silica support; the SHINERS particles were drop coated onto the silica and dried under nitrogen. Then a 10 mM pyridine solution was added to the dried colloid and covered with a quartz cover slip so the pyridine would not dry out. After 3-5 minutes, spectra were taken of the nanoparticles. If the particles were pinhole free no stretches would be present on the spectrum, but if pinholes were present, stretches would occur due to the aromatic ring. For example in Figure 3.3, the schematic shows the difference in the spectra of pinhole and pinhole free SHINERS particles. The other spectra present shows how sensitive the coating procedure was in relation to heating time. This pinhole testing procedure is the most sensitive in a series of tests to assess the quality of the silica shell. This procedure is the last step in a multi-step process that continually narrows in sensitivity to allow the precise tuning of the silica shell thickness. When first trying to make Au@SiO₂ of a certain size TEM images should be taken to confirm size and shape of the nanoparticles, if everything is correct then electrochemical testing will allow tuning of the shell thickness with a good degree of sensitivity. Finally, the pyridine test should be performed to obtain the thinnest pinhole-free coating possible.

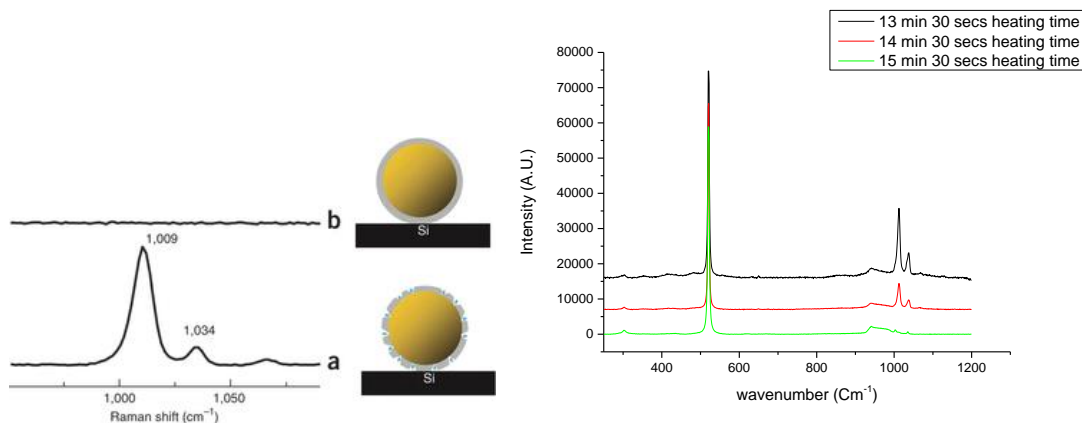


Figure 3.3: Pyridine testing procedure for pinholes in the silica shell of the Au@SiO₂

3.6 SERS and SHINERS Preparation Procedure

SERS experiments using the Au@Pt nanoparticles, utilizes a polycrystalline platinum bar electrode as a substrate for the nanoparticles. To prepare the platinum bar electrode, firstly, the surface is polished using grit paper and diamond spray to remove any previous nanoparticle on the surface. The electrode is then flamed and washed with ultra-pure water to remove any impurities. A 3 μ l sample of the Au@Pt colloid is drop cast onto the Pt bar and dried under nitrogen. Ensure the surface of the platinum bar is rinsed with ultra-pure water before introduction to the flowcell for experiments.

SHINERS experiments are carried out on platinum single crystal surfaces, the preparation of the single crystal is identical to the method outlined earlier. Then additional steps are required to introduce the Au@SiO₂ nanoparticles. The single crystal surface is dipped into an aqueous solution of potassium bromide (a few grains of KBr in 4 ml of ultra-pure water). The single crystal is washed with ultra-pure water to remove excess KBr and to ensure monolayer formation. The role of the KBr monolayer is to protect the Pt single crystal surface from contaminants, due to exposure to the air. A 3 μ l sample of the previously prepared Au@SiO₂ nanoparticle colloid is drop cast onto the crystal surface and dried under nitrogen.

The prepared electrode surfaces need to be electrochemically cleaned before spectroelectrochemical analysis. The procedures differ slightly for the SERS and SHINERS methods. For SERS, the platinum working electrode is cycled between -0.1 and 1.3 V vs. Pd/H at a scan rate of 0.1 V s^{-1} in either 0.1 M sulphuric acid or 0.1 M perchloric acid. This is carried out for 50 cycles or until a stable CV for polycrystalline Pt is produced. If this cannot be achieved the electrolyte is switched to 0.1 M sodium hydroxide and the working electrode was cycled between -0.3 and 1.1 V vs. Pd/H at the same scan rate. Finally, the electrolyte is switched back to the acidic version and a final scan of the Pt surface is taken to ensure the surface is free of impurities.

Due to the SHINERS experiments occurring almost exclusively on Pt single crystals the potential window for cycling the working electrode must be shortened to between -0.1 and 0.85 V at a scan rate of 0.1 V s^{-1} for 100 cycles. This is required as higher positive potentials can induce oxygen evolution and perturb the single crystal surface. The cycling of the working electrode will strip the KBr protective monolayer. It is important to note that the sodium hydroxide electrolyte cannot be used for this cleaning process as alkaline environments will cause the silica shell of the Au@SiO₂ nanoparticles to degrade. However, this cleaning method is usually very proficient in removing impurities. Hydrogen evolution has been identified as the key to removing impurities from the surface(7).

It is important for the SHINERS technique that the Au@SiO₂ nanoparticles do not perturb the single crystal surface, or have pinholes exposing gold as a catalytic surface and citrate as an impurity. The spectrum has been recorded for citrate on gold nanoparticles (figure 3.4), to ensure it is not a source of any of the new peaks identified in the subsequent experiments.

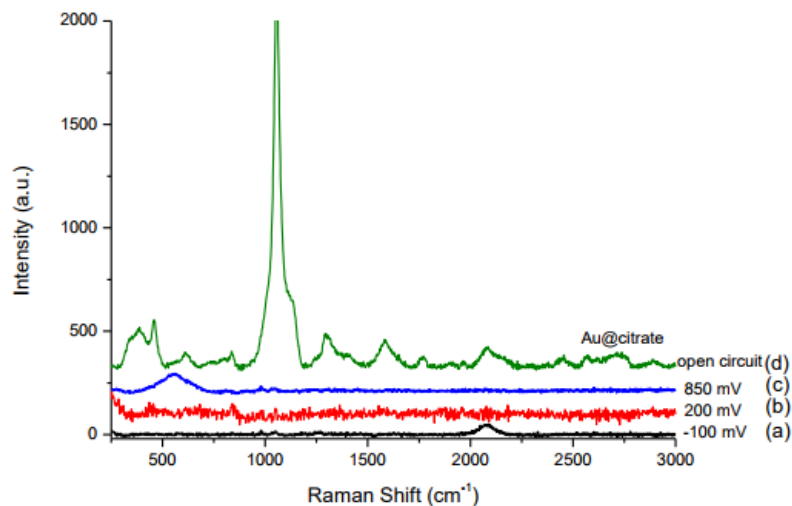


Figure 3.4: SERS spectra of Au@citrate NPs (d, open circuit) and clean Au@Pt NPs on polycrystalline Pt electrode in 0.1 M H₂SO₄ at (a) -100 mV, (b) 400 mV and (c) 800 mV vs. Pd/H. Reprinted from (8)

Figure 3.4 shows the intense peaks of citrate adsorbed on gold core nanoparticles, especially in the region just above 1000 cm⁻¹ and 1250 cm⁻¹. In the background spectra of Au@Pt and Au@SiO₂ no peaks are present that relate to the peaks at 1250 cm⁻¹ and 2500 cm⁻¹. Due to the proximity of the citrate to the gold core in the core-shell, it would be expected that pinholes would constitute an intense dominant peak in the 1000 cm⁻¹ region which is not observed in the spectra of experiments.

CV of the platinum single crystal surface with and without the presence of Au@SiO₂ nanoparticles were recorded (figure 3.4), to evaluate the extent of perturbation of the Pt surface with the presence of Au@SiO₂ nanoparticles.

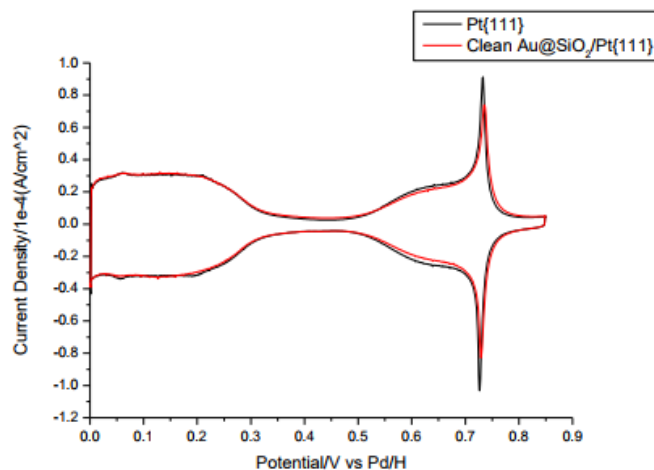


Figure 3.5: CV of clean Pt {111} (black) and Au@SiO₂ on Pt {111} (red) in 0.1 M perchloric acid. reprinted from (8)

As figure 3.5 demonstrates there is minimal loss of current density on the surface, proving that the surface by in large is unperturbed by the coating of Au@SiO₂ nanoparticles(7). This also reinforces the absence of impurities, as any impurities associated with the Au@SiO₂ nanoparticles would diminish the current response of the surface in CV by blocking Pt sites. If pinholes were present on the Au@SiO₂ nanoparticles, a CV response would be expected above 0.8 V due to oxide adsorption/desorption on the exposed Au surface.

The apparatus used to run the Raman experiments was a LabRam HR confocal microscope from HORIBA JobinYvon Ltd. With a 10 mW He-Ne 633 nm laser. Data collection and analysis was performed using the proprietary LabSpec 6 software. Calibration was performed before each session of experiments, using a silicon single crystal reference. Calibration data was recorded and kept ensuring the laser power and alignment was unaltered.

3.7 Shaped Pt Nanoparticle Synthesis methods

Spherical platinum nanoparticles were synthesised by the reduction of the H₂PtCl₆ with hydrazine using a water-in-oil-microemulsion(9). The microemulsion is formed by the addition of two solutions shown in table 3.1.

Solution A	Volume percentage/%	Actual volume/cm ³	Solution B	Volume percentage/%	Actual volume/cm ³
Polyethylene glycol dodecyl ether (BRIJ 30%)	16.5	2.07	Polyethylene glycol dodecyl ether (BRIJ 30%)	16.5	2.07
H ₂ PtCl ₆ 0.1 M	-	0.38	Hydrazine 1M	-	0.29
Heptane	80.5	10.00	H ₂ O	3	0.35
			Heptane	80.5	10.00

Table 3.1: Detailing the constituents of the solutions involved in forming the microemulsion

Once the two solutions are added it takes 5 minutes for the platinum precursor to be fully reduced and two distinct phases form. The nanoparticles are extracted and washed with acetone and several times with ultra-pure water.

PAA Cubic Shaped platinum nanoparticles were synthesised by the same method with varying degrees of success. With PAA cubic displaying the more prominent cubic shape with more ordered {100} terraces. To produce these nanoparticles 125 ml of 10⁻⁴ M K₂PtCl₄ was added to a 250 ml round bottom flask along with 625 µl of PAA. The flask was degassed with nitrogen for 20 minutes and reduced with hydrogen for 5 minutes. The flask was sealed and left overnight in a water bath at 30⁰C(9).

PAA Tetrahedral nanoparticles were synthesised following a similar method to the cubic nanoparticles. The same capping agent and ratio was used. The precursor used was H₂PtCl₆, upon addition of the capping agent the solution was adjusted to pH 7 with 0.1 M HCl solution. This suspension was degassed with nitrogen for 5 minutes and reduced with bubbling hydrogen gas through the suspension for 1 minute. The reaction was sealed and left overnight(9).

The KBr octahedral nanoparticles were created through an adaptation of the previous method; in which a 100 mM solution of KBr was added to the solution before degassing and reduction. The additive made use of halides promoting the growth of {111} terraces.

The oleylamine cubes were produced by adding Pt(acac)₂ (0.02g), Oleylamine (9ml) and Oleic acid (1ml) to a reaction vessel with a gas inlet. The reaction mixture was heated to 130°C under nitrogen, the gas line was switched to carbon monoxide and heated to 210°C for 30 minutes(10).

The H₂PtCl₆ and K₂PtCl₄ were made to the concentration of 10⁻⁴ M solutions with ultra-pure water; and aged for a minimum of 2 days.

Once the nanoparticles were synthesised, the bulk cleaning phase was carried out to remove capping agent from the nanoparticle surface. For the shaped nanoparticles this involved adding a 0.5M sodium hydroxide solution to the colloid, leaving overnight, decanting the supernatant and repeating the process twice more(11). For oleylamine cubes the newly synthesised nanoparticles were washed five times in Acetone, ethanol and sodium hydroxide(12).

Once these bulk cleaning processes have been completed a series of electrochemical cleaning processes were carried out, the advantages of electrochemical cleaning are that the cleaning progress can be monitored through CV. In order to clean electrochemically the CV is swept into negative potentials in order to evolve hydrogen at the working electrode surface. This was carried out in 0.5M sodium hydroxide solution and 0.5M sulphuric acid solution. The sample is left overnight in a 0.5M sodium hydroxide solution and the process is repeated until the CV can be reproduced on successive days, which constitutes the removal of any surface contaminants.

The {111} and {100} sites of the shaped platinum nanoparticles can be quantified through measuring the CV response of the platinum nanoparticles to surface selective adsorption of bismuth and germanium. The technique developed by Feliu *et al* can be briefly outlined as follows(13):

Before characterisation a clean CV of the nanoparticles being probed was recorded in the usual way as described above. For {111} characterisation a 10⁻³ M solution of bismuth nitrate (Bi(NO₃)₃·5H₂O) was made in 1 M sulphuric acid. The drop-coated gold electrode was put into contact with the vial of bismuth nitrate solution for 20 minutes; then a CV was taken of the electrode with a potential sweep of 0 – 0.85 V, if 0.85 V is exceeded the adsorbed bismuth becomes oxidised and desorbs. The scan segments were set to 25 to

allow the surface sufficient time to stabilise; it was noticed that the peaks in the H_{UPD} region decreased. The process was repeated until the {111} sites were blocked. The CV showed a unique bismuth redox peak at between 0.5 – 0.6 V. From use of the original clean CV of the nanoparticles the decrease in charge from the H_{UPD} can be determined and in combination with the charge of the bismuth peak the amount of {111} sites were quantified.

The method for quantifying {100} sites with germanium is very similar, the only changes being a 10^{-2} M germanium hydroxide solution was made in 1 M NaOH. The maximum potential value is reduced to 0.6 V and the germanium redox peak occurs between 0.4 – 0.5 V.

3.8 Collaborative data

For the DFT simulations and calculations provided by Dr Willock *et al* (Cardiff University). Calculations were performed using the VASP (Vienna Ab Initio Simulation Package)(14) using the PBE(15) functional. A plane wave basis set was used with a three-dimensional periodic boundary, with a cutoff value of 500eV for all calculations. The calculations included the DFT-D2 correction by Grimme(16) for long range dispersion forces, with a van der Waals radius of 10Å.

TEM images were captured by Dr Jan Hobot (School of medicine, Cardiff University), using a Philips CM12 transmission electron microscope operating at 80 kV. Images recorded on SIS MegaView III digital camera at screen magnifications of x11,500 and x40,000.

3.9 References

1. J. Clavilier, R. Faure, G. Guinet, R. Durand, Preparation of monocrystalline Pt microelectrodes and electrochemical study of the plane surfaces cut in the direction of the {111} and {110} planes. *Journal of Electroanalytical Chemistry and Interfacial Electrochemistry* **107**, 205-209 (1980).
2. N. Markovic, M. Hanson, G. McDougall, E. Yeager, The effects of anions on hydrogen electrosorption on platinum single-crystal electrodes. *Journal of electroanalytical chemistry and interfacial electrochemistry* **214**, 555-566 (1986).
3. R. J. Taylor, *Study on the surface adsorbates of an enantioselective, heterogeneously catalysed, hydrogenation reaction*. (Cardiff University (United Kingdom), 2010).
4. G. Frens, Controlled nucleation for the regulation of the particle size in monodisperse gold suspensions. *Nature physical science* **241**, 20 (1973).
5. L. Lu *et al.*, Fabrication of core-shell Au-Pt nanoparticle film and its potential application as catalysis and SERS substrate. *Journal of materials chemistry* **14**, 1005-1009 (2004).
6. J. F. Li *et al.*, Shell-isolated nanoparticle-enhanced Raman spectroscopy. *Nature* **464**, 392-395 (2010).
7. J.-F. Li, A. Rudnev, Y. Fu, N. Bodappa, T. Wandlowski, In Situ SHINERS at Electrochemical Single-Crystal Electrode/Electrolyte Interfaces: Tuning Preparation Strategies and Selected Applications. *ACS nano* **7**, 8940-8952 (2013).
8. S. Guan, Cardiff University, (2014).
9. F. Vidal-Iglesias *et al.*, Shape-dependent electrocatalysis: ammonia oxidation on platinum nanoparticles with preferential (100) surfaces. *Electrochemistry Communications* **6**, 1080-1084 (2004).
10. J. Wu, A. Gross, H. Yang, Shape and composition-controlled platinum alloy nanocrystals using carbon monoxide as reducing agent. *Nano letters* **11**, 798-802 (2011).
11. F. J. Vidal-Iglesias, R. M. Arán-Ais, J. Solla-Gullón, E. Herrero, J. M. Feliu, Electrochemical Characterization of Shape-Controlled Pt Nanoparticles in Different Supporting Electrolytes. *ACS Catalysis* **2**, 901-910 (2012).
12. R. M. Arán-Ais, F. J. Vidal-Iglesias, J. Solla-Gullón, E. Herrero, J. M. Feliu, Electrochemical Characterization of Clean Shape-Controlled Pt Nanoparticles Prepared in Presence of Oleylamine/Oleic Acid. *Electroanalysis* **27**, 945-956 (2015).
13. J. Solla-Gullón, P. Rodríguez, E. Herrero, A. Aldaz, J. M. Feliu, Surface characterization of platinum electrodes. *Physical Chemistry Chemical Physics* **10**, 1359-1373 (2008).
14. G. Kresse, J. Furthmüller, Efficiency of ab-initio total energy calculations for metals and semiconductors using a plane-wave basis set. *Computational materials science* **6**, 15-50 (1996).
15. G. Kresse, D. Joubert, From ultrasoft pseudopotentials to the projector augmented-wave method. *Physical Review B* **59**, 1758 (1999).
16. S. Grimme, Semiempirical GGA-type density functional constructed with a long-range dispersion correction. *Journal of computational chemistry* **27**, 1787-1799 (2006).

Chapter 4 - Enantioselective Hydrogenation of Ethyl Pyruvate

4.1 - Literature review

4.1.1 Proposed Adsorption States of EP on Platinum Surfaces

Significant advancement in the field of heterogeneous chiral catalysis has occurred in recent decades, gratitude for the development should be attributed to the innovative work of Alfons Baiker and others(1-6). The heterogeneous enantioselective hydrogenation of an activated prochiral ketone with a chirally modified platinum catalyst, was first observed by Orito *et al* in 1978(7). Considerable attention was garnered for this reaction, due to the notably high chiral efficiency(8, 9). Specifically, in the case of Ethyl Pyruvate (EP) hydrogenation over Cinchonidine (CD) platinum catalysts, which yields R-Ethyl Lactate (EL) in high enantiomeric excess (figure 4.1)(9). Enantiomeric excess is a measure of enantiomeric purity for chiral substances, it can be calculated using equation 4.1 and is expressed as a percentage. The higher the percentage the more abundant one enantiomer is over the other in the mixture, with a racemic mixture (50-50) having an enantiomeric excess of 0%. The enantiomeric excess of EP hydrogenation has been studied in depth and the impact of changing reaction variables on ee has also been explored. The enantiomeric excess has been shown to alter greatly depending on the reactions conditions employed, but can be optimised to < 90% in regards to R- Ethyl Lactate (10). When a flow reactor is employed with similar temperature, flow rate and reactant and modifier concentrations as in this study an ee of 63% was achieved for R-Ethyl Lactate (11). Another significant study by Baiker *et al* managed to obtain an enantiomeric excess range of 72 – 92% for various shapes of platinum nanoparticles (12).

$$\%ee = \left[\frac{(\text{moles of desired enantiomer} - \text{moles of other enantiomer})}{\text{total moles of both enantiomers}} \right] \times 100 \quad (\text{eq 4.1})$$

While the optimal conditions to achieve high enantiomeric excess for the reaction have been investigated and refined in detail, little insight has been offered on how EP interacts with the platinum surface and no consensus has been reached on the mechanism of chiral discrimination.

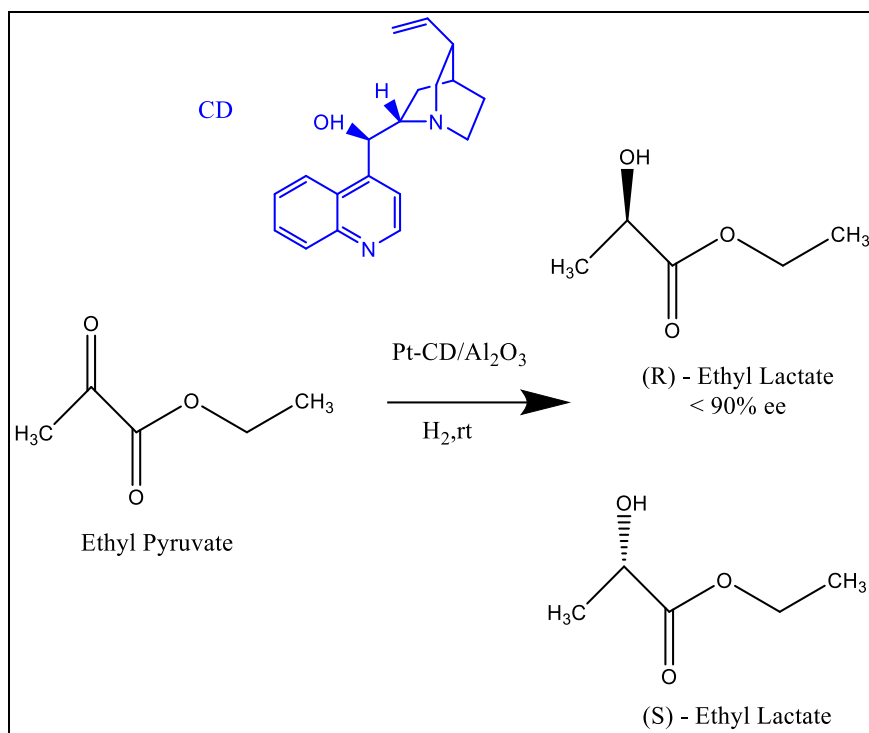


Figure 4.1: Enantioselective hydrogenation of EP

The complexity of the reaction provides many variables that influence the enantioselectivity of the reaction(13-16). Catalyst preparation methods such as sintering(17), sonication(18) and exposure to hydrogen at elevated temperatures(19) have all demonstrated influence over enantioselectivity, which can be rationalised by alterations to the Pt catalyst surface. How EP interacts with the platinum surface and the chiral modifier is an area of interest and could yield valuable insight into the mechanism of chiral discrimination. Attard *et al* demonstrated discernible differences between step and terrace sites for reaction rate and enantioselectivity(20). Through the co-adsorption of site-blocking adatoms, Bismuth for step sites and Sulphur for terrace sites, it was determined that impeding step sites enhanced the reaction rate and diminished the enantiomeric excess. The opposite was found when terrace sites were blocked, leading to the conclusion that edge sites provided the highest enantiodifferentiation. Baiker *et al* used shaped platinum nanoparticles to investigate how

the ratio of Pt{111}/Pt{100} sites impacted the rate and enantiomeric excess of the reaction, finding higher rates and enantiodifferentiation with higher ratios of Pt{111} sites(12). This trend was attributed to the differing adsorption energies of the alkaloid modifier on each surface. These two highlighted studies allude to the structure sensitivity of the EP hydrogenation mechanism, however, isolating the nature of the structural effect is obscured by common variables of catalytic nanoparticle systems such as: electronic effects, density of surface defects and additional support interactions.

To develop further understanding of a potential surface sensitive hydrogenation mechanism, a more fundamental analytical approach was required. Studies utilised single crystal surfaces to alleviate some of the issues associated with the nanoparticle surfaces. Baiker *et al* employed XP and UP spectroscopy to analyse EP adsorption on the Pt{111} surface at low temperature(21). It was proposed that EP bonded to the platinum surface via oxygen lone pairs in a predominately tilted adsorption mode. Baiker *et al* added additional insight through an in-situ XANES study(22), that lone pair and π -bonded species co-exist on the platinum surface. Transition from lone pair bonded to π -bonded species is possible and is promoted through co-adsorption of hydrogen. Furthermore, hydrogen bonding between the oxygen atom of the α -carbonyl moiety and the quinuclidine N of the coadsorbed cinchonidine should further favour the π -bonded species. This line of reasoning is in keeping with previously suggested adsorption modes of ethyl pyruvate(1, 3). McBreen and co-workers introduced the possibility of both oxygens being involved in an enediolate bonding state with the platinum surface and reinforcement for the end-on bonding of the ketone oxygen lone pair in a η^1 adsorption state (23). As shown in figure 4.2 spectrum 1 b, upon introduction of methyl pyruvate two bands appear at 1545 and 1290 cm^{-1} relating to the enediolate. Interestingly, as exposure to MP increases (spectrum 1c) peaks form at 1742 cm^{-1} and shoulder at 1307 cm^{-1} representative of a free carbonyl and C-O ester vibration, indicative of a trans-MP state. However, it is worth noting the RAIRS analysis used as evidence for the adsorption modes was collected at low temperatures and stability of these states at catalytic conditions could be questionable.

1-(1-naphthyl)ethylamine and Methyl Pyruvate on Pt(111) at 110K

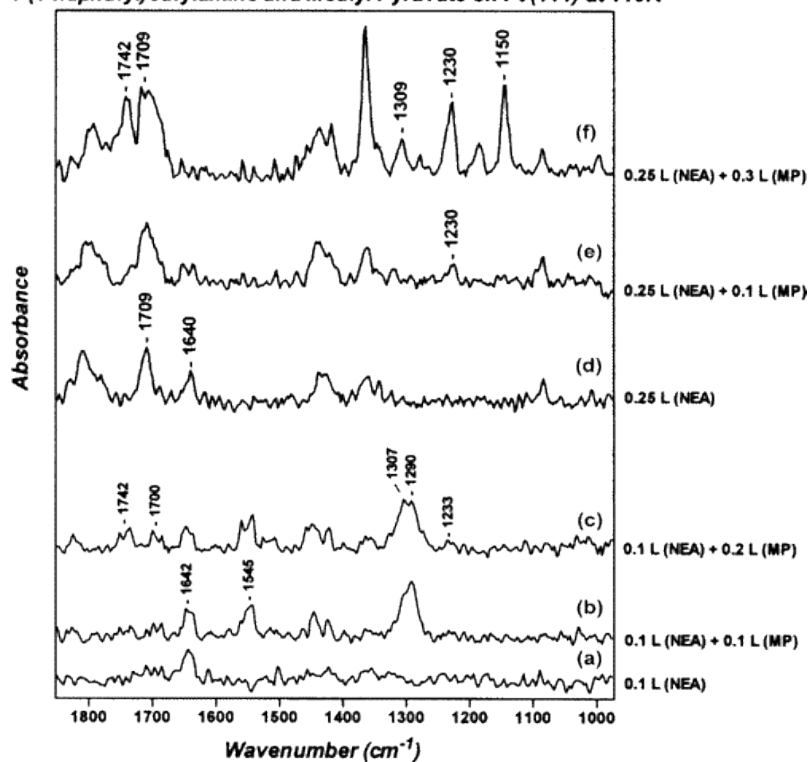


Figure 4.2: (a-c) RAIRS spectra for a 0.1 L ($1 \text{ L} = 1 \times 10^{-6} \text{ Torr}\cdot\text{sec}$) exposure of (\pm)-NEA on Pt(111) at 110 K, followed by consecutive exposures to methyl pyruvate. (d-f) RAIRS spectra for 0.25 L (\pm)-NEA followed by consecutive exposures to methyl pyruvate at 110 K. Reprinted from (23)

Four plausible adsorption modes of EP have been identified and are demonstrated in figure 2, transitions between the modes could be possible, taking into consideration stability and interactions with surface and modifier.

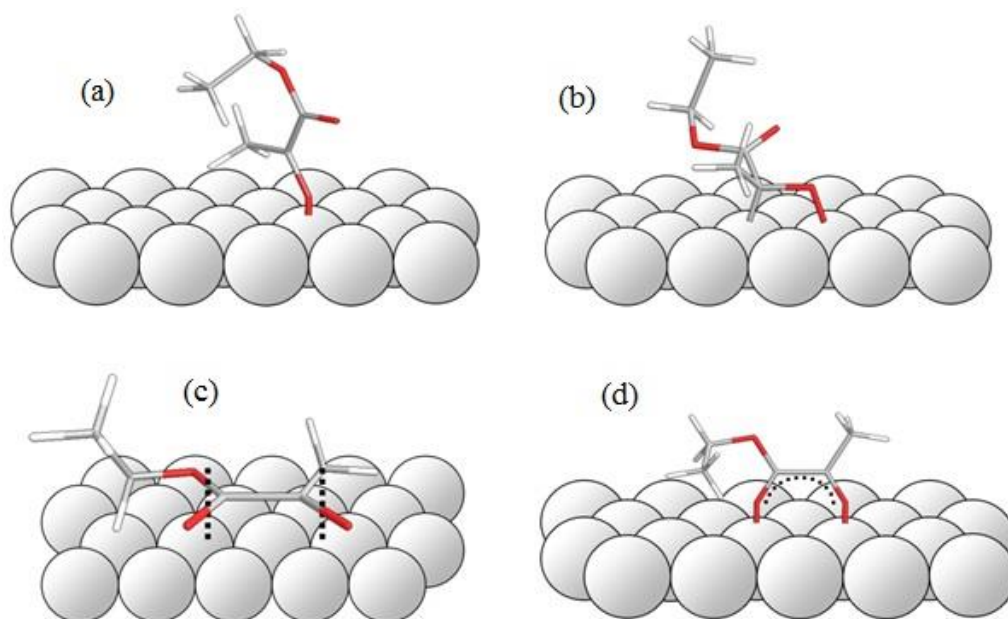


Figure 4.3: EP adsorption modes; (a) η^1 , (b) η^2 , (c) π -bonded, and (d) enediolate. Reprinted from ref(24).

4.1.2 Proposed Interactions Between EP and the Alkaloid Modifier

The alkaloid modifier plays a very important role in the reaction, but the exact details of the role are ambiguous in the literature. In 1994, Baiker and co-workers introduced the 1:1 interaction model(3). In which, the chiral Cinchonidine modifier adopts an “open” conformation, where the basic quinuclidine nitrogen atom points away from the aromatic quinoline ring, the anchoring moiety of Cinchonidine to the Pt catalyst surface. Cinchonidine interacts with the oxygen of the keto carbonyl of EP through the quinuclidine group, either through a N-H---O hydrogen bond in protic solvents or a N---H-O hydrogen bond involving the half-hydrogenated state of EP in aprotic solvents. This intermolecular interaction combined with steric repulsion exerted by the anchoring group causes the preferential adsorption of the reactant on one enantioface (re- or si-face) and is presented as the cause of enantiodifferentiation. A similar mechanism was proposed by Wells *et al*, who proposed a potential hydrogen bond between the tertiary nitrogen from the QN moiety of CD to the alcohol group of a half-hydrogenated intermediate state(4). Blausser *et al* also found supporting evidence for the 1:1 interaction model, noting a loss of enantioselectivity after the alkylation of the tertiary nitrogen group on Cinchonidine(6). Another proposed model for enantio-induction was the template model(25), the basis of this model was that the alkaloid modifier adsorbed in an ordered fashion, forming “exposed” chiral pockets of

platinum atoms on the surface. The ordered ensemble would direct adsorption of the α -ketoester of a specific enantioface, thus forming the specific enantiomer of the hydroxyester. This model was later discounted, due to the aforementioned study by Wells *et al*, which showed no evidence of ordered arrays of CD on a platinum {111} surface(4). Another alternative is the shielding model proposed by the Margitflavi group(26), which centred around interactions of the modifier with the reactant in the solution prior to adsorption. Upon interaction with the reactant, the modifier is proposed to change to the 'closed' conformation. The source of enantioselectivity in this model is through a π - π interaction between the delocalised π system of the quinoline ring and the conjugated double bond(s) of the carbonyl on the pyruvate molecule, causing a shielding effect that orientates the reactant. This model was disfavoured as it failed to explain reported enantioselectivity at low modifier concentrations, as the model related an increase in enantiomeric excess to being proportional to the modifier concentration. Another detraction of the model was presented by Bartok *et al* (27), who presented high enantiomeric excesses using α -isocinchonine as the modifier, which has a rigid structure that exists only in "anti-open" configuration.

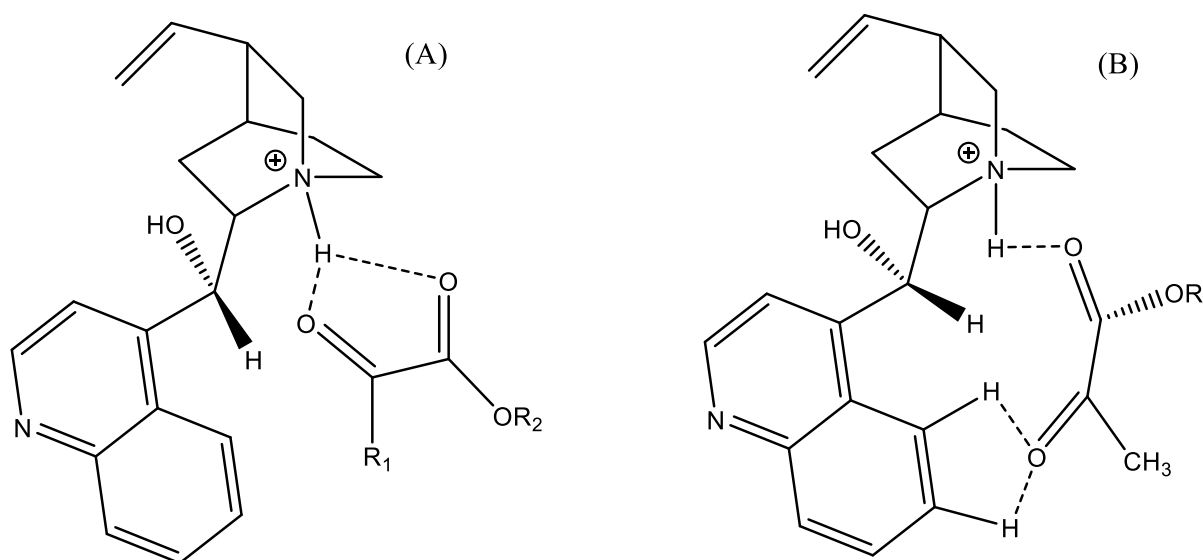


Figure 4.4: Modifier and reactant interactions, (A): Baiker's model and (B) McBreen's model(2)

As well as the modifier having an influence on the enantiomeric excess of the Orto reaction, a rate enhancement is associated with the presence of the modifier. For any mechanistic model to be credible it must also encompass an explanation for the rate enhancement. Considering that the alkaloid would undergo competitive adsorption with the α -ketoester and limit free platinum sites, the rate enhancement of 10 – 100 times of the racemic reaction is unexpected (28). The first explanation is through the suppression of side reactions, these include aldol polymerisation(29), ester condensation(30) and decarbonylation(31), the products of these side reactions cause surface fouling. Carbon monoxide is a product specific to the decarbonylation reaction, CO has been proposed to strongly adsorb on highly coordinated platinum sites, which are also considered to be favourable for the hydrogenation reaction. Co-adsorption with the modifier not only decreases the rate of decarbonylation significantly, but also displaces pre-existing CO surface species.

The Ligand Acceleration model is another approach to explain the associated rate increase on CD modified catalyst surface(32-35). It is proposed that through interactions between the reactant, modifier and presumably the catalyst surface induce a change in the energetics of the activated ketone, increasing hydrogenation susceptibility. The origin of the rate enhancement in the presence of the modifier is still debated, with literature arguing either an increased turnover rate on a constant number of platinum sites (Ligand acceleration) or the same turnover on an increased number of platinum sites, through elimination of catalyst poisons. There is not much evidence for a relationship between the rate acceleration and enantioselectivity associated with a modified surface. Attard *et al* introduced a correlation between rate and enantiomeric excess on terrace and step sites on the platinum surface(20). Bartók(36) and Murzin(35) have presented examples in which high enantiomeric excess has been achieved, with negligible rate acceleration. Concentration of the modifier plays an important role in influencing the rate and enantioselectivity. By monitoring rate and ee versus modifier concentration, Blaser *et al* showed that the reversible adsorption of one modifier molecule forms a modified active site(34). Maximum modification is achieved at low modifier concentrations, meaning enantiodifferentiation interactions between the reactant and the modifier must occur on the catalyst surface and

not in solution. Both rate and ee decrease at high modifier concentrations, Zaera has correlated the decrease with a change in adsorption geometry from flat to tilted for the cinchona molecule(37).

An important interaction in the enantioselective hydrogenation of α -ketoesters is proposed to take place between the quinuclidine moiety and the half hydrogenated state of the reactant, this stabilising interaction is suspected to occur through hydrogen bonding(38). A proposed mechanism for the formation of the HHS is depicted in figure 4. The importance of this long-lived surface intermediate has been alluded to with regards to the overall kinetics of the reaction, in particular rate acceleration(39, 40). On modified sites it is believed that the addition of the hydrogen to the HHS is the rate limiting step, with the addition of the first hydrogen being rate limiting on the unmodified catalyst(40). In this case the enantiodiffering step is the stabilisation of Si-complex of the HHS, However Attard *et al* proposed a differing mechanistic insight, in which, the chirality of the lactate is already established upon transfer of the first hydrogen. This means the interaction with CD in generating enantioselectivity should occur before this first H transfer step(41). Co-adsorption of the α -ketoester with CD reduced the surface coverage of the HHS, leading to the conclusion that the modifier promoted and activated adsorbed hydrogen(41). Another study has probed the hydrogenation of EP by IR spectroscopy after the substitution of deuterium for hydrogen and proposed an interaction of CD with the coadsorbed EP (42). Detailed within the interaction is that a tilted CD molecule with the quinuclidine overhanging the adsorbed EP molecule, interacts with the ester carbonyl of the η^1 (O) EP adsorbate pulling the ester group away from the surface. This is indicated by the red-shift and sharpening of the ν CCO stretch at 1283 cm^{-1} . In this example the quinuclidine nitrogen is hydrogenated and participates in a hydrogen bonding interaction with the ester carbonyl, sharing similarities with previous models presented by McBreen (43).

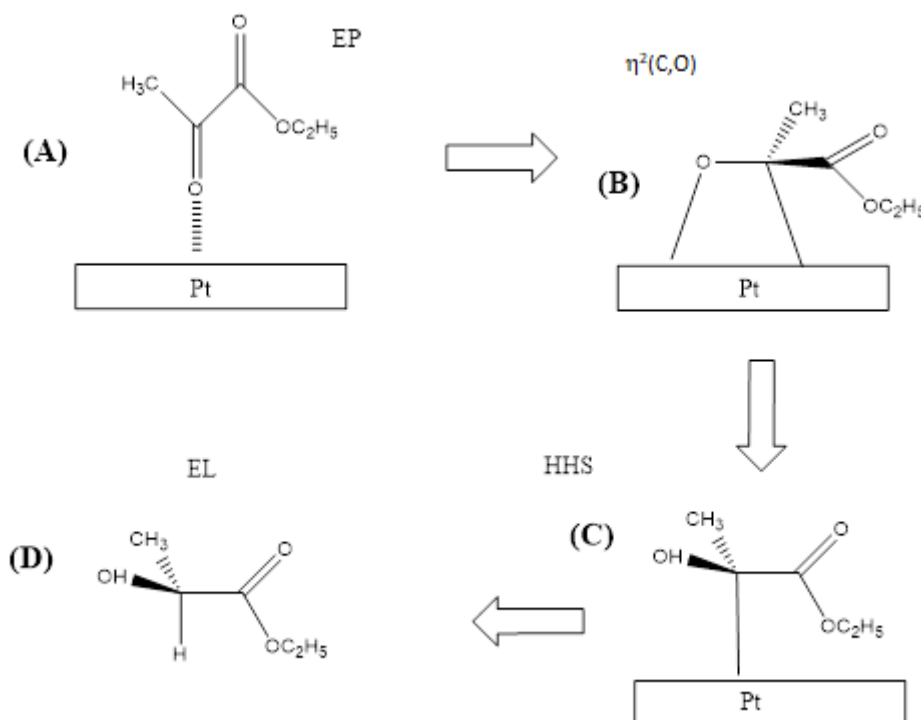


Figure 4.5: Proposed Reaction schematic for EP on Pt surfaces, with (A) being an interaction of the carbonyl with the Pt surface, (B) the $\eta^2(\text{C},\text{O})$ surface intermediate forms, (C) Partial hydrogenation forms the HHS and (D) hydrogenation is completed and the Ethyl Lactate product is formed.

The presence of adsorbed hydrogen on the catalyst surface is very important, not only concerning reaction rate, but also in preventing a keto-enol tautomerisation reaction. McBreen *et al* demonstrated that methyl pyruvate can undergo C-H scission at room temperature on the Pt {111} surface leading to enol formation and assembly of hydrogen bonding superstructures. This can be avoided by maintaining low temperature or at room temperature with a background hydrogen pressure of 10^{-6} Torr(44). Bonello *et al* concluded the formation of similar superstructures formed on the Pt {111} surface in the absence of the cinchona modifier or when the ratio of adsorbed hydrogen to ketoester is too low(45). However, this was attributed to a self-condensation reaction, as opposed to a keto-enol tautomerisation.

The literature for the enantioselective hydrogenation of ethyl pyruvate is extensive, but a lack of continuity in reaction conditions can make direct comparisons difficult. There are many variables involved in the reaction and interactions between them make mechanistic insight a very complex task. In an attempt to simplify the reaction, it can be broken down

into the behaviour of individual components. These components consist of the adsorption of the reactant, co-adsorption of the modifier, interactions between the modifier and the reactant, availability of adsorbed hydrogen, intermediate species, decomposition of reactant and surface poisoning. Various analytical methods have been employed to probe the enantioselective hydrogenation of α -ketoester, these include: XANES(22), NEXAFS(30), LEED(46), STM(29, 44), RAIRS(13, 37), ATR-IR(47), XPS(21), DFT(12, 48) and SERS(41). From these studies four adsorption modes have been identified:

1. An orientation parallel to the surface involving π -bonding from one or both carbonyls.
2. A Pt-O bond from both carbonyls with a delocalized π -orbital between them (enediolate).
3. An end-on configuration bound via an oxygen lone pair from the ketone (η^1).
4. A Pt-O and Pt-C σ -bonded entity with the C-O bond horizontal to the surface (η^2).

Each of these identified adsorption states can exist on the catalyst surface, but it is generally accepted that the η^1 adsorption state is dominant. A study combining SERS, CV and DFT identified an adsorption preference at certain single crystal sites(41), due to the use of SERS this revelation cannot be fully explored on single crystal surfaces. Recent developments in Raman spectroscopy has led to a new technique known as Shell-Isolated Nanoparticle Enhanced Raman Spectroscopy (SHINERS)(49), with the use of this technique in-situ spectroelectrochemical analysis of the Ethyl Pyruvate hydrogenation on platinum single crystals can be achieved(50).

The modifier, in this case CD is credited as the source of induction of enantioselectivity. The presence of the co-adsorbed modifier facilitates a 10 – 100 times rate increase on racemic hydrogenation and an enantiomeric excess increase for the R – Ethyl Lactate. The associated rate increase seems counterintuitive as the modifier is occupying catalytic sites, one explanation is that the modifier suppresses catalyst deactivation via reactant decomposition or side reactions (20, 35). Baiker *et al* contested these findings noting that the non-acidic solvent used in the study (toluene) would make the control of side reactions difficult(51), this was supported by the investigation by Bartok *et al* reporting a significant rate enhancement using the same catalytic system employing acetic acid as the solvent(36). This

highlights the sensitivity of the enantioselective reaction, meaning even the somewhat facile details of the reaction must be carefully considered. There is clearly a link between enantioselectivity and rate acceleration upon the introduction of the modifier to the catalytic system, therefore any attempt to propose a mechanism for the reaction needs to consider an explanation that encompasses both the phenomena. For this exact reason the theory that enantioselectivity occurs through a templating method, which proposes that the modifier blocks surface sites to produce a chiral surface. This would not adequately explain the rate enhancement, making this an implausible mechanism. The two most prominent methods are the shielding method and the 1:1 interaction method(3, 52). The shielding method proposes that the α -ketoester and the alkaloid form a complex that shields one side of the reactant, only allowing hydrogenation of the unrestricted enantioface of the reactant. However, the prerequisite for this model to work is that the modifier must adopt a “closed” conformation with the quinuclidine nitrogen pointing towards the quinoline ring (surface anchor). The confirmation of the modifier has been probed and conflicting data to the shielding method was published. The study demonstrates a similar enantiodifferentiation for a alkaloid in a rigid “open” conformation as the parent cinchona alkaloids (53). The final and most promising enantiodifferentiation model is the 1:1 interaction theory proposed by Baiker and co-workers(3). This model links enantiodifferentiation to the different stability of the diastereomeric complexes formed between cinchonidine anchored to the Pt catalyst surface and ethyl pyruvate adsorbed in its two enantiofacial forms (via re- and si-faces), leading to S- and R-ethyl lactate. The modifier is in the “open” configuration for this mechanism and interacts through hydrogen bonding of a protonated quinuclidine moiety and the keto carbonyl oxygen from the adsorbed reactant. This proposed mechanism also satisfies the accompanied rate acceleration with the modifier as a relationship can be established relationship between keto carbonyl orbital and hydrogenation rate, it is proposed that the interaction between the quinuclidine group and the keto carbonyl lowers the activation barrier for the hydrogenation. In aprotic solvents (toluene) the interaction is proposed to occur between the quinuclidine group and the hydrogenated keto carbonyl of the half hydrogenated state proposed by Attard *et al* (54) . The HHS is a proposed intermediate state in the hydrogenation reaction that is prominent on high index platinum surfaces and in the absence of the alkaloid modifier, the role of the HHS in the hydrogenation mechanism is ambiguous and contentious. For the HHS to be present and

detected on the catalyst surface the second hydrogen addition needs to be slow and the rate determining step for the hydrogenation. Interactions between CD and the HHS have not been detected spectroscopically to date and observations suggest that both are in competition for surface sites. The HHS also raises questions about enantioselectivity as once the HHS forms chirality of the reactant has been induced and the enantiomer of ethyl lactate formed is determined at this point. This is contradictory to previous mechanistic insights all involving the modifier inducing chirality. This gives an appreciation on the depth of information on the system and the complexity of the task of formulating an all-encompassing reaction mechanism.

4.1.3 Electrochemical Investigation of EP Hydrogenation on Pt Basal Planes

Hazzazi *et al* investigated the irreversible adsorption of EP on platinum single crystals electrodes, determining adsorption to be structure sensitive(55). This initial work was expanded upon by monitoring the surface after hydrogenation. Figure 4.6 (a) shows the Pt {111} surface, adsorption of EP attenuates the characteristic “Butterfly Peak” between 0.4 and 0.5V(62). This is a sign of disruption of the long-range order of the {111} terraces, however, the majority of HUPD region for the {111} surface is un-perturbed relating to a 10% loss in area. This is in agreement with the previous investigation as the {111} surface had the least amount of adsorption(55). Upon hydrogen evolution, appreciable amounts of adsorbed EP were removed, freeing up platinum surface sites and recovering order of the {111} terraces. The {100} and {110} surfaces facilitate higher adsorption amounts of EP, with the {100} surface free platinum sites reduced by roughly two thirds (Figure 4.6b). New features are also present in this CV, with a cathodic peak at 0.1V and an anodic peak at 0.74V. This is attributed to reductive EP desorption and electrooxidative stripping of CO from the decarbonylation of EP respectively(31). Evolving hydrogen removed significant amounts of adsorbed EP from the {100} surface, demonstrating efficient hydrogenation of EP. The Pt{110} surface (Figure 4.6c) demonstrated similar traits to the {100} surface, although characteristic HUPD region was attenuated to a lesser extent. The same can be said for the minor anodic peak above 0.7V to signify marginal amounts of CO removal. The anodic peak just before 0V is attributed to hydrogenative desorption of EP with increasing

surface hydrogen available, this coupled with the almost complete removal of EP after hydrogen evolution reflects on the efficiency of hydrogenation on this type of surface(20).

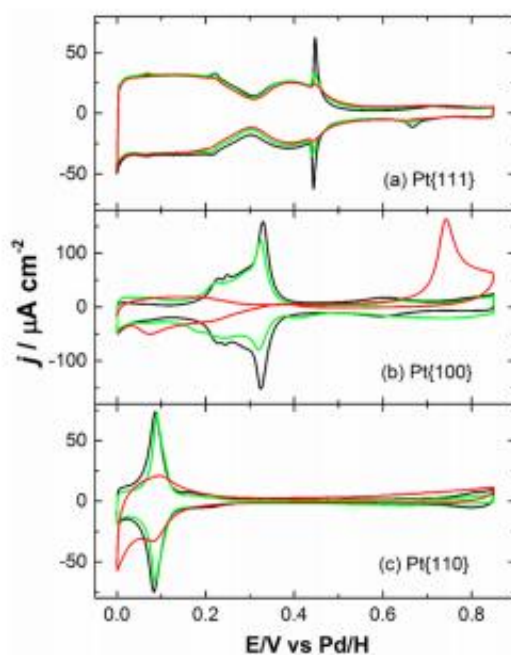


Figure 4.6: CVs of Pt basal electrodes in 0.1 M H₂SO₄ (sweep rate 50 mV s⁻¹) before adsorption of EP (black curve), after exposure to EP for 5 s (red curve), and after EP adsorption followed by hydrogen evolution at -0.1 V (green curve): (a) Pt{111}; (b) Pt{100}; (c) Pt{110}. Reprinted from(50).

4.2 - Results

4.2.1 Raman and SERS Investigation of EP Hydrogenation on Polycrystalline Pt

Raman Spectra of neat liquid samples of Ethyl Pyruvate and the hydrogenation product Ethyl Lactate were collected (Figure 4.7), each spectrum was characterised in accordance with reference material(57). The stretching assignments for each band are displayed in table 4.1, this forms the foundation of the spectroscopic analysis. The Bulk peaks allow us to identify common skeletal peaks, alterations from these spectra in subsequent spectra at hydrogenating conditions will give information about orientation, intermediates and so forth.

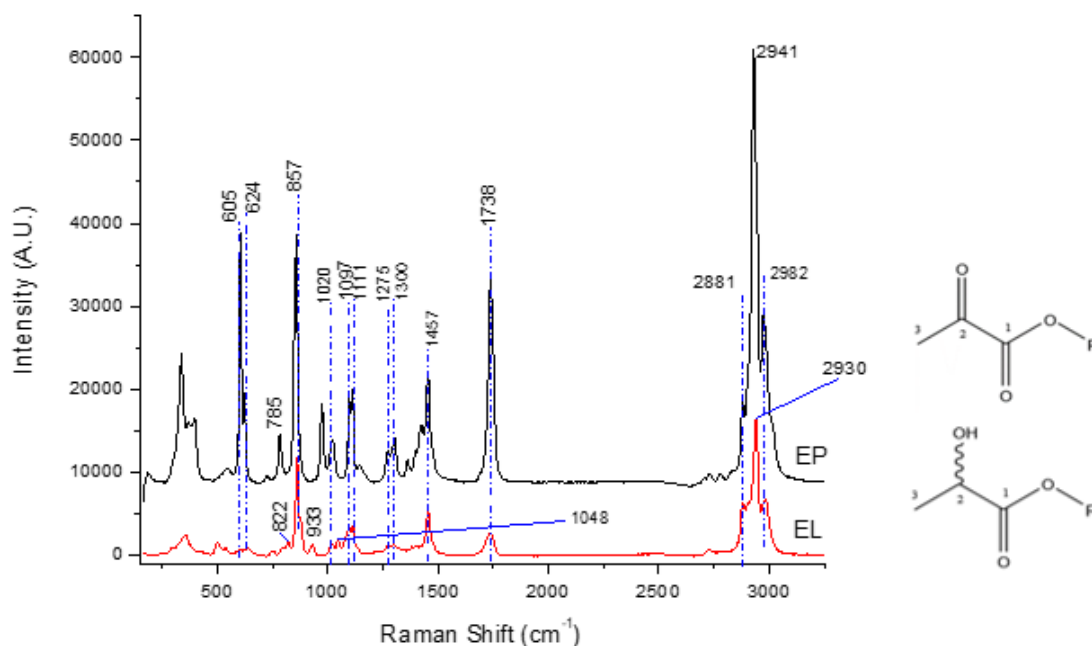


Figure 4.7: Raman Spectra of Bulk Ethyl Pyruvate and Ethyl Lactate

Peak Position (cm ⁻¹)		Assignment
Ethyl Pyruvate	Ethyl Lactate	
3017	2982	va (C ³ -H ₃)
2941	2930	vs (C ³ -H ₃)
2881	2881	vs (C ⁴ -H ₂)
1738	1738	v (C=O)
1457	1455	δd (C ⁵ -H ₃)
1304	1300	v (O-C ⁴ H ₂ CH ₃) <i>anti</i>
1273	1275	v (O-C ⁴ H ₂ CH ₃) <i>gauche</i>
1111	1114	δr (C ⁴ -C ⁵ H ₃) <i>anti</i>
1097	1096	δr (C ⁴ -C ⁵ H ₃) <i>gauche</i>
-	1048	v (C ² -C ³) / δr (H ₃ C ³ -C ²) / δr (C ² -OH)
1020	1019	v (C ⁴ -C ⁵ H ₃)
972	-	va (O-C ⁴ H ₂ -C ⁵ H ₃) / Skeletal
-	933	δr (C ³ -H ₃)
857	861	v (O-C ⁴) / δr (C ⁵ -H ₃) / δ (C ² -C ¹ -O)
-	822	v (C ² -OH) / δr (C ³ -H ₃) / Skeletal
785	-	δr (C ⁴ -H ₂)
624	635	δr (C=O)
605	605	Skeletal (O-C ¹ -C ²)

Table 4.2: Raman Band Assignment for Bulk EP and EL

It is important to distinguish Raman bands that are a result of surface intermediates rather than a condensed ad-layer of bulk ethyl pyruvate, therefore, the stretches assigned to skeletal ethyl pyruvate will be continually referenced throughout the investigation.

Interestingly, the band assignment of the 1048 cm^{-1} position relating to δ_r ($\text{C}^2\text{-OH}$) stretching mode. This is a significant peak as the Au@Pt SERS investigation has attributed the appearance of this peak in the spectra as an indication that the HHS has formed on the platinum surface (Figure 4.8).

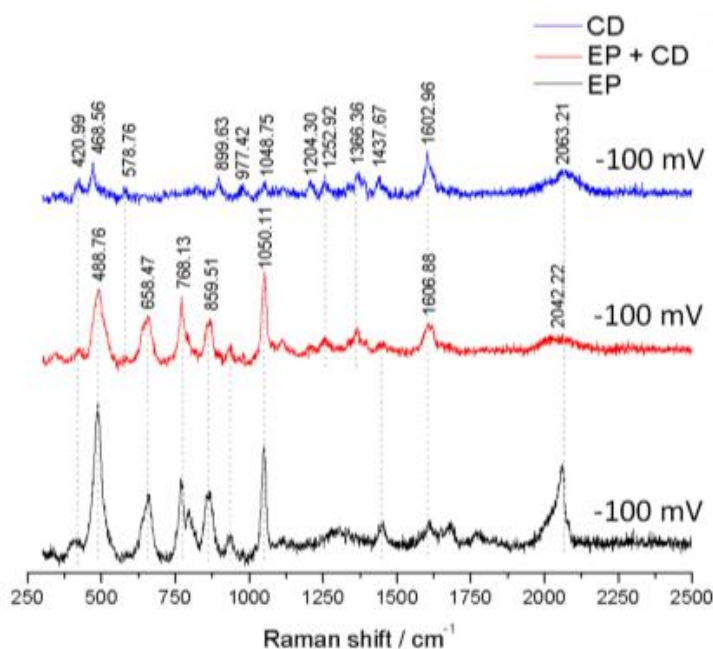


Figure 4.8: Au@Pt SERS under hydrogenation conditions in $0.1\text{M H}_2\text{SO}_4$ of $2 \times 10^{-5}\text{M CD}$ (blue), 0.1M EP with $2 \times 10^{-5}\text{M CD}$ (red) and 0.1M EP only (black)(24).

New features on the polycrystalline Au@Pt surface at ~ 2060 and 490 cm^{-1} are related to the on-top adsorption configuration of CO. The peak at 490 cm^{-1} is indicative of a Pt-C bond which can be related to CO and the HHS bound to the platinum surface, as the large intensity of the 490 cm^{-1} peak suggests that CO isn't the sole contributor. The sharp peak at 1050 cm^{-1} is a very prominent feature of the C-OH stretch of the hydrogenated keto carbonyl, forming the HHS. Another significant feature of the EP spectrum is the absence of any peak in the carbonyl region ($\sim 1740\text{ cm}^{-1}$), this reveals that the orientation of the carbonyl must be parallel to the platinum surface to render it silent with regards to the selection rules. Upon co-adsorption with CD all peaks associated with EP are reduced in intensity, this can be associated with CD displacing ethyl pyruvate. As mentioned previously CD also displaces CO, which is evident from the substantial decrease of the 2040 cm^{-1} peak. A tell-tale sign of adsorbed CD is the band situated at $\sim 1600\text{ cm}^{-1}$, which can be attributed to the C=C stretching mode of the quinoline ring(37). The dominance of the aforementioned

peak suggests the modifier is adsorbed flat on the surface with regards to the quinone group, tilting would be accompanied by a rise in intensity of at 1366 and 1253 cm^{-1} (37, 58). The band at 2063 cm^{-1} has some ambiguity attributed as the Pt-H peak is red-shifted to a similar wavenumber(41). A further level of obscurity in defining the individual peaks of the spectra can be associated with the solvent media used, in this case sulphuric acid has two distinct peaks at 980 and 1040-1050 cm^{-1} (59). This can make it difficult to identify whether the HHS is present at low concentrations, however, it is not an issue in this example. For this reason, the SHINERS experiments are conducted with perchloric acid as the electrolytic media.

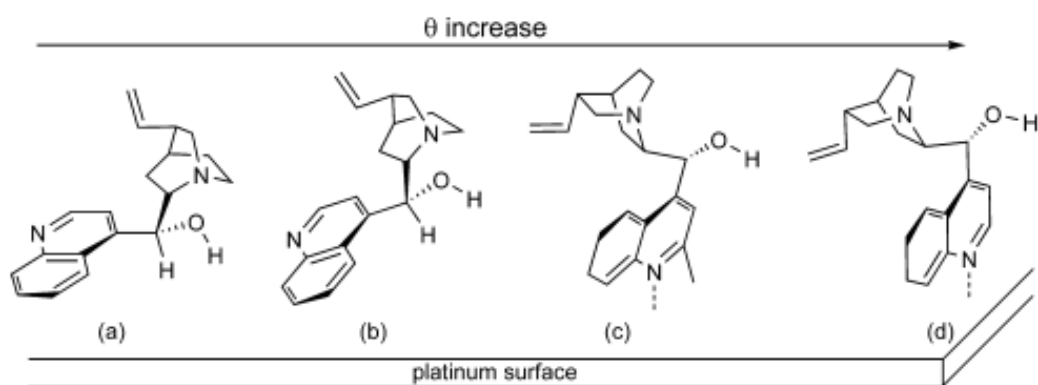


Figure 4.9: The adsorption modes of cinchonidine: (a) parallel π -bonded; (b) tilted π -bonded; (c) α -H-abstracted quinolylic; (d) quinoline-N-lone pair bonded(60).

4.2.2 SHINERS Investigation of EP Hydrogenation on Pt Basal Planes

The Pt {111} surface has been widely probed by many different techniques with regards to the selective hydrogenation of α -ketoesters(21, 29, 61). Schmidt *et al* achieved a high enantiomeric excess with shaped platinum nanoparticles with a high ratio of {111}/{100} sites, this was attributed to increased stability of the modifier on Pt {111} sites(12). SHINERS analysis was performed on the Pt {111} single crystal surface in varying conditions for adsorbed EP (Figure 4.10).

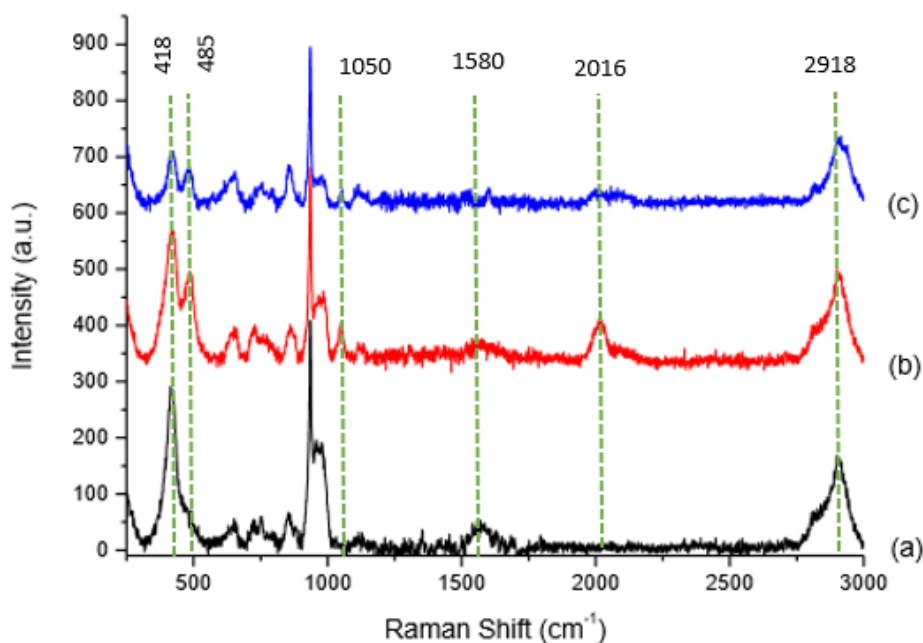


Figure 4.10: SHINER Spectra of 0.1M EP in 0.1M HClO₄ at hydrogenation potentials on (a) Pristine Pt {111}, (b) electrochemically roughened Pt {111}, (c) electrochemically roughened Pt {111} with coadsorbed 2x10⁻⁵M CD.

Similarities can be made between the Au@Pt SER spectra (Figure 6) in terms of skeletal stretches of EP, bands at 649, 750 and 857 cm⁻¹ can be identified as C=O rocking, O-C-O scissoring and C-C-O stretching respectively. Also, a commonly featured vibrational band at 2918 cm⁻¹ is due to C-H stretching. The small band at 1580 cm⁻¹ is slightly ambiguous and can be justifiably assigned to several vibrations. Popular assignments have been suggested such as small amounts of carbonaceous contaminants on the platinum, which is unlikely due to the extensive cleaning cycles prior to analysis. This region can also encompass bending modes of water on the platinum surface, but in general the peak is sharper and more intense for water in these cases(63). Taylor *et al* purposed that the 1580 cm⁻¹ could arise through a carbonyl interaction with the platinum surface(41), or be an indication of C=C in the enolic form of EP(44). The presence of an enolic form of EP is unlikely in hydrogenating conditions, as it is unstable in the presence of adsorbed hydrogen(64). The sharp peak at 936 cm⁻¹ is due to the Cl-O stretch perchloric acid electrolyte used(65). On the pristine Pt {111} surface two new vibrational bands were discovered at 418 and 965 cm⁻¹, which have not been reported on polycrystalline surface. Also, neither of the peaks associated with the HHS are present at 1050 and 490 cm⁻¹, this result implies that the HHS does not form on terrace sites and requires defects to be present. To substantiate this hypothesis, the {111}

surface was electrochemically roughened and further spectra were recorded. The spectrum of the electrochemically roughened surface (figure 8(b)) shows three new bands present at 2016 cm^{-1} representing surface CO, at 1050 cm^{-1} attributed to a C-O-H stretch of the HHS as well as a peak at 485 cm^{-1} representative of a Pt-C stretch which has contributions from both the HHS and CO surface species. With the emergence of the new peaks after roughening the new established peaks at 418 and 965 cm^{-1} were attenuated, possibly alluding that both are linked to terrace sites on the surface. The addition of coadsorbed CD (figure 4.10(c)) results in lower intensity of all peaks related to EP as competition for Pt surface sites would occur. The bands relating to are very minimal and hard to distinguish from the baseline.

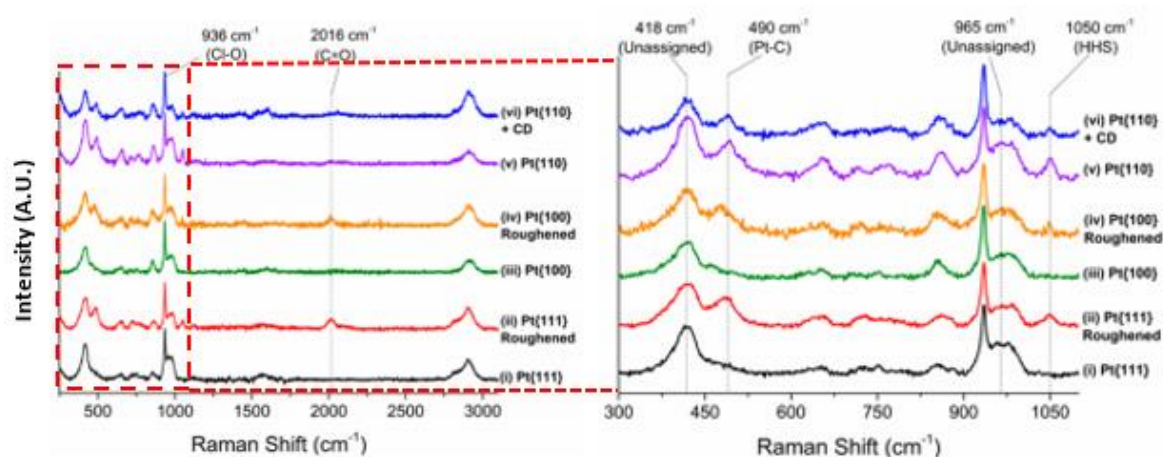


Figure 4.11: SHINER Spectra of Spectra of 0.1M EP in 0.1M HClO_4 at hydrogenation potentials on (i) Pristine Pt {111}, (ii) electrochemically roughened Pt {111}, (iii) Pristine Pt {100}, (iv) electrochemically roughened Pt {100}, (v) Pristine Pt {110}, (vi) Pt {110} with coadsorbed $2 \times 10^{-5}\text{M}$ CD. Reprinted from(50).

To gain further understanding of the new bands established on the Pt {111} spectra, the rest of the platinum basal planes underwent SHINERS analysis (Figure 4.11). The Pt {100} spectra exhibited almost identical features as the Pt {111} surface, with both the unidentified bands discovered on the Pt {111} surface present. This reinforces the belief that these bands are a result of an adsorption species of EP on the terrace sites. Contrary to previous literature concerning the Pt {100} surface no CO was present on the surface, this is surprising as the Pt {100} surface in the CV studies demonstrated significant CO stripping (Figure 4.6(b)). Upon roughening the {100} surface further proof was provided for the need of high index Pt sites to form the HHS and participate in the decarbonylation reaction to produce adsorbed CO.

On the Pt {110} single crystal both the “Terrace intermediate” and the HHS co-exist on the surface with all four of the bands present in the spectrum. This result was obtained without any electrochemical roughening, suggesting the {110} surface is innately defected in these experiments. The true nature of the Pt {110} surface is an area of contention; the stability of surface and hence possible surface reconstruction is an issue that is challenging to monitor. It has been acknowledged in literature that the {110} (1x1) surface can reconstruct into a “missing row” (2x1) structure(66, 67). The preparation of the platinum single crystal is imperative in dictating the structure of the surface, Markovic *et al* used surface XRD to demonstrate either (1x1) or (1x2) arrangements can form when cooling (in 3%H₂ in Ar) by altering at what temperature quenching begins(68). More recent work by Rodriguez *et al* presented data showing both the (1x1) and (1x2) structures coexisting to different extents on the Pt {110}(69), which agrees with data from Attard *et al*(66). Considering the preparation conditions used in the current study a combination of (1x1) and (1x2) surface structures would be most likely. This agrees with both the terrace intermediate and the HHS being present on the {110} surface. Upon co-adsorption with CD the peaks related to the HHS and adsorbed CO are attenuated, most likely due to the displacement of the two species.

4.2.3 SHINERS Investigation of EP Hydrogenation on High Index Pt Surfaces

Each of the three basal planes exhibited an unknown adsorption state, which has been attributed to an adsorption mode of EP on platinum terrace sites. This has not been demonstrated on the polycrystalline Au@Pt surface. Higher index platinum single crystal surfaces were analysed to gain further understanding of the “Terrace intermediate” and to what extent it can form with diminished terrace sites in comparison to the basal planes. The three high index planes selected were: Pt {321} S, Pt {721} S and Pt {531} S. Structures of each of the surfaces are demonstrated in Figure 4.12.

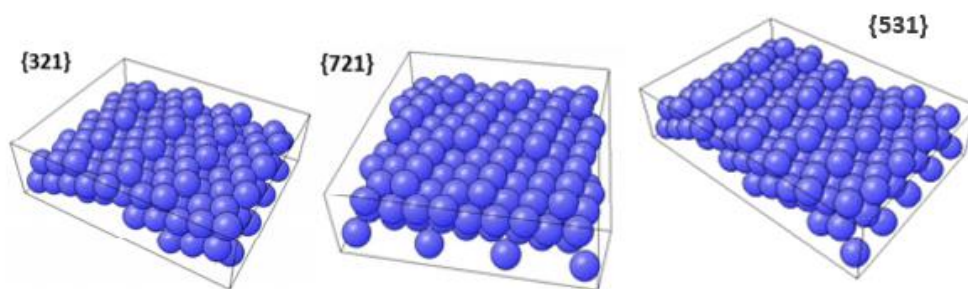


Figure 4.12: Atomic model depictions of the high index Pt surfaces used in this investigation (generated in BALSAC Surface Explorer)

Each of the high index surfaces analysed contain steps, kinks and differing amounts of {111} and {100} terrace, there is a chirality associated to the surface (all S configuration) due to the arrangement of the terrace, step and kink site. Probing how the kink sites and differing terrace lengths will impact the previously established adsorption intermediates.

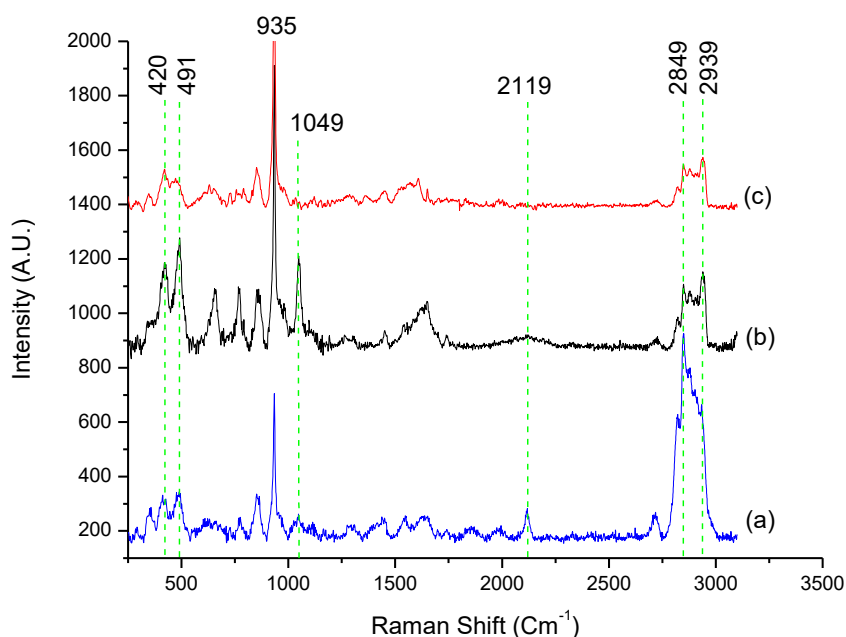


Figure 4.13: SHINER Spectra of 0.1M EP in 0.1M HClO₄ at hydrogenation potentials on (a) Pristine Pt {321}, (b) Pristine Pt {721}, (c) Pt {721} with coadsorbed 2x10⁻⁵M CD.

Comparison of the adsorption of EP on the Pt {321} and {721} surfaces (Figure 4.13) has shown some subtle differences and similarities. The surfaces have short 3 atom wide terraces, with the {321} surface based on a {111} terrace and {721} surface based on a {100} surface. Both surfaces contain {111} x {100} step sites and a short {110} step of a kink site.

Both surfaces have the bands associated with the “terrace intermediate” identified on the Pt basal plane analysis (420 and 965 cm^{-1}) present, but to a more diminished extent than those displayed on the {111} and {100} surfaces. A dominant feature on the {721} surface is that corresponding to the HHS of EP with a sharp peak at 1050 and 420 cm^{-1} , this was expected with density of high index sites on the surface. Surprisingly, there is minimal presence of the HHS on the {321} surface. This may suggest that the combination of a long {111} step adjacent to a {100} terrace can stabilize the HHS either through increasing the rate of formation or suppressing the subsequent hydrogen transfer(50). Both surfaces resemble the characteristics of the {110}, but lack the band associated with adsorbed CO, instead a band is present at $\sim 2100 \text{ cm}^{-1}$ which could be attributed to adsorbed hydrogen, but is uncharacteristically intense for the {321}. This could link into the lack of HHS present of the surface, due to an abundance of coadsorbed hydrogen, another explanation is that the silica shell of the SHINERS particles had broken down and this band is due to an Si-H stretch(70). Usually the degradation of the silica shell is accompanied by very sharp intense peaks as a result of adsorbates onto the gold core, these are not present in these spectra discrediting the shell degradation explanation. From the comparison of the {321} and {721} surfaces it is demonstrated that subtle alterations to the platinum surface can significantly alter the adsorption of ethyl pyruvate. The density of kink sites on the platinum surface has been shown to have an impact on reactions, for example the enantioselectivity of glucose oxidation(71, 72). The Pt {531} surface is based on a {111} terrace like the {321} surface, but has shorter terrace length and a higher kink density. The spectra for the Pt {531} demonstrated some interesting behaviour of EP on the surface (figure 4.14). Intense bands of the “terrace intermediate” dominate the pristine Pt {531} spectrum, this result was unexpected for a high index surface with such short terraces. It may be possible that the step sites are bridged by the adsorption stage, giving similar adsorption behaviour of a flat terrace. This has been reported for alanine adsorption on Pt {531}, although this involves bonding to two kink sites each side of the terrace(73). It is conceivable that on the {531} surface that EP will adsorb onto the low-coordination and highly reactive kink sites and manage to maintain a configuration similar to that on terrace sites. Roughening the {531} surface attenuates the peaks at 418 and $\sim 970 \text{ cm}^{-1}$ and gives rise to peaks at 1050 and 488 cm^{-1} , similar to the {111} and {100} surfaces, constituting the disruption of the “terrace intermediate” and promotion of the HHS. The comparison of data from the high index

platinum surfaces and the low index surfaces, shows the adsorption of EP is complex and the surface can have an integral role in this.

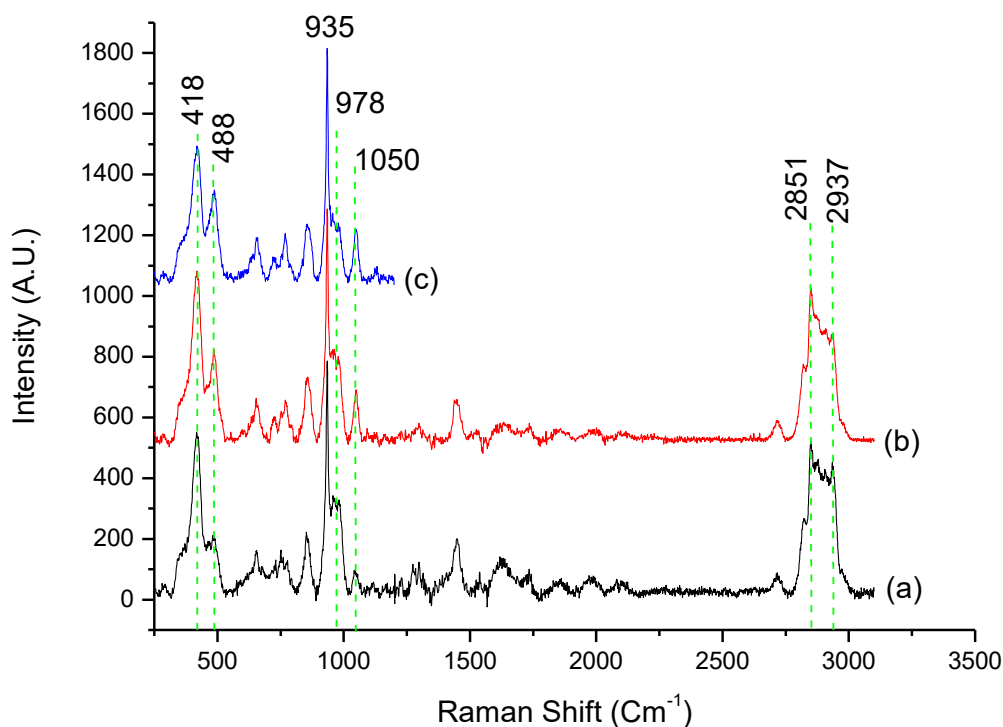


Figure 4.14: SHINER Spectra of 0.1M EP in 0.1M HClO₄ at hydrogenation potentials on (a) Pristine Pt {531}, (b) Roughened Pt {531} 50 cycles, (c) further roughened Pt {531} 100 cycles.

Knowledge of the HHS intermediate of EP has been alluded to previously and has been found to be stable at hydrogen evolution potentials(41). This study has reinforced the requirement of defect sites as well as possibly terrace sites for the formation of the HHS under hydrogenation conditions. This is a significant development for the understanding of the structure sensitivity of the reaction, but in order to further understand this relationship the bands at ~ 420 and 970 cm^{-1} needs to be assigned. These bands have been present to varying degrees on all the single crystal surfaces presented, but absent on polycrystalline platinum nanoparticle surfaces. These bands are the most intense on the {111} and {100} surfaces, suggesting these bands have some degree of association with terrace sites.

Numerous possible assignments were explored for the two bands, with the viabilities of each explored. The first logical explanation is that the Au@SiO₂ nanoparticles used for

SHINERS has some associated contaminants that give rise to these new bands, which would explain this new feature for the SHINERS spectra as opposed to SERS spectra, but SHINERS spectra in the absence of EP does not show the two bands and yields a predominately featureless spectrum. Another possible explanation for the 418 cm^{-1} band is a red-shifted Pt-C stretch from a multi-coordinated CO, but the corresponding stretch at $1750 - 1800\text{ cm}^{-1}$ is absent from the $\{111\}$ and $\{100\}$ spectra, which discredits this explanation. It was proposed that the 965 cm^{-1} band could be attributed to the vinyl carbon of the enolic form of EP, presented by McBreen *et al* for MP(44). HREELS data presented by the same group can correlate the 418 cm^{-1} and 965 cm^{-1} bands with those of the enol(64). While in-keeping with the band position, the presence of the enol is not a viable explanation as it has been demonstrated to be unstable in the presence of hydrogen, even at low coverages(44). To further disparage the link between the 418 cm^{-1} and 965 cm^{-1} bands and the presence of an enol on the platinum surface, Ethyl Acrylate (an analogue of the keto-enol tautomer) was analysed on the Pt $\{111\}$ surface with the presence and absence of hydrogen (figure 4.15). Neither of the bands were identified in the spectra and a significant sharp peak at 1580 cm^{-1} attributed to C=C stretch was present for the enol analogue, but absent in any EP related spectra (Figure 4.13). Another possible interpretation is that EP adsorbs with full charge transfer from the keto C=O to the metal, accompanied by hydrogen atom transfer to the carbon of the keto carbonyl. The resulting alkoxide species could exhibit a Pt-O stretch at 418 cm^{-1} and an alkoxide C-O stretch at 965 cm^{-1} (50). This adsorption mechanism is unlikely to occur as DFT calculations presented by Hammer and co-workers demonstrated a comparatively high activation barrier for the addition of hydrogen to the carbon as opposed to the oxygen of the keto carbonyl(74).

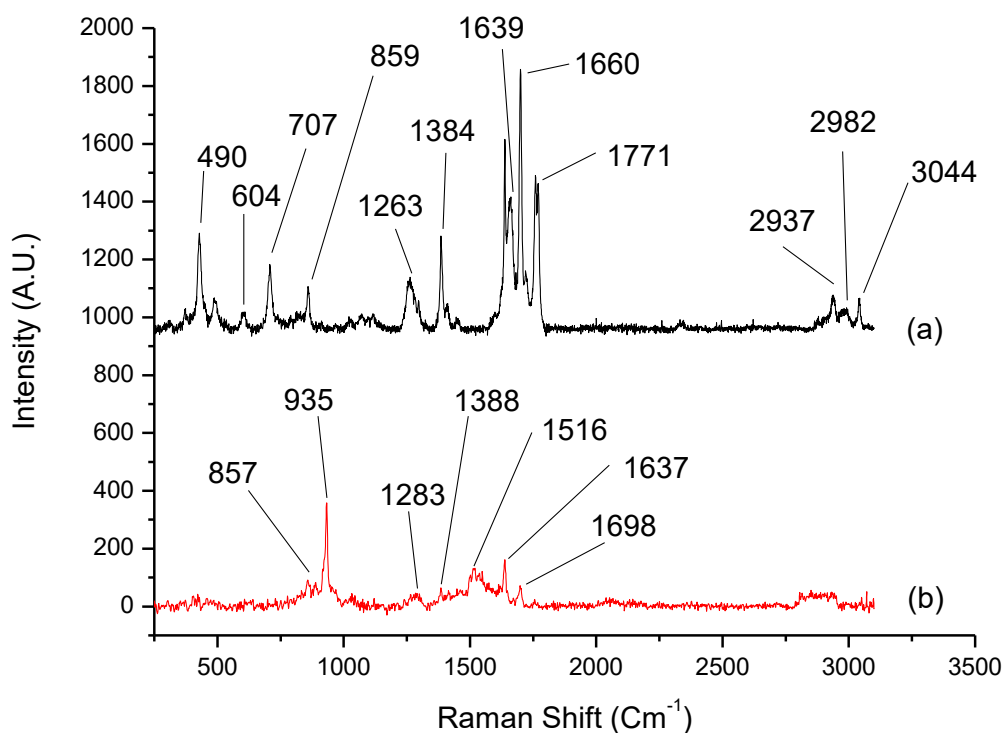


Figure 4.15: SHINERS Spectra of Bulk Ethyl Acrylate (a) and 0.1M EA in 0.1M HClO₄ at hydrogenation potentials

4.2.4 DFT Modelling and Calculations of EP Adsorption on Terrace and Step Sites

Given the lack of a plausible assignment of the 419 cm⁻¹ and 960 cm⁻¹ bands in previous literature, this study proposes that these bands are a result of a previously unreported adsorption intermediate. Both peaks are intense on basal platinum surfaces, but on the high index surfaces or through the introduction of defects by roughening became attenuated, which would relate to an adsorbed species of EP with a strong association with terrace sites. In order to suggest the adsorption mode of the intermediate, previously proposed adsorption modes of EP need to be considered. Three popular configurations have been suggested in literature, which include $\eta^1(\text{O})$ (end-on, *via* the keto O), $\eta^2(\text{C},\text{O})$ (horizontal *via* the keto C and O) and enediolate (upright, *via* keto and ester carbonyl O) configurations(21, 23, 48, 75). Due to the instability of the of the enediolate at room temperatures in the absence of the chiral modifier and the absence of a C=O stretch at ~ 1740 cm⁻¹ it will be excluded from consideration(23, 75). Baiker *et al* has presented DFT modelling data that

validates the feasibility of both the $\eta^1(\text{O})$ and $\eta^2(\text{C},\text{O})$ binding modes of EP and further stating that the $\eta^2(\text{C},\text{O})$ state of EP is preferred in the presence of coadsorbed hydrogen(48). The $\eta^2(\text{C},\text{O})$ adsorption state would orientate the carbonyl group horizontal to the surface, which with selection rules would render the stretch silent, in-keeping with the spectra presented in this study. Also, it has been suggested by previous work that upon $\eta^2(\text{C},\text{O})$ adsorption the C=O bond is significantly rehybridized(22, 48), favouring di- σ bonding which has a sensitivity towards the long range order of the surface. Through collaborative work in this study the proposed notation by Willock *et al* is adopted(76), as the $\eta^2(\text{C},\text{O})$ state binds across two platinum atoms it is referred to as a $\mu_2(\text{C},\text{O})$ state.

The assignment of the unknown spectral bands was explored through DFT modelling of both the $\eta^1(\text{O})$ and $\mu_2(\text{C},\text{O})$ states of EP adsorption. The adsorption energies of both configurations were calculated for the $\eta^1(\text{O})$ (- 17 kJ mol⁻¹) and $\mu_2(\text{C},\text{O})$ (- 59.3 kJ mol⁻¹) states on the Pt {111} surface, the stability of the $\mu_2(\text{C},\text{O})$ over the $\eta^1(\text{O})$ mode is in stark contrast to equivalent calculations carried out with acetone(76). The unrivalled stability of the $\mu_2(\text{C},\text{O})$ adsorption mode made it a plausible candidate for the unknown spectral bands, so further calculations were carried out on this binding mode on the Pt {111} and Pt (77) surfaces, to observe the impact of long range order and defects on the adsorbate (Figure 4.16).

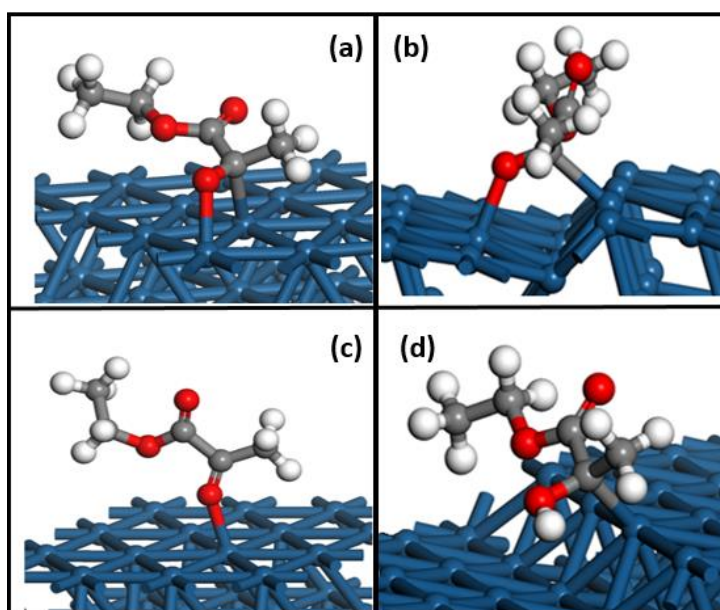


Figure 4.16: Calculated structure of (a) EP adsorbed in $\mu_2(\text{C},\text{O})$ configuration on Pt {111}, (b) EP adsorbed in $\mu_2(\text{C},\text{O})$ configuration on Pt {221}, (c) EP adsorbed in $\eta^1(\text{O})$ configuration on Pt {111} and (d) HHS on Pt {221}.

The simulations managed to attribute the band at 965 cm^{-1} to a methyl rocking mode of the $\mu_2(\text{C,O})$ - bound EP adsorbate, with the calculated band wavenumber at 971 cm^{-1} in close agreement with the previously unassigned band. The assignment of the 418 cm^{-1} band was more of a challenge as parity between calculated bands was more ambiguous as well as numerous skeletal stretching bands appearing in the region to further complicate things. The DFT modelling proposed a band at 462 cm^{-1} on Pt {111} and 456 cm^{-1} on Pt {221}, which was attributed to a Pt-O stretch. While there is some ambiguity associated with the $\sim 40\text{ cm}^{-1}$ difference between the experimental and simulated bands, it can be rationalised as oversights in the DFT model with regards to solvent effects, coadsorbed hydrogen and complexities in the plasmon enhancement related to the SHINERS technique. The role of coadsorbed hydrogen in this proposed mechanism is a significant one, as hydrogen transfer to the oxygen will form the HHS. This leads to the assumption that Pt-H --- O=C interactions will occur and may be a precursor to the hydrogenation of the carbonyl, these interactions could feasibly be strong enough to redshift the predicted Pt-O stretching frequency. A similar scenario was presented by McBreen *et al* in which an interaction occurred between the carbonyl of MP and methyl group of a coadsorbed aromatic on the Pt {111} surface(43).

The $\mu_2(\text{C,O})$ - bound EP adsorbate was further investigated under differing electrode potentials on the Pt {111} surface. As shown in figure 4.17, the hydrogen evolution potential of -100 mV gives rise to the previously discussed bands at 416 and 965 cm^{-1} . A positive potential increase to 0 V produces a slight increase in the intensity of both bands, a contrast to the HHS, which is mostly depleted at potentials above hydrogen evolution potentials(78). The increase in potential may be attributed to a reorientation of the $\mu_2(\text{C,O})$ state towards the platinum surface, or a decrease in the hydrogenative desorption of the intermediate at the increased potential. Incremental increase in potential above 0 V displays significant attenuation of both peaks, despite a reduction in the surface hydrogen coverage, which should allow a coverage increase for the $\mu_2(\text{C,O})$ adsorbate. The decarbonylation reaction could play a role in occupying the platinum surface with CO, but this is unlikely with lack of a CO related peak in the spectra. The most feasible explanation is that the orientation of the adsorbate alters with the changing potentials, becoming less SERS active at more anodic potentials. This proposal is supporting by the slight shift of the 965 cm^{-1} band to higher wavenumbers, which is consistent with the adsorbate orientation causing frequency

dampening, also DFT modelling demonstrates that the methyl rocking mode can be hindered with close proximity to the surface. Baiker *et al* also commented on the EP molecule changing orientation to the surface under certain conditions(22).

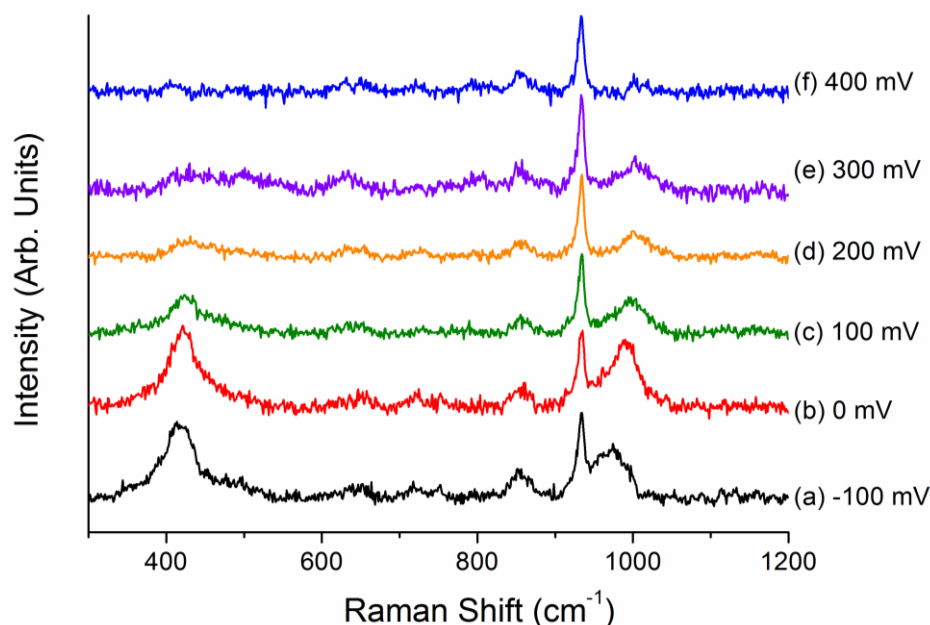


Figure 4.17: SHINERS spectra of 0.1 EP adsorption in 0.1 M HClO₄ on Pt{111} at different potentials: (a) -100 mV, (b) 0 mV, (c) 100 mV, (d) 200 mV, (e) 300, and (f) 400 mV vs. Pd/H. reprinted from (50)

It is important to analyse the structure dependencies of both the HHS and $\mu_2(\text{C},\text{O})$ intermediates, as the two states have been shown to coexist on the platinum surfaces to varying degrees with the SHINERS data. The $\mu_2(\text{C},\text{O})$ state appears to thrive on the long range order of terrace dominant surfaces like the Pt {111} and {100} surfaces, whereas the HHS requires defect sites to form. DFT calculations for the adsorption energies of the $\mu_2(\text{C},\text{O})$ and HHS intermediates of EP and Ethyl Lactate on the Pt {111} terrace sites and the Pt {221} step site supports this. While we cannot link the $\mu_2(\text{C},\text{O})$ bound state of EP as a direct precursor to the HHS, without further significant reaction simulations. A proposed reaction mechanism in which the $\mu_2(\text{C},\text{O})$ adsorbate undergoes rehybridization and elongation of the carbonyl bond, followed by hydrogen transfer to form the HHS and subsequent hydrogen transfer to form the EL product, a plausible mechanism which has been proposed for other activated ketones(79).

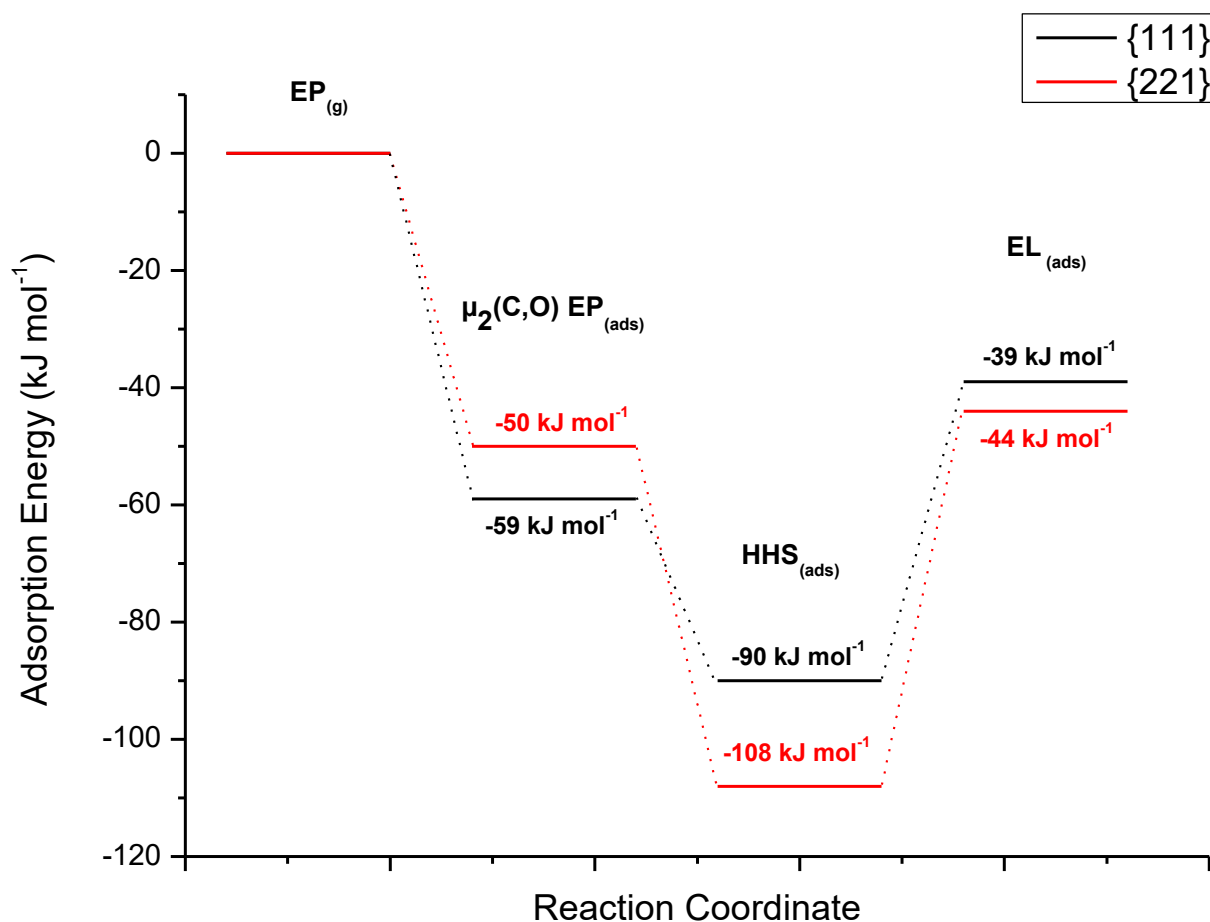


Figure 4.18: Reaction Schematic for EP Hydrogenation on the Pt {111} and Pt {221} surfaces, based upon calculated adsorption energies.

The calculated adsorption energies demonstrate interesting trends of the involved reaction intermediates and the difference between the binding energies of each adsorbate on the two surfaces, 9 kJ mol^{-1} for the $\mu_2(\text{C,O})$ bound state and 18 kJ mol^{-1} for the HHS respectively, which mirrors the SHINERS data presented. The increased stability of the HHS on the {221} surface over the {111} is consistent with the dominance of the HHS on the high index and roughened platinum surfaces. However, the superior stability of the HHS on both surfaces over the $\mu_2(\text{C,O})$ state means the HHS should be dominate on both surfaces, in spite of the increased stability of the $\mu_2(\text{C,O})$ adsorbate on the {111} over the {221} surface. So, a rational explanation for the absence of the HHS on the Pt {111} and {100} surfaces would be approached from a kinetic viewpoint. Hydrogenative desorption of EP has been demonstrated to occur significantly on the {111} surface by CV analysis. To substantiate the SHINERS data the kinetics of the first hydrogen transfer to allow transition from the $\mu_2(\text{C,O})$ species to the HHS must be slow, compared to the rapid subsequent hydrogen transfer to

yield the EL product. This is supported by kinetic studies by Blaser and co-workers, who determined the first hydrogen transfer to be rate determining(40). This means the HHS cannot form a detectable surface coverage, before being hydrogenated and desorbed due to the weak van der Waals forces between EL and the surface, allowing the $\mu_2(\text{C},\text{O})$ species to accumulate on the surface. It is proposed that the kinetics differ on defect sites and either the rate of the first hydrogen transfer is increased or the rate of the second hydrogen transfer is slowed, to allow the accumulation of the HHS state.

4.3 Discussion

EP adsorption on platinum surfaces under racemic conditions has displayed structure sensitive tendencies, which has a profound effect on the hydrogenation reaction. The promotion of a stable HHS on defective surfaces can impact on the reactions kinetics as a catalytic poison as proposed in previous studies(41). The long-lived HHS intermediate and subsequent lack of surface hydrogen coverage can lead to the decarbonylation side reaction, which can be signified by the increased coverage of CO with high amounts of the HHS or upon the introduction of defects observed in the Raman spectra. The absence of any evidence of adsorbed CO in both the electrochemical and spectroscopic analysis of the pristine Pt {111} surface, reinforces that the HHS intermediate is short lived on that particular surface. Unlike the {111} surface the {100} surface does display a CO stripping peak at anodic potentials on the CV, but does not display any adsorbed CO in the spectroscopic data. The Pt {100} surface is clearing generating CO, but must be efficient in removing CO from the surface under hydrogenating conditions, until the introduction of defects disrupts this from occurring. It is difficult to equate without performing catalytic testing on the single crystal surfaces if the absence of the HHS state on {111} and {100} surfaces will lead to an enhanced hydrogenation rate over surfaces with defects. Chirally modified surfaces exhibit competitive adsorption, hence peaks related to CO, $\mu_2(\text{C},\text{O})$ and HHS adsorbates are attenuated in the presence of the modifier. Similar traits were presented on studies with polycrystalline surfaces(41), but the impact this has on the enantioselectivity and rate of the reaction is still up for debate(51). Nevertheless, this study proposes that the differences in intermediates on terrace and defect sites can play an important role. In terms of enantioselectivity, orientation and induction of

chirality must occur before the HHS is formed, as the orientation is fixed through the Pt-C bond to the surface. A similar instance is recognised for the $\mu_2(\text{C},\text{O})$ -bound state of EP, by bonding to the surface forms its chiral centre, therefore enantiomeric induction needs to occur before the surface species forms. Unlike the HHS, this is weakly bound to the surface and can facilitate a dynamic equilibrium between (chiral) $\mu_2(\text{C},\text{O})$ bound and (pro-chiral) liquid phase EP. This allows reversible conversion between the two enantiomers, with the {111} and {100} surfaces allowing a longer lived $\mu_2(\text{C},\text{O})$ intermediate. This forms the basis for the proposal that the terrace sites would be best suited to achieve a high degree of enantiodifferentiation, as those sites favour the most stable docking complex between EP and the alkaloid modifier. When comparing the bands on the Raman spectra of the {100} and {111} normalised relative to the perchlorate band, the {111} surface has the most intense bands relating to the $\mu_2(\text{C},\text{O})$ intermediate, suggesting the {111} surface has the longest living intermediate and would yield the highest enantiomeric excess upon chiral modification. This is consistent with a study from Baiker *et al*, which presented data for a higher enantiomeric excess and rate on shape controlled particles with {111} surfaces dominant, than nanoparticles with predominantly {100} surfaces(12). The explanation provided by Baiker for the inherent rate and enantioselectivity differences was due to the differing adsorption energies of CD on the various facets, however, this study proposes this data could be impacted by the lifetime of the intermediates on the particular surfaces. Attard *et al* alluded to a contrasting view by demonstrating a decrease in enantiomeric excess when defect sites are blocked by the adsorption of Bismuth(54). To satisfy both these diverging interpretations of the enantiodifferentiation mechanism, this study suggests that terraces are required for the adsorption of CD and the correctly orientated η^2 species of EP to favour high *ee*. An alternative chiral environment can be created by the quinuclidine substituent overhanging defect sites, possibly with greater chiral discrimination. A point of note is that the methyl group of the η^2 state has slightly different orientations relative to the terrace and defect sites (figure 14), which may assist in forming a chiral pocket. Such a centre would be diastereomeric in nature since defect sites such as kinks may be chiral and combined with the quinuclidine of CD would give rise to two chemically distinct docking positions for EP, namely +/+ and +/- where + signifies the handedness of CD and + or – the chirality of the kink site(50). This model would suggest that both terraces and defects are required for the highest levels of enantioselectivity.

4.4 Conclusion

The SHINERS technique has expanded the viable substrates for SERS investigations, with single crystal surfaces now suitable platforms to probe. The technique has been used to great success on the Orito reaction, in identifying a newly proposed surface site specific adsorption intermediate of EP. The η^2 intermediate species of EP was found to form on sites of long-range order, also known as terrace sites. It is unclear if this species is involved in the surface mechanisms that govern enantiodiffraction or reaction rate, but it has been proposed that the orientation of the η^2 adsorbate could be beneficial to enantiomeric excess.

4.5 References

1. A. Baiker, Progress in asymmetric heterogeneous catalysis: Design of novel chirally modified platinum metal catalysts. *Journal of Molecular Catalysis A: Chemical* **115**, 473-493 (1997).
2. T. Bürgi, A. Baiker, Heterogeneous enantioselective hydrogenation over cinchona alkaloid modified platinum: mechanistic insights into a complex reaction. *Accounts of chemical research* **37**, 909-917 (2004).
3. O. Schwalm, B. Minder, J. Weber, A. Baiker, Enantioselective hydrogenation of α -ketoesters over Pt/alumina modified with cinchonidine: theoretical investigation of the substrate-modifier interaction. *Catalysis letters* **23**, 271-279 (1994).
4. K. Simons *et al.*, A model for the enantioselective hydrogenation of pyruvate catalysed by alkaloid-modified platinum. *Recueil des Travaux Chimiques des Pays-Bas* **113**, 465-474 (1994).
5. S. Lavoie, M.-A. Laliberté, I. Temprano, P. H. McBreen, A Generalized Two-Point H-Bonding Model for Catalytic Stereoselective Hydrogenation of Activated Ketones on Chirally Modified Platinum. *Journal of the American Chemical Society* **128**, 7588-7593 (2006).
6. H. Blaser, H. Jalett, D. Monti, A. Baiker, J. Wehrli, Enantioselective hydrogenation of ethyl pyruvate: effect of catalyst and modifier structure. *Studies in Surface Science and Catalysis* **67**, 147-155 (1991).
7. Y. Orito, S. Imai, S. Niwa, ASYMMETRIC HYDROGENATION OF METHYL PYRUVATE USING PT-C CATALYST MODIFIED WITH CINCHONIDINE. *Nippon Kagaku Kaishi*, 1118-1120 (1979).
8. C. LeBlond, J. Wang, J. Liu, A. Andrews, Y.-K. Sun, Highly enantioselective heterogeneously catalyzed hydrogenation of α -ketoesters under mild conditions. *Journal of the American Chemical Society* **121**, 4920-4921 (1999).
9. H. Blaser, H. Jalett, J. Wiehl, Enantioselective hydrogenation of α -ketoesters with cinchona-modified platinum catalysts: Effect of acidic and basic solvents and additives. *Journal of molecular catalysis* **68**, 215-222 (1991).
10. K. Balázsik, M. Bartók, New data on enantiomeric excess versus conversion during enantioselective hydrogenation of activated ketones on a platinum catalyst. *Journal of Catalysis* **224**, 463-472 (2004).

11. D. RUIZ, P. Reyes, ENANTIOSELECTIVE HYDROGENATION OF ETHYL PYRUVATE IN FLOW REACTOR OVER Pt-CD/SiO₂ CATALYSTS. *Journal of the Chilean Chemical Society* **53**, 1740-1742 (2008).
12. E. Schmidt, A. Vargas, T. Mallat, A. Baiker, Shape-selective enantioselective hydrogenation on Pt nanoparticles. *Journal of the American Chemical Society* **131**, 12358-12367 (2009).
13. Z. Ma, F. Zaera, Role of the solvent in the adsorption–desorption equilibrium of cinchona alkaloids between solution and a platinum surface: correlations among solvent polarity, cinchona solubility, and catalytic performance. *The Journal of Physical Chemistry B* **109**, 406-414 (2005).
14. X. Li, R. P. Wells, P. B. Wells, G. J. Hutchings, Premodification of Pt/ γ -Al₂O₃ with Cinchonidine for the Enantioselective Hydrogenation of Ethyl Pyruvate: Effect of Premodification Conditions on Reaction Rate and Enantioselection. *Catalysis letters* **89**, 163-167 (2003).
15. A. Vargas, T. Bürgi, A. Baiker, Model of Reactant–Modifier Interaction in Enantioselective Hydrogenation of Ethyl Pyruvate on Platinum–Cinchona Catalysts: Extension to Synthetic Chiral Modifiers. *Journal of Catalysis* **197**, 378-384 (2001).
16. H. Blaser, M. Garland, H. Jallet, Enantioselective hydrogenation of ethyl pyruvate: kinetic modeling of the modification of Pt catalysts by cinchona alkaloids. *Journal of Catalysis* **144**, 569-578 (1993).
17. G. Attard, K. Griffin, D. Jenkins, P. Johnston, P. Wells, Enantioselective hydrogenation of ethyl pyruvate catalysed by Pt/graphite: Superior performance of sintered metal particles. *Catalysis today* **114**, 346-352 (2006).
18. B. Török, K. Felföldi, G. Szakonyi, K. Balázsik, M. Bartók, Enantiodifferentiation in asymmetric sonochemical hydrogenations. *Catalysis letters* **52**, 81-84 (1998).
19. T. Mallat, S. Frauchiger, P. Kooyman, M. Schürch, A. Baiker, Restructuring during pretreatment of platinum/alumina for enantioselective hydrogenation. *Catalysis letters* **63**, 121-126 (1999).
20. D. J. Jenkins *et al.*, Enantioselectivity and catalyst morphology: step and terrace site contributions to rate and enantiomeric excess in Pt-catalysed ethyl pyruvate hydrogenation. *Journal of Catalysis* **234**, 230-239 (2005).
21. T. Bürgi, F. Atamny, R. Schlögl, A. Baiker, Adsorption of Ethyl Pyruvate on Pt(111) Studied by XPS and UPS. *The Journal of Physical Chemistry B* **104**, 5953-5960 (2000).
22. T. Bürgi *et al.*, Adsorption mode of ethyl pyruvate on platinum: An in situ XANES study. *Catalysis letters* **66**, 109-112 (2000).
23. S. Lavoie, M.-A. Laliberté, P. McBreen, Adsorption States and Modifier–Substrate Interactions on Pt (111) Relevant to the Enantioselective Hydrogenation of Alkyl Pyruvates in the Orito Reaction. *Journal of the American Chemical Society* **125**, 15756-15757 (2003).
24. R. J. Taylor, *Study on the surface adsorbates of an enantioselective, heterogeneously catalysed, hydrogenation reaction*. (Cardiff University (United Kingdom), 2010).
25. I. Sutherland, A. Ibbotson, R. Moyes, P. Wells, Enantioselective hydrogenation I. Surface conditions during methyl pyruvate hydrogenation catalyzed by cinchonidine-modified platinum/silica (EUROPT-1). *Journal of Catalysis* **125**, 77-88 (1990).
26. J. L. Margitfalvi, M. Hegedüs, E. Tfirst, Enantioselective hydrogenation of α -keto esters over cinchona-PtAl₂O₃ catalyst. Kinetic evidence for the substrate-modifier interaction in the liquid phase. *Tetrahedron: Asymmetry* **7**, 571-580 (1996).
27. M. Bartók, B. Török, K. Balázsik, T. Bartók, Heterogeneous asymmetric reactions. 23. Enantioselective hydrogenation of ethyl pyruvate over cinchonine- and α -isocinchonine-modified platinum catalysts. *Catalysis letters* **73**, 127-131 (2001).
28. A. Baiker, Transition state analogues—a guide for the rational design of enantioselective heterogeneous hydrogenation catalysts. *Journal of Molecular Catalysis A: Chemical* **163**, 205-220 (2000).

29. J. M. Bonello, F. J. Williams, A. K. Santra, R. M. Lambert, Fundamental aspects of enantioselective heterogeneous catalysis: the surface chemistry of methyl pyruvate on Pt {111}. *The Journal of Physical Chemistry B* **104**, 9696-9703 (2000).
30. J. Bonello *et al.*, Fundamental aspects of enantioselective heterogeneous catalysis: a NEXAFS study of methyl pyruvate and (S)-(-)-1-(1-naphthyl) ethylamine on Pt {111}. *Surface science* **482**, 207-214 (2001).
31. D. Ferri, T. Bürgi, A. Baiker, The Fate of Ethyl Pyruvate during Adsorption on Platinum Chirally Modified by Cinchonidine Studied by ATR- IR Spectroscopy. *The Journal of Physical Chemistry B* **108**, 14384-14391 (2004).
32. E. N. Jacobsen, I. Marko, W. S. Mungall, G. Schroeder, K. B. Sharpless, Asymmetric dihydroxylation via ligand-accelerated catalysis. *Journal of the American Chemical Society* **110**, 1968-1970 (1988).
33. M. Garland, H. U. Blaser, A heterogeneous ligand-accelerated reaction: enantioselective hydrogenation of ethyl pyruvate catalyzed by cinchona-modified platinum/aluminum oxide catalysts. *Journal of the American Chemical Society* **112**, 7048-7050 (1990).
34. H.-U. Blaser, M. Studer, Cinchona-modified platinum catalysts: from ligand acceleration to technical processes. *Accounts of chemical research* **40**, 1348-1356 (2007).
35. E. Toukoniitty, D. Y. Murzin, Origin of ligand acceleration in heterogeneous ethyl pyruvate hydrogenation. *Journal of Catalysis* **241**, 96-102 (2006).
36. M. Sutyinszki, K. Szöri, K. Felföldi, M. Bartók, 98% Enantioselectivity in the asymmetric synthesis of a useful chiral building block by heterogeneous method: Enantioselective hydrogenation of ethyl-benzoylformate over cinchona modified Pt/Al₂O₃ catalysts in the acetic acid. *Catalysis Communications* **3**, 125-127 (2002).
37. J. Kubota, F. Zaera, Adsorption geometry of modifiers as key in imparting chirality to platinum catalysts. *Journal of the American Chemical Society* **123**, 11115-11116 (2001).
38. G. Bond, P. Meheux, A. Ibbotson, P. Wells, Origin of enhanced rate in the platinum-catalysed enantioselective hydrogenation of methyl pyruvate. *Catalysis Today* **10**, 371-378 (1991).
39. N. V. Rees *et al.*, In Situ Surface-Enhanced Raman Spectroscopic Studies and Electrochemical Reduction of α -Ketoesters and Self Condensation Products at Platinum Surfaces†. *The Journal of Physical Chemistry C* **115**, 1163-1170 (2010).
40. H.-U. Blaser *et al.*, Kinetic studies of the enantioselective hydrogenation of ethyl pyruvate catalyzed by a cinchona modified Pt/Al₂O₃ catalyst. *Journal of Catalysis* **173**, 282-294 (1998).
41. R. J. Taylor *et al.*, Enantioselective Hydrogenation of α -Ketoesters: An in Situ Surface-Enhanced Raman Spectroscopy (SERS) Study. *The Journal of Physical Chemistry C* **115**, 21363-21372 (2011).
42. F. Meemken, L. Rodríguez-García, Revealing Catalytically Relevant Surface Species by Kinetic Isotope Effect Spectroscopy: H-Bonding to Ester Carbonyl of trans-Ethyl Pyruvate Controls Enantioselectivity on a Cinchona-Modified Pt Catalyst. *The journal of physical chemistry letters* **9**, 996-1001 (2018).
43. S. Lavoie, P. H. McBreen, Evidence for C-H \cdots OC Bonding in Coadsorbed Aromatic-Carbonyl Systems on Pt (111). *The Journal of Physical Chemistry B* **109**, 11986-11990 (2005).
44. S. Lavoie, M.-A. Laliberté, G. Mahieu, V. Demers-Carpentier, P. McBreen, Keto-Enol Driven Assembly of Methyl Pyruvate on Pt(111). *Journal of the American Chemical Society* **129**, 11668-11669 (2007).
45. J. M. Bonello, R. M. Lambert, N. Künzle, A. Baiker, Platinum-catalyzed enantioselective hydrogenation of α -ketoesters: An unprecedented surface reaction of methyl pyruvate. *Journal of the American Chemical Society* **122**, 9864-9865 (2000).
46. A. Carley, M. Rajumon, M. Roberts, P. Wells, XPS and LEED studies of 10, 11-dihydrocinchonidine adsorption at Pt (111). Implications for the role of cinchona alkaloids in

- enantioselective hydrogenation. *Journal of the Chemical Society, Faraday Transactions* **91**, 2167-2172 (1995).
47. N. Bonalumi, T. Bürgi, A. Baiker, Interaction between ketopantolactone and chirally modified Pt investigated by attenuated total reflection IR concentration modulation spectroscopy. *Journal of the American Chemical Society* **125**, 13342-13343 (2003).
 48. A. Vargas, T. Bürgi, A. Baiker, Adsorption of cinchonidine on platinum: a DFT insight in the mechanism of enantioselective hydrogenation of activated ketones. *Journal of Catalysis* **226**, 69-82 (2004).
 49. J. F. Li *et al.*, Shell-isolated nanoparticle-enhanced Raman spectroscopy. *Nature* **464**, 392-395 (2010).
 50. S. Guan *et al.*, Structure Sensitivity in Catalytic Hydrogenation at Platinum Surfaces Measured by Shell-Isolated Nanoparticle Enhanced Raman Spectroscopy (SHINERS). *ACS Catalysis*, (2016).
 51. D. M. Meier, D. Ferri, T. Mallat, A. Baiker, Molecular insight into the dynamics of chiral modification of Pt/alumina. *Journal of Catalysis* **248**, 68-76 (2007).
 52. J. L. Margitfalvi, M. Hegedüs, E. Tfirst, in *Studies in Surface Science and Catalysis*. (Elsevier, 1996), vol. 101, pp. 241-250.
 53. M. Bartók, K. Felföldi, B. Török, T. Bartók, A new cinchona-modified platinum catalyst for the enantioselective hydrogenation of pyruvate: the structure of the 1: 1 alkaloid–reactant complex. *Chemical Communications*, 2605-2606 (1998).
 54. D. Jenkins *et al.*, Enantioselectivity and catalyst morphology: step and terrace site contributions to rate and enantiomeric excess in Pt-catalysed ethyl pyruvate hydrogenation. *Journal of Catalysis* **234**, 230-239 (2005).
 55. O. A. Hazzazi *et al.*, Electrochemical studies of irreversibly adsorbed ethyl pyruvate on Pt {hkl} and epitaxial Pd/Pt {hkl} adlayers. *Journal of Electroanalytical Chemistry* **640**, 8-16 (2010).
 56. J. Clavilier, D. Armand, S. Sun, M. Petit, Electrochemical adsorption behaviour of platinum stepped surfaces in sulphuric acid solutions. *Journal of electroanalytical chemistry and interfacial electrochemistry* **205**, 267-277 (1986).
 57. G. Socrates, *Infrared and Raman characteristic group frequencies: tables and charts*. (John Wiley & Sons, 2004).
 58. D. Ferri, T. Bürgi, An in situ attenuated total reflection infrared study of a chiral catalytic solid– liquid interface: Cinchonidine adsorption on Pt. *Journal of the American Chemical Society* **123**, 12074-12084 (2001).
 59. K. Tomikawa, H. Kanno, Raman study of sulfuric acid at low temperatures. *The Journal of Physical Chemistry A* **102**, 6082-6088 (1998).
 60. I. Busygin *et al.*, Interaction of cinchonidine and 1-phenyl-1, 2-propanedione on the surface of a chirally modified Pt/Al₂O₃ hydrogenation catalyst. *The Journal of Physical Chemistry C* **111**, 9374-9383 (2007).
 61. V. Demers-Carpentier *et al.*, Stereodirection of an α -Ketoester at Sub-molecular Sites on Chirally Modified Pt(111): Heterogeneous Asymmetric Catalysis. *Journal of the American Chemical Society* **135**, 9999-10002 (2013).
 62. S. Guan, Cardiff University, (2014).
 63. Y. Chen, Z. Tian, Dependence of surface enhanced Raman scattering of water on the hydrogen evolution reaction. *Chemical Physics Letters* **281**, 379-383 (1997).
 64. V. Demers-Carpentier, M.-A. Laliberté, S. p. Lavoie, G. Mahieu, P. H. McBreen, Two-Dimensional Self-Assembly and Catalytic Function: Conversion of Chiral Alcohols into Self-Assembled Enols on Pt(111)[†]. *The Journal of Physical Chemistry C* **114**, 7291-7298 (2009).
 65. C. Ratcliffe, D. Irish, Vibrational spectral studies of solutions at elevated temperatures and pressures. VI. Raman studies of perchloric acid. *Canadian journal of chemistry* **62**, 1134-1144 (1984).

66. G. A. Attard, A. Brew, Cyclic voltammetry and oxygen reduction activity of the Pt {110}-(1× 1) surface. *Journal of Electroanalytical Chemistry* **747**, 123-129 (2015).
67. P. Thostrup, E. K. Vestergaard, T. An, E. Lægsgaard, F. Besenbacher, CO-induced restructuring of Pt (110)-(1× 2): bridging the pressure gap with high-pressure scanning tunneling microscopy. *The Journal of chemical physics* **118**, 3724-3730 (2003).
68. N. Marković, B. Grgur, C. Lucas, P. Ross, Surface electrochemistry of CO on Pt (110)-(1× 2) and Pt (110)-(1× 1) surfaces. *Surface Science* **384**, L805-L814 (1997).
69. P. Rodríguez, G. García, E. Herrero, J. M. Feliu, M. T. Koper, Effect of the surface structure of Pt (100) and Pt (110) on the oxidation of carbon monoxide in alkaline solution: an FTIR and Electrochemical study. *Electrocatalysis* **2**, 242 (2011).
70. K. O. Bugaev, A. A. Zelenina, V. A. Volodin, Vibrational spectroscopy of chemical species in silicon and silicon-rich nitride thin films. *International Journal of Spectroscopy* **2012**, (2011).
71. G. A. Attard, C. Harris, E. Herrero, J. Feliu, The influence of anions and kink structure on the enantioselective electro-oxidation of glucose. *Faraday Discussions* **121**, 253-266 (2002).
72. G. A. Attard. (ACS Publications, 2001).
73. J.-H. Franke, D. Kosov, Chiral selectivity of amino acid adsorption on chiral surfaces—The case of alanine on Pt. *The Journal of chemical physics* **142**, 054708 (2015).
74. E. Rauls, B. Hammer, The Role of the Chiral Modifier on the Enantioselective Hydrogenation of Methyl Pyruvate on Pt(111). *Catalysis Letters* **106**, 111-114.
75. S. Lavoie, M.-A. Laliberté, P. McBreen, Coadsorption of methyl pyruvate and (±)-1-(1-naphthyl) ethylamine on Pt (111): insights on the mechanism for asymmetric hydrogenation. *Catalysis letters* **97**, 111-114 (2004).
76. E. L. Jeffery, R. K. Mann, G. J. Hutchings, S. H. Taylor, D. J. Willock, A density functional theory study of the adsorption of acetone to the (111) surface of Pt: Implications for hydrogenation catalysis. *Catalysis today* **105**, 85-92 (2005).
77. H. H. Voge, C. R. Adams, Catalytic oxidation of olefins. *Advances in Catalysis* **17**, 151-221 (1967).
78. N. V. Rees *et al.*, In Situ Surface-Enhanced Raman Spectroscopic Studies and Electrochemical Reduction of α -Ketoesters and Self Condensation Products at Platinum Surfaces †. *The Journal of Physical Chemistry C* **115**, 1163-1170 (2010).
79. A. Vargas, S. Reimann, S. Diezi, T. Mallat, A. Baiker, Adsorption modes of aromatic ketones on platinum and their reactivity towards hydrogenation. *Journal of Molecular Catalysis A: Chemical* **282**, 1-8 (2008).

Chapter 5 - Ethyl Pyruvate Hydrogenation on Shape Controlled Pt Nanoparticles

5.1 Literature Review

5.1.1 Shaped Platinum Nanoparticles

Despite the rapid progression of enantioselective catalysis there is a clear disconnect between the catalytic-synthetic approach to developing high performance enantioselective catalysts and the theoretical surface science approach of understanding the phenomena through idealised reaction conditions. Shape controlled nanoparticles have been proposed as a viable alternative to bridging this gap, due to significant work in developing the technique by MA El-Sayed(1-3), GA Somorjai(4-6) and J.M. Feliu(7-9). Which has led to various techniques to control the shape of the synthesised nanoparticles, such as: capping agents(10-12), halide addition(13), oxidative etching(14, 15), seed mediated growth(16) and templated growth(17). These methods have been used to produce an array of shaped nanoparticles, ranging from simple shapes like cubes(18) and triangles(19), to complex structures like cages(20) and nanowires(21). In-keeping with the narrative of this study, the development and application of shaped nanoparticles was aided immensely by advances in characterisation methods. While TEM can give a good representation of nanoparticle size ranges and shape, but orientation of the nanoparticle can complicate the analysis. CV can be utilised to yield key qualitative and quantitative data about the synthesised nanoparticles, by understanding the selective adsorption of Bi and Ge adatoms, the quantitative ratio of {100} and {111} sites can be determined(22). Qualitative information on the nanoparticle shape can be indicated with the H_{upd} region of the voltammogram, which demonstrates the ratio and cleanliness of the three basal planes(7). The presence of impurities on the surface of shape controlled nanoparticles is an often neglected issue in catalytic research, as residual capping agent from the synthesis can block active surface sites and skew catalytic testing data(23, 24). To alleviate this issue, cleaning techniques were required that were strong enough to remove the capping agents, but wouldn't disrupt the atomic arrangement on the nanoparticle surface(25). A relatively facile method was proposed by Feliu *et al*, which involved treating the nanoparticles with an aqueous alkaline solution(7).

With these stability and impurity issues associated with the shaped controlled nanoparticles, it would appear the presence of an in-situ characterisation technique during

catalytic testing is essential. Coupling a spectroscopic technique with CV would allow comprehensive characterisation of the catalytic reaction and the ability to monitor any alterations to the nanoparticle surface. In-situ infrared spectroscopy is a widely used surface analysis technique and in this capacity can provide a depth of information about surface structure(26), active sites(27) and reaction mechanisms(28). However, it can be difficult for IR spectroscopy to detect intermediates that produce signals in the low wavenumber region of the spectrum. This is not the case for Raman spectroscopy, which is important for identifying intermediate common intermediate species in catalysis such as: metal carbon bonds(29), active oxygen species(30), surface oxides(31) and hydroxyl groups(32). The stability and high surface sensitivity of the SHINERS technique establishes it as a promising characterisation method for utilisation in studies of catalytic nanoparticles(33).

The adsorption of Ethyl Pyruvate on platinum single crystals has been studied on platinum single crystal surfaces, through a spectroelectrochemical approach. The investigation predicated two structure sensitive adsorption states of EP and alluded to them playing a role in the enantiodifferentiation of EP during hydrogenation(34). Shape controlled nanoparticles have also been employed in this catalytic reaction. Baiker *et al* used platinum shapes of varying ratios of {111}/{100} sites and found the enantiomeric excess increased with the increased ration of {111}/{100} sites(35). The increased enantiodifferentiation was attributed to the higher stability of the modifier on the Pt {111} sites. Ruiz and co-workers noted an increase in enantioselectivity and activity when small Pt nanoparticles were utilised in EP hydrogenation(36). Reporting 1.7 nm diameter nanoparticles to have the best enantiomeric excess (34%), this contradicts another study by Baiker *et al*, which reported enantioselectivity increased with particle size to a maximum of 80% with nanoparticles of 3-4 nm diameter(37). The contrasting results of the investigations may be contributed to the use of different catalyst supports, as the adsorptive properties of the support may result in a competition for modifier molecules between metal sites and the support surface(38). It is also worth noting that residual capping agent on the nanoparticles can have suppressive effects on both the reaction rate and ee(39).

The size and surface structure of a nanoparticle have an intricate relationship, with defect sites being more of a presence on the smaller nanoparticles(2, 40). A study by Attard *et al* added further debate to this area of research, by probing the influence of defect and terrace

sites on the enantioselectivity(41). The investigation established that blocking terrace sites with sulphur adatoms increased enantiomeric excess, but lowered activity. The impact of the nanoparticle surface structure on the enantioselective hydrogenation of EP has clearly been demonstrated, but the mechanistic details of the structure sensitivity is an area of contention. A spectroelectrochemical investigation of EP adsorption on shape controlled Pt nanoparticles is a logical extension of the work in the previous chapter on single crystal surfaces.

5.2 Results

5.2.1 Characterisation of shaped Pt nanoparticles

Five shape controlled Pt nanoparticles of varying shapes and sizes were implemented in this investigation, the nanoparticles were characterised through TEM and CV. The TEM images of the nanoparticles gave information on the shape, size and distribution of both. CV will give quantitative and qualitative information on the surface sites of the nanoparticles and ensure nanoparticle surfaces are impurity free before analysis. By analysing, comparing and contrasting the CV's of each nanoparticle sample, the abundance of defects, {100} and {111} sites and the ratio of {111}/{100} can be discerned from a qualitative perspective. These are important aspects of the nanoparticle surface with regards to the adsorption of EP and subsequent behaviour of EP during hydrogenation on the surface. It is important to highlight that unlike for single crystal cyclic voltammetry in which the area of the electrode is discerned and current density is plotted against potential. A volume of the nanoparticle colloid is drop cast onto the platinum bar electrode, meaning the amount and more specifically the surface area of the platinum nanoparticles is variable and unknown. Therefore, the CV is measured is absolute current as opposed to current density.

PAA tetrahedral nanoparticles are synthesised to preferentially form {111} sites, the TEM images from figure 5.1 show the nanoparticles to be predominately octahedral or truncated cubes. These shapes would allow the corporation of significant amounts of both the {100} and {111} sites, this is demonstrated in the CV of the nanoparticle surface. The H_{UPD} region of the CV can give information on the basal sites on the surface(7). Firstly, the peak at 0.085 V is related to {110} sites and defect sites on the surface, which will be an ever-present feature for the CV's of the shape-controlled nanoparticles. The peak at 0.27 V has two

contributions relating to step sites, one from the {100} steps on the {111} terraces and one from the sites close to the steps on the {100} terrace. The signal between 0.30 and 0.37 V is related to {100} bi-dimensional terraces, a stronger current signal and if a peak forms at \sim 0.37 V are indicative of substantial well-ordered {100} terraces. The final feature between 0.40 and 0.55 V relates to the {111} bi-dimensional terraces, again a stronger current signal and if the signal shifts to lower potentials are indicative of larger well-ordered {111} terraces. The CV of the PAA tetrahedral nanoparticles shows a significant contribution from defect sites, which would account for the rounded shapes and irregular truncated shapes from the TEM images. These nanoparticle shapes could be regarded as heavily defected on the surface, owing to the complexity of the synthesis method to produce {111} orientated shapes(1). It is worth noting that the CV in figure 1 has an offset between the signal on the upper forward scan and the lower backwards scan, this can be attributed to ohmic drop caused by resistance of the nanoparticle film on the electrode(42). The average diameter of the nanoparticles is 13 nm and the size distribution is relatively narrow (within 2 nm of the average).

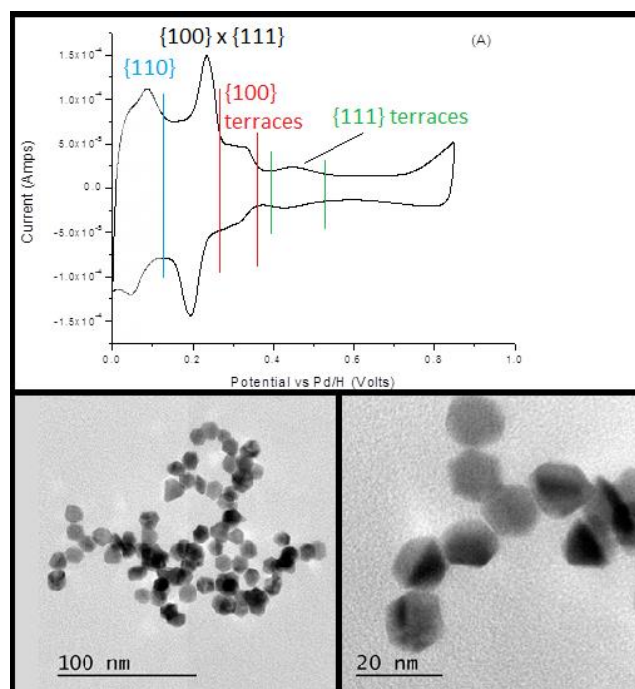


Figure 5.1: PAA tetrahedral nanoparticles TEM images and CV in 0.5 M H_2SO_4 at a scan rate of 50 mVs^{-1}

PAA cubic nanoparticles share many similarities with the PAA tetrahedral nanoparticles, which can be attributed to subtle differences in the method. PAA cubes are synthesised to produce $\{100\}$ orientated cubic nanoparticles with an average diameter of 12 nm and a narrow size distribution (within 3 nm of the average). While it is evident more defined cubic shapes are present in the TEM's of PAA cubic nanoparticles, varying degrees of truncation is still observable (figure 5.2). The CV of the PAA cubes reinforces the perspective that nanoparticles have a more ordered surface structure, with the sharper peaks of the signals at 0.085 and 0.27 V constituting a more defined and distinct step/defect site. A considerably contribution from the $\{100\}$ terrace signal is evident with the rising slant of that feature at ~ 0.36 V, which is also in-keeping with the predominately cubic shape of the TEM images. The $\{111\}$ terraces also give a significant signal contribution, but less than the $\{100\}$ terrace contribution.

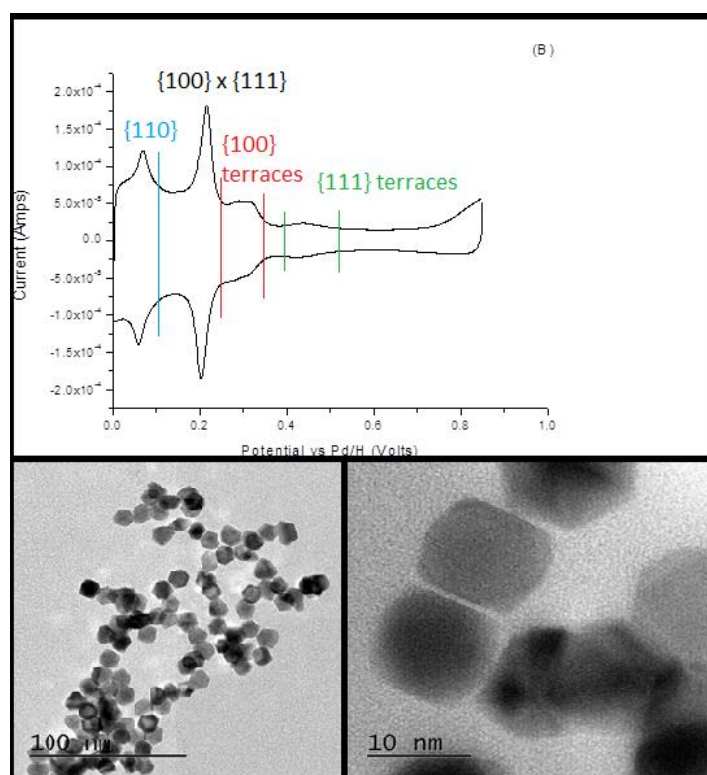


Figure 5.2: PAA cubic nanoparticles TEM images and CV in 0.5 M H_2SO_4 at a scan rate of 50 mVs^{-1}

KBr octahedral nanoparticles are formed from a synthesis method that favour the formation of $\{111\}$ orientated facets, which was deemed successful when referring to the CV of the KBr

octahedral nanoparticles (figure 5.3). The dominance of the signal feature relating to the {111} terraces in the CV, in conjunction with the minimal contributions from {100} terraces demonstrates the strong {111} character of the nanoparticles. The nanoparticles from the TEM images appears to be faceted spherical and octahedral shapes, which would explain the lack of {100} site contribution to the CV. Interestingly, for nanoparticles demonstrating spherical-like shapes the contributions to the CV from the {110} sites are lower than expected, which alludes to significant {111} terrace incorporation into the nanoparticle surface structure. The significant size difference between KBr octahedral nanoparticles and the two previous shaped nanoparticles is apparent when reviewing the TEM images. KBr octahedral nanoparticles have an average diameter of 63 nm.

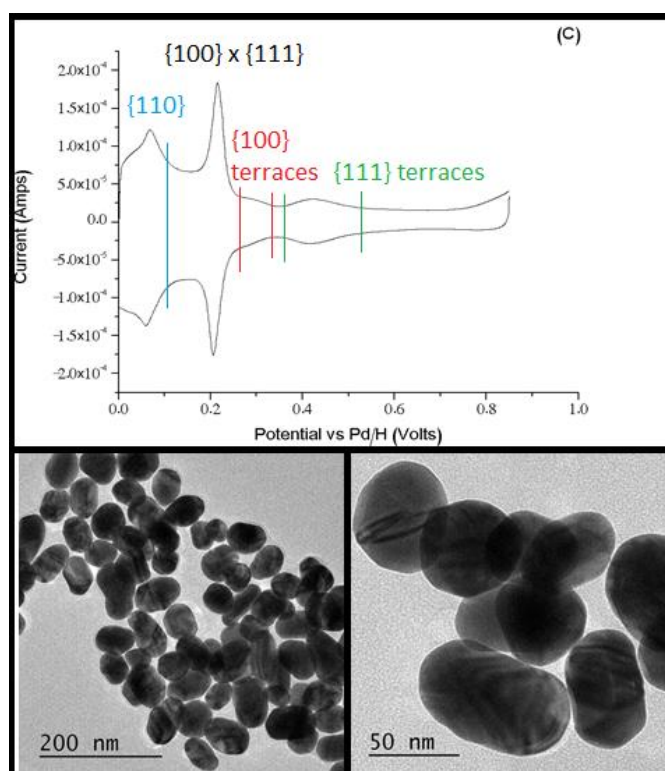


Figure 5.3: KBr octahedral nanoparticles TEM images and CV in 0.5 M H_2SO_4 at a scan rate of 50 mVs^{-1}

Oleylamine cubic nanoparticles are nanocubes with astonishingly well-formed shapes, illustrated in the TEM images with near perfect cubic shapes with little to no truncation of the corner sites (figure 5.4). The peak in the CV at $\sim 0.32\text{V}$ is indicative of the presence of

substantial {100} terrace sites with long range order on the nanoparticle surface. The well-defined {100} terrace sites are also substantiated by the minimal contributions from {110} sites at 0.09 V. However, the shape dispersion of the sample has a greater degree of variance in comparison to the other analysed samples. This also impacts on the size dispersion of the sample, with many of the elongated cuboid structures causing discrepancy in the sizes of the nanoparticles

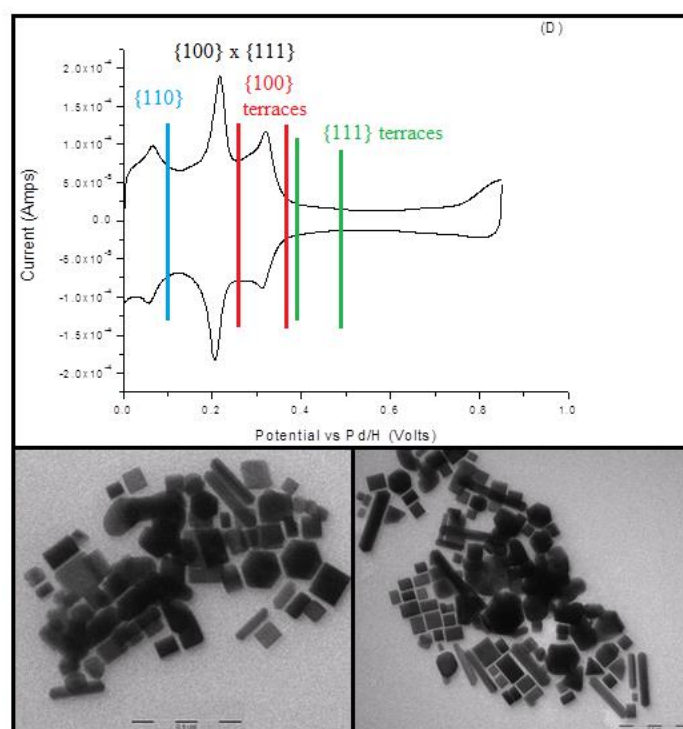


Figure 5.4: Oleylamine cubic nanoparticles TEM images and CV in 0.5 M H_2SO_4 at a scan rate of 50 mVs^{-1}

The final nanoparticle sample, spherical nanoparticles are synthesised to produce predominantly spherical nanoparticles. The nanoparticles shape from the TEM images is a mixture of spherical and significantly truncated octahedral shapes (figure 5.5). The nanoparticles have an average diameter similar to PAA tetrahedral and PAA cubes at 11 nm, with a narrow size distribution. The CV demonstrates a large contribution from the {110}/defect sites, with minimal involvement from the terrace sites. Which of the two, the {111} sites have the greater contribution to the CV signal. Samples A, B and C have similar sizes, but contrasting surface structures. This may aid us in probing the surface sensitivity of

EP adsorption on the platinum nanoparticles, by minimising any potential impact the nanoparticle size may have on the adsorption behaviour of EP.

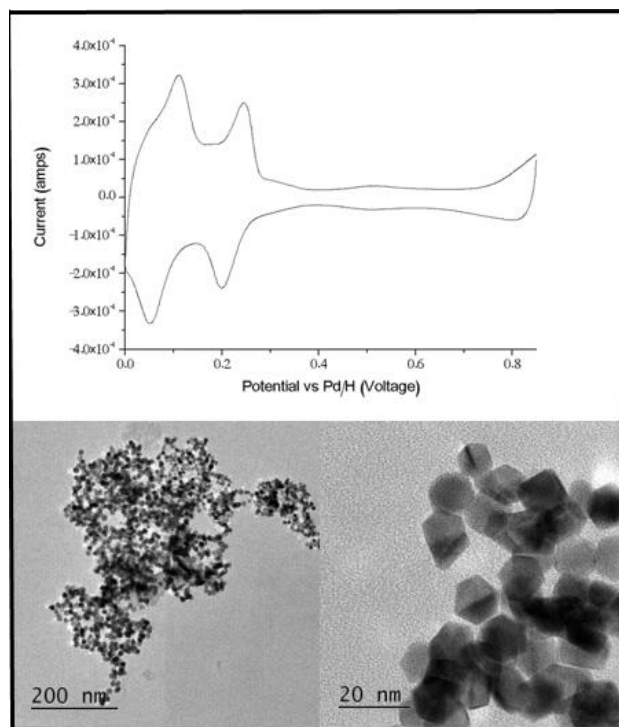


Figure 5.5: Spherical nanoparticles TEM images and CV in 0.5 M H_2SO_4 at a scan rate of 50 mVs^{-1}

A quantitative analysis of the surface structures of each of the samples would give a greater appreciation of the subtle differences in the surface configurations. By using a previously outlined characterisation (chapter 3.7), which exploits the selective adsorption of Bi and Ge and the associated current changes in the CV, the percentage of $\{100\}$ and $\{111\}$ sites can be estimated. It is worth noting that the assumptions of the calculation can lead to an appreciable associated error, so the data should be used to loosely identify trends.

	qBi/ $\{111\}$ %	qGe/ $\{100\}$ %
PAA Tetrahedral	7.1 ± 4	14.7 ± 4
PAA Cubes	11 ± 4	52 ± 4
Spherical	12 ± 4	8 ± 4

Table 5.3: Surface percentage of $\{111\}$ and $\{100\}$ sites on tetrahedral, cubic and spherical shaped nanoparticle samples.

The quantitative data agrees with the information garnered from the combinative CV and TEM analysis. With the PAA cubic nanoparticles having a considerable percentage of {100} sites and also highlights the ineffectiveness of the synthesis methods to produce a considerable amount {111} surface sites. If the values of the {100} and {111} sites are combined, we can gain an appreciation for the amount of terrace and defect sites for the three samples. The following trend for terraces on the nanoparticles can be proposed:

Spherical (20%) < PAA Tetrahedral (21.8%) < PAA Cubes (63%)

The amount of terrace and defect sites on the platinum surface has been established in the previous chapter to have a proposed influence on the adsorption behaviour of EP, but it remains to be seen if the shaped nanoparticles in this investigation have sufficient surface order to replicate the observed intermediates from the single crystal investigation.

5.2.2 Spectroscopic analysis of EP adsorption on Pt shaped nanoparticles

The SERS and SHINERS investigation into the adsorption of EP on shaped Pt nanoparticles raised the issue of residual impurities on the Pt nanoparticle surface, making the identification of bands relating to EP adsorption a complex and ambiguous task. Taking advantage of the Raman enhancement associated with platinum nanoparticle films(43), SERS analysis of the platinum nanoparticles was first undertaken. This allowed acid and alkaline cleaning processes prior to acquisition of the spectra. Alkaline cleaning cannot be achieved in the presence of Au@SiO₂ (SHINERS) particles, as it will cause the silica shell to degrade.

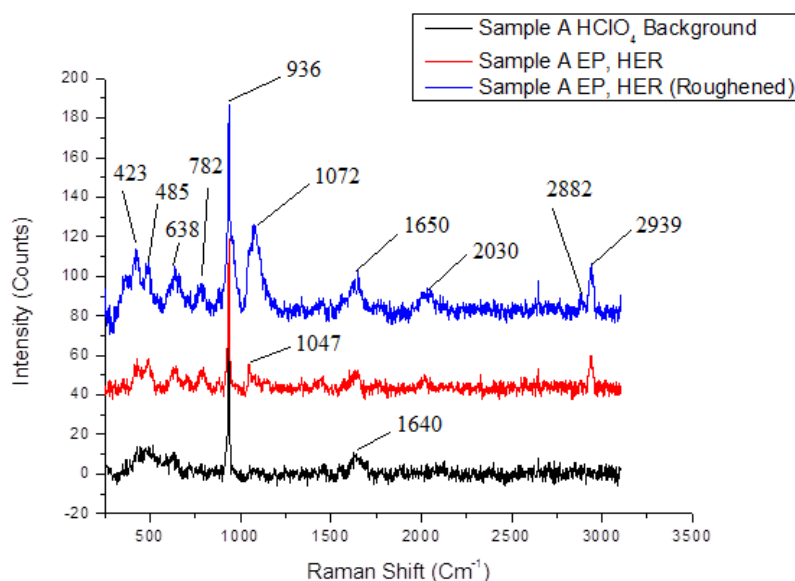


Figure 5.6: SERS spectra of PAA tetrahedral nanoparticles at -0.1 V and a scan rate of 50 mV s^{-1} in: (black) 0.1 M HClO_4 , (red) 0.1M HClO_4 , 0.1 M EP and (blue) 0.1M HClO_4 , 0.1 M EP and 50 roughening cycles

The background spectra in the SERS analysis of the PAA tetrahedral nanoparticles in figure 6 demonstrates a relatively featureless spectrum, which suggests minimal impurities. However, the small band at 500 cm^{-1} suggests a carbonaceous species may be present on the nanoparticle surface and the band at 1640 cm^{-1} can be attributed to water on the nanoparticle surface(44). Upon adsorption of EP skeletal peaks associated with EP are distinctively present in the spectra at 2882 , 2939 , 782 , and 638 cm^{-1} . There are small features at ~ 490 and 1047 cm^{-1} , but the intensity of the bands is too low to confidently assign these as evidence of the HHS. A small band is forming at 2030 cm^{-1} which can be attributed to adsorbed CO, which you would expect from the number of defects on the surface. Electrochemical roughening of the nanoparticles increases this peak further, suggesting decarbonylation of EP is occurring on the surface. The peak at 1047 cm^{-1} significantly increases in intensity and shifts to higher wavenumbers. This behaviour has not been noted on single crystals and could be proposed as a surface species related to the degradation of EP.

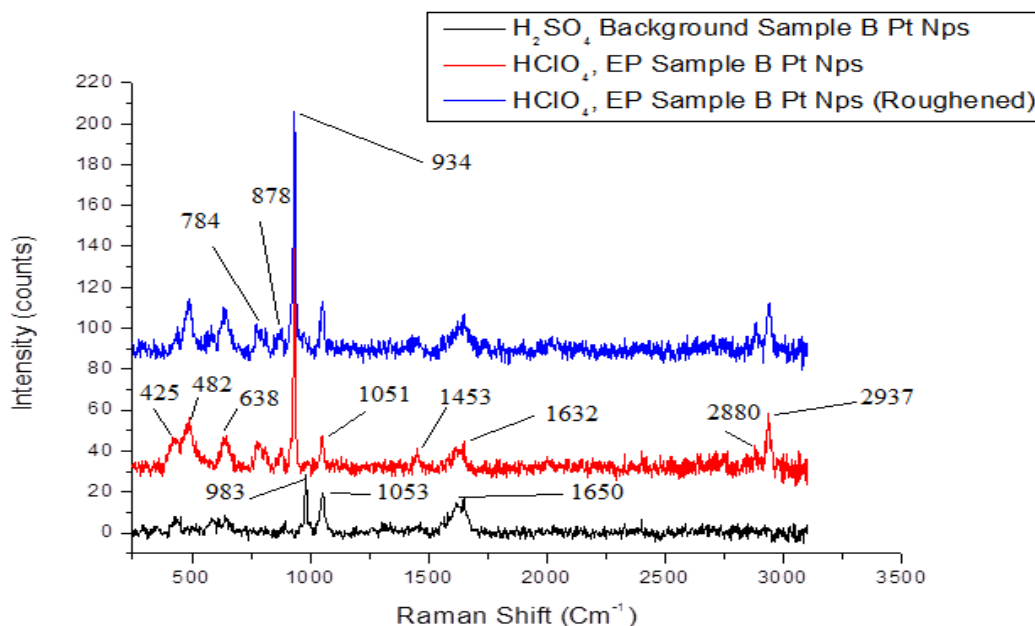


Figure 5.7: SERS PAA cubic nanoparticles at -0.1 V and a scan rate of 50 mV s^{-1} in: (black) 0.1 M H_2SO_4 , (red) 0.1 M HClO_4 , 0.1 M EP and (blue) 0.1 M HClO_4 , 0.1 M EP and 50 roughening cycles

The SERS investigation of PAA cubic nanoparticles mirrors spectra presented for the high index single crystal surfaces from the previous spectra (figure 5.7). During the cleaning process and acquisition of the background, sulphuric acid was utilised as the electrolyte. The advantage of using sulphuric acid over perchloric acid in this capacity is the strong specific adsorption to the platinum surface(45), which should help to remove residual impurities. This proposal is vindicated by the apparent cleanliness of the background spectra, with the presence of the two peaks at 983 and 1053 cm^{-1} related to sulphuric acid on the platinum surface(346). The adsorption of EP on PAA cubes produces signals at 1051 and ~ 480 cm^{-1} which can be attributed to the formation of the HHS on the cubic nanoparticle surface, this proposal is reinforced by the increased intensity of the two peaks after electrochemical roughening of the nanoparticle surface. Comparing the differing behaviours of EP adsorption on PAA tetrahedral nanoparticles and PAA cubes and the increase in ordered terrace sites in PAA cubes over PAA tetrahedral nanoparticles, this does appear to validate suggestions that the HHS intermediate requires both terrace and defect sites to form.

SERS spectra for samples C and E very much mimicked the spectra demonstrated for PAA tetrahedral nanoparticles, with little to no bands associated with EP adsorption discernible

from the background noise of the spectra or are obscured by impurities present on the nanoparticle surface for these reasons the results were not deemed relevant to the investigation. With the TEM images of both samples showing predominantly spherical structures, is it a case that the nanoparticles lack the required order of the surface to form the related EP adsorption intermediate.

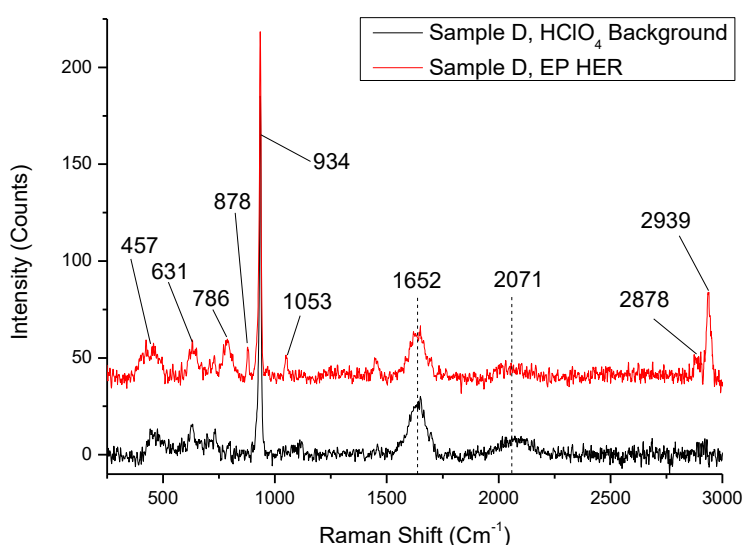


Figure 5.8: SERS spectra of Oleylamine cubic nanoparticles at -0.1 V and a scan rate of 50 mV s^{-1} in: (black) 0.1 M HClO_4 , (red) 0.1 M HClO_4 , 0.1 M EP

Oleylamine cubic nanoparticles have the most structured surface of all the samples analysed and feasibly if the adsorbate intermediates of EP require long-range order as well as defect sites, oleylamine cubes would be the most suitable surface to identify the intermediate presence. However, the SERS analysis only shows skeletal stretches of EP and bands that allude to the presence of surface impurities.

As the PAA cubic nanoparticles were the only nanoparticles to show signs of the HHS intermediate in the SERS spectra (figure 5.7), SHINERS analysis was carried out in order to definitively establish the presence of the intermediate (figure 5.9). The SHINERS spectra exhibited signs of EP adsorption and possible features of HHS intermediate state, having

said that, the validity of these bands should be questioned due to two unassigned bands dominating the spectrum at 1303 and 1578 cm^{-1} .

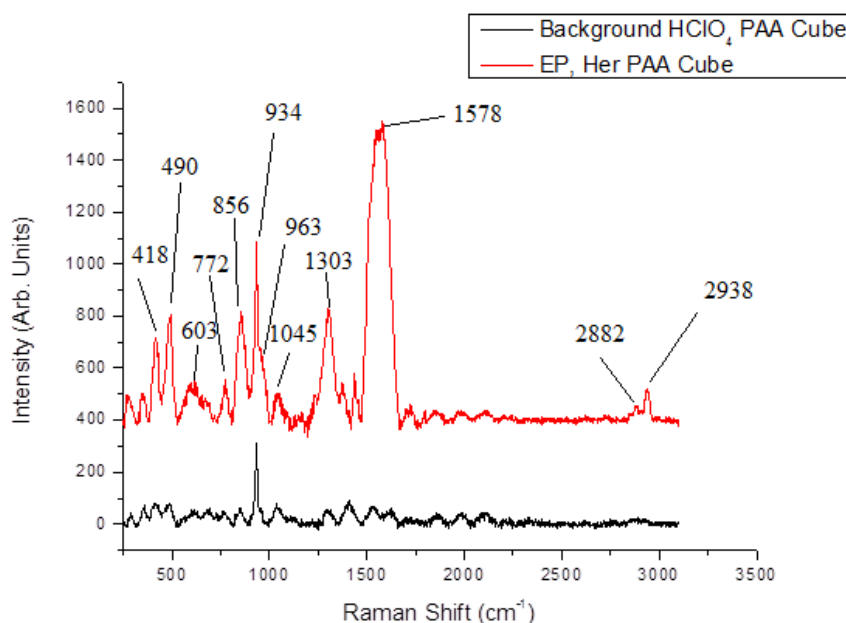


Figure 5.9: SHINERS spectra of PAA cubic nanoparticles at -0.1 V and a scan rate of 50 mV s^{-1} in: (black) 0.1 M HClO_4 , (red) 0.1 M HClO_4 , 0.1 M EP

5.3 Discussion

The goal of this investigation was to elucidate potential structure sensitivity in the hydrogenation of Ethyl pyruvate in the absence of a modifier. SHINERS experiments on single crystal surfaces in the previous chapter have detected a proposed a $\mu_2(\text{C},\text{O})$ intermediate form of EP. The intermediate is predominately associated with terrace sites on the platinum surface, the investigation is evaluating if the shaped nanoparticles have enough surface order to facilitate this newly detected species. The first and most obvious observation is the apparent cleanliness of the nanoparticle surfaces. It must be considered that the unassigned bands that feature in the majority of the spectroscopic analysis on the shape-controlled platinum nanoparticles can be attributed to residual capping agent from the synthesis of said nanoparticles. In fact, Baiker *et al* made reference to this occurrence in the catalytic investigation of EP hydrogenation with shaped platinum nanoparticles(35). They revealed the presence of a significant amount of organic residue through XPS, which

was attributed to the strongly adsorbed colloid stabiliser Polyacrylic acid (PAA). The blocking effect of residual PAA was further probed by DRIFT spectroscopy of CO adsorption on the Pt nanoparticles, the notably low intensity signal related to on-top adsorption of CO elucidates the significant surface blocking by the stabiliser. However, Baiker dismissed the notion that the capping agent had a poisoning effect on the catalytic hydrogenation reaction, citing similar turnover rates between the shaped nanoparticles and a Pt/Al₂O₃ reference catalyst. The minimal poisoning effect of the capping agent was ascribed to efficient competitive adsorption between the stabiliser, substrate, hydrogen and the solvent. Particular attention was paid to role of the solvent (acetic acid) being important in displacing the capping agent, due to chemical similarities with the polycarboxylic acid nature of the stabiliser(47). This investigation does not utilise acetic acid as a solvent and the presence of impurities on the nanoparticles during spectroscopic analysis of EP hydrogenation is evident. These impurities may be masking or disrupting the proposed adsorption intermediates, we are attempting to probe in this investigation. An FTIR study into the adsorption of capping material on differently shaped Pt nanoparticles has been conducted by El-Sayed and co-workers and similar bands associated with PAA can be identified in this study(48). The strong bands at 1578 and 1303 cm⁻¹ displayed in figure 9 can be attributed to a COO⁻ asymmetric and CH deformation stretching modes of PAA. Another important band to consider is the signal between 400 and 500 cm⁻¹, which can be attributed to presence of Pt-C and Pt-O bonds. The presence of a Pt-O bond in the background spectra of each nanoparticle surface can be argued, with it being more prominent and defined in the SHINERS spectra (figure 5.9). This is indicative of a proposed strong bond from the carbonyl of the capping agent to the Pt surface(49). With each stabilising agent used in the synthesis methods for the shaped nanoparticles (PAA, oleic acid and ethylene glycol dodecyl ether) making use of a Pt – carbonyl interaction.

The presence of residual capping agent on the platinum nanoparticles seems irrefutable from the evidence provided from this study and Baiker *et al*(35). However, limited insight has been offered into the effects this has on the hydrogenation of EP. Focusing on shaped nanoparticles formed using the PAA stabilising agent, both cubic and tetrahedral nanoparticles can be produced by altering the ratio of platinum precursor to capping agent. It is proposed that the capping material forms an ester-like linkage to the platinum surface

on the tetrahedral shapes through the hydroxyl oxygen of the carboxylic acid group of PAA. This can be classified as a linear adsorption configuration. For cubic nanoparticles the adsorption is through both carboxylic oxygen atoms, which is classified as a bridge adsorption configuration(48). The differing adsorption configurations of PAA on the {100} and {111} facets can have important implications for the effect of residual stabilising agent in catalysis. If both cubic and tetrahedral nanoparticles are cleaned to similar standards, more of the cubic platinum sites would be blocked due to the differing adsorption configurations. This may have been the source of the trend discovered by Baiker and co-workers that the activity and enantiodifferentiation of EP hydrogenation increased with increasing ratios of {111}/{100} sites on shaped Pt nanoparticles. It would be expected that the blocked surface sites would cause a greater disruption to the hydrogenation reaction in the presence of the modifier over the unmodified reaction, since the former requires a greater amount of free surface sites. This would be consistent with data from Baiker's study demonstrating each of the shaped nanoparticles had similar catalytic performances for the racemic reaction, but found greater enhancements for the {111}-rich surface sites upon introduction of the modifier(35). One interesting observation from the spectra of the PAA cubic nanoparticles is the presence of peaks at 1051 cm^{-1} and 980 cm^{-1} which is indicative of the presence of the half-hydrogenated state of EP. This specie is synonymous with low coordination surface sites, but the PAA cubic nanoparticles have a much higher percentage terrace sites in comparison to the tetrahedral and spherical nanoparticles which show no signs of the HHS. It could be proposed that the HHS requires both terrace and defect sites to form (possibly at a step site on a terrace). This is an interesting proposition and could be applicable to observations by Attard *et al* of increased activity and lower enantiomeric excess upon the adsorption of bismuth to block defect sites (41). However, with the sheer amount of impurities present in the investigation, confidence in assigning the spectral peaks is far from absolute.

5.4 Conclusion

This investigation reinforces the importance of identifying and eliminating impurities, when analysing catalytic reactions from a fundamental stand point. This also relates to the implementation and development of shape-controlled Pt nanoparticles for catalytic

reaction, which is ever increasing in popularity. While somewhat capable cleaning methods have been proposed(7, 50), further research into this area is vital for the continued development of the technique overall. The complexity of the EP hydrogenation reaction becomes more evident when transitioning from single crystal surfaces to viable catalytic surfaces, with the solvent being incredibly important in this instance. This also highlights a limitation of the CV technique in definitively determining the presence of impurities on nanoparticle surfaces and champions a multiple technique analytical approach.

5.5 References

1. T. S. Ahmadi, Z. L. Wang, T. C. Green, A. Henglein, M. A. El-Sayed, Shape-controlled synthesis of colloidal platinum nanoparticles. *SCIENCE-NEW YORK THEN WASHINGTON-*, 1924-1925 (1996).
2. R. Narayanan, M. A. El-Sayed, Shape-dependent catalytic activity of platinum nanoparticles in colloidal solution. *Nano letters* **4**, 1343-1348 (2004).
3. R. Narayanan, M. A. El-Sayed. (ACS Publications, 2005).
4. H. Lee *et al.*, Morphological control of catalytically active platinum nanocrystals. *Angewandte Chemie* **118**, 7988-7992 (2006).
5. G. A. Somorjai, J. Y. Park, Colloid science of metal nanoparticle catalysts in 2D and 3D structures. Challenges of nucleation, growth, composition, particle shape, size control and their influence on activity and selectivity. *Topics in Catalysis* **49**, 126-135 (2008).
6. K. An, G. A. Somorjai, Size and shape control of metal nanoparticles for reaction selectivity in catalysis. *ChemCatChem* **4**, 1512-1524 (2012).
7. F. J. Vidal-Iglesias, R. M. Arán-Ais, J. Solla-Gullón, E. Herrero, J. M. Feliu, Electrochemical Characterization of Shape-Controlled Pt Nanoparticles in Different Supporting Electrolytes. *ACS Catalysis* **2**, 901-910 (2012).
8. J. Solla-Gullon *et al.*, Shape-dependent electrocatalysis: methanol and formic acid electrooxidation on preferentially oriented Pt nanoparticles. *Physical Chemistry Chemical Physics* **10**, 3689-3698 (2008).
9. C. M. Sánchez-Sánchez *et al.*, Imaging structure sensitive catalysis on different shape-controlled platinum nanoparticles. *Journal of the American Chemical Society* **132**, 5622-5624 (2010).
10. Y. Yu, B. Xu, Selective formation of tetrahedral Pt nanocrystals from K₂PtCl₆/PVP. *Chinese Science Bulletin* **48**, 2589-2593 (2003).
11. D. K. Smith, B. A. Korgel, The importance of the CTAB surfactant on the colloidal seed-mediated synthesis of gold nanorods. *Langmuir* **24**, 644-649 (2008).
12. Q. Zhang, N. Li, J. Goebel, Z. Lu, Y. Yin, A systematic study of the synthesis of silver nanoplates: is citrate a “magic” reagent? *Journal of the American Chemical Society* **133**, 18931-18939 (2011).
13. J. S. DuChene *et al.*, Halide anions as shape-directing agents for obtaining high-quality anisotropic gold nanostructures. *Chemistry of Materials* **25**, 1392-1399 (2012).
14. B. Wiley, T. Herricks, Y. Sun, Y. Xia, Polyol synthesis of silver nanoparticles: use of chloride and oxygen to promote the formation of single-crystal, truncated cubes and tetrahedrons. *Nano Letters* **4**, 1733-1739 (2004).

15. R. Long, S. Zhou, B. J. Wiley, Y. Xiong, Oxidative etching for controlled synthesis of metal nanocrystals: atomic addition and subtraction. *Chemical Society Reviews* **43**, 6288-6310 (2014).
16. N. R. Jana, L. Gearheart, C. J. Murphy, Seed-mediated growth approach for shape-controlled synthesis of spheroidal and rod-like gold nanoparticles using a surfactant template. *Advanced Materials* **13**, 1389 (2001).
17. M. Zhang, M. Drechsler, A. H. Müller, Template-controlled synthesis of wire-like cadmium sulfide nanoparticle assemblies within core– shell cylindrical polymer brushes. *Chemistry of materials* **16**, 537-543 (2004).
18. C. Wang, H. Daimon, Y. Lee, J. Kim, S. Sun, Synthesis of monodisperse Pt nanocubes and their enhanced catalysis for oxygen reduction. *Journal of the American Chemical Society* **129**, 6974-6975 (2007).
19. S. S. Shankar, S. Bhargava, M. Sastry, Synthesis of gold nanospheres and nanotriangles by the Turkevich approach. *Journal of nanoscience and nanotechnology* **5**, 1721-1727 (2005).
20. S. Xie *et al.*, Synthesis of Pd-Rh Core–Frame Concave Nanocubes and Their Conversion to Rh Cubic Nanoframes by Selective Etching of the Pd Cores. *Angewandte Chemie International Edition* **51**, 10266-10270 (2012).
21. J. Hu, T. W. Odom, C. M. Lieber, Chemistry and physics in one dimension: synthesis and properties of nanowires and nanotubes. *Accounts of chemical research* **32**, 435-445 (1999).
22. J. Solla-Gullon *et al.*, In situ surface characterization of preferentially oriented platinum nanoparticles by using electrochemical structure sensitive adsorption reactions. *The Journal of Physical Chemistry B* **108**, 13573-13575 (2004).
23. Z. Niu, Y. Li, Removal and utilization of capping agents in nanocatalysis. *Chemistry of Materials* **26**, 72-83 (2013).
24. D. Li *et al.*, Surfactant removal for colloidal nanoparticles from solution synthesis: the effect on catalytic performance. *Acs Catalysis* **2**, 1358-1362 (2012).
25. F. Vidal-Iglesias *et al.*, Evaluating the ozone cleaning treatment in shape-controlled Pt nanoparticles: Evidences of atomic surface disordering. *Electrochemistry Communications* **13**, 502-505 (2011).
26. B. Qiao *et al.*, Single-atom catalysis of CO oxidation using Pt₁/FeO_x. *Nature chemistry* **3**, 634-641 (2011).
27. K. Ding *et al.*, Identification of active sites in CO oxidation and water-gas shift over supported Pt catalysts. *Science* **350**, 189-192 (2015).
28. I. X. Green, W. Tang, M. Neurock, J. T. Yates, Spectroscopic observation of dual catalytic sites during oxidation of CO on a Au/TiO₂ catalyst. *Science* **333**, 736-739 (2011).
29. R. J. Taylor *et al.*, Enantioselective Hydrogenation of α -Ketoesters: An in Situ Surface-Enhanced Raman Spectroscopy (SERS) Study. *The Journal of Physical Chemistry C* **115**, 21363-21372 (2011).
30. W. Z. Weng, H. L. Wan, J. M. Li, Z. X. Cao, Laser-Induced Formation of Metal–Peroxide Linkages on the Surface of Lanthanum Sesquioxide under Oxygen. *Angewandte Chemie International Edition* **43**, 975-977 (2004).
31. S. Chan, I. Wachs, L. Murrell, L. Wang, W. K. Hall, In situ laser Raman spectroscopy of supported metal oxides. *The Journal of Physical Chemistry* **88**, 5831-5835 (1984).
32. T. Egerton, A. Hardin, The application of Raman spectroscopy to surface chemical studies. *Catalysis Reviews Science and Engineering* **11**, 71-116 (1975).
33. H. Zhang *et al.*, In situ dynamic tracking of heterogeneous nanocatalytic processes by shell-isolated nanoparticle-enhanced Raman spectroscopy. *Nature Communications* **8**, (2017).
34. S. Guan *et al.*, Structure Sensitivity in Catalytic Hydrogenation at Platinum Surfaces Measured by Shell-Isolated Nanoparticle Enhanced Raman Spectroscopy (SHINERS). *ACS Catalysis*, (2016).

35. E. Schmidt, A. Vargas, T. Mallat, A. Baiker, Shape-selective enantioselective hydrogenation on Pt nanoparticles. *Journal of the American Chemical Society* **131**, 12358-12367 (2009).
36. D. P. Ruiz, J. L. Fierro, P. A. Reyes, Enantioselective hydrogenation of ethyl pyruvate and 1-phenyl-1, 2-propanedione on catalysts prepared by impregnation of colloidal platinum on SiO₂. *Journal of the Brazilian Chemical Society* **21**, 262-269 (2010).
37. J. Wehrli, A. Baiker, D. Monti, H. Blaser, Enantioselective hydrogenation of α -ketoesters: Preparation and catalytic behavior of different alumina-supported platinum catalysts modified with cinchonidine. *Journal of molecular catalysis* **61**, 207-226 (1990).
38. I. Sutherland, A. Ibbotson, R. Moyes, P. Wells, Enantioselective hydrogenation I. Surface conditions during methyl pyruvate hydrogenation catalyzed by cinchonidine-modified platinum/silica (EUROPT-1). *Journal of Catalysis* **125**, 77-88 (1990).
39. P. J. Collier, J. A. Iggo, R. Whyman, Preparation and characterisation of solvent-stabilised nanoparticulate platinum and palladium and their catalytic behaviour towards the enantioselective hydrogenation of ethyl pyruvate. *Journal of Molecular Catalysis A: Chemical* **146**, 149-157 (1999).
40. S. Mukerjee, Particle size and structural effects in platinum electrocatalysis. *Journal of Applied Electrochemistry* **20**, 537-548 (1990).
41. D. J. Jenkins *et al.*, Enantioselectivity and catalyst morphology: step and terrace site contributions to rate and enantiomeric excess in Pt-catalysed ethyl pyruvate hydrogenation. *Journal of Catalysis* **234**, 230-239 (2005).
42. H. Reller, E. Kirowa-Eisner, E. Gileadi, Ensembles of microelectrodes: Digital simulation by the two-dimensional expanding grid method: Cyclic voltammetry, iR effects and applications. *Journal of electroanalytical chemistry and interfacial electrochemistry* **161**, 247-268 (1984).
43. K. Kim, K. L. Kim, H. B. Lee, K. S. Shin, Surface-enhanced Raman scattering on aggregates of platinum nanoparticles with definite size. *The Journal of Physical Chemistry C* **114**, 18679-18685 (2010).
44. Y. Chen, Z. Tian, Dependence of surface enhanced Raman scattering of water on the hydrogen evolution reaction. *Chemical Physics Letters* **281**, 379-383 (1997).
45. J. Clavilier, D. Armand, Electrochemical induction of changes in the distribution of the hydrogen adsorption states on Pt (100) and Pt (111) surfaces in contact with sulphuric acid solution. *Journal of electroanalytical chemistry and interfacial electrochemistry* **199**, 187-200 (1986).
46. A. Mineshige, N. Ohata, T. Tanaka, M. Kobune, T. Yazawa, In-situ Raman spectroscopy of Pt/C electrodes in H₂SO₄ aqueous solution. *Electrochemistry* **75**, 179-181 (2007).
47. D. Liu, J. Gao, C. J. Murphy, C. T. Williams, In situ attenuated total reflection infrared spectroscopy of dendrimer-stabilized platinum nanoparticles adsorbed on alumina. *The Journal of Physical Chemistry B* **108**, 12911-12916 (2004).
48. J. Petroski, M. A. El-Sayed, FTIR study of the adsorption of the capping material to different platinum nanoparticle shapes. *The Journal of Physical Chemistry A* **107**, 8371-8375 (2003).
49. Y. Borodko *et al.*, Probing the Interaction of Poly (vinylpyrrolidone) with Platinum Nanocrystals by UV-Raman and FTIR. *The Journal of Physical Chemistry B* **110**, 23052-23059 (2006).
50. R. M. Arán-Ais, F. J. Vidal-Iglesias, J. Solla-Gullón, E. Herrero, J. M. Feliu, Electrochemical Characterization of Clean Shape-Controlled Pt Nanoparticles Prepared in Presence of Oleylamine/Oleic Acid. *Electroanalysis* **27**, 945-956 (2015).

Chapter 6 - Selective Hydrogenation of α,β Unsaturated Aldehydes

6.1 Literature review

6.1.1 Reaction Pathway for the hydrogenation of α,β -unsaturated Aldehydes

The targeted modification of specific functional groups in somewhat complex starting materials, is a fundamental aspect of catalysis(1, 2). This aspect garners a great deal of attention in both academia and industry, with chemoselectivity playing vital roles in the fragrance, flavour, agrochemicals and pharmaceuticals sectors(3-5). The targeting of specific moieties can be achieved using protecting groups, however being conscious of green chemistry a purely catalytic route is most desirable. A particularly challenging case is that of the selective catalytic hydrogenation of α,β -unsaturated aldehydes (figure 6.1).

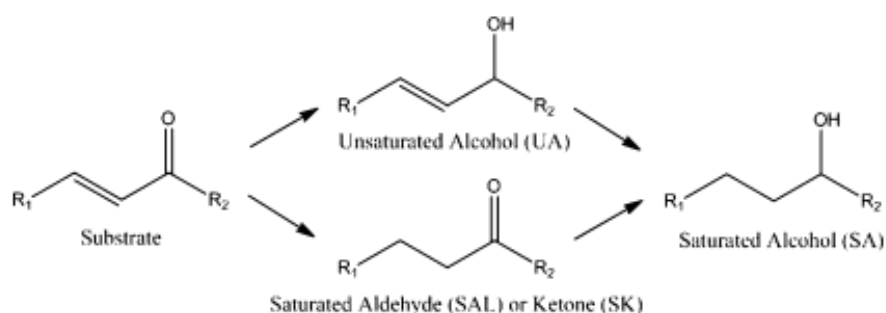


Figure 6.1: The Reaction Pathway for the hydrogenation of α,β -unsaturated aldehydes. Reprinted from (6)

This reaction is interesting specifically due to industrial need to selectively reduce the C=O bond in the presence of the thermodynamically less stable C=C bond, to generate the unsaturated alcohol product(7). The aforementioned hurdle as well as a lack of insight into the relationship between catalyst structure and how it functions in the reaction, has hindered the development of heterogeneous catalysts for this reaction(6, 8). It is important to address this impediment by analysing the impact of altering the morphology of the catalytic nanoparticles as well as applying various well-defined catalytic surfaces to the hydrogenation of α, β -unsaturated aldehydes. This will provide a comprehensive perspective from both a fundamental and practical aspect. It is also very important to be aware that the factors that influence the catalytic hydrogenation of α, β -unsaturated aldehydes are not solely limited to the type and structure of the catalyst(6, 9, 10). It is

important to consider the role of the catalyst support(11, 12), adsorption geometry(13), unwanted side reactions and additional surface constituents (9, 14-18). Pursuing research in these areas will allow greater insight into to the complex nature of heterogeneous catalytic hydrogenation. A range of different substrate molecules are of interest from both a research and industrial perspective, for reasons already discussed. These substrates include acrolein, crotonaldehyde, prenal and cinnamaldehyde (figure 6.2).

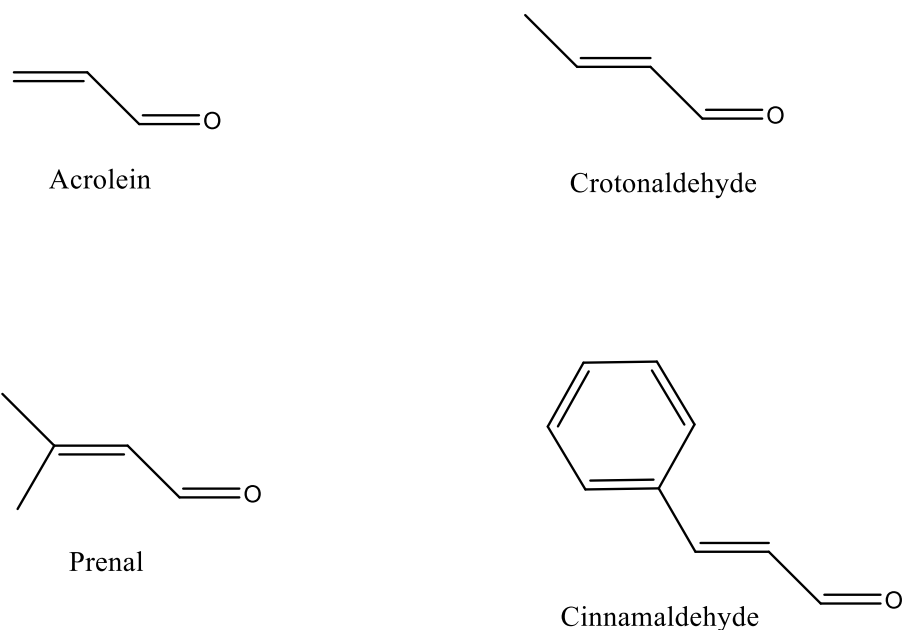


Figure 6.2: Structures of prominent α,β -unsaturated aldehydes.

6.1.2 Adsorption of α,β -unsaturated Aldehydes on Pt surfaces

One widely employed metal in heterogeneous catalytic hydrogenation is platinum. This popularity can be attributed to the ability of platinum to reduce a myriad of functional groups, including C=C(19), C=O(20), NO₂(21), C \equiv C(22), C \equiv N(23) and aromatics(24, 25). This ability makes platinum based catalysts very applicable in the hydrogenation of α, β -unsaturated aldehydes and an abundance of literature is available on this area of research(6, 14, 26-28). Adsorption geometry of the reactant is believed to play a governing role in directing the pathway of the hydrogenation reaction and could plausibly be manipulated to circumvent the previously highlighted thermodynamic stability of the C=O

bond over the C=C bond(7). In order to scrutinise this hypothesis, all viable adsorption geometries of α , β -unsaturated aldehydes would need to be determined (figure 6.3).

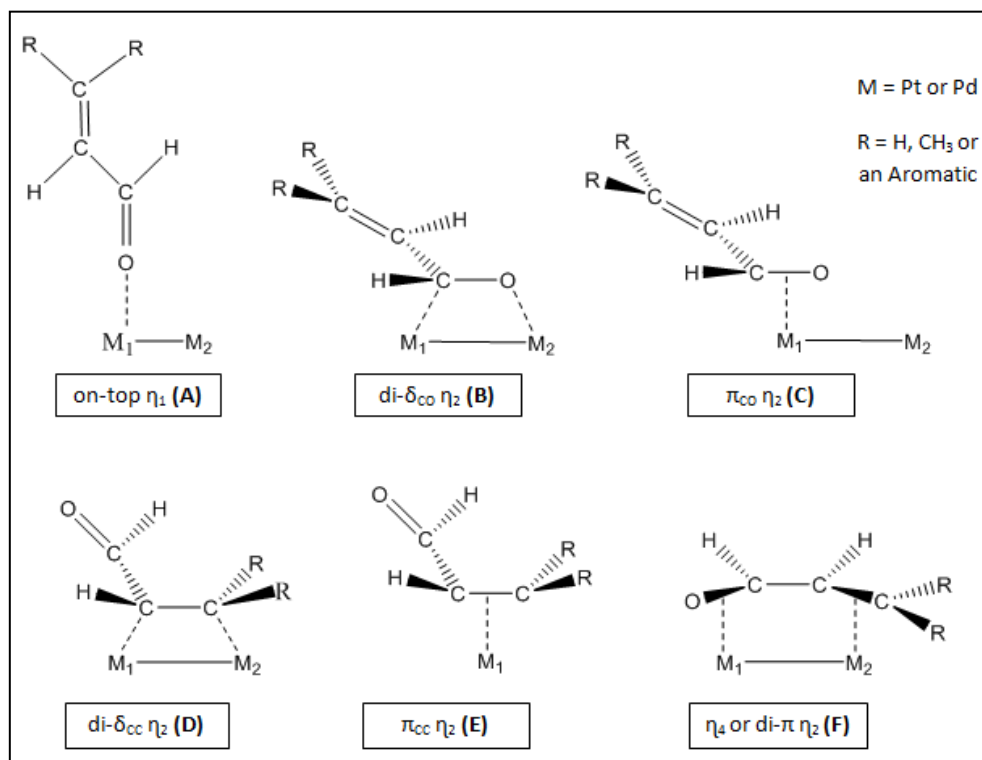


Figure 6.3: Possible adsorption modes of α , β -unsaturated aldehydes adapted from (363)

Figure 6.3 demonstrates how vastly different the range of viable adsorption modes of α , β -unsaturated aldehydes can be, with adsorption modes involving the C=O and C=C functional groups and well as a combination of the two. It is conceivable that altering the adsorption mode of the reactant will not only have an impact on the reaction pathway, but will also limit the amount of reactant adsorption to the catalyst surface. The relationship between the catalyst surface and the reactant has been investigated by numerous research groups(13, 26, 28, 29), the intricate understanding of which could be the key to directing the reaction pathway towards the desirable unsaturated alcohol form. Delbecq and Sautet used a theoretical approach to probe the selectivity of the hydrogenation reaction in relation to the competitive C=C and C=O adsorption(13). Four common α , β -unsaturated aldehydes are highlighted in Figure 3, the adsorption for each of these has been computationally mapped on various well-defined platinum surfaces. This specific line of research also brings into to consideration the role of the alkyl group in directing adsorption as well as the morphology of the catalyst surface. It has been established that olefins, aromatics and alkyl groups

participate in interactions with that catalyst surface(30-34). These interactions and steric effects will differ between each example in Figure 6.3, especially in the case of cinnamaldehyde. The phenyl ring of cinnamaldehyde participates in a stabilising interaction with the surface, which has to be taken into consideration(13, 34). The theoretical work by Delbecq and Sautet highlighted the following trends with α,β -unsaturated aldehyde adsorption on different crystal faces(13):

- On Pt {111}, acrolein prefers a trihapto di - σ_{cc} + (O) mode (figure 6.3(D) with C=O interaction), but crotonaldehyde, prenal and cinnamaldehyde prefer the di - σ_{co} mode (figure 6.3(B)).
- On Pt {100}, a η_4 geometry bound both by the C=C and C=O bonds is strongly preferred whatever the substituents (figure 6.3(F)).
- On Pt {110}, adsorption through the C=C bond is preferred in a π (\perp) geometry (trihapto form) (figure 6.3(E) with C=O interaction), except for cinnamaldehyde for which the η_4 (di - π) mode is slightly favoured (figure 6.3(F)).
- On a n [n (111) x (100)] stepped surface, the $\pi_{cc}(\perp)$ geometry (figure 6.3(E)) is in competition with the η_4 one (figure 6.3(F)) for acrolein and cinnamaldehyde and with the di - σ_{co} one (figure 6.3(B)) for prenal.

These observations reinforce the belief that structure of the crystal face and the nature of the substituents on the molecule influence the nature of the adsorption. It was concluded from this work that substitution of the carbon double bond of the aldehyde decreased the binding energy of the η_2 (CC) adsorption mode, inducing a modification in the preferred adsorption geometry of the molecule. In terms of the crystal face, the Pt {111} surface yields a strong four electron repulsion with the adsorbate. This repulsion favours a di - σ adsorption mode, while altering the surface to a more open face tends to favour η_4 or π coordination(13). Establishing a link between the preferential adsorption of the aldehyde to the crystal face and selective hydrogenation of the molecule is a contentious one. The literature surrounding this topic presents conflicting views and elucidating the role of geometric effects in platinum catalysed hydrogenation of α, β -unsaturated aldehydes appears a complicated task.

6.1.3 Selective Hydrogenation of Cinnamaldehyde

The focus of this investigation is the selective hydrogenation of cinnamaldehyde. Particularly, the catalysts influence on the hydrogenation pathway (figure 6.4).

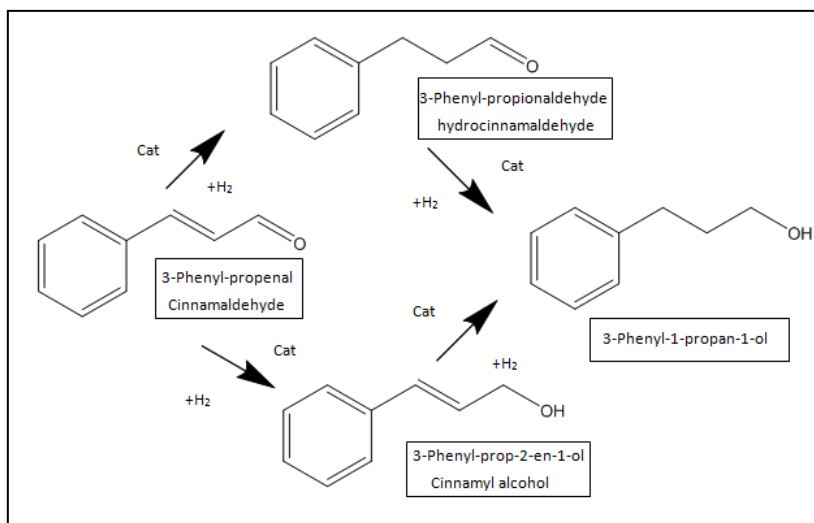


Figure 6.4: Hydrogenation Pathway of Cinnamaldehyde

Generally, the literature is concerned with platinum nanoparticles as opposed to single crystal catalyst structures. It is important then to rationalise the surfaces employed as low or high index, this can be achieved when taking into consideration the inverse relationship between low coordination sites and nanoparticle size(35). Tsang *et al.* evaluated the size effect of monodispersed platinum nanoparticles on the hydrogenation of cinnamaldehyde, the desirable product being cinnamyl alcohol (35).

Nanoparticle Size and Selectivity Towards Cinnamyl Alcohol	
Particle Size (nm)	Cinnamyl Alcohol Selectivity (%)
2.8	24.3
3.1	30.2
3.3	44.6
4.8	49.1
6.0	80.8
14.4	85.6
24.8 (sintered)	85.3

Table 6.4: Nanoparticle Size Relationship with Cinnamyl Alcohol Selectivity Tsang *et al.*(35)

The results reported by Tsang *et al.*, summarised in Table 6.1, show a remarkable increase in cinnamyl alcohol selectivity for nanoparticle sizes upwards of 4.8 nm and seems to reach a

maximum at 14.4 nm (figure 6.4). This trend has been attributed to size and population increases of low index {111} facets and decrease of the high coordination sites as the size of the nanoparticle increases. The fact that a maximum is reached at approximately 85% selectivity could be due to the selectivity being limited by the coverage of the substrate molecule. The trend described by Tsang *et al.* is consistent with the adsorption data of Delbecq and Sautet, wherein cinnamaldehyde adsorption on platinum {111} is most stable through the di- σ_{CO} adsorption mode and disrupts the π_{CC} adsorption mode. It is suggested by both pieces of literature that the preferential adsorption of the α , β -unsaturated aldehyde directs which hydrogenation pathway is taken and in this case the cinnamyl alcohol is the favoured product.

The existence of a link between the metal catalyst surface structure/morphology and the selective hydrogenation product is an area of debate in the literature. The aforementioned reports are in support of this link, however, conflicting articles have been published on this matter. Zhu and Zaera reported no significant alterations in selectivity associated with changes in average diameter of the metal nanoparticle, but did conclude an increase in catalytic activity can be associated with an increase in nanoparticle size(27). It is worth noting that the nanoparticle size range of this study is relatively narrow, being between 1.5 and 2.5 nm approximately. This study also raises concerns with potential errors in estimating nanoparticle size with TEM images and the role of the catalyst support in the hydrogenation reaction. With numerous kinetic and steric investigations being carried out on the selective hydrogenation of the α , β -unsaturated aldehydes(37), the platinum catalysts are coupled with different supports(12, 13). When comparing the data presented from these investigations, if the effect of the support on the reaction cannot easily be identified, making comparison of the data on different supports very challenging. This ultimately hinders identifying the nature of the active site and identifying a mechanistic model that can be applied to the majority of the conjugated aldehydes.

Pradier and co-workers compared the gas phase hydrogenation of prenal on the Pt (111) and (110) surfaces and found the selectivity to be very structure sensitive(38). With adsorption of reactants being influenced by reactant pressure and surface geometry, also adding that monoatomic steps on a Pt (533) surface in comparison to the Pt (111) geometry can significantly modify adsorption characteristics. The selectivity difference between high

and low index sites is referenced in another study, in which blocking the high index sites with cobalt metal dopants promoted selectivity towards cinnamyl alcohol(39). In this study, the electronic effects of the metal dopant would also need to be considered as an influencing factor. Durndell *et al.* have attempted to gain mechanistic insight into the hydrogenation of cinnamaldehyde through kinetic mapping(26). The report concluded that cinnamaldehyde hydrogenation is structure in-sensitive with respect to metallic platinum, but a high selectivity towards the unsaturated alcohol requires large metal ensembles.

6.1.4 Influence of the Catalyst and Support on Selectivity

Although this is not an area of concern for this particular study, the nature of the support and the catalytic material employed can result in stark contrasts in selectivity. Enriching the surface with electrons through the interaction of an active support such as graphite or TiO₂, which tend to favour back-bonding interactions with the π^*_{CO} to a larger extent than with the π^*_{CC} , favours C=O coordination. It has been established that the polarity of the support influences the selectivity of the reaction. By comparison, the polar SBA-15 mesoporous silica is superior in enhancing the hydrogenation of the C=O bond than weakly hydroxylated, fumed, low area silica support. Hydrogen pressure also influences the selectivity of the reaction, regardless of the type of support employed. For example, increasing hydrogen pressure from 1 to 10 bar induced a drastic alteration in the reaction pathway, with predominantly C=C hydrogenation at 1 bar to >90% C=O at 10 bar. This significant selectivity promotion was attributed to surface crowding effects favouring less sterically demanding adsorption modes of cinnamaldehyde ($\text{di} - \sigma_{CO} \eta_2$). Kinetic modelling by Vergunst *et al.* highlighted adsorption, desorption and surface reactions all as rate controlling, with each having a complex dependency on hydrogen pressure(37). By employing metals with more extended d-bands like osmium or iridium the repulsive four-electron interactions with the surface are increased(40, 41), so the binding of the C=C bond is decreased. This is to the contrary on a palladium surface, which is widely employed to reduce C=C double bonds (42-44).

6.1.5 Influence of Substituent Groups on Selectivity

The issue of steric demands directing adsorption is a common explanation in the differing adsorption modes of the highlighted α , β -unsaturated aldehydes. Comparison between crotonaldehyde and prenal indicates the role of the methyl group in decreasing the hydrogenation rate of the C=C bond(45). The aromatic ring of cinnamaldehyde is also shown to have the same effect, and it has been calculated theoretically that the closest approach of the aromatic ring is 0.3 nm(29). A closer approach is prevented by an energy barrier which, on a flat surface hinders the approach of the C=C bond. This is not observed on small nanoparticles as the C=C bond interaction is not disrupted; this concept is demonstrated in Figure 6.5.

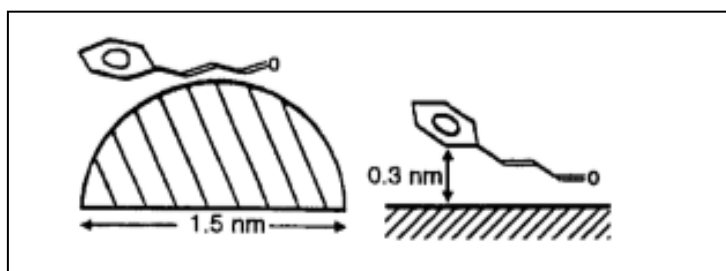


Figure 6.5: Adsorption of cinnamaldehyde on flat and small nanoparticle surfaces(29)

The theory surrounding the presence of the energy barrier, accounts for the contrasting results reported by Zhu and Zaera(27). With the small and relatively narrow size distribution of 1.5 to 2.5 nm used in the study adhering to the approach restraints of the aromatic, while not impeding the interaction of the C=C bond with the catalyst surface.

The influence of the catalyst surface on the pathway of the reaction remains a convoluted subject. Durndell *et al.* stated a compelling argument that the turn over frequency (TOF) for cinnamaldehyde hydrogenation was independent of surface structure, and in the face of conflicting literature highlighted errors in characterisation of the active surface and size distributions employed. This does raise the issue of the quality of the nanoparticles used in such studies and the high level of control required to produce nanoparticles with remotely comparable structure to a single crystal surface. Serrano-Ruiz *et al.* have demonstrated an ability to produce nanoparticles with a high level of morphological control and have extensively characterised the surfaces of the nanoparticles using a combination of CO

adsorption/desorption, cyclic voltammetry, TEM and Bi/Ge adsorption (28). These methods not only enabled determination of the number of active sites, but also allowed quantitative assessment of the number of low coordination sites and highly coordinated terraces. Significantly, Serrano-Ruiz *et al.* concluded that the TOF was face dependent for cinnamaldehyde and crotonaldehyde hydrogenation(28), (the TOF trend identified was Pt(100) >Pt(111)>Pt), which conflicts with the work of Durndell *et al.* who concluded this reaction is face independent(26). This work brings a significant aspect of the reaction into question and demonstrates a need for further fundamental research into this field.

While focusing research to obtain detailed information about an aspect of the reaction is necessary, it is also important to consider the reaction as a whole and how interactions of the molecule with the surface in the initial stages of the reaction influences the subsequent steps of the reaction towards completion. A mono-hydrogenated product of prenal is 3-methyl-butenol, which adsorbs in the η_1 on-top geometry through the lone pair of the oxygen on a Pt {111} surface. This adsorption mode is lower in energy than that of the di- σ_{CO} mode of prenal, which limits the production of the saturated alcohol 3-methyl-butanol(46). This limitation is only alleviated at high conversion or low partial pressure of prenal (or similarly cinnamaldehyde). Acrolein follows a different pathway, via the preferential hydrogenation of the C=C bond yielding the saturated aldehyde (propanal). Propanal coordinates to the Pt {111} surface through a di- σ_{CO} interaction and can be competitively desorbed by the presence of Acrolein on the surface. It was previously established that a tetrahapto η_4 form was most stable on the Pt {100} surface, being less hybridised and lying flatter on the surface than previously mentioned di- σ adsorption modes. A consequence of this position on the surface means the methyl substituents are more susceptible to dehydrogenation, yielding cracking products. As well as a dehydrogenation reaction, it is possible for a Pt-H bonding interaction to occur between the methyl group and the surface. Knowledge of the aforementioned bonding traits can be exploited to influence selectivity. Examples include increasing the partial pressure of the reactant to coordination towards to the more selective, less stable di- σ_{CO} mode.

The literature is divided on whether the selectivity of cinnamaldehyde hydrogenation is influenced by surface structure. This has been further obscured by additional factors proposed as having an influence on selectivity. A fundamental spectroelectrochemical

approach to this issue may give valuable insight into the adsorption of cinnamaldehyde on different platinum surfaces.

6.2 Results and Discussion

6.2.1 Cyclic Voltammetry Investigation into Cinnamaldehyde adsorption

Initial investigations into the interaction of cinnamaldehyde (CALD) and the mono-hydrogenated derivatives (hydrocinnamaldehyde (HCALD), cinnamyl alcohol (COL)) with differing platinum single crystal surfaces ($\{100\}$, $\{111\}$, $\{110\}$) was carried out by probing surface coverages through cyclic voltammetry (figure 6.6).

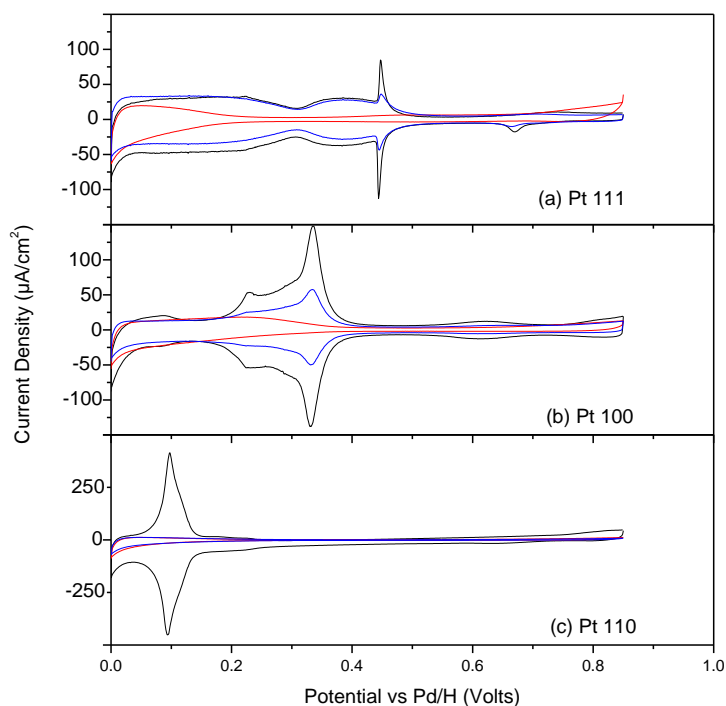


Figure 6.6: CVs of Pt basal electrodes in 0.1 M H₂SO₄ (sweep rate 50 mV s⁻¹) before adsorption of CALD (black curve), after exposure to CALD for 1 minute (red curve), and after CALD adsorption followed by hydrogen evolution at -0.1 V (blue curve): (a) Pt{111}; (b) Pt{100}; (c) Pt{110}.

Figure 6 shows for each surface that the hydrogen adsorption area is significantly attenuated and surface specific features are absent after exposure to cinnamaldehyde. In the case of the Pt {111} surface, after a short period of hydrogen evolution, the surface returns to a near pristine state. The reappearance of the rounded peak between 0.32 – 0.44V suggests the presence of clean {111} terraces, furthermore the sharp peak at 0.44V, also referred to as the “Butterfly peak”, demonstrates return of the long range bi-dimensional order of the {111} terraces after hydrogen evolution. Whilst this peak is broadened and less intense than in the background voltammogram, it is sufficient evidence to state that the structure of the Pt {111} surface is largely preserved after cinnamaldehyde adsorption and subsequent hydrogenation. Similar behaviour is qualitatively observed for the Pt {100} surface, albeit to a lesser extent, with the peak at 0.34V related to {100} bi-dimensional terraces and the shoulders at 0.23V relating to sites close to steps on the {100} terrace, both of which grow in intensity after hydrogenation. The {110} surface behaved differently to the {111} and {100} surfaces, in that the characteristic {110} type site peak at 0.1V was not even partially recovered after hydrogen evolution, suggesting irreversible blocking of the platinum sites. However, stability and surface contamination with impurities was found to present a major issue with the {110} surface in this work, so this data should be interpreted with caution. Nevertheless, these results allude to differing behaviour of cinnamaldehyde on each surface respectively and, considering the result for the {110} surface, cinnamaldehyde appears to behave differently on step sites compared to terraces.

Pt Surface	Background Charge/ $\times 10^{-4}$ C	After 10mM CALD		After 1 minute HER	
		Charge/ $\times 10^{-4}$ C	% CALD Coverage	Charge/ $\times 10^{-4}$ C	% CALD Coverage
Pt{111}	2.023	1.472	27	1.997	2
Pt{100}	2.244	0.539	76	1.186	47
Pt{110}	1.022	0.082	92	0.092	91

Table 6.5: Cinnamaldehyde coverage comparison between the platinum basal planes

Table 6.2 summarises the coverage of a 10mM solution of cinnamaldehyde on the three basal surfaces of platinum. These results were achieved by measuring the differences in charges between the three recorded conditions of each basal plane. As the area of the

single crystal is known charge density can be used for the CV, normalising each surface by area for direct comparison. Comparisons can be made between the surface in the clean, coated and post hydrogen evolution states. The coverages between the surfaces drastically vary. The {111} surface exhibits the lowest initial coverage after exposure to CALD and hydrogen evolution results in almost complete recovery of the clean platinum surface. By contrast, the {110} surface is blocked considerably by CALD adsorption and most of the adsorbates remain after hydrogen evolution. The {100} surface also has considerable CALD coverage, but can remove the adsorbate to some extent. This data suggests fundamental differences between the interaction with CALD with the different platinum surfaces, including the tendency for CALD to undergo desorption under hydrogenation conditions. Taking into consideration the extended Hückel type calculations on model {111} and {100} surfaces by Delbecq and Sautet(363), the binding energies of each preferred adsorption configuration on each specific surface can explain the contrasting coverages of cinnamaldehyde. On the Pt {111} surface the preferred di- σ_{CO} adsorption mode of cinnamaldehyde has a calculated binding energy of -14.1 Kcal/mol. The favoured η_4 adsorption model on the Pt {100} surface has a much higher binding energy of -26.1 Kcal/mol. Hence, the increased stability associated with the Pt {100} surface could be a plausible explanation for the increased surface coverage of cinnamaldehyde and the larger residual coverage after the brief hydrogenation period. It should also be taken into consideration that the coadsorption of hydrogen will be limited at high surface coverages of cinnamaldehyde, further limiting hydrogenation. This observation would appear to conflict with the structure insensitivity reported by Durndell *et al.*(26), although the higher TOF for CALD hydrogenation on Pt{100} compared to Pt(111) reported by Serrano-Ruiz *et al.* (28) may be linked to the stronger interaction observed above. However, it is important to stress that rate is not necessarily related to adsorption energy.

6.2.2 Cyclic Voltammetry Investigation into Cinnamyl Alcohol and Hydrocinnamaldehyde Adsorption.

The hydrogenation of cinnamaldehyde is a very complex reaction, the partially hydrogenated states playing prominent roles in the reaction. With the possibility of readsorption and producing undesirable hydrogenated states, analysing the interactions of two partially hydrogenated states on the Pt {100} and {111} surfaces would be a worthwhile endeavour. Due to ambiguities in the experimental stability and reliability of Pt{110} electrodes, this surface was not studied further in this chapter. The same experiments carried out for cinnamaldehyde were applied to the mono-hydrogenated derivatives hydrocinnamaldehyde and cinnamyl alcohol.

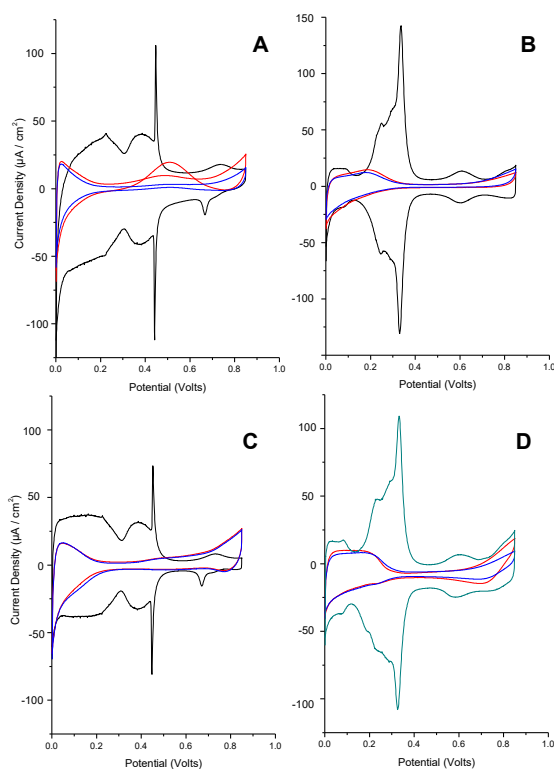


Figure 6.7: CVs of Pt basal electrodes in 0.1 M H_2SO_4 (sweep rate 50 mV s^{-1}) before adsorption of CALD derivative (black curve), after exposure to CALD derivative for 5 s (red curve), and after CALD derivative adsorption followed by hydrogen evolution at -0.1 V (blue curve): (A) Pt{111} hydrocinnamaldehyde; (B) Pt{100} hydrocinnamaldehyde; (C) Pt{111} cinnamyl alcohol; (D) Pt{100} cinnamyl alcohol.

The cyclic voltammograms shown in Figure 6.7 exhibit very similar characteristics to the voltammograms in Figure 6 for the adsorption of cinnamaldehyde. Upon the adsorption of the respective cinnamaldehyde derivative most of the characteristic peaks of the {100} and {111} surfaces are obscured. Each CV exhibits some degree of an anodic peak at higher potentials, which is a plausible and well-studied oxidation reaction pathway(47, 48). An interesting feature of CV (A) in Figure 6.7 is a peak that arises around 0.55V on the reverse sweep/ Although the precise origin of this behaviour is ambiguous, it is likely associated with the reduction of platinum oxide formed during the forward scan, the removal of which exposes fresh platinum sites for hydrocinnamaldehyde catalytic electro-oxidation.

Pt Surface	Background Charge/ $\times 10^{-4}$ C	After 10 mM HCALD		After 1 minute HER	
		Charge/ $\times 10^{-4}$ C	% HCALD Coverage	Charge/ $\times 10^{-4}$ C	% HCALD Coverage
Pt{111}	2.533	0.052	98	0.053	98
Pt{100}	2.228	0.370	83	0.829	63

Table 6.6: Coverage of Hydrocinnamaldehyde on Pt{111} and Pt{100} surfaces.

Pt Surface	Background Charge/ $\times 10^{-4}$ C	After 10 mM COL		After 1 minute HER	
		Charge/ $\times 10^{-4}$ C	% COL Coverage	Charge/ $\times 10^{-4}$ C	% COL Coverage
Pt{111}	2.747	1.313	52	1.406	49
Pt{100}	2.418	1.629	33	1.696	30

Table 6.7: Coverage of Cinnamyl alcohol on Pt{111} and Pt{100} surfaces.

The data from Tables 6.3 and 6.4 demonstrates some behavioural trends of the mono-hydrogenated derivatives of the Pt {111} and {100} surfaces, which include:

- Higher coverages of hydrocinnamaldehyde than cinnamyl alcohol on both surfaces.

- Higher coverages of both hydrocinnamaldehyde and cinnamyl alcohol on Pt {111} than on Pt {100}.
- Minimal displacement of cinnamyl alcohol on both {111} and {100} surfaces after hydrogen evolution.
- Hydrocinnamaldehyde is significantly displaced on the Pt {100} surface, however a negligible coverage change occurs on the Pt {111} surface.

Cinnamyl alcohol shows similar behaviour on the two surfaces, however the interaction of hydrocinnamaldehyde with platinum appears to be stronger and more structure sensitive. The increased stability of both adsorbates on the Pt {111} surface could play a vital role in directing the hydrogenation pathway. Regardless of the favourability of the first preferential hydrogenation step, if the mono-hydrated derivative has difficulty desorbing from the surface then isolating this product will be challenging. Research in this area is complex and sparse, but an interesting article on the topic has been provided by Loffreda *et al*(49). The article delves into the numerous viable pathways for the hydrogenation of acrolein on a Pt {111} surface. This work introduces a theoretical approach that shows the attack on the C=O moiety is always preferred over the C=C functional group on the Pt {111} surface, through a mechanism intermediate between Langmuir-Hinshelwood and Rideal-Eley classical schemes. This study has attributed the preferential activity of the C=O bond to the existence of precursor state, where hydrogen can coadsorb closer to the partially de-coordinated molecule. A significant secondary point raised in the article is that the barrier for desorption of the unsaturated alcohol was markedly higher than the saturated aldehyde, which was key in controlling selectivity. The very small displacement of cinnamyl alcohol under hydrogen evolution conditions compared to hydrocinnamaldehyde (at least in the case of Pt{100}) presented in Table 6.3 appears consistent with this.

It is also worth highlighting that, with hydrocinnamaldehyde coverages close to saturation (98%) in the case of Pt{111}, coadsorption of hydrogen onto the platinum surface would be limited and hence further hydrogenation would be restricted. This result therefore adds further legitimacy to the prescribed notion that the C=C hydrogenation can be “switched off” rapidly during the early stages of cinnamaldehyde hydrogenation, due to the possibility of surface crowding by strongly bound adsorbates. The differences in the coverages of hydrocinnamaldehyde between {100} and {111} surfaces, may therefore allude to some

possible structure sensitivity in terms of hydrogenation selectivity. This can only be proposed tentatively as this research lacks catalytic testing and analysis of the products.

6.2.2 SERS Investigation of Cinnamaldehyde Hydrogenation on Platinum

With very subtle differences in the structures of cinnamaldehyde, cinnamyl alcohol and hydrocinnamaldehyde, it can be challenging to differentiate the involvement of each molecule during hydrogenation reactions. The primary difference is of course the presence or absence of conjugated C=O and C=C bonds. Molecular spectroscopy can provide useful insights into these functional groups, particularly because of its sensitivity to the local chemical environment, molecular orientation and, where surfaces are involved, binding strength. Hence numerous vibrational spectroscopy studies have been published which focus on the hydrogenation of cinnamaldehyde(50-52).

Molecule	ν (C=C)/ cm^{-1}	ν (C=O)/ cm^{-1}
Cinnamaldehyde	1629	1673
Cinnamyl Alcohol	1660	-
Hydrocinnamaldehyde	-	1720

Table 6.5: Raman shift comparison of the key moieties associated with cinnamaldehyde and its hydrogenated derivatives(53).

Table 6.5 summarises the associated Raman shifts for the molecules of interest. The differences in the positions of the bands can be accounted for by the red shift associated with conjugation of the molecule. These values correspond to the bulk chemical, but it is important to understand that the wavenumber of specific bands can be shifted through interactions with the catalyst surface, be they due to steric or electronic effects(54). For example, in the case of adsorption on Au@Pt core-shell nanoparticles, a blue-shift has been shown to occur with differing shell thicknesses (55). Furthermore, with regards to hydrogenation reactions, the orientation of adsorbed molecules in the presence and absence of co-adsorbed hydrogen can play an important role in the spectral behaviour observed, which can be correlated with catalytic activity or selectivity.

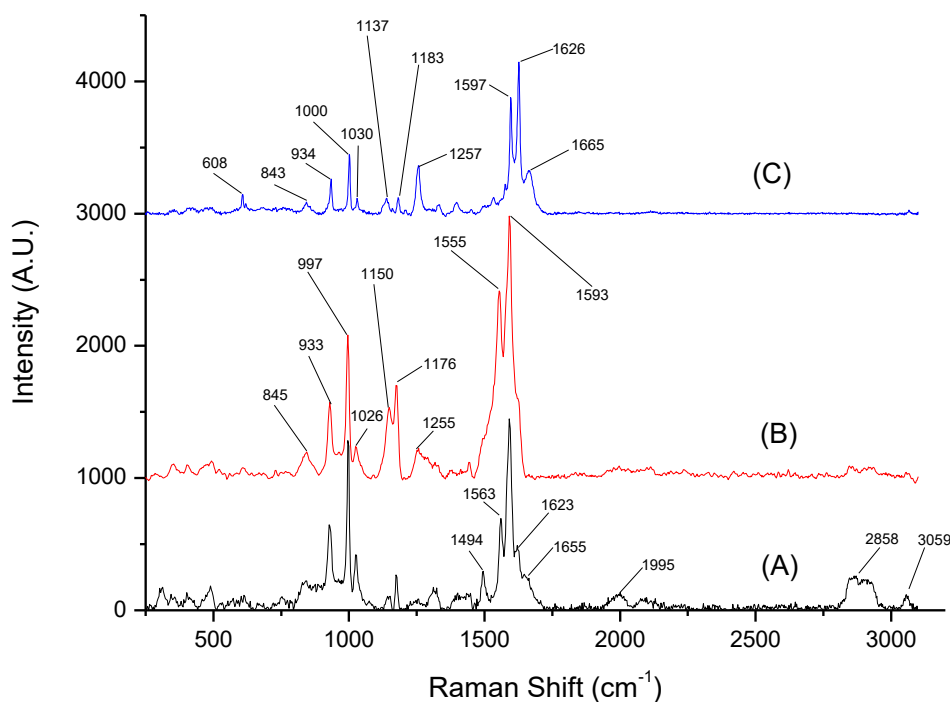


Figure 6.8: SERS spectra of cinnamaldehyde on Au@Pt in A) HER Potentials, B) double layer potentials, C) saturated platinum surface.

All The notable peaks of the SERS spectra are assigned stretching modes in table 6.6. Comparison of spectra (A) and (B) from Figure 6.8 gives an insight into the influence of co-adsorbed hydrogen on the orientation of the cinnamaldehyde. As expected, many of the peaks that are present at double layer potentials are also observed at hydrogen evolution potentials. However, the peak associated with the aldehyde C=O stretch (1665 cm^{-1}) is present at the hydrogen evolution potential, but is absent at double layer potentials. This observation could be considered counterintuitive in that one might expect the loss of this band if the aldehyde group was reduced at hydrogen evolution potentials. However, it is possible that the C=O bond is parallel to the platinum surface at double layer potentials, resulting in a Raman silent stretch, whilst this group may tilt towards the surface in the presence of co-adsorbed hydrogen, satisfying the surface selection rule and leading to observation of this Raman band. The band assigned to the C=C stretch of the conjugated aldehyde (1626 cm^{-1}) is present at hydrogenation potentials, but may also be present as a shoulder in the double layer potential spectra. The intensity of both stretches is diminished

compared to the multilayer (bulk) spectra (C), with the aromatic ring stretching modes dominating in all cases. The final notable peaks present in the SER spectra of cinnamaldehyde on Au@Pt nanoparticles are at 1995 cm^{-1} and 2858 cm^{-1} relating to an on-top C \equiv O and C-H stretch respectively. These peaks may be a sign of cracking products formed mostly under hydrogen evolution conditions, with unwanted side reaction known to take place on platinum surfaces(359). It is also possible that these peaks are due to other impurities on the surface, however their decrease in intensity at double layer potentials suggests this is unlikely.

(A) HER/ cm^{-1}	(B) Double Layer/ cm^{-1}	(C) Saturated (Bulk) / cm^{-1}	Assignment
-	-	608	C-H out of plane deformation (benzene), In-plane ring deformation
844	845	843	C-H out of plane deformation (benzene)
933	933	934	Cl-O Perchlorate (electrolyte)
997	997	1000	C=C stretching Benzene
1026	1026	1030	=CHC twist, =CH wag
1150	1150	1137	Meta-CH, Para-CH In-plane bend
1176	1176	1183	=C-H In-plane deformation (benzene)
-	1255	1257	=C-H In-plane deformation (benzene)
1494	-	-	C=C bending mode of benzene
1563	1555	-	C=C stretching mode of benzene
1593	1593	1597	Benzene ring deformation stretch
1623	-	1626	C=C Aldehyde Stretch

1655	-	1665	C=O Aldehyde Stretch
1995	-	-	Terminal C≡O
2858	-	-	C-H Stretch
3059	-	-	Aromatic =C-H stretch, possible O-CH stretch

Table 6.6: SER Spectra peak assignment and comparison for HER, double layer and bulk cinnamaldehyde

6.3 Conclusion and further work

The electrochemical section of this investigation appears to have demonstrated a difference in adsorption of cinnamaldehyde on the platinum basal planes. With a possible difference in adsorption between terrace and defect sites, but this is a very tentative proposal. These results do provide grounds for further investigation into the structure sensitivity of the reaction. With uncertainty in the literature and a lack of research on well-defined platinum single crystal surfaces, the use of SHINERS on platinum single crystal surfaces would provide valuable insight into the interactions of cinnamaldehyde with the platinum catalyst surface. However, this was beyond the scope of the investigation.

6.4 - References

1. M. Carter, in *ABSTRACTS OF PAPERS OF THE AMERICAN CHEMICAL SOCIETY*. (AMER CHEMICAL SOC 1155 16TH ST, NW, WASHINGTON, DC 20036, 1997), vol. 213, pp. 99-FUEL.
2. P. J. Walsh, M. C. Kozlowski, *Fundamentals of asymmetric catalysis*. (University Science Books, 2009).
3. K. Bauer, D. Garbe, H. Surburg, *Common fragrance and flavor materials: preparation, properties and uses*. (John Wiley & Sons, 2008).
4. J. Magano, J. R. Dunetz, Large-scale carbonyl reductions in the pharmaceutical industry. *Organic Process Research & Development* **16**, 1156-1184 (2012).
5. K. Weissmehl, *Industrial organic chemistry*. (John Wiley & Sons, 2008).
6. H. U. Blaser *et al.*, Selective hydrogenation for fine chemicals: recent trends and new developments. *Advanced Synthesis & Catalysis* **345**, 103-151 (2003).
7. M. S. Ide, B. Hao, M. Neurock, R. J. Davis, Mechanistic Insights on the Hydrogenation of α,β -Unsaturated Ketones and Aldehydes to Unsaturated Alcohols over Metal Catalysts. *ACS Catalysis* **2**, 671-683 (2012).
8. G. Bond, G. Webb, P. Wells, J. Winterbottom, Patterns of behavior in catalysis by metals. *Journal of Catalysis* **1**, 74-84 (1962).
9. C. Baddeley, Fundamental investigations of enantioselective heterogeneous catalysis. *Topics in catalysis* **25**, 17-28 (2003).
10. C. J. Kliewer, M. Bieri, G. A. Somorjai, Hydrogenation of the α, β -unsaturated aldehydes acrolein, crotonaldehyde, and prenal over Pt single crystals: a kinetic and sum-frequency generation vibrational spectroscopy study. *Journal of the American Chemical Society* **131**, 9958-9966 (2009).
11. S. Galvagno, G. Capannelli, G. Neri, A. Donato, R. Pietropaolo, Hydrogenation of cinnamaldehyde over Ru/C catalysts: effect of Ru particle size. *Journal of molecular catalysis* **64**, 237-246 (1991).
12. M. Lashdaf, A. Krause, M. Lindblad, M. Tiitta, T. Venäläinen, Behaviour of palladium and ruthenium catalysts on alumina and silica prepared by gas and liquid phase deposition in cinnamaldehyde hydrogenation. *Applied Catalysis A: General* **241**, 65-75 (2003).
13. M. Lashdaf, J. Lahtinen, M. Lindblad, T. Venäläinen, A. Krause, Platinum catalysts on alumina and silica prepared by gas-and liquid-phase deposition in cinnamaldehyde hydrogenation. *Applied Catalysis A: General* **276**, 129-137 (2004).
14. F. Delbecq, P. Sautet, Competitive C • C and C • O Adsorption of α - β -Unsaturated Aldehydes on Pt and Pd Surfaces in Relation with the Selectivity of Hydrogenation Reactions: A Theoretical Approach. *Journal of Catalysis* **152**, 217-236 (1995).
15. V. Ponec, On the role of promoters in hydrogenations on metals; α, β -unsaturated aldehydes and ketones. *Applied Catalysis A: General* **149**, 27-48 (1997).
16. V. Satagopan, S. B. Chandalia, Selectivity aspects in the multi-phase hydrogenation of α, β -unsaturated aldehydes over supported noble metal catalysts: Part II. *Journal of chemical technology and biotechnology* **60**, 17-21 (1994).
17. C. A. Schoenbaum, D. K. Schwartz, J. W. Medlin, Controlling the surface environment of heterogeneous catalysts using self-assembled monolayers. *Accounts of chemical research* **47**, 1438-1445 (2014).
18. K. R. Kahsar, D. K. Schwartz, J. W. Medlin, Control of metal catalyst selectivity through specific noncovalent molecular interactions. *Journal of the American Chemical Society* **136**, 520-526 (2013).
19. F. Zaera, G. Somorjai, Hydrogenation of ethylene over platinum (111) single-crystal surfaces. *J. Am. Chem. Soc.:(United States)* **106**, (1984).

20. G. F. Santori, M. L. Casella, O. A. Ferretti, Hydrogenation of carbonyl compounds using tin-modified platinum-based catalysts prepared via surface organometallic chemistry on metals (SOMC/M). *Journal of Molecular Catalysis A: Chemical* **186**, 223-239 (2002).
21. C. Barroo, Y. De Decker, T. Visart de Bocarmé, N. Kruse, Complex oscillation patterns during the catalytic hydrogenation of NO₂ over platinum nanosized crystals. *The Journal of Physical Chemistry C* **118**, 6839-6846 (2014).
22. S. Siegel, Heterogeneous catalytic hydrogenation of C=C and C≡C. *Comprehensive Organic Synthesis; Trost, BM, Fleming, I., Eds*, 417-442 (1991).
23. M. Arai, Y. Takada, Y. Nishiyama, Effects of metal particle size in gas-phase hydrogenation of acetonitrile over silica-supported platinum catalysts. *The Journal of Physical Chemistry B* **102**, 1968-1973 (1998).
24. P. Maity, S. Basu, S. Bhaduri, G. K. Lahiri, Superior performance of a nanostructured platinum catalyst in water: Hydrogenations of alkenes, aldehydes and nitroaromatics. *Advanced Synthesis & Catalysis* **349**, 1955-1962 (2007).
25. V. Pandarus, R. Ciriminna, F. Beland, M. Pagliaro, A new class of heterogeneous platinum catalysts for the chemoselective hydrogenation of nitroarenes. *Advanced Synthesis & Catalysis* **353**, 1306-1316 (2011).
26. L. J. Durndell *et al.*, Selectivity control in Pt-catalyzed cinnamaldehyde hydrogenation. *Scientific reports* **5**, (2015).
27. Y. Zhu, F. Zaera, Selectivity in the catalytic hydrogenation of cinnamaldehyde promoted by Pt/SiO₂ as a function of metal nanoparticle size. *Catalysis Science & Technology* **4**, 955-962 (2014).
28. J. Serrano-Ruiz *et al.*, Hydrogenation of α , β unsaturated aldehydes over polycrystalline, (111) and (100) preferentially oriented Pt nanoparticles supported on carbon. *Journal of Catalysis* **253**, 159-166 (2008).
29. A. Giroir-Fendler, D. Richard, P. Gallezot, Chemoselectivity in the catalytic hydrogenation of cinnamaldehyde. Effect of metal particle morphology. *Catalysis letters* **5**, 175-181 (1990).
30. K. Baron, D. Blakely, G. Somorjai, Low energy electron diffraction studies of the surface structures of adsorbed hydrocarbons (n-heptane, toluene, benzene, ethylene, and cyclohexane) on stepped (high miller index) platinum surfaces. *Surface Science* **41**, 45-66 (1974).
31. A. Morgan, G. Somorjai, Low-Energy Electron-Diffraction Studies of the Adsorption of Unsaturated Hydrocarbons and Carbon Monoxide on the Platinum (111) and (100) Single-Crystal Surfaces. *The Journal of Chemical Physics* **51**, 3309-3320 (1969).
32. J. Anderson, N. Avery, The mechanism of isomerization of aliphatic hydrocarbons at a platinum surface. *Journal of Catalysis* **7**, 315-323 (1967).
33. J. Basset, G. Dalmai-Imelik, M. Primet, R. Mutin, A study of benzene hydrogenation and identification of the adsorbed species with PtAl₂O₃ catalysts. *Journal of Catalysis* **37**, 22-36 (1975).
34. S. Mukerjee, Particle size and structural effects in platinum electrocatalysis. *Journal of Applied Electrochemistry* **20**, 537-548 (1990).
35. H. J. Freund, J. Libuda, M. Bäumer, T. Risse, A. Carlsson, Cluster, facets, and edges: Site-dependent selective chemistry on model catalysts. *The Chemical Record* **3**, 181-201 (2003).
36. S. C. Tsang *et al.*, Engineering preformed cobalt-doped platinum nanocatalysts for ultrasensitive hydrogenation. *Acs Nano* **2**, 2547-2553 (2008).
37. T. Vergunst, F. Kapteijn, J. Moulijn, Kinetics of cinnamaldehyde hydrogenation—concentration dependent selectivity. *Catalysis today* **66**, 381-387 (2001).
38. C. Pradier, T. Birchem, Y. Berthier, G. Cordier, Hydrogenation of 3-methyl-butenal on Pt (110); comparison with Pt (111). *Catalysis letters* **29**, 371-378 (1994).

39. W. O. Oduro, N. Cailuo, K. M. K. Yu, H. Yang, S. C. Tsang, Geometric and electronic effects on hydrogenation of cinnamaldehyde over unsupported Pt-based nanocrystals. *Physical Chemistry Chemical Physics* **13**, 2590-2602 (2011).
40. J. Breen, R. Burch, J. Gomez-Lopez, K. Griffin, M. Hayes, Steric effects in the selective hydrogenation of cinnamaldehyde to cinnamyl alcohol using an Ir/C catalyst. *Applied Catalysis A: General* **268**, 267-274 (2004).
41. P. N. Rylander, D. R. Steele, Selective hydrogenation of α , β -unsaturated aldehydes to unsaturated alcohols over osmium catalysts. *Tetrahedron Letters* **10**, 1579-1580 (1969).
42. E. Erasmus, Hydrogenation of cinnamaldehyde over an ionic cobalt promoted alumina-supported palladium catalyst. *South African Journal of Chemistry* **66**, 00-00 (2013).
43. M. L. Toebes *et al.*, Support effects in the hydrogenation of cinnamaldehyde over carbon nanofiber-supported platinum catalysts: characterization and catalysis. *Journal of catalysis* **226**, 215-225 (2004).
44. J.-P. Tessonnier, L. Pesant, G. Ehret, M. J. Ledoux, C. Pham-Huu, Pd nanoparticles introduced inside multi-walled carbon nanotubes for selective hydrogenation of cinnamaldehyde into hydrocinnamaldehyde. *Applied Catalysis A: General* **288**, 203-210 (2005).
45. P. Beccat, J. Bertolini, Y. Gauthier, J. Massardier, P. Ruiz, Crotonaldehyde and methylcrotonaldehyde hydrogenation over Pt (111) and Pt₈₀Fe₂₀ (111) single crystals. *Journal of Catalysis* **126**, 451-456 (1990).
46. T. Birchem, C. M. Pradier, Y. Berthier, G. Cordier, Reactivity of 3-Methyl-Crotonaldehyde on Pt(111). *Journal of Catalysis* **146**, 503-510 (1994).
47. B. Podlovchenko, O. Petry, A. Frumkin, H. Lal, The behaviour of a platinized-platinum electrode in solutions of alcohols containing more than one carbon atom, aldehydes and formic acid. *Journal of Electroanalytical Chemistry (1959)* **11**, 12-25 (1966).
48. L. W. H. Leung, M. J. Weaver, Influence of adsorbed carbon monoxide on electrocatalytic oxidation of simple organic molecules at platinum and palladium electrodes in acidic solution: a survey using real-time FTIR spectroscopy. *Langmuir* **6**, 323-333 (1990).
49. D. Loffreda, F. Delbecq, F. Vigné, P. Sautet, Chemo- Regioselectivity in Heterogeneous Catalysis: Competitive Routes for CO and CC Hydrogenations from a Theoretical Approach. *Journal of the American Chemical Society* **128**, 1316-1323 (2006).
50. H. M. Badawi, W. Förner, Vibrational spectra and assignments of 3-phenylprop-2-en-1-ol (cinnamyl alcohol) and 3-phenyl-1-propanol. *Journal of Molecular Structure* **1003**, 62-66 (2011).
51. C.-M. Grimaud, D. Radosavkic, S. Ustaze, R. Palmer, Vibrational spectroscopy of cinnamaldehyde on graphite and supported Pd islands. *Applied surface science* **178**, 1-6 (2001).
52. J. Zakzeski, P. C. Bruijninx, B. M. Weckhuysen, In situ spectroscopic investigation of the cobalt-catalyzed oxidation of lignin model compounds in ionic liquids. *Green chemistry* **13**, 671-680 (2011).
53. G. Socrates, *Infrared and Raman characteristic group frequencies: tables and charts*. (John Wiley & Sons, 2004).
54. M. F. Mrozek, M. J. Weaver, Periodic trends in electrode-chemisorbate bonding: ethylene on platinum-group and gold electrodes as probed by surface-enhanced Raman spectroscopy. *The Journal of Physical Chemistry B* **105**, 8931-8937 (2001).
55. J.-F. Li *et al.*, Surface-enhanced Raman spectroscopy using gold-core platinum-shell nanoparticle film electrodes: toward a versatile vibrational strategy for electrochemical interfaces. *Langmuir* **22**, 10372-10379 (2006).

Chapter 7 - Conclusion

7.1 Introduction

This investigation focused on the interaction of adsorbed molecules on platinum surfaces during the hydrogenation process. This was achieved through a combinative spectroelectrochemical approach, which utilised Cyclic Voltammetry as an electrochemical technique and SERS/SHINERS as a spectroscopic technique. The SERS technique is a robust and very competent technique for spectroscopic analysis on polycrystalline platinum surfaces. However, the SHINERS technique has unlocked single crystal surfaces for spectroelectrochemical investigations. The intricate interactions of reactants with the catalytic surface can now be examined, with particular focus on potential surface sensitive catalytic reactions. *In situ* spectroelectrochemical investigations have been performed on the platinum single crystals and shape-controlled nanoparticles, for EP and cinnamaldehyde hydrogenation.

7.2 Hydrogenation of Ethyl Pyruvate

The hydrogenation of Ethyl Pyruvate on platinum catalysts is a very well-studied model reaction. By applying the SHINERS technique to the reaction, a new surface specific adsorption intermediate has been discovered. The η^2 intermediate species of EP was found to dwell on terrace sites, it was proposed that this intermediate is in an orientation that interacts favourably with the alkaloid modifier to achieve high enantiomeric excess(1). Suggesting that a high amount of well-ordered terrace sites is preferred for enantiodifferentiation. This proposed mechanism agrees with work produced by Baiker *et al* on the preferential adsorption behaviour of the cinchona alkaloid on terrace surface sites (2). However, this proposed mechanism doesn't account for the findings of Attard *et al*, that blocking defect sites of platinum nanoparticles lead to a decrease in enantiomeric excess for the reaction (3). Defect sites are also the origin for the formation of the HHS, if this intermediate state was to take part in enantioselective hydrogenation it must interact with the modifier prior to forming for the chirality to be imparted. This leads to a proposal that as well as the η^2 modifier interaction on the terrace sites an additional discriminatory

interaction can occur at defect sites. A “chiral pocket” could be formed by the quinuclidine overlapping or being in the vicinity of a defect site. Defect sites such as kinks have an associated chirality and in combination with the modifier would give rise to two chemically distinct docking positions for EP, namely $+/+$ and $+/-$ where $+$ signifies the handedness of CD and $+$ or $-$ the chirality of the kink site. As it is occurring on a defect site the initial hydrogen addition would be rapid, forming the HHS to be subsequently hydrogenated to the ethyl lactate product.

The same process was performed on shape-controlled platinum nanoparticles. The complexity of the EP hydrogenation reaction becomes more evident when transitioning from single crystal surfaces to viable catalytic surfaces. Unfortunately, impurities blighted the investigation but signs of the formation of the HHS was present in the SERS spectra for PAA cubic nanoparticles. This could be a significant observation as the PAA cubic nanoparticles have a high amount of terrace sites when compared to the tetrahedral nanoparticles which did not exhibit any sign of the HHS. It could be tentatively proposed that the HHS requires a combination of terrace and defect sites (such as a step) to form, which would complement the mechanism outlined from the previous chapter on single crystals. More work would be required to test this occurrence, perhaps acetic acid could be utilised as a solvent to combat the capping agent presence on the catalyst surface. Naturally this study would then investigate the behaviour when the modifier is co-adsorbed and bismuth doping of the shape-controlled nanoparticles could elucidate the role of defect sites in the enantioselective reaction.

The enantioselective hydrogenation of α , β -unsaturated aldehydes is another interesting catalytic reaction much like the Orito reaction. The hydrogenation is complex with competing reaction pathways of C=C and C=O hydrogenations. The structure sensitivity of the catalytic reaction is debated, but for the case of cinnamaldehyde selectivity towards cinnamyl alcohol increased with increased nanoparticle size up to a limit (4). The trend attributed to size and population increases of low index $\{111\}$ facets and decrease of the high coordination sites as the size of the nanoparticle increases. This was supported by adsorption data by Delbecq and Sautet, wherein cinnamaldehyde adsorption on platinum $\{111\}$ is most stable through the di- σ_{CO} adsorption mode and disrupts the π_{CC} adsorption mode (5). Comparisons can be made with the studies of Baiker with Orito reaction on

platinum surfaces. The implementation of the CV/SHINERS Spectro electrochemical technique to the enantioselective hydrogenation of Cinnamaldehyde was an exciting prospect, but due to time constraints no meaningful data was acquired on the date of writing this thesis.

7.3 Further Work

More analysis is required for the η^2 intermediate species of EP, to ascertain the role it plays in the reaction. Liquid chromatography or NMR analysis of the electrolyte solution after the intermediate is formed on the low index platinum surfaces may help to elucidate if the formation of the η^2 intermediate is beneficial for the enantiomeric excess of the reaction. Analysis of the reaction rate when either the η^2 intermediate or HHS is dominant on the surface may also give so useful mechanistic insights.

A different approach to the analysis of the intermediate species may help to acquire more information on the nature of the intermediate species. A combination of XPS and SHINERS could be a powerful technique to identify the species than gather molecular information at working conditions. Tian *et al* have employed a similar combinative technique to great effect for the investigation of CO oxidation over PtFe bimetallic nanoparticles (6). Another applicable technique is electrochemical tip enhanced Raman spectroscopy in conjunction with electrochemical scanning tunnelling microscopy, presented by Ren *et al* (7). This technique would be capable of detecting the outlined surface species, while characterising the surface environment in detail. If this spectroelectrochemical method was successfully implemented to the asymmetric systems probed in this thesis, the postulations of intermediate surface species being specific to terrace or defect sites can be properly elucidated. In general, integrating further techniques into a SEC approach to each system would be a worthwhile endeavour to garner as much information as possible on the systems in question. Expanding the single crystal substrates utilised in the reaction would also be beneficial, as presented in the research there is still a theoretical and technological shortfall when trying to recreate phenomena present on single crystal substrates on practical nanoparticle surfaces. A more detailed investigation into defect sites on single crystals

surfaces with an emphasis on pairs of chiral SC surfaces could be a fruitful further investigation.

Regarding electrochemical reactions in combination with SHINERS, it can sometimes be beneficial to be able to switch from acidic to alkaline solutions. An example would be the cleaning process for platinum shaped nanoparticles. The Au@SiO₂ nanoparticles degrade in alkaline solutions, but an aluminium coated gold nanoparticle can be used. This core-shell nanoparticle however, degrades in acidic solutions(8). A nanoparticle capable of SHINERS that could transition between acidic and aqueous media would be very beneficial, when coupled with electrochemistry. With the SHINERS technique still being a rather niche analytical technique few well established alternatives to the Au@SiO₂ or Au@Al₂O₃ nanoparticles are available. However, it has been reported that Ag@ZrO₂ nanoparticles have shown remarkably improved stability in both acidic and alkaline media when compared to the Au@SiO₂ nanoparticles (9, 10).

Finally, regarding the SHINERS technique as a powerful modern analytical tool. This thesis has demonstrated the influence SHINERS can have on developing the theory of interfacial catalytic interactions. The SHINERS method is enjoying widespread applications in significant catalytic, electrochemical and biological investigations (11). However, the future success of the SHINERS technique will be dependent on the theoretical and practical development of the method. From experience, a key area to address is the synthesis and application of the Au@SiO₂ nanoparticles. The wide size distribution of the gold nanoparticle cores and differences in silica coating thicknesses can lead to inconsistencies with the SERS hot spots. The drop casting method of applying the SHINERS particles to the nanoparticle surface can further compound the inconsistencies, thus, an alternative method that utilises printing or moulding would be preferential. The technique is constantly developing and expanding at a significant rate and will be a valuable analytical resource in the coming years.

7.4 References

1. S. Guan *et al.*, Structure Sensitivity in Catalytic Hydrogenation at Platinum Surfaces Measured by Shell-Isolated Nanoparticle Enhanced Raman Spectroscopy (SHINERS). *ACS Catalysis*, (2016).
2. E. Schmidt, A. Vargas, T. Mallat, A. Baiker, Shape-selective enantioselective hydrogenation on Pt nanoparticles. *Journal of the American Chemical Society* **131**, 12358-12367 (2009).
3. D. J. Jenkins *et al.*, Enantioselectivity and catalyst morphology: step and terrace site contributions to rate and enantiomeric excess in Pt-catalysed ethyl pyruvate hydrogenation. *Journal of Catalysis* **234**, 230-239 (2005).
4. S. C. Tsang *et al.*, Engineering preformed cobalt-doped platinum nanocatalysts for ultrasensitive hydrogenation. *Acs Nano* **2**, 2547-2553 (2008).
5. F. Delbecq, P. Sautet, Competitive C • C and C • O Adsorption of α - β -Unsaturated Aldehydes on Pt and Pd Surfaces in Relation with the Selectivity of Hydrogenation Reactions: A Theoretical Approach. *Journal of Catalysis* **152**, 217-236 (1995).
6. H. Zhang *et al.*, In situ dynamic tracking of heterogeneous nanocatalytic processes by shell-isolated nanoparticle-enhanced Raman spectroscopy. *Nature communications* **8**, 15447 (2017).
7. Z.-C. Zeng *et al.*, Electrochemical Tip-Enhanced Raman Spectroscopy. *Journal of the American Chemical Society* **137**, 11928-11931 (2015).
8. J.-F. Li *et al.*, Synthesis and characterization of gold nanoparticles coated with ultrathin and chemically inert dielectric shells for SHINERS applications. *Applied spectroscopy* **65**, 620-626 (2011).
9. H. Abdulrahman, Synthesis and characterisation of selected nanoresonators for Raman analysis of surfaces. (2017).
10. R. T. Tom *et al.*, Freely dispersible Au@ TiO₂, Au@ ZrO₂, Ag@ TiO₂, and Ag@ ZrO₂ core-shell nanoparticles: one-step synthesis, characterization, spectroscopy, and optical limiting properties. *Langmuir* **19**, 3439-3445 (2003).
11. P.-P. Fang, X. Lu, H. Liu, Y. Tong, Applications of shell-isolated nanoparticles in surface-enhanced Raman spectroscopy and fluorescence. *TrAC Trends in Analytical Chemistry* **66**, 103-117 (2015).